RIGA TECHNICAL UNIVERSITY

Igors Ušakovs

# SMART THERMAL MANAGEMENT OF ELECTRICAL EQUIPMENT

Doctoral Thesis

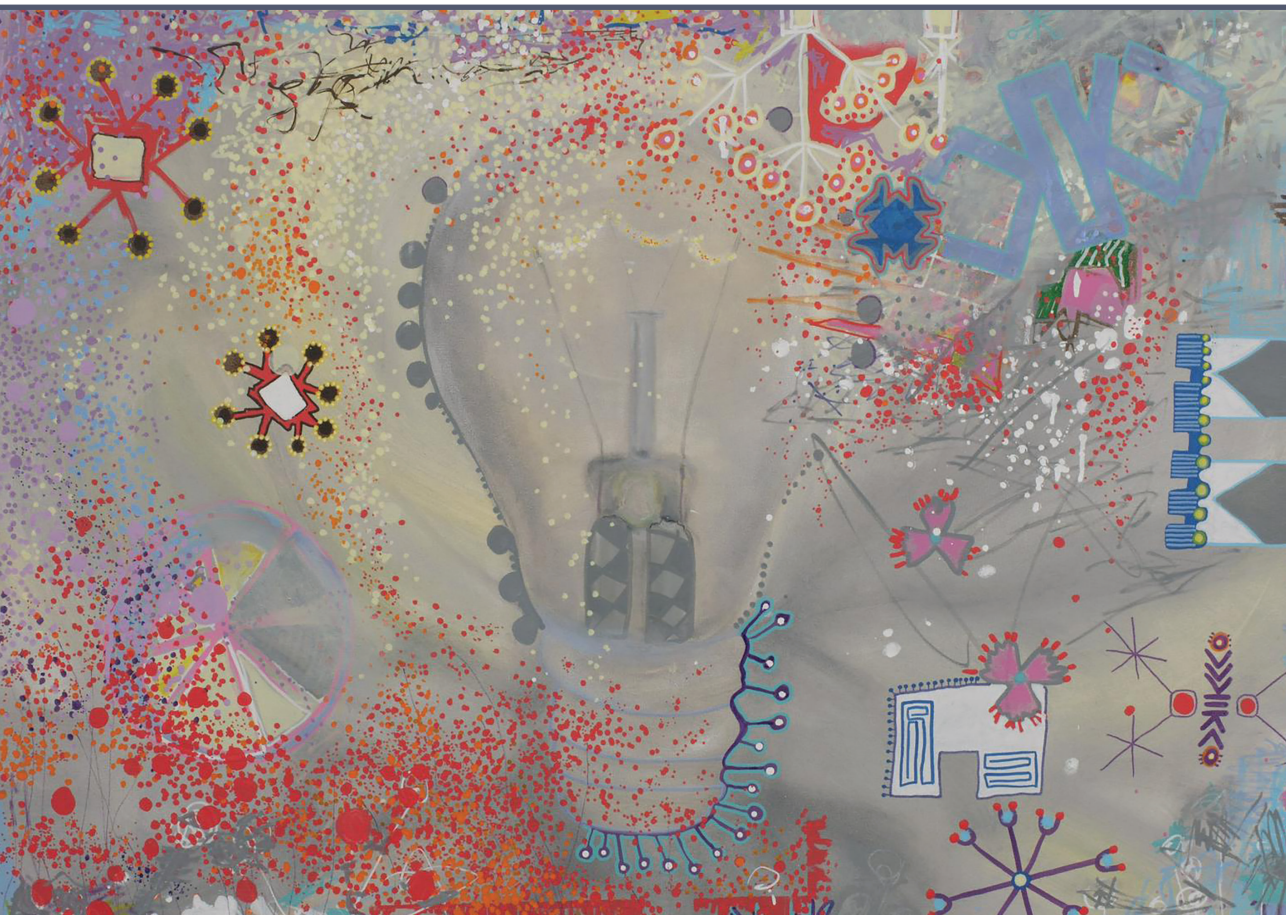

RTU Press
Riga 2026

**RIGA TECHNICAL UNIVERSITY**

Faculty of Computer Science, Information Technology and Energy
Institute of Industrial Electronics, Electrical Engineering and Energy

**IGORS UŠAKOVS**
Doctoral Student of Study Programme “Computerised Control of Electrical Technologies”

# SMART THERMAL MANAGEMENT OF ELECTRICAL EQUIPMENT

**Doctoral Thesis**

Scientific supervisor
Professor Dr. sc. ing.
ILYA A. GALKIN

Riga 2026

Ušakovs, I. Smart Thermal Management of Electrical Equipment, Doctoral Thesis. Riga: RTU Press, 2026. 176 p.

Published in accordance with the decision of the Promotion Council “P-14” of 30 March 2026, Minutes No. 04030-9.12/1.

The author expresses sincere gratitude to his colleagues at Allatherm for long-standing and fruitful collaboration in the field of two-phase heat-transfer system development.

Special appreciation is extended to Dr. Donatas Mishkinis and Mr. Luka Ivanovskis for their professional support, joint research efforts, and contribution to the development of experimental and engineering solutions.

This activity/work was supported by the EU Recovery and Resilience Facility within Project No 5.2.1.1.i.0/2/24/I/CFLA/003 “Implementation of consolidation and management changes at Riga Technical University, Liepaja University, Rezekne Academy of Technology, Latvian Maritime Academy and Liepaja Maritime College for the progress towards excellence in higher education, science and innovation” academic career doctoral grant (ID 1145).

Cover image by Kristīne Kutepova.

# DOCTORAL THESIS PROPOSED TO RIGA TECHNICAL UNIVERSITY FOR THE PROMOTION TO THE SCIENTIFIC DEGREE OF DOCTOR OF SCIENCE

To be granted the scientific degree of Doctor of Science (Ph. D.), the present Doctoral Thesis has been submitted for the defence at the open meeting of RTU Promotion Council "RTU P-14" on 29 May 2026, at 14.00 in the Conference Hall of RTU Conference and Sports Centre "Ronīši", Klapkalnciems, Engure County.

OFFICIAL REVIEWERS:

Professor Dr. habil. sc. ing. Leonīds Ribickis
Riga Technical University

Professor Dr. sc. techn. Dmitri Vinnikov
Tallinn University of Technology

Associate Professor, Ph.D Gytis Svinkunas
Kaunas University of Technology

DECLARATION OF ACADEMIC INTEGRITY

I hereby declare that the Doctoral Thesis submitted for the review to Riga Technical University for the promotion to the scientific degree of Doctor of Science (Ph. D.) is my own.

I confirm that this Doctoral Thesis had not been submitted to any other university for the promotion to a scientific degree.

Igors Ušakovs……. (signature)
Date: ……

The Doctoral Thesis has been prepared as a monograph. The Doctoral Thesis has been written in English. It consists of an Introduction, 5 Chapters, Conclusions, 84 Figures, 8 Tables, and 0 Appendices. The total number of pages is 176 (excluding appendices). The Bibliography contains 82 titles.

# ANOTĀCIJA

Promocijas darbs ir veltīts pasīvo divfāžu siltuma cilpu izmantošanas zinātniski pamatotas pieejas izstrādei kā universālai platformai elektroiekārtu viedajai termiskajai pārvaldīšanai.

Pētījuma aktualitāti nosaka mūsdienu elektroiekārtu un elektronisko sistēmu pieaugošais siltuma plūsmas blīvums un konstrukciju kompaktums, kas arvien biežāk pārsniedz tradicionālo dzesēšanas sistēmu iespējas. Atšķirībā no aktīvām dzesēšanas sistēmām, kurām nepieciešama ārēja enerģijas padeve un regulēšana, pasīvās divfāžu ierīces balstās uz fāžu pārejām, kapilārajiem spēkiem un gravitācijas iedarbību, nodrošinot enerģētiski neatkarīgu siltuma pārdali ar augstu uzticamību.

Darba mērķis ir formulēt fizikālos principus, matemātiskos modeļus un inženiertehniskās metodoloģijas, kas ļauj pāriet no specializētiem siltuma cilpu pielietojumiem uz universālām modulārām divfāžu dzesēšanas platformām, kuras iespējams integrēt dažādu klašu elektroiekārtās.

Pētījuma hipotēze paredz, ka tradicionālo dzesēšanas sistēmu aizstāšana ar atbilstoši projektētām pasīvām divfāžu siltuma cilpām būtiski maina elektroiekārtu termisko režīmu, nodrošinot paaugstinātu siltuma plūsmas blīvumu, uzlabotu efektivitāti, samazinātu konstrukcijas masu un palielinātu ekspluatācijas ilgumu.

Darba zinātniskā novitāte ietver viedās termiskās pārvaldīšanas koncepcijas formulēšanu kā pašregulējošu divfāžu termisko sistēmu klasi; modulāras daudziztvaikotāju arhitektūras izstrādi, balstītu uz "Altom" tehnoloģiju; stacionāra un pārejas režīma matemātisko modeļu izveidi cilpas tipa siltuma caurulēm (Loop Heat Pipe, LHP); termodinamiski konsekventas siltuma noplūdes un pārdzesēšanas interpretācijas formulēšanu; darba šķidruma kvalitātes parametru ieviešanu cilpas termosifoniem (Loop Thermosyphon, LTS); kā arī oriģinālas programmatūras "Altom-LHP" izstrādi siltuma cilpu projektēšanai un analīzei.

Darbā veikta pasīvo divfāžu ierīču (siltuma cauruļu, LHP, kapilāri darbināmu cilpu, LTS) salīdzinoša fizikālā analīze, parādot šķidruma un tvaika atdalītu transporta līniju un kapilārās cirkulācijas priekšrocības. Izstrādāts kvaziviendimensionāls LHP stacionārais modelis, balstīts uz enerģijas, masas un spiediena bilances vienādojumiem, iekļaujot siltuma apmaiņu ar apkārtējo vidi un gravitācijas ietekmi. Papildus formulēts pārejas režīma modelis, ņemot vērā kompensācijas kameras termisko dinamiku.

Piedāvātās pieejas ir eksperimentāli validētas četrās dažādu klašu elektroiekārtās: rumbā integrētā elektromotorā, LED gaismeklī, degvielas šūnu blokā un vilces elektromotorā. Rumbā integrētajam elektromotoram izstrādāta un pārbaudīta uz LHP balstīta dzesēšanas sistēma, kā arī piedāvāta jauna statora konstrukcija ar integrētu iztvaikotāja arhitektūru. LED gaismeklim realizēta un eksperimentāli pārbaudīta jauna siltuma cilpas caurules (HLP) koncepcija, kas apvieno klasiskās siltuma caurules un LHP īpašības. Degvielas šūnu pielietojumam izstrādāta konceptuāla, uz cilpas termosifona balstīta dzesēšanas arhitektūra, kā arī izgatavoti un testēti

prototipa iztvaikotāji.Vilces elektromotoram izstrādāta, izgatavota un eksperimentāli pārbaudīta dzesēšanas sistēma, kas balstīta uz sešiem cilpas termosifoniem.

Rezultāti apliecina, ka pasīvās divfāžu siltuma cilpas var kalpot kā universāla fizikāla un inženiertehniska platforma mērogojamai un enerģētiski neatkarīgai elektroiekārtu termiskajai pārvaldīšanai. Izstrādātās modulārās arhitektūras ļauj pāriet no lokāliem dzesēšanas risinājumiem uz daudziztvaikotāju divfāžu aukstās plāksnes sistēmām, kas piemērotas augstas jaudas un telpiski izkliedētām siltuma slodzēm.

Promocijas darbs pamato pasīvo divfāžu siltuma cilpu pielietošanas paplašināšanas iespējas ārpus tradicionālajām specializētajām jomām un izveido teorētisku un eksperimentālu pamatu to plašākai ieviešanai elektroinženierijas sistēmās.

# ABSTRACT

This Doctoral Thesis is devoted to the development of a scientifically grounded approach to the application of passive two-phase heat loops as a universal platform for Smart Thermal Management of electrical and electronic equipment.

The relevance of the research is determined by the continuous growth of heat-flux densities, and compactness of modern electrical devices, which increasingly exceed the capabilities of conventional single-phase cooling systems. While active cooling solutions require external energy input and control systems, passive two-phase devices rely on internal physical mechanisms—phase transitions, capillary forces, and gravity—providing energy-independent heat redistribution with high reliability.

The objective of the research is to formulate physical principles, mathematical models, and engineering methodologies enabling the transition from specialized heat-loop applications toward universal modular two-phase cooling platforms adaptable to different classes of electrical equipment.

The research hypothesis states that replacing conventional cooling systems with properly designed passive two-phase heat loops modifies the thermal regime of electrical devices in a way that leads to improved performance characteristics, including increased heat-flux density, enhanced efficiency, reduced mass, and extended operational lifetime.

The scientific novelty of the work includes the introduction of the concept of Smart Thermal Management as a class of self-regulating two-phase thermal systems; the proposal of a modular multi-evaporator architecture based on the “Altom” technology; the development of steady-state and transient mathematical models of loop heat pipes (LHPs); the formulation of a thermodynamically consistent interpretation of heat leak and subcooling; the introduction of working-fluid quality parameters for loop thermosyphons (LTSs); and the development of the original software tool “Altom-LHP” for loop design and analysis.

A comparative physical analysis of passive two-phase devices (heat pipes, LHPs, CPLs, LTSs) is performed, demonstrating the advantages of separated liquid–vapor transport lines and capillary-driven circulation. A quasi-one-dimensional steady-state model of LHP operation is developed, based on energy balance, pressure balance, and mass conservation equations, including heat exchange with the environment and gravitational effects. A transient model accounting for thermal dynamics of compensation chambers is also formulated.

The proposed approaches are experimentally validated on four different classes of electrical devices: an in-wheel electric motor, an LED luminaire, a fuel-cell stack and traction motor. For the in-wheel motor, an LHP-based cooling system and a novel stator-integrated evaporator architecture are developed and tested. For the LED luminaire, a new Heat Loop Pipe (HLP) concept combining features of heat pipes and LHPs is implemented and experimentally verified. For fuel-cell applications, a conceptual loop-thermosyphon-based cooling architecture is

developed, and prototype evaporators are fabricated and tested. For the traction motor, a cooling system based on six loop thermosyphons was developed, manufactured, and tested.

The results confirm that passive two-phase heat loops can serve as a universal physical and engineering platform for scalable, energy-independent thermal management. The developed modular architectures enable transition from localized cooling solutions to multi-evaporator “two-phase cold plate” systems suitable for high-power and spatially distributed heat loads.

The Thesis substantiates the feasibility of expanding the application domain of passive two-phase heat loops beyond traditional specialized fields and establishes a theoretical and experimental foundation for their broader implementation in electrical engineering systems.

# TABLE OF CONTENTS

# NOMENCLATURE AND ABBREVIATIONS

**Nomenclature**

| | |
|---|---|
| $A, B$ | Proportionality coefficients, parameters in the Churchill correlation |
| $C$ | Chisholm parameter |
| $C_{la}$ | Convection factor for laminar flow |
| $C_{tu}$ | Convection factor for turbulent flow |
| $C_s$ | Specific heat capacity of the structure |
| $c_p$ | Specific heat capacity at constant pressure |
| $c_{p,l}$ | Specific heat capacity of liquid at constant pressure |
| $c_{p,v}$ | Specific heat capacity of vapor at constant pressure |
| $c_{v,l}$ | Specific heat capacity of liquid at constant volume |
| $c_{v,v}$ | Specific heat capacity of vapor at constant volume |
| $d$ | Diameter |
| $D_{out}$ | Outer diameter |
| $D_{in}$ | Inner diameter |
| $D_{cc}$ | Compensation chamber diameter |
| $D_{sh}$ | Outer shield diameter of the compensation chamber |
| $E$ | Internal energy |
| $F$ | Auxiliary function |
| $F_m$ | Figure of merit |
| $f$ | Electric Current Frequency |
| $G$ | Overall thermal conductance |
| $G_{sdl}$ | Overall thermal conductance of saddle |
| $G_{LHP}$ | Overall thermal conductance of Loop Heat Pipe |
| $G_{sink}$ | Overall thermal conductance of heat sink |
| $g$ | Thermal conductance per unit length |
| $g_m$ | Thermal conductance per unit length of material |
| $g_{in}$ | Thermal conductance per unit length internal |
| $\mathcal{g}$ | Gravity acceleration |
| $H, h$ | Height |
| $h_{ev}$ | Specific enthalpy of vaporization |
| $K$ | Permeability |
| $K_{nc}$ | Proportionality coefficient for natural convection |
| $k_o$ | Spatial orientation factor |

| | |
|---|---|
| $L$ | Length |
| $L_w$ | Wick length |
| $L_{cc}$ | Compensation chamber length |
| $L_{cp}$ | Cold plate length |
| $M$ | Mass |
| $M_s$ | Mass of structure |
| $M_{sdl}$ | Interface mass |
| $\dot{m}$ | Mass flow rate |
| $N_{ev}$ | Number of capillary pumps |
| $Nu$ | Nusselt number |
| $P$ | Pressure |
| $P_{ev}$ | Vapor pressure in the evaporation zone |
| $P_{cd}$ | Vapor pressure in the condensation zone |
| $P_{cc}$ | Vapor pressure in the compensation chamber |
| $\Delta P$ | Loop pressure drop |
| $\Delta P_{ev}$ | Evaporator pressure drop |
| $\Delta P_{cd}$ | Condenser pressure drop |
| $\Delta P_{vl}$ | Vapor line pressure drop |
| $\Delta P_{ll}$ | Liquid line pressure drop |
| $\Delta P_b$ | Bayonet pressure drop |
| $Pr$ | Prandtl number |
| $\dot{Q}$ | Heat Flow |
| $\dot{Q}_{in}$ | Input heat flow from the heat source |
| $\dot{Q}_{ea}$ | Heat flow between the evaporator and the ambient |
| $\dot{Q}_{ca}$ | Heat flow between the compensation chamber and the ambient |
| $\dot{Q}_{ev}$ | Heat flow used for working-fluid evaporation |
| $\dot{Q}_{hl}$ | Heat leak to the compensation chamber |
| $\dot{Q}_{sc}$ | Heat of subcooling (heat carried into the compensation chamber by subcooled liquid from the condenser) |
| $\dot{Q}_{co}$ | Control heat flow from the heater on the compensation chamber |
| $R$ | Thermal resistance |
| $R_{sdl}$ | Interface thermal resistance |
| $R_{LHP}$ | Loop Heat Pipe thermal resistance |
| $R_{HL}$ | Thermal resistance of an alternative heat-leak path |
| $Ra$ | Rayleigh number |
| $Re$ | Reynolds number |
| $r_b$ | Bayonet radius |
| $r_p$ | Pore radius |

| | |
|---|---|
| $S$ | Area |
| $\Delta s$ | Discretization element size for condenser calculation |
| $S_x, s_x$ | Area per unit length |
| $S_{cp}$ | Cold plate area |
| $T$ | Temperature |
| $T_{ev}$ | Vapor temperature in the evaporator |
| $T_{cd}$ | Condensation temperature |
| $T_{vl}$ | Temperature of vapor in the vapor line |
| $T_{ll}$ | Temperature of liquid in the liquid line |
| $T_{cc}$ | Compensation chamber temperature |
| $T_{co}$ | Wick core temperature |
| $T_{amb}$ | Ambient environment temperature |
| $T_{sur}$ | Surface temperature |
| $T_{src}$ | Heat source temperature |
| $T_{sink}$ | Heat sink temperature |
| $T_f$ | Fluid temperature |
| $T_\sigma$ | Capillary limit temperature |
| $\Delta t$ | Time iteration step in non-stationary LHP model |
| $v$ | Fluid velocity |
| $V_{cc}$ | Compensation chamber volume |
| $X$ | Martinelli parameter |
| $\alpha$ | Film coefficient |
| $\delta$ | Skin-effect depth |
| $\delta_Q$ | Computational tolerance by heat flow |
| $\varepsilon$ | Emissivity |
| $\varphi$ | Wick porosity |
| $\phi^2$ | Two-phase Multiplier |
| $\sigma$ | Surface tension, Stephen-Boltzmann constant |
| $\Pi$ | Wet perimeter |
| $\lambda$ | Thermal conductivity |
| $\xi$ | Darcy friction factor |
| $\eta$ | Dynamic viscosity |
| $\eta_f$ | Fin efficiency |
| $\tau$ | Fin thickness, shear stress |
| $\chi$ | Vapor quality |

**Abbreviations**

| | |
|---|---|
| Amb | Ambient |
| BP | Bipolar Plate |
| CC | Compensation Chamber |
| CD | Condenser |
| CHP | Combined Heat and Power |
| CL | Catalyst Layer |
| CP | Cold Plate |
| CPL | Capillary Pumped Loop |
| ED | Electric Drive |
| EM | Electric Motor |
| EPS | Electric Propulsion System |
| EV | Evaporator |
| FC | Fuel Cell |
| GDL | Gas Diffusion Layer |
| HEV | Hybrid Electric Vehicle |
| HL | Heat Loop |
| HLP | Heat Loop Pipe |
| HP | Heat Pipe |
| LL | Liquid Line |
| LHP | Loop Heat Pipe |
| LTS | Loop Thermosiphon |
| MAFT | Microchannel Aluminium Flat Tubes |
| PCM | Phase Change Material |
| PEM | Proton Exchange Membrane |
| PEMFC | Proton Exchange Membrane Fuel Cell |
| LT- PEMFC | Low Temperature PEMFC |
| HT-PEMFC | High Temperature PEMFC |
| TS | Thermosiphon |
| TZ | Transport Zone |
| VL | Vapor Line |

# 1 INTRODUCTION

## 1.1 Relevance of Research

Thermal management is one of the key interdisciplinary challenges of modern engineering, determining the reliability, efficiency, and service life of electrical and electronic systems. In a broad sense, thermal management encompasses the set of methods and technical means used to maintain a prescribed temperature regime of devices. In a narrower sense, thermal management systems are understood primarily as cooling systems of various types. The increase in specific power, device miniaturization, and growing heat-flux densities lead to situations where conventional cooling methods increasingly become insufficient. According to data reported in [1], temperature-related factors are responsible for more than half of electronic equipment failures, highlighting the critical importance of improving thermal management systems.

In other words, despite the wide diversity of electrical devices and their functional purposes, they are united by a common thermal-management problem that does not diminish with technological progress. On the contrary, increasing power density, compactness, and functional integration continuously intensify thermal constraints. This creates a demand for universal thermal-management platforms based on the most efficient heat-transfer mechanisms.

In support of this statement, the present work focuses on fundamentally different classes of electrical equipment, including in-wheel electric motors, high-power LED luminaires, and fuel-cell stacks. In these systems, electrical energy is converted either into mechanical work or light radiation, while in fuel cells chemical energy is converted into electrical energy; however, in all cases a substantial fraction of the processed energy is inevitably transformed into heat. In electric traction systems, increased current densities required for high torque and compact design lead to elevated Joule losses in stator windings and impose strict thermal constraints on allowable electromagnetic loading. In LED-based lighting systems, despite continuous improvements in luminous efficacy, a significant portion of electrical power is dissipated as heat, with local heat-flux densities reaching values characteristic of high-power electronics [2]. Similarly, fuel cells directly convert chemical energy into electricity and heat, and approximately half of the input energy must be removed as thermal load to ensure stable operation [3]. Thus, in advanced electrical systems, thermal management is not an auxiliary function but a primary design constraint that directly influences power density, efficiency, reliability, and architectural configuration of the device.

In LED luminaires, thermal limitations restrict spatial clustering of emitters and affect optical design, often leading to bulky multi-source configurations and additional optical losses [4]. In high power-density electric motors, insufficient heat removal limits allowable current density and reduces reliability margins. In fuel-cell stacks, temperature must be maintained within a narrow operating window to preserve electrochemical performance and durability. Therefore, across

fundamentally different physical energy conversion principles, a common bottleneck emerges: the inability of conventional cooling systems to efficiently collect, transport, and dissipate high localized heat fluxes without increasing mass, volume, and parasitic energy consumption. A more detailed description of the thermal management challenges for each type of the considered electric equipment is provided in the respective *Problem Relevance* sections of Chapters 4, 5, and 6 of the present work.

Although heat transfer from a hotter body to a colder one follows the natural direction of thermodynamic processes, cooling is a significantly more complex task than heating. Heat generation represents the natural final stage of energy transformations, whereas the generation of "cold" requires additional work input.

In general, a cooling system must perform three main functions:

- heat collection from the heat source,
- heat transport to a heat sink,
- heat rejection from the heat sink to the environment.

Modern cooling technologies include a wide range of solutions: air cooling, single-phase liquid cooling, microchannel heat exchangers, immersion cooling, jet and spray cooling, thermoelectric systems, phase change material (PCM) cooling, as well as two-phase devices such as heat pipes and vapor chambers [1]. Despite the diversity of approaches, the general trend in thermal management development is the increasing use of phase-change heat transfer as the most efficient mechanism for heat removal under high heat-flux conditions.

Another fundamental classification of thermal-management systems is based on the mechanism of coolant circulation and divides them into active and passive systems. Active systems require an external power source to operate pumps or fans. Passive systems rely on internal physical mechanisms—capillary forces or gravity—and contain no moving parts, offering high reliability, autonomy, and long service life.

Among passive two-phase devices, a special role is played by heat loops (HL), including loop heat pipes (LHP), capillary pumped loops (CPL), and loop thermosyphons (LTS). These devices are capable not only of efficiently removing heat from localized sources but also of transporting it over significant distances with small temperature differences. However, despite more than sixty years of development history [5], heat loops remain complex and costly systems whose application is still largely limited to highly specialized fields.

Thus, in the field of thermal management, a contradiction exists between the increasing demands for efficiency, compactness, and autonomy of cooling systems and the limited applicability of existing solutions capable of providing highly efficient passive two-phase heat removal under modern thermal loads. This forms a scientific and technical problem related to the development of universal approaches for the design and integration of passive two-phase heat loops into thermal management systems for electrical equipment.

The use of passive two-phase heat-transfer systems as a fundamental platform for thermal management enables a transition to a new technological level, referred to in this work as Smart

Thermal Management, implying the use of internal physical mechanisms for self-regulated and energy-independent redistribution of heat flows.

## 1.2 Objective of Research

The objective of this Doctoral Thesis is to develop a scientifically grounded approach to the application of passive two-phase heat loops as a universal platform for Smart Thermal Management of electrical and electronic equipment, including:

- development of physical and mathematical models of heat loops,
- formulation of design methodologies for such systems,
- creation and experimental validation of technical solutions for different classes of devices,
- development of universal platforms operating according to the “cold plate” principle, based on modular multi-evaporator architectures consisting of several capillary pumps integrated into a single system.

The work is aimed at expanding the application of heat loops beyond traditional specialized systems and at reducing their structural and technological complexity while maintaining high efficiency.

## 1.3 Research Hypothesis

The working hypothesis states that replacing conventional cooling systems of electrical and electronic devices with passive two-phase heat loops, designed with consideration of the structural and thermal features of a particular device, leads to a modification of its thermal regime in such a way that its technical characteristics are improved, expressed as:

- increased useful power and efficiency,
- reduced size and mass,
- improved operational reliability and service life,
- extension of the application range.

It is assumed that this effect is general in nature and is governed by the fundamental mechanisms of two-phase heat transfer and therefore can be realized for different classes of electrical devices provided that the heat loop is properly adapted to their geometry and thermal operating conditions.

The hypothesis is verified using four types of devices that differ in heat-load level, geometry, spatial distribution of heat generation, operating modes, and requirements for temperature stability:

- in-wheel electric motor,
- LED luminaire,

- fuel cell,
- traction motor.

The results obtained for the first three devices are presented in Chapters 4, 5, and 6 and have been published in the form of scientific articles [6],[7], [8].

For the traction motor application, a cooling system based on six loop thermosiphons was developed and experimentally tested. The complete results of this study are not included in the present thesis; however, selected findings have been partially published in [9].

Within the hypothesis verification, a universal solution for complex multi-component electronic systems with non-localized heat loads is also considered. This solution is based on a modular architecture enabling the implementation of two-phase loops operating according to the multi-evaporator cold plate concept.

## 1.4 Research Novelty

The scientific novelty of the work includes the following contributions:

- Introduction of the concept of Smart Thermal Management as a class of systems that use internal physical mechanisms of two-phase heat transfer for self-regulated redistribution of heat flows without external energy input or active control.
- Proposal of a universal architecture of modular multi-evaporator heat loops suitable for integration into electrical devices of various geometries and power levels.
- Formulation of the principle of transition from specialized heat loops to universal two-phase cold-plate platforms providing scalability of thermal management.
- A quantitative analysis was performed that allows the advantages of two-phase heat transfer systems over single-phase systems, as well as LHPs over conventional heat pipes, to be evaluated on a unified physical basis.
- Development of a mathematical model for the calculation of steady-state and transient operating regimes of LHPs.
- Development of a thermodynamically consistent interpretation of heat leak and subcooling in LHPs, demonstrating the fundamental role of heat leak in closing the steady-state energy balance of the LHP cycle.
- Development of the original software tool “Altom-LHP” for LHP design with modular evaporators and various condenser configurations.
- Development of an algorithm for tuning the mathematical model using experimental data.
- Proposal of a method for estimating LHP parameters that are not directly measurable from experimental data.

- Introduction of working-fluid quality parameters for loop thermosyphons, analogous to figures of merit (FOM) for LHPs but accounting for gravity-driven circulation.
- Proposal of a hypothesis and physical explanation of a low-efficiency heat-transfer regime in LHPs.
- Design, fabrication, and experimental testing of a two-phase heat loop for cooling an in-wheel motor, demonstrating the effectiveness of LHP-based cooling in this application.
- Proposal of a novel in-wheel electric motor architecture with evaporators structurally integrated into the stator body, enabling direct heat removal from stator teeth and reducing winding-to-evaporator thermal resistance; quantitative justification of the expected increase in allowable thermal load and power density enabled by such integration.
- Proposal a new heat-transfer device design (HLP, Heat Loop Pipe) combining features of heat pipes and LHPs.
- Design, fabrication, and testing of an LED luminaire with an HLP-based cooling system.
- Development of a conceptual design of a two-phase cooling system for a fuel-cell stack based on a loop thermosyphon.
- Fabrication and testing of loop thermosyphons with various evaporator configurations as prototypes of a cell-level fuel-cell cooling loop.

## 1.5 Statements to be Defended

- Passive two-phase heat loops can be considered a universal physical and engineering platform for thermal management of electrical devices, providing heat-flow redistribution without external power input by relying on internal physical mechanisms such as phase transitions, capillary forces, and gravity.
- The mathematical model developed by the author adequately describes steady-state and transient regimes of heat loops of different architectures and enables prediction of temperature distributions, effective thermal conductance, and maximum transferable power.
- The introduction of working-fluid quality parameters for loop thermosyphons enables justified fluid selection and prediction of effective operating temperature ranges.
- The use of modular multi-evaporator architectures enables scaling of two-phase heat loops from local cooling systems to universal platforms of the “two-phase cold plate” type.

- Application of the developed heat loops leads to a modification of thermal constraints of electrical devices, manifested in an expansion of operating regimes, improved energy efficiency, and increased service life.

## 1.6 Publications and Patents Related to the Thesis

The main results of the Thesis have been published in the following peer-reviewed journal articles and conference proceedings.

**Journal Articles**

1. **I. Ušakovs**, D. Mishkinis, I. A. Galkin "Concept and experimental study of two-phase cooling loops for PEM fuel cells with a flat aluminum evaporator", Case Studies in Thermal Engineering, 2026 (Under review)
2. Ghahfarokhi, P.S., Rasilo, P., Cardoso, A.J.M., **Ušakovs, I**., Mishkinis, D., Podgornovs, A., 2025. Proof of Concept of a Two-Phase Thermal Management System for Railway Traction Motors. IEEE Trans. Energy Convers. 1–10. https://doi.org/10.1109/TEC.2025.3583076
3. **Igors Ušakovs**, Luka Ivanovskis "Advanced Loop Heat Pipe Application for Cooling High Power LED Lights", Case Studies in Thermal Engineering 57 (2024) 104320 https://doi.org/10.1016/j.csite.2024.104320
4. **I. Ušakovs**, D. Mishkinis, I. A. Galkin, A. Bubovich, and A. Podgornovs, "Experimental thermal characterization of the in-wheel electric motor with loop heat pipe thermal management system," Case Stud. Therm. Eng., vol. 47, p. 103069, Jul. 2023, https://doi.org/10.1016/j.csite.2023.103069

**Conference Proceedings**

1. Donatas Mishkinis, **Igors Ušakovs**, Luka Ivanovskis, Marco Gottero, Albino Quaranta, Federica Negri, Antonio Rotondi, Stéphane Lapensée, Paula Prado "MECOP -A Novel Two Phase Capillary Technology for the Thermal Control of Space Systems", 54th International Conference on Environmental Systems, ICES-2025-300, 13-17 July 2025, Prague, Czech Republic
2. Luka Ivanovskis, **Igors Ušakovs**, Donatas Mishkinis, Marco Gottero, Albino Quaranta, Stéphane Lapensée "Multievaporator Cold Plate (MECOP) Heat Loop characterization with butane and R134a" Joint 22st IHPC and 16th IHPS, Thailand, November, 2024
3. Donatas Mishkinis, **Igors Ušakovs**, Luka Ivanovskis and Ilya A. Galkin "Heat Loop Pipe for Thermal Management of Powerful LED-based Applications", Joint 21st IHPC and 15th IHPS, Melbourne, Australia, February 5-8, 2023
4. P Gakal, D Mishkinis, A Leilands, **I Usakovs**, R Orlov and Y Rogoviy, Analysis of working fluids applicable for high-temperatureloop heat pipe applications, IOP Conf. Series: Materials Science and Engineering 1226 (2022) 012036 doi:10.1088/1757-899X/1226/1/012036.https://iopscience.iop.org/article/10.1088/1757-899X/1226/1/012036

5. Mishkinis D., **Ušakovs I**., Nasibulin D. (2018) “Novel Modular Evaporator Architecture for Electronics Cooling Applications”, Joint 19th International Heat Pipe Conference and 13th International Heat Pipe Seminar Pisa, Italy, 2018

**Patents**

1. Mishkinis, D.; **Ušakovs, I**. SILTUMA CILPAS CAURULE (HEAT LOOP PIPE). LV 15883 A — patent application publication. Application No. LVP2023000021; filing date 2023-03-07; publication date 2024-09-20. Applicant: ALLATHERM, SIA, LV.

# 2 PASSIVE TWO-PHASE HEAT LOOPS AS SMART THERMAL MANAGEMENT DEVICES

## 2.1 Comparative Analysis of Passive Two-Phase Heat-Transfer Devices

The circulation of a working fluid involving evaporation in the heat-input zone and subsequent condensation in the heat-rejection zone is a common feature of all two-phase heat-transfer devices.

Passive devices include thermosyphons (TS), heat pipes (HP), pulsating heat pipes, and HLs: CPLs, LHPs, and LTSs. The absence of active components in these devices enhances their operational reliability and service life. The use of latent heat of phase change as the principal heat-transfer mechanism provides two-phase devices with exceptionally high heat-transfer capability, and in the scientific literature they are often referred to as “thermal superconductors.”

HPs contain an internal capillary structure that ensures motion of the working fluid by capillary forces, allowing HPs to partially counteract gravity. Owing to their simple design and low cost, HPs are widely used in electronics cooling and are mass-produced devices. However, HPs have significant limitations: they effectively transfer heat only over relatively short distances (up to about 0.5 m), and they perform poorly against gravity.

The structure of a cylindrical heat pipe is shown in Figure 2-1

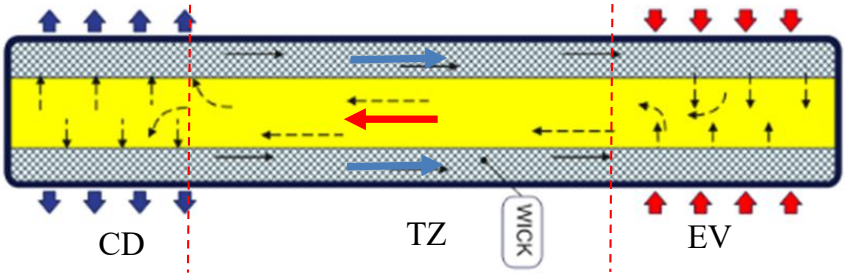


Figure 2-1. Construction of a heat pipe. EV – evaporator, TZ – transport zone, CD – condenser, blue thin arrow – liquid flow, red thin arrow – vapor flow.

One end of the HP, called the evaporator (EV), is in thermal contact with the heat source, while the other end, the condenser (CD), is connected to the heat sink. The internal volume of the HP is hollow and intended for vapor flow. A capillary structure (wick) covers the entire inner surface and provides liquid transport. The HP is charged with such an amount of working fluid that the wick remains wet under all operating conditions, ensuring continuous circulation. Heat from the source passes through the HP wall, causing evaporation of the working fluid in the

evaporator wick and liberating pores of the capillary structure. A new portion of liquid is drawn in by capillary forces. Vapor enters the internal channel and moves to the condensation zone. In the condenser, vapor condenses, and the liquid is absorbed by the wick, completing the operating cycle of the heat pipe.

The most efficient passive two-phase heat-transfer devices are considered to be heat loops. Owing to their design features, heat loops can transfer heat over distances exceeding 10 m and operate against gravity. LHP-type heat loops were developed in the Soviet Union, whereas CPLs were first developed in the United States. They differ in component arrangement, leading to certain functional differences. Figure 2-2 presents two schematic diagrams illustrating the differences between LHPs and CPLs.

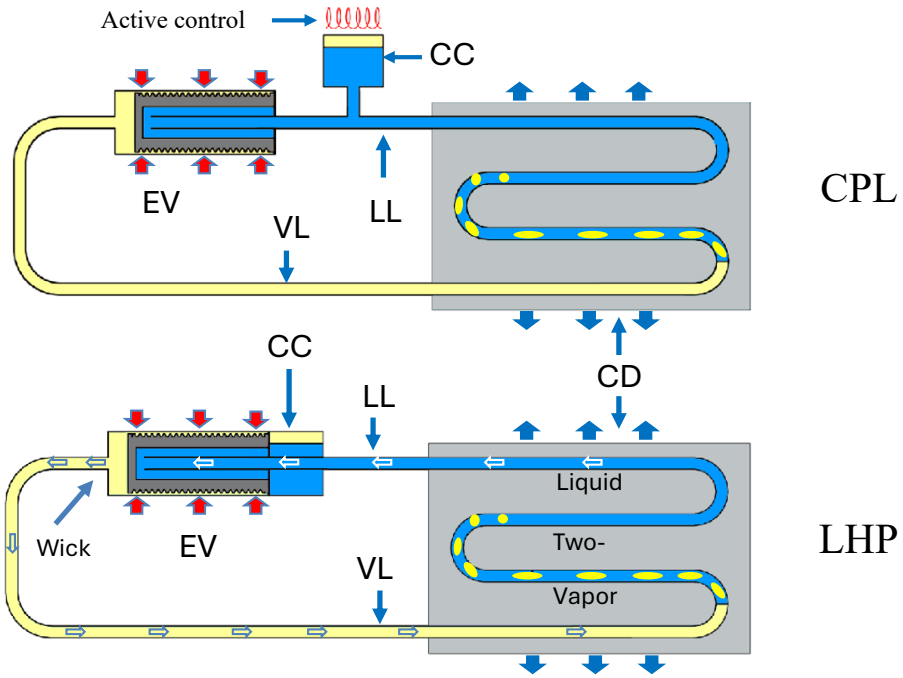


Figure 2-2 Comparative layouts of a CPL and an LHP.

Both LHP and CPL systems are sealed volumes filled with working fluid. In both concepts, circulation of the working fluid is driven by capillary forces generated within a porous wick. Both systems consist of five main elements: an EV, a CD, a compensation chamber (CC), a vapor line (VL), and a liquid line (LL), which are mechanically and thermally separated. The wick structure is located exclusively within the evaporator.

The principal distinction between CPLs and LHPs lies in the location of the compensation chamber. In LHPs, the compensation chamber is directly attached to the evaporator, providing improved and more reliable liquid supply to the evaporation zone. In CPLs, the compensation chamber is located in the liquid line and typically requires active external control, commonly implemented via an electrical heater, to ensure sufficient liquid supply to the wick during start-up or under rapid transient operating conditions. In contrast, LHPs address this issue by placing the compensation chamber in close proximity to the evaporator and employing secondary wicks—capillary structures that connect the chamber to the evaporator. At present, the LHP design is considered the primary configuration for HLs; therefore, CPLs are not considered further in this work.

The operating principle of an LHP can be described as follows. Heat from the source is supplied to the evaporator through a thermal interface that ensures thermal contact with the cooled element. Heat then passes through the evaporator wall to the outer surface of the wick, causing evaporation of the working fluid in the wick pores. The liquid–vapor interface in the wick pores, formed by menisci, creates a capillary barrier that prevents vapor from entering the compensation chamber and provides liquid supply through the wick to the evaporation zone. The compensation chamber, located in close proximity to the wick, performs two functions: it stores a liquid reserve used to feed the wick during transient processes, and its volume is designed so that free space is always available to compensate for thermal expansion of the liquid. Vapor flows from the evaporation zone to the condensation zone through the vapor line due to the pressure difference arising from the temperature difference between the evaporator and condenser. In the condenser, vapor cools, condenses, and the resulting liquid is subcooled. The subcooled liquid returns through the liquid line to the compensation chamber, completing the loop cycle.

The advantages of employing an LHP instead of a conventional HP can be identified through a comparative analysis of the two devices, which are presented together in Figure 2-3.

As can be seen, both devices comprise the same main zones: EV, CD, and TZ. The LHP additionally includes CC, whose function has been described above. Both devices employ a wick structure to ensure circulation of the working fluid.

The principal difference between LHP and HP is that in LHP the wick is located only in the region of contact with the heat source, i.e., in the evaporator, while vapor and liquid flow through separate transport lines without direct interaction. In conventional HP, the porous structure covers the entire transport zone, increasing the hydraulic resistance to the returning liquid, while the vapor directly interacts with the returning liquid, heating it and partially entraining it back toward the condenser.

This LHP architecture significantly reduces the hydraulic resistance of the loop and enables the use of microporous wicks (on the order of one micron or less), which allows heat transfer over long distances and against gravity.

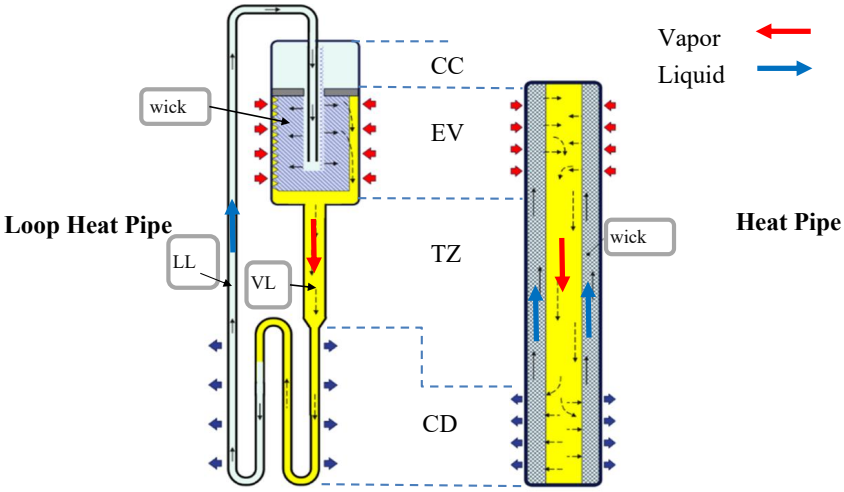


Figure 2-3. Comparison of HP and LHP.

The quality of heat-transfer devices is commonly characterized by thermal resistance:

$$R = \frac{\Delta T}{\dot{Q}} \tag{2.1.}$$

or by thermal conductance:

$$G = \frac{1}{R} = \frac{\dot{Q}}{\Delta T} \tag{2.2.}$$

where

$$\Delta T = T_{src} - T_{sink} \tag{2.3.}$$

is the temperature difference between the heat source and the heat sink. Another important parameter is the maximum transferable power $\dot{Q}_{max}$.

The performance of both HPs and LHPs depends on the hydraulic resistance of the working-fluid circulation. The lower the hydraulic resistance, the better the heat-transfer device performance. Hydraulic resistance determines the pressure drop in the loop. Since two-phase heat-transfer systems operate along the saturation curve of the working fluid, condensation and evaporation temperatures are functions of pressure, and $P(T)$ is a monotonically increasing

function. Therefore, the larger the pressure drop $\Delta P$, the larger the temperature difference $\Delta T$ in (2.1) and (2.2) and the poorer the device performance.

As can be seen from Figure 2-3, while the vapor in an HP flows through a channel whose characteristics are similar to those of the vapor line in an LHP, the liquid returning from the condenser flows through the wick. Therefore, the pressure drop in the liquid channel of the HP is governed by Darcy's law for flow in a porous medium:

$$\Delta P_1 = \frac{\eta_l}{K} \cdot \frac{\dot{m}}{\rho_l S_1} \cdot L \tag{2.4.}$$

In contrast, in an LHP the working fluid flows through the liquid line, typically in the laminar regime, and the pressure drop can therefore be calculated using the Hagen–Poiseuille law:

$$\Delta P_2 = 8\pi\eta_l \cdot \frac{\dot{m}}{\rho_l S_2^2} \cdot L \tag{2.5.}$$

For two devices of comparable size, dividing (2.4) by (2.5) yields an expression that allows the heat-transfer performance of the HP and LHP to be compared:

$$\frac{\Delta P_1}{\Delta P_2} = \frac{1}{8\pi K} \cdot \frac{S_2^2}{S_1} \tag{2.6.}$$

The permeability of the wick, $K$, typically lies in the range from $10^{-13}$ m$^2$ to $10^{-11}$ m$^2$, and for most applications the cross-sectional areas of the channels are on the order of $S \sim 10^{-6}$ m$^2$. Substituting these values into (2.6) gives a numerical estimate of the advantage of the LHP over the HP:

$$\frac{\Delta P_1}{\Delta P_2} \sim 10^5 - 10^7 \tag{2.7.}$$

At the same time, the simple geometry of an HP (typically a cylindrical tube filled with a working fluid and lined with a porous structure on the inner surface) remains an advantage in many applications.

Among two-phase heat-loop devices, the LTS represents the simplest solution from a technical standpoint and therefore has numerous examples of practical terrestrial implementation [10]. CPLs and LHPs, in contrast, are capable of operating under microgravity conditions and consequently find widespread use in space systems. However, their application in terrestrial systems is often limited by the complexity of their evaporator design and manufacturing

technology, as well as by the associated cost. The schematic diagram of the loop thermosyphon is shown in Figure 2-4.

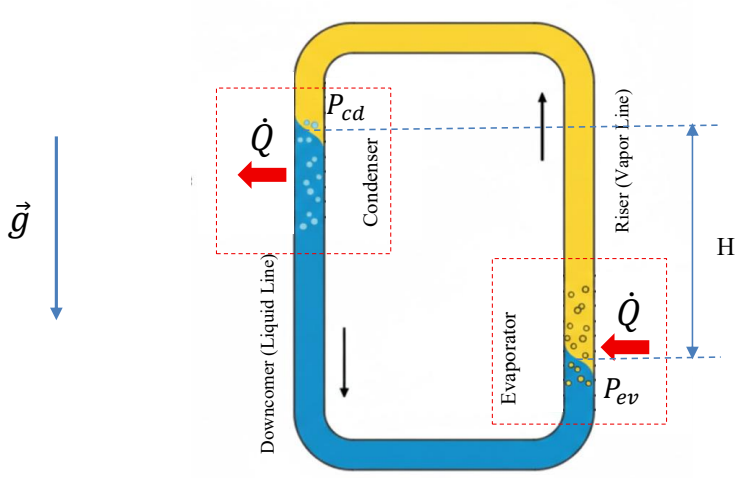


Figure 2-4. LTS layout.

A fundamental condition for LTS operation is that the condenser must be located above the evaporator. Under this condition, circulation of the working fluid is driven by the difference in hydrostatic pressure between the downcomer (liquid line) and the riser (vapor line), which arises due to the density difference between the liquid and vapor phases.

In the classical configuration Figure 2-4, the evaporator is positioned at the beginning of the riser, while the condenser is located at the beginning of the downcomer. This arrangement establishes a preferred direction of circulation: vapor generated in the evaporator rises through the vapor line toward the condenser, while condensate returns downward through the liquid line to the evaporator. The evaporating zone is thus continuously cleared of vapor, and the condensed liquid is naturally supplied back to the heat source. Such a layout is advantageous but not strictly mandatory. A preferred circulation direction can also be established through hydraulic asymmetry between the transport lines. For example, increasing the hydraulic resistance of the liquid line makes the vapor line more favourable for vapor flow.

Thus, the comparative analysis shows that different classes of passive two-phase heat-transfer devices are limited by different factors. Thermosyphons are structurally simple but orientation-dependent. Heat pipes are widely used mass-produced devices, but their performance is limited by transport length and gravity sensitivity. LHP-type heat loops enable long-distance heat transport and operation against gravity, but at the cost of evaporator complexity, manufacturing difficulty, and miniaturization constraints.

## 2.2 Heat Loop Pipe – A New Thermal Management Device

To overcome the performance limitations of HP technology and integration challenges associated with LHPs, a new thermal architecture, the Heat Loop Pipe (HLP), has been proposed [11]. Its layout is shown in Figure 2-5.

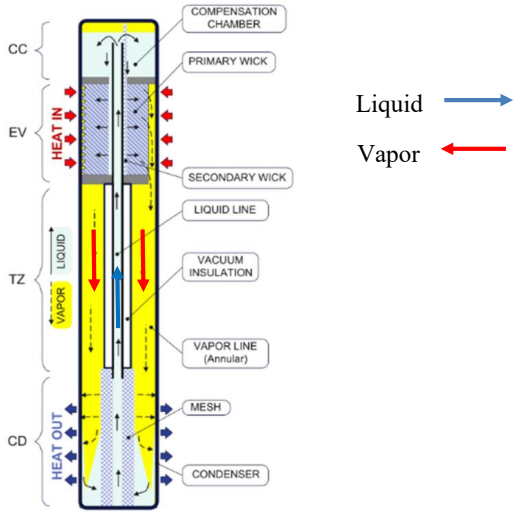


Figure 2-5. HLP layout. EV - Evaporator; CD - Condenser; CC - Compensation chamber; TZ - Transport zone,

The evaporator, condenser, compensation chamber, and transport zone are located within a single cylindrical housing, as in a conventional heat pipe. The compensation chamber is a direct extension of the evaporator. The evaporator wick has a cylindrical shape with a through-hole. One side of this through-hole is connected to the compensation chamber, while the other side is connected to the cylindrical liquid line, which is a tube coaxial with the LHP housing. The outer surface of the wick is in contact with the housing and contains grooves for vapor removal. The vapor channel is the annular space between the liquid line and the LHP housing. To prevent heat transfer between the liquid and the vapor, a vacuum gap is created around the liquid line.

A mesh rolled into a spiral is placed in the condenser section. The cell size of this mesh is tens of times larger than the pore size of the wick in order not to introduce additional resistance to the working fluid, while still being sufficient to perform its main function—collecting condensate from the vapor channel near the inlet of the liquid line. As noted previously, the thermal resistance of an LHP depends on its hydraulic resistance. For identical geometries, the hydraulic resistance of the LHP vapor line is orders of magnitude higher than that of the liquid line; therefore, the inner diameter of the vapor line is usually increased relative to that of the liquid

line. In the HLP design, this is achieved by placing the vapor channel around the liquid line. Thus, the resistance of the vapor channel is determined by the diameter of the HLP housing, while the diameter of the liquid-line tube can be reduced to the required size.

The performance of an LHP is significantly influenced by heat exchange with the surrounding environment, with the liquid line being particularly sensitive in this regard. The vacuum gap insulates the liquid line not only from the vapor line but also from the external environment.

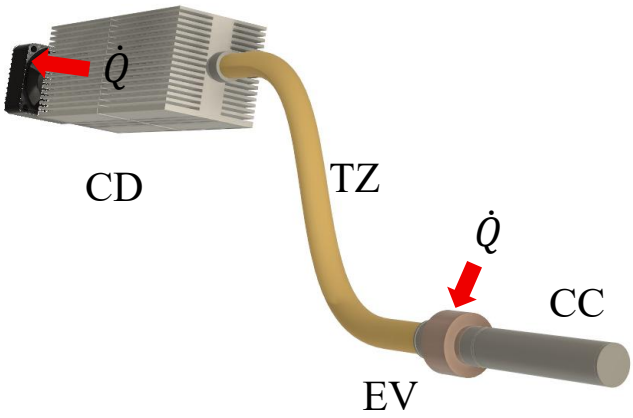


Figure 2-6. HLP with flexible transport line. EV - Evaporator; CD - Condenser; CC - Compensation chamber; TZ - Transport zone, vapor and liquid lines.

This device can replace conventional heat pipes in applications where their performance is no longer sufficient, but where the geometry of the cooled system requires the use of cylindrical tubes. The transport zone of an HLP can be extended because it is no longer limited by the hydraulic resistance associated with the porous structure in the liquid channel. Additionally, the transport zone can be made flexible, thereby creating flexible heat superconductors suitable for cooling devices with complex geometries (Figure 2-6). Several HLPs have been manufactured and tested, including in an LED luminaire cooling system.

## 2.3 Smart Thermal Management

In the preceding sections, it was substantiated that two-phase heat loops are currently the most efficient heat-transfer devices. It is therefore of interest to compare them in greater detail with classical single-phase loops. Figure 2-7 schematically illustrates two heat transfer loops designed to accomplish identical objectives— single-phase loop and passive two-phase loop.

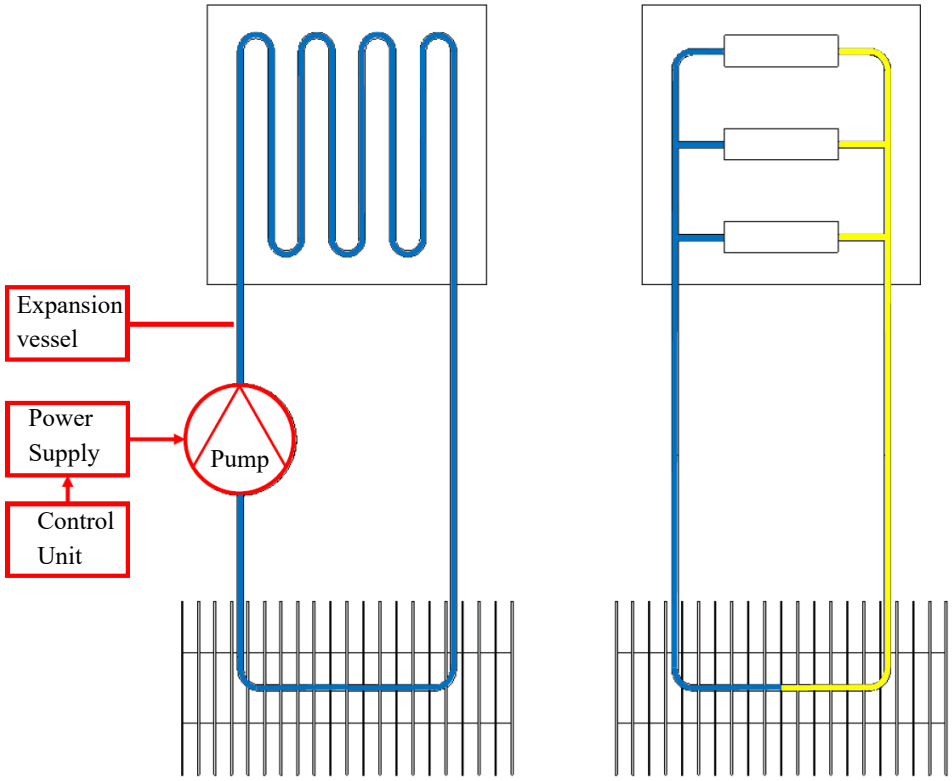


Figure 2-7. Comparison of single-phase and two-phase cooling loops.

A comparison of the two configurations leads to the following conclusions. A single-phase loop operates only in active mode and requires forced circulation of the working fluid; consequently, it incorporates a circulation pump that requires both control and an external power supply. A passive two-phase loop, by contrast, operates without forced circulation and therefore does not require a pump or associated subsystems, nor does it depend on external energy input. This provides not only an energetic advantage for the two-phase configuration but also an advantage in reliability, since each additional component increases the probability of system failure.

In actively controlled cooling systems based on single-phase loops, a feedback channel must be implemented to activate the system when a thermal load appears. A passive two-phase thermal loop requires no auxiliary equipment; it automatically initiates heat transport as soon as a temperature difference arises between the heat source and the heat sink. In this sense, passive two-phase thermal loops can be regarded as inherently smart thermal-management systems.

The heat-transfer capability of the two loops can be compared as follows. The heat flow rate transferred by a single-phase loop, $\dot{Q}_{1p}$, is proportional to the specific heat capacity of the coolant $c_p$, the mass flow rate $\dot{m}_{1p}$, and the temperature difference $\Delta T$ between the inlet and outlet of the heat exchanger:

$$\dot{Q}_{1p} = c_p \cdot \dot{m}_{1p} \cdot \Delta T \tag{2.8.}$$

Accordingly, the heat-transfer rate can be increased either by increasing the mass flow rate or by increasing the temperature difference.

In two-phase heat transfer, the heat flow rate $\dot{Q}_{2p}$ is proportional to the latent heat of vaporization $h_{ev}$ and the mass flow rate of the working fluid $\dot{m}_{2p}$:

$$\dot{Q}_{2p} = h_{ev} \cdot \dot{m}_{2p} \tag{2.9.}$$

In this case, heat transfer occurs at nearly constant temperature, which significantly reduces temperature gradients throughout the system. Another important aspect is that, for most working fluids, the latent heat of vaporization greatly exceeds the specific heat capacity. For example, for water at 20 °C, the latent heat of vaporization is $h_{ev} \approx 2.45 \times 10^6$ J/kg, while the specific heat capacity is $c_p \approx 4.2 \times 10^3$ J/(kg·K), i.e., the former is approximately 600 times larger. By comparing (3.8) and (3.9), it follows that, for the same heat flow rate, the ratio of the required mass flow rates is:

$$\frac{\dot{m}_{1p}}{\dot{m}_{2p}} = \frac{h_{ev}}{c_p \cdot \Delta T} \tag{2.10.}$$

If a temperature difference of $\Delta T = 50$ °C is assumed for the single-phase loop, the estimate for water becomes

$$\frac{\dot{m}_{1p}}{\dot{m}_{2p}} \approx 12 \tag{2.11.}$$

An order-of-magnitude difference in mass flow rates is directly reflected in the structural characteristics of the two loops. The diameters of the transport lines in a single-phase system may therefore be an order of magnitude larger than those in a two-phase system. Accordingly, the volume of coolant in a single-phase loop will be significantly greater than in an equivalent two-phase loop. In addition, compensation for thermal expansion in a single-phase loop requires a

relatively large expansion tank. All these factors lead to single-phase systems being substantially bulkier than two-phase ones.

In summary, passive two-phase loops surpass comparable single-phase systems in key technical parameters and do not require active control, as they enter the operating mode automatically when a temperature difference appears in the loop. However, despite these advantages, their widespread application is constrained by several other factors. First, their manufacturing complexity leads to high cost. Second, a two-phase thermal loop is typically a non-serviceable system. While this is a significant advantage in applications such as space systems, where maintenance is generally impossible, it may represent a drawback in terrestrial applications. In the event of mechanical damage, loss of hermeticity, or the formation of non-condensable gases inside the loop, field repair is practically infeasible. Third, thermophysical processes involving phase change are inherently more complex to model, which complicates the design of thermal management systems. The development of two-phase heat-transfer technologies is therefore largely directed toward overcoming these limitations.

## 2.4 “Altom” Modular Technology — Universal Platform for the Two-Phase Heat Loops

To overcome the technological difficulties associated with the design and manufacturing of LHPs, and taking into account that the evaporator is the most complex and costly component of an LHP, a modular technology for evaporator construction, referred to as the “Altom” technology, was developed. Figure 2-8 illustrates the principle of the modular approach. According to this concept, LHP evaporators are assembled from standardized building blocks — capillary pumps (CPs). The use of unified modules ensures well-characterized and reproducible parameters of individual units, which makes it possible to predict the performance of the complete LHP evaporator. The evaporator can be configured by connecting modules in series and/or in parallel, thereby achieving the required heat-transfer characteristics. Figure 2-8 shows an evaporator composed of four individual modules (Altom-10) connected in parallel through common manifolds.

The capillary pumps contain a cylindrical wick sintered in vacuum from metallic powder, as well as a system of vapor-removal channels. The pump casing is made of copper, which ensures high thermal conductivity of the evaporator. The end sections are manufactured from stainless steel, which minimizes parasitic heat leakage from the capillary pump to the compensation chambers. This evaporator design was specifically developed for microchip cooling and is capable of removing up to 500 W of heat from a 40 mm × 40 mm area.

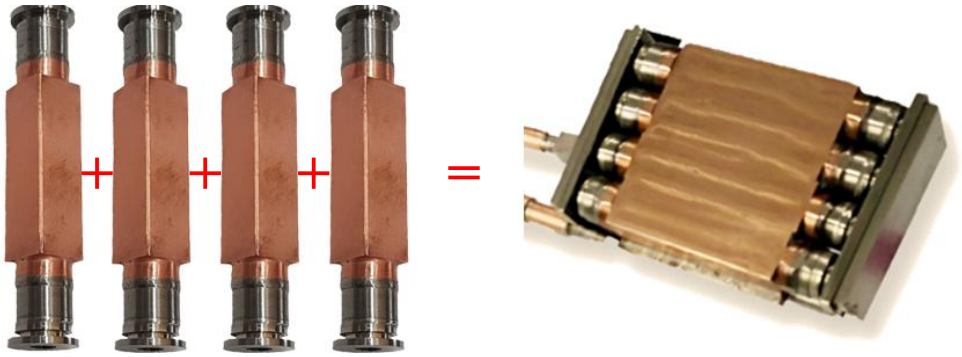

Figure 2-8. Illustration of the application of “Altom” modular technology. Four capillary pumps form a single evaporator.

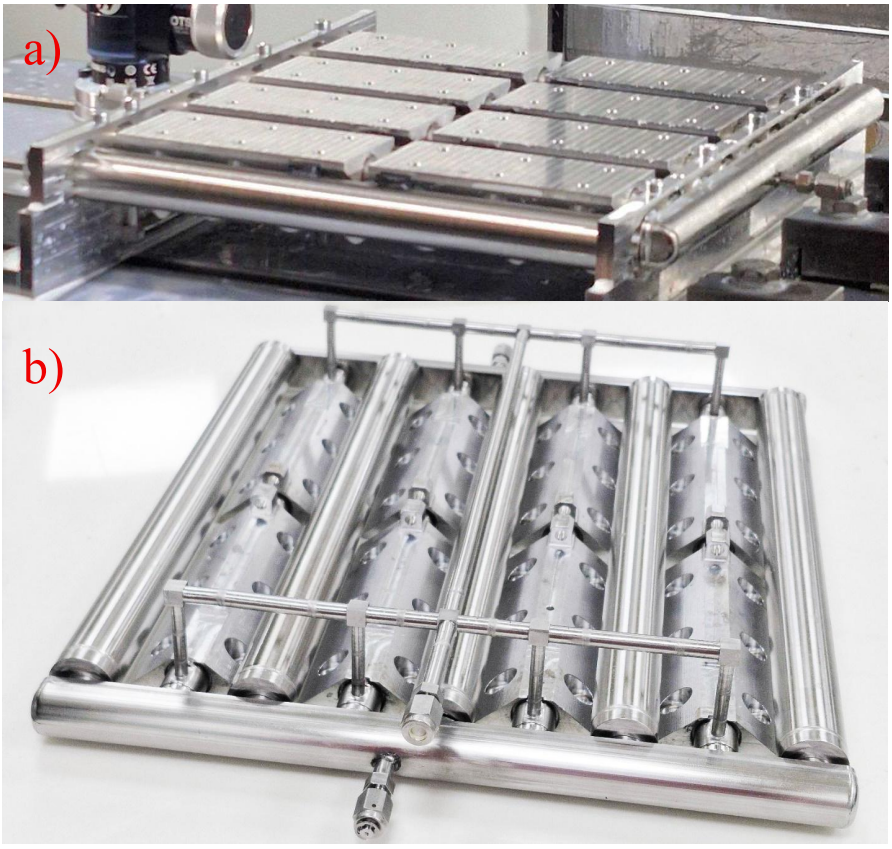


Figure 2-9 MECOP evaporator: (a) rear side view; (b) top view.

Figure 2-9 shows another type of evaporator manufactured using the “Altom” technology. It consists of eight Altom-14 modules and five compensation chambers. The capillary pumps are arranged in four pairs connected in parallel on the liquid side. Within each pair, the pumps are connected in series. On the vapor side, all pumps are connected to a common manifold. The casings of the capillary pumps are made of stainless steel, while the trapezoidal thermal interface is made of aluminium. The wide side of each interface is attached to an aluminium plate on which the cooled electronics can be mounted. This evaporator configuration enables heat collection from large surfaces and is referred to as Multi-Evaporator Cold Plate (MECOP).

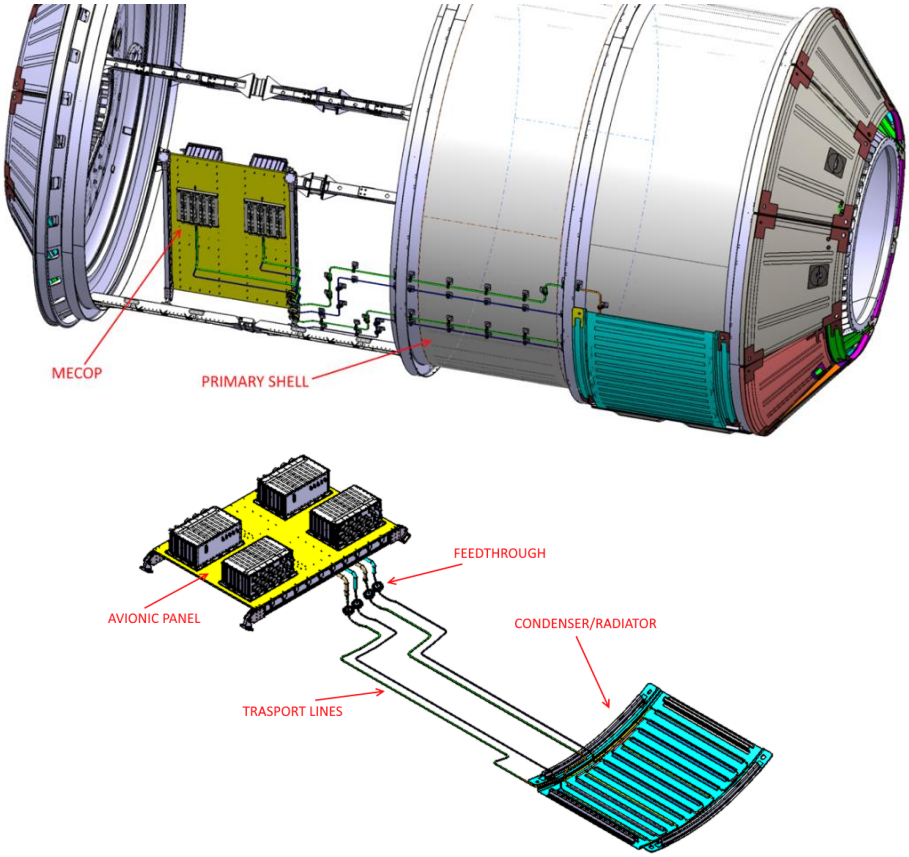


Figure 2-10, Potential application of a MECOP LHP for cooling avionics pallets of a spacecraft.

The device shown in Figure 2-9 collects heat from an area of 250 mm × 250 mm. It has successfully passed testing and demonstrated the capability to transfer 3200 W of thermal power

over 6 m using ammonia as the working fluid. This performance allows the device to compete with two-phase pumped systems currently used for transporting large heat loads in spacecraft.

A potential application of the MECOP concept is shown in Figure 2-10. The figure presents a conceptual cooling system for an avionics pallet of a future space station, employing two parallel LHPs equipped with MECOP evaporators.

# 3 MODELING OF PASSIVE TWO-PHASE HEAT LOOPS

## 3.1 General Principles of Modelling Passive Two-Phase Loops

As noted in Chapter 1.1, in the general case a thermal control loop solves three principal tasks: 1) heat collection from the source, 2) heat transport to the heat sink, and 3) heat rejection from the heat sink to the environment. The role of the environment may also be played by an external cooling loop in the case of a cascaded cooling system.

The first task is associated with the design of the thermal interface between the evaporator and the cooled device. The thermal interface is typically bounded by the surface of the cooled device on one side and by the inner surface of the capillary pump housing on the other. The second task encompasses heat transport within the heat-transfer loop, from the evaporator to the external surface of the condenser, as well as circulation of the working fluid within the loop. The third task refers to external heat exchange at the condenser surface.

Accordingly, modelling of a heat-transfer system consists in the sequential solution of the above tasks, in which the elements of the loop are replaced by their mathematical models coupling the elements by the conservation laws of mass and energy, complemented by continuity conditions for pressure and temperature at their interfaces. In this way, a model of the entire loop is constructed.

Further modelling approaches depend on whether a steady-state or transient problem is considered, and a steady-state or transient model is applied accordingly. The transient model is significantly more computationally demanding and is required when the heat source provides a time-varying thermal load or when simulating transient processes such as start-up or shutdown of the cooled equipment. Although thermal processes generally exhibit high inertia, a two-phase heat loop can rapidly transition from one steady state to another in response to load changes.

Another important aspect is that the cooling loop performs a service function, and designers of electrical equipment are primarily interested in the temperature established in the device as a function of the applied load. Therefore, in practice, transient processes are often neglected, and the analysis focuses on steady states. In other words, for most practically relevant cases, a steady-state model is sufficient.

Heat-transfer loops with a massive evaporator, such as the MECOP design, which consists of eight capillary pumps and five compensation chambers and heat loop may contain approximately 900 mL of working fluid at a time, represent an exceptional case where the steady state may be reached only after several hours. If the thermal load varies on a shorter time scale, the loop may remain in a practically continuous transient state. A transient model was developed for the analysis of such loops and will be described in Chapter 3.5

## 3.2 Thermodynamic Cycles of a Loop Heat Pipe and a Loop Thermosyphon

The mathematical model of a heat loop is intended for the evaluation of quantitative performance characteristics of the heat-transfer system. However, many processes and behavioural features of the loop under various operating conditions can also be described qualitatively through analysis of its thermodynamic cycle. Traditionally, the thermodynamic analysis of a LHP is carried out in pressure–temperature (P–T) coordinates. Figure 3-1 presents the (P–T) diagram of the LHP operating cycle. The figure schematically shows the saturation line of the working fluid and eight principal control points of the loop. The arrows indicate the direction of working-fluid circulation.

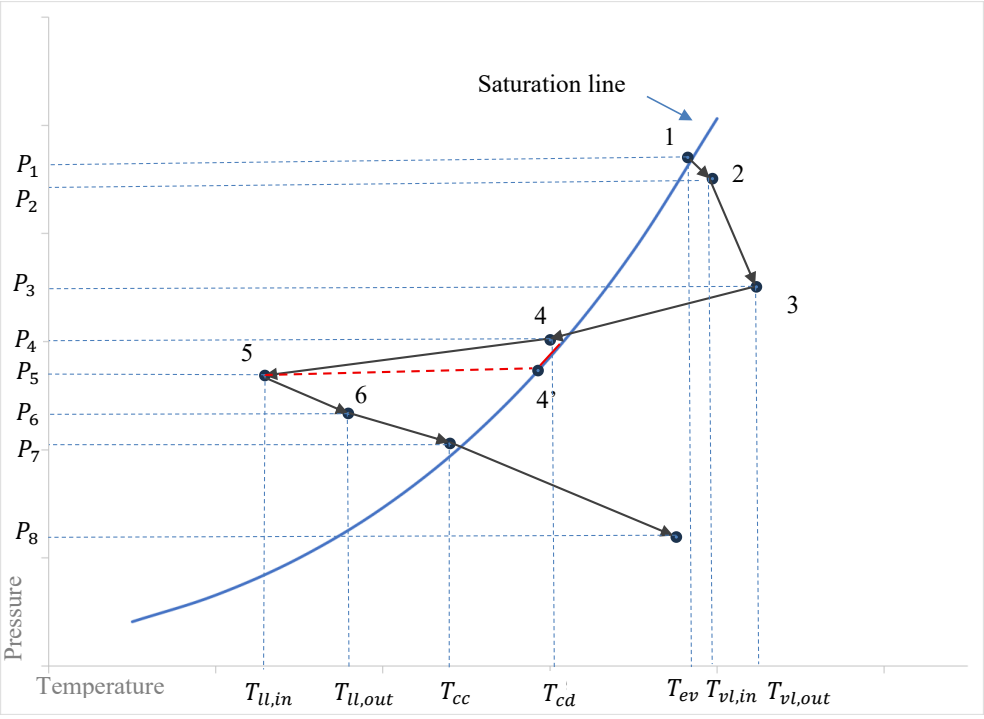


Figure 3-1. P-T diagram of the LHP operating cycle.

Point 1, located on the saturation line, is conventionally taken as the beginning of the cycle. It corresponds to saturated vapor above the meniscus of the working fluid in the evaporation zone of the primary wick. The vapor temperature at point 1 is denoted as $T_{ev}$, and the pressure as $P_1 = P_{ev}$. Section 1–2 corresponds to vapor flow through the vapor-collection grooves inside the evaporator to the entrance of the vapor line (i.e., the evaporator outlet), represented by point 2 on

the diagram. While passing through the internal channels of the evaporator, the vapor receives additional heat from the heat source and becomes superheated. $T_{vl,in}$ denotes the temperature at point 2, i.e., at the vapor-line inlet. The hydraulic resistance of the vapor-collection grooves results in a pressure drop $\Delta P_{ev} = P_1 - P_2$.

Section 2–3 describes vapor flow along the vapor line from the evaporator to the condenser. Point 3 corresponds to the vapor-line outlet (condenser inlet), with temperature $T_{vl,out}$. In the diagram shown, the vapor temperature increases, which corresponds to the case where the ambient temperature $T_{amb}$ is higher than the vapor temperature and the surroundings heat the vapor. If the ambient temperature is lower, the vapor will cool, and in extreme cases (e.g., very long lines) condensation may begin directly in the vapor line. Then section 2–3 may terminate on the saturation line or even cross it if complete condensation occurs. Such limiting cases are not considered here. Under normal conditions, the working fluid enters the condenser in a superheated state. The pressure drop along section 2–3 is attributed to the vapor-line resistance and denoted as $\Delta P_{vl} = P_2 - P_3$.

In section 3–4 the vapor flows through the condenser channels and is cooled to the condensation temperature. Point 4 lies on the saturation line and corresponds to two-phase flow, during which condensation takes place. The condensation temperature is $T_{cd}$. Strictly speaking, point 4 should be replaced by a segment 4–4′ along the saturation curve, since the pressure decreases during two-phase flow and the condensation state shifts accordingly. For qualitative analysis, this effect is usually neglected.

Section 4–5 corresponds to liquid flow through the condenser to the condenser outlet (liquid-line inlet), represented by point 5. The working-fluid temperature at this point is $T_{ll,in}$. Along section 4–5 the liquid becomes subcooled. The condenser contribution to the total pressure drop is $\Delta P_{cd} = P_3 - P_5$.

Section 5–6 represents liquid flow along the liquid line to the compensation chamber. The liquid temperature at the liquid-line outlet (compensation-chamber inlet) $T_{ll,out}$, as will be shown later, is one of the key parameters in LHP performance analysis. The pressure drop along the liquid line is $\Delta P_{ll} = P_5 - P_6$.

Section 6–7. In practice, the liquid does not enter the compensation chamber directly at its inlet but passes through it via a dedicated liquid channel, which is a continuation of the liquid line and is known as the bayonet. The bayonet typically terminates in the core of the evaporator wick. This arrangement ensures that the wick is supplied with liquid first, preventing dry-out. While flowing through the bayonet, the liquid exchanges heat with the liquid inside the compensation chamber, cooling it. At equilibrium, the chamber reaches temperature $T_{cc}$ and pressure $P_7 = P_{cc}$, corresponding to the thermodynamic state of the fluid in the compensation chamber. The chamber volume is generally designed so that both phases are always present; therefore, point 7 lies on the saturation curve. The pressure drop across the bayonet is $\Delta P_b = P_6 - P_7$.

The final section 7–8 corresponds to liquid flow through the primary wick from its core to the evaporation zone. The liquid in this region is in a superheated state; however, boiling is suppressed by the fine-pore structure of the primary wick. The working-fluid temperature rises to the evaporation temperature $T_{ev}$ due to counter-flow heat transfer through the wick.

Point 8, characterized by the minimum pressure and a temperature equal to the evaporation temperature $T_{ev}$, corresponds to the liquid region beneath the meniscus in the evaporation zone.

The pressure rise from $P_8$ to $P_1$ is provided by the capillary pressure generated by surface tension at the menisci. This completes the thermodynamic cycle of working-fluid circulation in the LHP.

The mathematical description of LTS differs from that of a conventional thermosyphon. In many respects, it is closer to the modelling of LHP. In LTS, similarly to an LHP, the motion of liquid and vapor is separated: vapor generated in the evaporator flows toward the condenser through the riser (vapor line), while the liquid returns to the evaporator through the downcomer (liquid line). This separation prevents undesirable interaction between counterflowing phases and allows the use of conventional pipe-flow formalisms for estimating hydraulic resistance of the channels.

In LTS, circulation of the working fluid is driven by gravitational head, whereas in an LHP the dominant driving force is provided by the capillary forces generated in the primary evaporator wick. In LHPs, the gravitational head may either assist or oppose circulation depending on the orientation of the system with respect to gravity: when the evaporator is located above the condenser, gravity hinders the flow, while the opposite arrangement is favourable. In contrast, LTS can operate only when the condenser is positioned above the evaporator.

This apparent simplification of the device architecture does not imply simplification of the mathematical model. On the contrary, in LHP there is a clear functional specialization of the flow paths: vapor always flows through the vapor line, provided that condensation does not occur there due to external heat exchange. In LTS, however, a two-phase liquid–vapor mixture may flow through the vapor line, which significantly complicates the mathematical description of the working fluid motion.

This difference originates from the presence of a well-defined liquid–vapor separation in LHPs, ensured by the capillary barrier formed by the primary evaporator wick. Vapor generation in LHP takes place in a strictly localized region above the menisci of the primary wick. In LTS, by contrast, the evaporator may become fully flooded with liquid, so that vapor generation can occur in the form of volumetric boiling.

Another important distinction is the absence, in the general case, of a compensation chamber in LTS—an element that plays a key role in the stable operation of LHPs. In LTS, thermal expansion of the working fluid is accommodated by the position of the liquid–vapor interface in the condenser. This manifests itself as a reduction of the effective condensation zone as the transferred power increases. Such differences in the underlying physical mechanisms are also reflected in the thermodynamic cycle of LTS, which differs fundamentally from that of LHP.

Figure 3-2 schematically presents the thermodynamic cycle of a loop thermosyphon in (P-T) coordinates. The direction of the arrows corresponds to the direction of working fluid circulation.

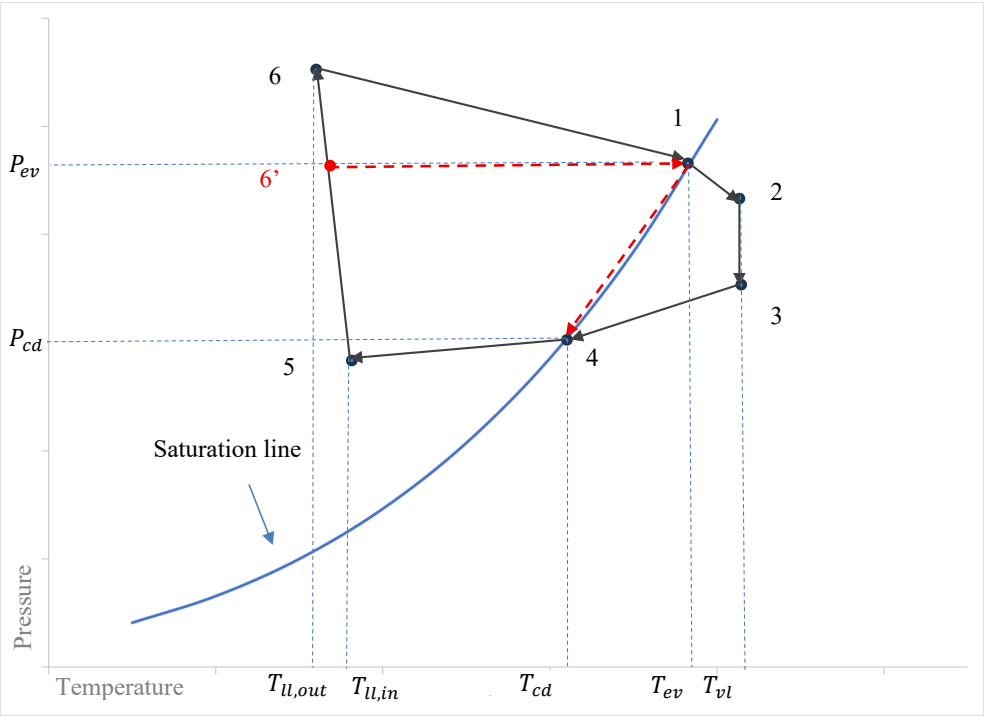


Figure 3-2. P-T diagram of LTS operation cycle.

Point 1 lies on the saturation curve and corresponds to evaporation of the working fluid in the evaporator. It is characterized by the evaporation temperature $T_{ev}$ and pressure $P_{ev}$. From this point, two scenarios are possible. In the first case, superheated vapor exits the evaporator, similarly to an LHP. In this case, segment 1–2 corresponds to vapor flow through the vapor channels of the evaporator. The pressure drop along segment 1–2 is caused by the hydraulic resistance of these vapor channels.

Segment 2–3 represents vapor flow through the vapor line. In the thermodynamic analysis of the LHP, the surrounding environment was assumed to heat the vapor; here, a case more typical for heat loops is intentionally shown, in which the vapor traverses the vapor line under nearly isothermal conditions. This behaviour is reflected in the diagram by the nearly vertical orientation of segment 2–3. The pressure drop along this segment is caused by two factors: the hydraulic

resistance of the vapor line and the gravitational head associated with the upward motion of the vapor.

Segment 3–4 corresponds to vapor flow within the condenser. Along this segment, the vapor cools down to the condensation temperature $T_{cd}$. The pressure drop is associated with the hydraulic resistance of the condenser. Point 4 lies on the saturation curve and corresponds to the condensation process of the working fluid. Here, a commonly used simplification is adopted: condensation is assumed to occur at constant temperature. In reality, condensation takes place over an extended region of the condenser under flowing conditions, accompanied by a pressure drop due to hydraulic resistance. In addition, deceleration of the working fluid caused by density changes leads to a pressure increase within the condenser. A rigorous description of heat transfer and fluid dynamics in the condenser is therefore a rather complex task in loop modelling. Similar considerations apply, to some extent, to the evaporator. In this case, however, the analysis must be tied to the specific evaporator design and should account for vapor generation processes at the microscale. Clearly, vapor generation is accompanied by acceleration of the working fluid up to vapor velocities, which introduces an inertial term associated with the kinetic energy of the vapor into the pressure balance. In overall loop analyses, inertial contributions are usually neglected, as they tend to compensate each other.

Segment 4–5 corresponds to liquid flow through the condenser. Along this segment, the liquid becomes subcooled down to the temperature $T_{ll,in}$, i.e., the liquid temperature at the inlet of the liquid line.

Segment 5–6 represents liquid flow through the liquid line from the condenser to the evaporator. Along this segment, the pressure increases due to the gravitational head of the liquid, which constitutes the driving force of the thermosyphon, reduced by the hydraulic resistance of the liquid line. In the diagram, the liquid in the liquid line is shown to cool slightly down to the temperature $T_{ll,out}$. This situation is typical when the liquid line is not thermally insulated from the ambient environment, whose temperature is lower than that of the liquid. Point 6 corresponds to the evaporator inlet and usually represents the lowest point of the loop thermosyphon. At this location, the pressure reaches its maximum value.

Segment 6–1 is highlighted separately. It appears when a wick is installed in the evaporator and corresponds to liquid filtration through the wick toward the evaporation zone. The introduction of a wick stabilizes the evaporation process, increases the effective heat transfer surface area, and may assist liquid supply to the evaporation zone by capillary forces when the gravitational head is reduced due to loop inclination. At the same time, the wick increases the overall hydraulic resistance of the loop, which is reflected as an additional pressure drop along segment 6–1. Alternatively, point 6′ and segment 6′–1 are shown in the diagram, corresponding to a classical loop thermosyphon configuration without a wick. Along segments 6–1 and 6′–1, the liquid is heated to the evaporation temperature under single-phase conditions.

The thermodynamic cycle of the loop thermosyphon described above corresponds to operating conditions close to the upper limit of its heat-transport capacity. At lower heat loads, a

two-phase vapor–liquid mixture may flow through the vapor line. In the case of two-phase flow, segment 1–2–3–4 of the cycle should be replaced by an alternative path along the saturation line, indicated in the diagram by the dashed red line 1–4.

The use of thermodynamic cycles for analysing heat-transfer devices is, in general, an idealization of real processes, which are inherently strongly non-equilibrium. Nevertheless, this approach has proven effective in the thermodynamic analysis of heat engines, which creates a natural temptation to extend it to other devices, such as LHPs and LTSs, as done above. The choice of pressure–temperature (P–T) coordinates in this context is not accidental, and the following remark explains why.

The thermodynamic analysis of LTS operation presented above is important because it often causes difficulties even in contemporary studies [12]. Another common approach is to describe LTS thermodynamics in temperature–entropy (T–S) coordinates. In this representation, researchers encounter an apparent inconsistency. LTSs and LHPs are not heat engines and do not perform mechanical work; therefore, over a closed cycle of the working fluid, the net work is zero. According to the first law of thermodynamics, the cyclic integral $\oint T\,dS$ is therefore also zero. On a (T–S) diagram, this may lead to the incorrect conclusion that evaporation and condensation occur at the same temperature (see, for example, thermosyphon cycles in [10]), which contradicts the second law of thermodynamics, according to which heat transfer without work can proceed only from a higher to a lower temperature, implying the necessity of a finite temperature difference between the evaporator and the condenser. Attempts to resolve this contradiction by separating evaporator and condenser temperatures within a (T–S) framework result in the appearance of uncompensated heat within the loop [13].

Therefore, the use of (T–S) coordinates for the thermodynamic description of irreversible heat-transfer devices operating under continuous entropy generation and pressure losses [14] is not the most appropriate approach. For this reason, the use of pressure–temperature (P–T) coordinates is more suitable for the thermodynamic analysis of LTSs and LHPs.

## 3.3 Heat Collection from the Source: Modelling of the Thermal Interface

The part of the HL responsible for transferring heat from the cooled device to the evaporator is referred to as the thermal interface, or the evaporator saddle. Its design is largely dictated by the geometry of the specific application, as will be demonstrated in Chapters 4 and 5, which address the cooling of an in-wheel motor and a LED luminaire, respectively.

The most common situation involves heat collection from a flat surface, for example in microchip cooling. In such cases, one side of the thermal interface must be flat, while the opposite side conforms to the surface of the capillary pump. “Altom” capillary pumps have a cylindrical geometry; therefore, the thermal interface must provide efficient heat transfer from a flat surface to a cylindrical one.

If manufacturing simplicity is taken into account as a design constraint, the most straightforward interface geometry is a prismatic body made of a high-thermal-conductivity material (typically aluminium) with an embedded capillary pump. Figure 3-3 shows a saddle composed of two parts—an upper and a lower section—with a machined cylindrical seat for installing the capillary pump.

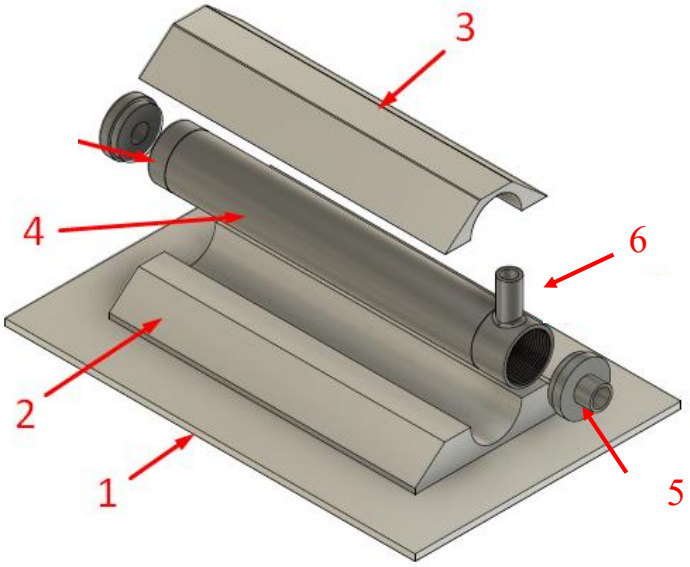


Figure 3-3. Design of the prismatic composite saddle: 1 - Cooled surface; 2 - Lower saddle section; 3 - Upper saddle section; 4 - Capillary pump housing; 5 - Liquid inlet; 6 - Vapor outlet.

The lower part of the saddle (2) is attached to the cooled surface (1), while the upper part (3) is fastened to the lower section using screws and brazing.

A more advanced manufacturing approach, providing higher mechanical strength of the evaporator assembly and improved thermal conductivity, involves machining the saddle from a single piece of aluminium, followed by installation of the capillary pump by means of vacuum brazing (Figure 3-4).

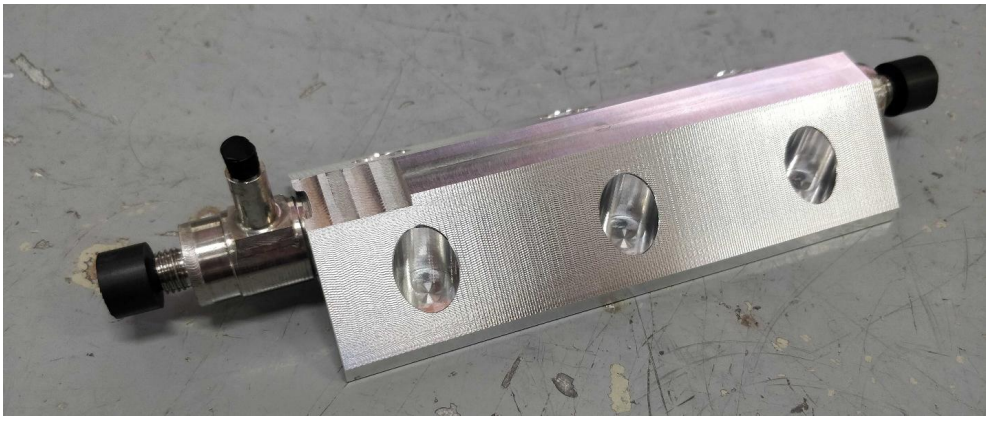

Figure 3-4. A saddle machined from a single piece of aluminium, with the capillary pump installed by vacuum brazing.

The selection of interface dimensions represents a compromise between its mass and thermal conductance. Devices developed for space applications typically face strict mass limitations; therefore, a parametric study was carried out to determine the dependence of saddle conductance and mass on its geometric dimensions in order to identify an optimal configuration.

For a prismatic interface, the geometry is defined by its cross-section, which in the general case has the shape of an isosceles trapezoid (Figure 3-5).

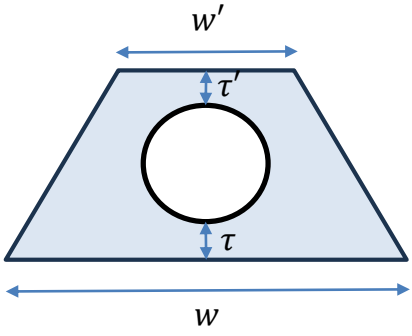


Figure 3-5. Geometric parameters of the prismatic evaporator saddle.

The diameter of the inner circle corresponds to the outer diameter of the capillary pump; therefore, the trapezoidal geometry can be defined by the parameters $w, w', \tau, \tau'$. The parametric

study of heat transfer from the cooled surface to the wick was carried out using CAE ANSYS. The following design considerations were taken into account:

The evaporator should be positioned as close as possible to the cooled surface; therefore, the distance $\tau$ between the evaporator and the cooled surface was chosen to be the minimum achievable from a manufacturing standpoint.

The saddle should completely enclose the evaporator housing. The choice of a closed saddle configuration is justified by two factors: first, it provides higher thermal conductance, and second, greater mechanical strength. For comparison, Figure 3-6 illustrates open and closed saddle designs. An open (lightweight) saddle may be used in cases where thermal conductance and mechanical strength are not the primary design drivers and weight reduction is the dominant objective.

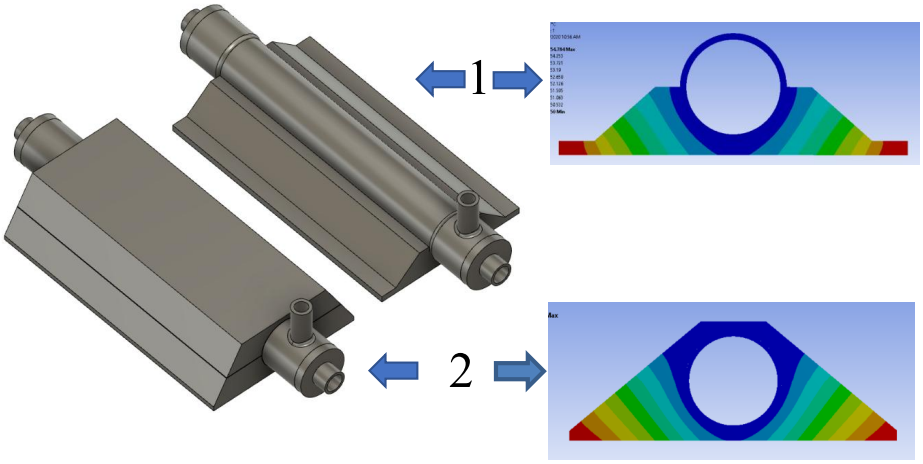


Figure 3-6. 1 – Open saddle; 2 -Closed saddle.

The width $w$ of the saddle in the contact region with the cooled surface should be approximately $w \approx \pi\, d_{\text{out}}$, where $d_{\text{out}}$ is the outer diameter of the capillary pump. This relationship ensures that the average heat-flux density is preserved between the cooled surface and the surface of the capillary pump.

According to the above considerations, the parameters $w$ and $\tau$ can be treated as fixed, while $w'$ and $\tau'$—the width of the upper saddle surface and the distance from the capillary-pump housing to the upper saddle surface—are varied. For the Altom-14 capillary pump, $w = 50$ mm and $\tau = 2.4$ mm. The variation ranges were selected as $10\text{ mm} \le w' \le 50\text{ mm}\ (= w), \tau' \ge 2.4$ mm. The minimum values of $w'$ and $\tau'$ were chosen on the same basis as for $\tau$, namely

mechanical constraints. At smaller values, the saddle structure would not provide sufficient mechanical strength.

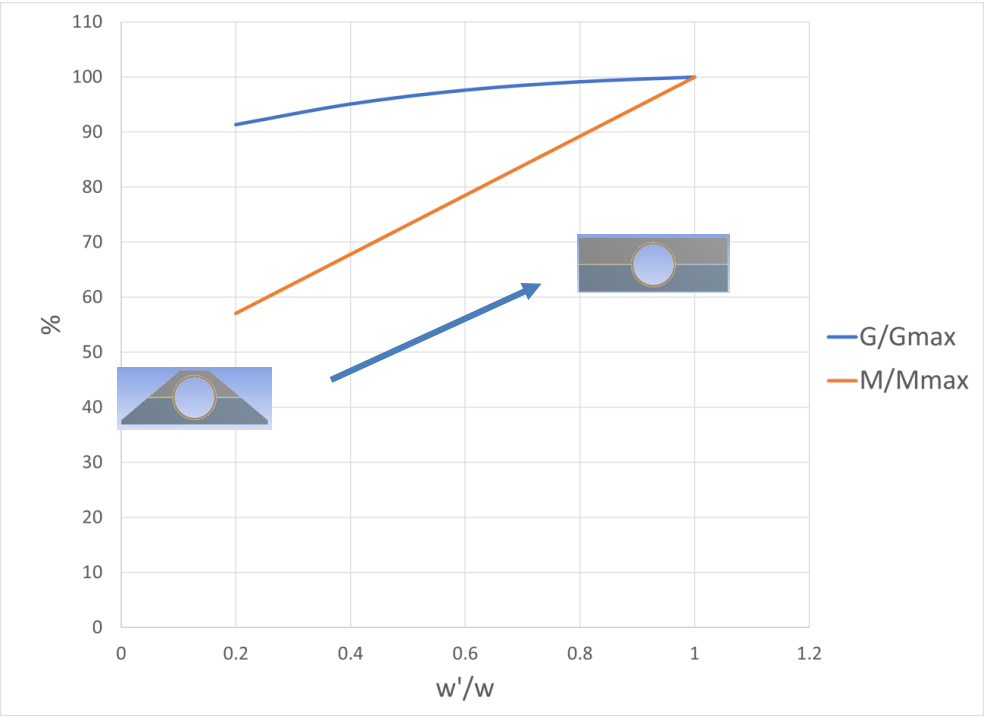


Figure 3-7. Dependence of the saddle's effective thermal conductance on its geometry.

The calculations showed that both conductance and mass increase with increasing $w'$and $\tau'$, while the mass increases significantly faster. Therefore, the key performance parameter can be defined as the specific conductance (the ratio of conductance to mass), which reaches a maximum at the minimum values of $w'$and $\tau'$, i.e., at $w' = 10$ mm and $\tau' = 2.4$ mm. The calculation results are presented in Figure 3-7. The x-axis shows the ratio $w'/w$, while the y-axis shows $G_{\text{sdl}}/G_{\text{sdl, max}}$and $M_{\text{sdl}}/M_{\text{sdl, max}}$. From this relationship it follows that a 10 % increase in saddle conductance leads to approximately a 43 % increase in mass.

The same reasoning leads to the conclusion that increasing the parameter $\tau'$ in order to obtain a 10 % increase in saddle conductance results in an even larger increase in mass. This effect is illustrated in Figure 3-8, which shows the relationship between saddle mass and conductance for various values of the parameters $w'$and $\tau'$. The calculations were performed for an evaporator length of 100 mm.

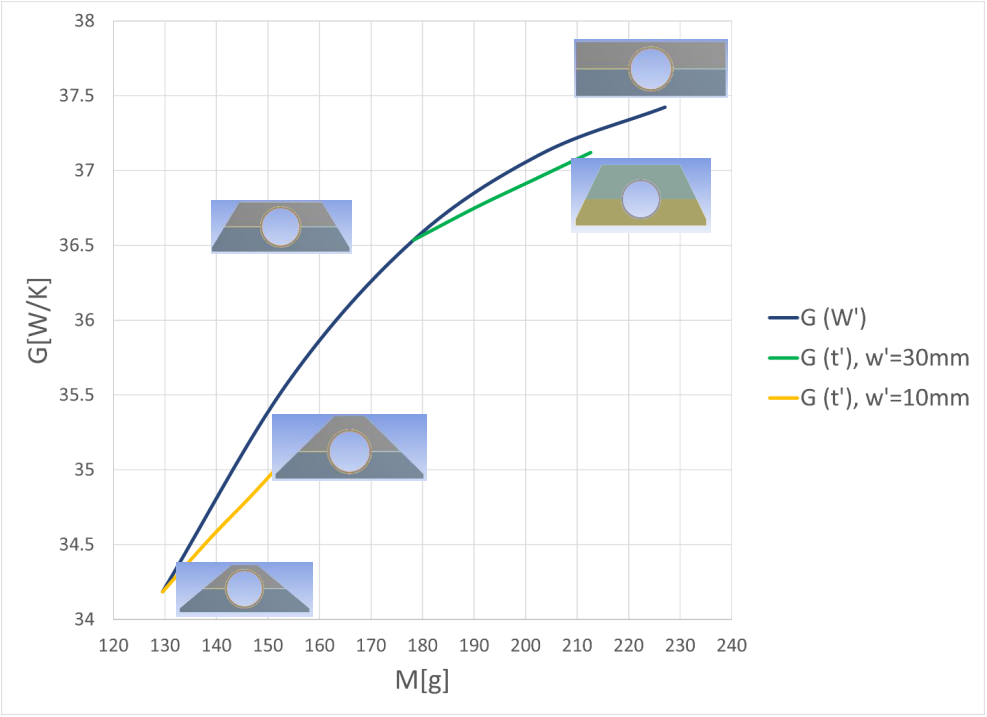


Figure 3-8. Dependence of the saddle's thermal conductance on its mass for different geometric parameters.

In the general case, in addition to heat transfer from the cooled surface to the capillary pump, heat exchange between the evaporator and the surrounding environment must also be taken into account. For this purpose, the conductance of the interface must be evaluated for other possible directions of heat flow. Owing to the linearity of the heat-conduction equation and the associated boundary conditions, the superposition principle can be applied to temperature fields and heat fluxes. An illustration of such a calculation is presented in Figure 3-9.

Aluminium alloys such as 6061 or 6082, with a thermal conductivity of approximately $150\ W/(m \cdot K)$, are typically used for manufacturing the interface. The calculations yield the following conductance values per unit saddle length: $g_{sdl,dn} \approx 340\ W/(m \cdot K)$ for heat transfer toward the heat source, and $g_{sdl,up} \approx 870\ W/(m \cdot K)$ for the average conductance toward the surrounding environment.

In practice, these calculations overestimate the actual conductance because they do not account for the thermal contact resistance between the wick and the capillary pump housing. Experience shows that contact resistance reduces the calculated values by approximately a factor of two.

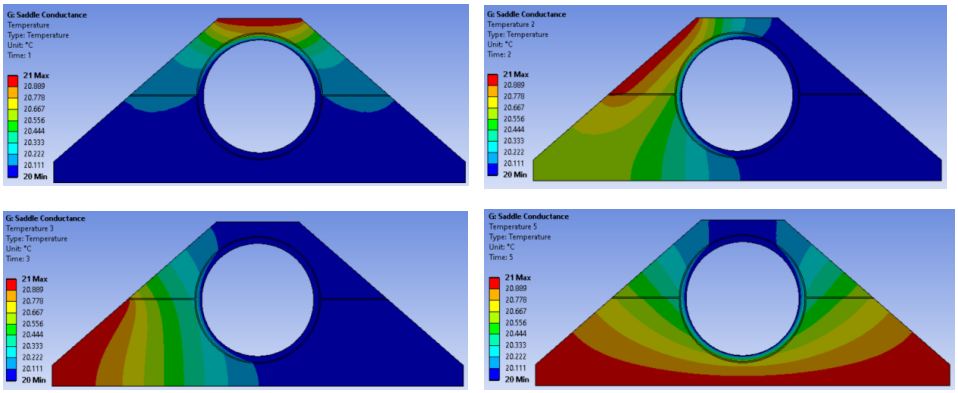


Figure 3-9. Example of a CAE ANSYS temperature-field simulation used to evaluate the saddle's thermal conductance for different heat-flow directions.

This does not invalidate the analysis presented above, as it still enables appropriate selection of the interface geometry and provides a reliable relative assessment of the possible heat-transfer paths.

## 3.4 Heat Transport to the Heat Sink: Steady-State Mathematical Model of Loop Heat Pipe

A steady-state mathematical model seeks the stable operating points of a cooling system, i.e., the states to which it returns after an equilibrium disturbance caused by a change in one of the external parameters. In the most general form, the external parameters that define the operating regime of a cooling system are the input thermal power (heat load) $\dot{Q}_{in}$ supplied by the cooled device (e.g., an electronics unit) and the ambient temperature $T_{amb}$, if the rejected heat is ultimately dissipated to the environment. The model output is the temperature of the cooled device $T_{src}$, which is typically specified by the customer at the level of requirements. The calculated temperature is compared with the specified one, and, depending on the result, the parameters of the cooling system are adjusted.

Given the factorization into three sub-tasks introduced above, at least two additional characteristic temperatures must be defined: $T_{ev}$ and $T_{sink}$. The former is the working-fluid saturation (evaporation) temperature in the evaporator, whereas the latter is the mean temperature of the condenser surface. Under this representation, the first sub-task corresponds to heat transfer between $T_{src}$ and $T_{ev}$; the LHP transports heat between $T_{ev}$ and $T_{sink}$; and heat rejection to the ambient occurs from the condenser at $T_{sink}$. Accordingly, the overall thermal

$$R = R_{sdl} + R_{LHP} + R_{sink} \tag{3.1.}$$

or, if the system is described in terms of thermal conductances, then

$$\frac{1}{G} = \frac{1}{G_{sdl}} + \frac{1}{G_{LHP}} + \frac{1}{G_{sink}} \tag{3.2.}$$

where, respectively

$$R_{sdl} = \frac{T_{src} - T_{ev}}{\dot{Q}_{in}} \tag{3.3.}$$

$$R_{LHP} = \frac{T_{ev} - T_{sink}}{\dot{Q}_{in}} \tag{3.4.}$$

$$R_{sink} = \frac{T_{sink} - T_{amb}}{\dot{Q}_{in}} \tag{3.5.}$$

Thermal conductances, by definition, are the reciprocals of thermal resistances.

In addition to computing the operating temperatures, a key objective of the modelling is to determine the maximum heat-transfer capability of the loop, $\dot{Q}_{max}$. This parameter is strongly dependent on the specific LHP design and on the properties of the selected working fluid.

The developed mathematical model belongs to the class of quasi-one-dimensional steady-state models. It determines the steady operating points of an LHP based on: 1) the energy-balance equation, 2) the pressure-balance equation, 3) the mass-conservation law, and an iterative numerical procedure, the concept of which is described in [15]. The model accounts for heat exchange with the environment and for gravitational effects. The one-dimensional assumption is relaxed when calculating heat transfer between the evaporator and condenser and the surrounding environment.

Figure 3-10 shows the heat-flow paths considered in the energy balance and the main temperatures computed by the model.

In addition to the temperatures introduced above ($T_{src}, T_{ev}, T_{sink}, T_{amb}$), the main computed temperatures include: $T_{cd}$, the working-fluid condensation temperature in the condenser; $T_{cc}$, the working-fluid temperature in the compensation chamber; $T_{vl,in}$, the vapor temperature at the inlet of the vapor line (i.e., at the evaporator outlet); $T_{vl,out}$, the vapor temperature at the outlet of the vapor line (i.e., at the condenser inlet); $T_{ll,in}$, the liquid temperature at the inlet of the liquid line (i.e., at the condenser outlet); and $T_{ll,out}$, the liquid temperature at the outlet of the liquid line (i.e., at the evaporator inlet).

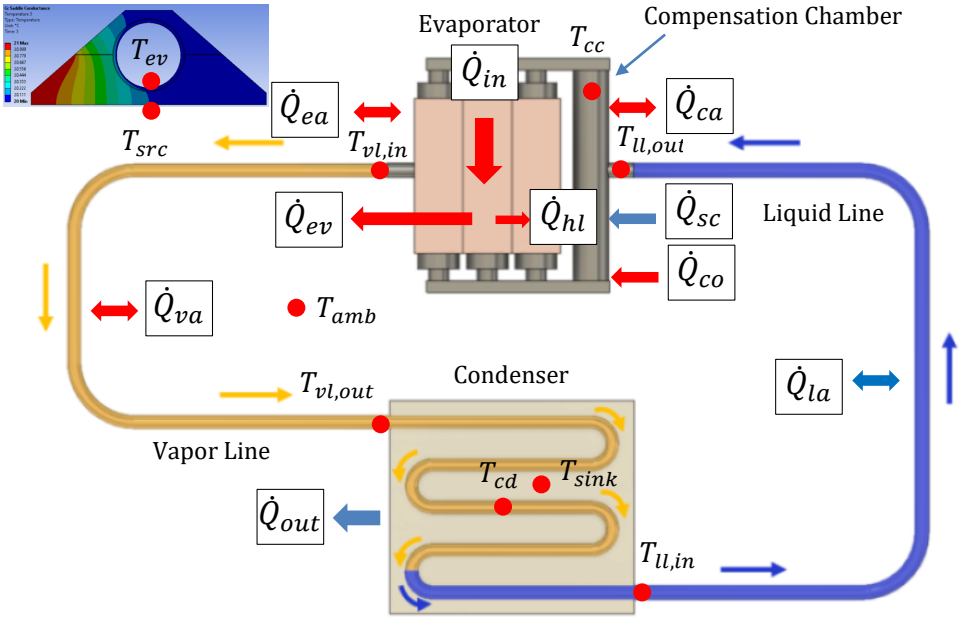


Figure 3-10. Heat flows and temperatures are used in LHP modeling.

The latter temperatures are the most important, since they are readily measurable in experiments. For a well-performing evaporator, $T_{vl,in} \approx T_{ev}$, while $T_{ll,out}$ provides information on heat leakage from the evaporator to the compensation chamber. In steady-state operation of an LHP, all temperatures are constant and all heat flows are balanced.

The evaporator energy-balance equation can be written as follows:

$$\dot{Q}_{in} + \dot{Q}_{ea} = \dot{Q}_{ev} + \dot{Q}_{hl} \tag{3.6.}$$

$\dot{Q}_{in}$ is the heat flow generated by the heat source (the cooled device). $\dot{Q}_{ea}$ is the heat flow entering the evaporator from the ambient environment. It can be positive if the ambient temperature is higher than the evaporator temperature, and negative if the ambient environment is colder. The right-hand side of equation (3.6) describes the distribution of heat flows within the evaporator. $\dot{Q}_{ev}$ is the heat flow consumed for the evaporation of the working fluid, while the second term, $\dot{Q}_{hl}$, represents the so-called "heat leak"—the conductive heat transfer into the compensation chamber. Although "heat leak" is often referred to as parasitic heat, in reality it is simply another heat-transfer pathway to the condenser and plays a fundamental role in the operation of an LHP.

The mass conservation law for the loop can be written as follows:

$$\dot{m} = \frac{\dot{Q}_{ev}}{h_{ev}} = const \tag{3.7.}$$

The energy-balance equation for the compensation chamber:

$$\dot{Q}_{cc} = \dot{Q}_{hl} + \dot{Q}_{co} + \dot{Q}_{ca} \tag{3.8.}$$

Here, $\dot{Q}_{ca}$ describes the heat exchange between the chambers and the ambient environment and, similarly to $\dot{Q}_{ea}$, it may be either positive or negative. $\dot{Q}_{co}$is the heat flow generated by an external heater that may be installed on the compensation chamber to control the operating modes of the loop. If a Peltier element is used instead of a heater, the chambers can be not only heated but also cooled.

In equations (3.6) and (3.8), the quantities $\dot{Q}_{in}$ and $\dot{Q}_{co}$ are prescribed, whereas $\dot{Q}_{ea}$, $\dot{Q}_{hl}$, and $\dot{Q}_{ca}$ can be calculated if the temperature distribution along the loop is known. In turn, the temperature distribution depends on the heat flow $\dot{Q}_{ev}$, which is transported by the working fluid toward the condenser. This interdependence is resolved using an iterative computational algorithm.

The equation closing the thermal balance of the loop is expressed as follows:

$$\dot{Q}_{cc} = \dot{Q}_{sc} \tag{3.9.}$$

It means that, in steady-state operation, the total heat flow into the compensation chamber, $\dot{Q}_{cc}$, must be balanced by the "cold" (i.e., subcooling heat) $\dot{Q}_{sc}$ brought from the condenser by the subcooled liquid. When condition (3.9) is satisfied, the LHP operates in a steady state; that is, all temperatures remain constant. This serves as the basis for the computational algorithm used to determine the steady-state operating point for a given heat-source power and ambient conditions.

If the sink temperature $T_{sink}$ is prescribed, the variable parameter is the evaporator temperature $T_{ev}$. An initial assumption is made for the value of $\dot{Q}_{ev}$, after which all other temperatures and heat flows are computed. If no value of $\dot{Q}_{ev}$ can be found that satisfies $\dot{Q}_{cc} = \dot{Q}_{sc}$, this indicates that the chosen $T_{ev}$ is incorrect and must be increased or decreased. An analogous calculation procedure applies when $T_{ev}$ is fixed and $T_{sink}$ is varied.

The value of the sink temperature is determined by the condenser design and the type of external heat-transfer mechanism implemented on the condenser. Heat transfer from the condenser to the ambient environment corresponds to the third task listed at the beginning of this chapter and will be discussed later. The following sections describe the methods used to compute all terms appearing in equations (3.6) and (3.8).

### Heat Transfer Between the Compensation Chamber and the Ambient Environment

In general case, heat transfer from the compensation chamber to the ambient environment may occur through radiation and convection:

$$\dot{Q}_{ca} = \dot{Q}_{ca}^{con} + \dot{Q}_{ca}^{rad} \tag{3.10.}$$

$\dot{Q}_{ca}^{rad}$ is calculated using the Stefan–Boltzmann law:

$$\dot{Q}_{ca}^{rad} = \varepsilon \cdot \sigma \cdot S_{sur} \cdot (T_{sur}^4 - T_{amb}^4) \tag{3.11.}$$

Since compensation chambers typically have a cylindrical shape, the convective component $\dot{Q}_{ca}^{con}$ can be evaluated using the heat-transfer relations for a cylindrical tube exposed to an external environment. In this case, it is convenient to express the conductance $g$ per unit length, which can be written in terms of the Nusselt number as follows:

$$g = \lambda \cdot \pi \cdot Nu \tag{3.12.}$$

For internal heat transfer, $\lambda$ denotes the thermal conductivity of the working fluid, whereas for external heat transfer it represents the thermal conductivity of air. The Nusselt number $Nu$ for internal forced convective heat transfer can be calculated using the following correlations:

$$Nu_{in} = \begin{cases} 3.66, & Re \leq 2300 \\ 0.023 \cdot Re^{0.8} \cdot Pr^{m}, & Re > 2300 \end{cases} \tag{3.13.}$$

Where $m = 0.4$ for heating and $m = 0.3$ for cooling. $Re$ and $Pr$ are the Reynolds and Prandtl numbers, respectively. If no special conditions are imposed, external heat transfer occurs by natural convection; therefore, in this case, the heat-transfer coefficient is determined by the Rayleigh number $Ra$:

$$Nu_{out} = \begin{cases} Nu_l = 0.75 \cdot Ra^{1/4}, 10^3 < Ra < 10^9 \\ Nu_t = 0.15 \cdot Ra^{1/3}, 6 \cdot 10^{10} < Ra \\ \frac{1}{2} \cdot (Nu_l + Nu_t), 10^9 < Ra < 6 \cdot 10^{10} \end{cases} \tag{3.14.}$$

The Rayleigh number, in turn, depends on the temperature difference between the outer surface of the chamber, $T_{sur}$, and the ambient air, $T_{amb}$, as well as on the outer diameter of the chamber, $D_{out}$:

$$Ra = K_{nc} \cdot |T_{sur} - T_{amb}| \cdot D_{out}^3 \tag{3.15.}$$

The factor $K_{nc}$ collects all parameters related to air (subscript "a" for air):

$$K_{nc} = \frac{g \cdot c_{p,a} \cdot \rho_a^2}{\eta_a \cdot \lambda_a \cdot T_{amb}} \tag{3.16.}$$

Summarizing the above, the general expression for $\dot{Q}_{ca}^{con}$ is:

$$\dot{Q}_{ca}^{con} = (C_{la} \cdot |T_{sur} - T_{amb}|^{\frac{1}{4}} + C_{tu} \cdot |T_{sur} - T_{amb}|^{\frac{1}{3}}) \cdot S_{sur} \cdot (T_{sur} - T_{amb}) \tag{3.17.}$$

Where factors $C_{la}$ and $C_{tu}$ are defined in Table 3-1:

Table 3-1.

Parameters for convective heat transfer calculating

| Criterion | $C_{la}$ | $C_{tu}$ |
|---|---|---|
| $10^3 < Ra < 10^9$ | $0.75 \cdot \lambda_a \cdot (\frac{K_{nc}}{D_{out}})^{1/4}$ | 0 |
| $10^9 < Ra < 6 \cdot 10^{10}$ | $\frac{1}{2} \cdot 0.75 \cdot \lambda_a \cdot (\frac{K_{nc}}{D_{out}})^{1/4}$ | $\frac{1}{2} \cdot 0.15 \cdot \lambda_a \cdot (K_{nc})^{1/3}$ |
| $Ra > 6 \cdot 10^{10}$ | 0 | $0.15 \cdot \lambda_a \cdot (K_{nc})^{1/3}$ |
| Isolated | 0 | 0 |

For a thin-walled metallic tube, the thermal resistance of the wall can be neglected, and the temperatures of the inner and outer surfaces may be assumed equal:

$$T_{sur} \approx T_{cc} \tag{3.18.}$$

For plastic tubes, or in cases where the tubes are equipped with thermal insulation, condition (3.18) does not hold. In such cases, the thermal conductance of the tube wall per unit length, $g_m$, is calculated as:

$$g_m = \frac{2 \cdot \pi \cdot \lambda_m}{ln\left(\frac{D_{out}}{D_{in}}\right)} \tag{3.19.}$$

The surface temperature $T_{sur}$ is then obtained as the solution of the equation:

$$\begin{aligned} g_m \cdot (T_{cc} - T_{sur}) = \\ = \pi D_{out} \cdot [\left(C_{la} \cdot |T_{sur} - T_{amb}|^{\frac{1}{4}} + C_{tu} \cdot |T_{sur} - T_{amb}|^{\frac{1}{3}}\right) \cdot \\ \cdot (T_{sur} - T_{amb}) + \varepsilon \cdot \sigma \cdot (T_{sur}^4 - T_{amb}^4)] \end{aligned} \tag{3.20.}$$

Such equations are easily solved numerically and have a unique solution within the temperature interval $[T_{cc}, T_{amb}]$.

As follows from the discussion above, control of the heat flow into the compensation chambers plays a key role in regulating the operating state of the thermal loop. In some cases, in order to reduce the heat exchange between the chamber and the ambient environment, it is beneficial to construct the chamber housing from two shells and create a vacuum gap between them. The vacuum gap acts as an insulator, and heat transfer between the chamber and the ambient environment occurs only through radiation. In this configuration, the outer shell functions as a radiative shield. If both the chamber tube and the shield are made of the same material, with the same surface treatment and thus the same emissivity $\varepsilon$, then the heat exchange between the chamber and the ambient environment is described by the following expression:

$$\dot{Q}_{ca} \approx \pi L_{cc} \cdot \frac{\varepsilon}{2 - \varepsilon} \cdot \sigma \cdot (D_{cc} \cdot T_{cc}^4 - D_{sh} \cdot T_{sh}^4) \tag{3.21.}$$

Here, $L_{cc}$ and $D_{cc}$ are the length and diameter of the chamber, respectively, and $D_{sh}$ is the diameter of the shield. The shield temperature $T_{sh}$ is obtained from an equation analogous to (3.20), except that the left-hand side must contain the expression from (3.21) divided by $L_{cc}$:

$$\begin{aligned} \frac{\varepsilon}{2 - \varepsilon} \cdot \sigma \cdot \left(\frac{D_{cc}}{D_{sh}} \cdot T_{cc}^4 - T_{sh}^4\right) = \\ = [\left(C_{la} \cdot |T_{sh} - T_{amb}|^{\frac{1}{4}} + C_{tu} \cdot |T_{sh} - T_{amb}|^{\frac{1}{3}}\right) \cdot \\ \cdot (T_{sh} - T_{amb}) + \varepsilon \cdot \sigma \cdot (T_{sh}^4 - T_{amb}^4)] \end{aligned} \tag{3.22.}$$

**Heat Transfer Between the Evaporator and the Ambient Environment**

Heat exchange between the evaporator and the ambient environment is represented by the heat flow $\dot{Q}_{ea}$ in (3.6). This term can be significant at low heat loads and when the ambient

temperature differs substantially from the evaporator temperature. The method used to calculate the evaporator–ambient heat exchange is largely analogous to that described in the previous subsection. As in the case of the compensation chamber, two components of the heat flow must be considered: the convective component $\dot{Q}_{ea}^{con}$ and the radiative component $\dot{Q}_{ea}^{rad}$:

$$\dot{Q}_{ea} = \dot{Q}_{ea}^{con} + \dot{Q}_{ea}^{rad} \tag{3.23.}$$

To evaluate each component, the geometry of the evaporator and its interface must be taken into account. For the purpose of illustrating the subsequent analysis, Figure 3-11 is provided.

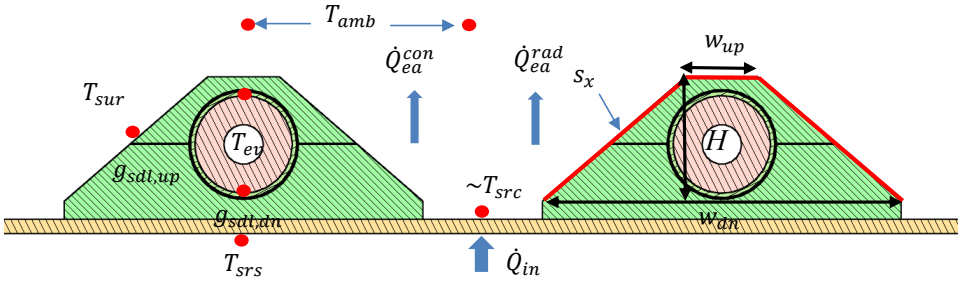


Figure 3-11. Illustration of the evaporator–ambient heat-exchange calculation

In the figure, a system comprising two evaporators with prismatic interfaces mounted on a thermally conductive flat plate (MECOP configuration) is presented as an illustrative example. The device to be cooled is installed on the opposite side of the plate and dissipates a thermal power $\dot{Q}_{in}$. It is evident that, for a device of different geometry, the subsequent analysis must be adapted accordingly; however, the fundamental principles and methodological approach remain unchanged.

In practice, a fraction of the heat flow $\dot{Q}_{ea}$ will almost inevitably be dissipated directly to the ambient environment, bypassing the interface, since certain parts of the cooled device will be in direct contact with the environment. In the present case, this corresponds to the heat rejected from the exposed regions of the plate surface. Therefore, each term entering (3.23) should be represented as the sum of two contributions: the heat removed from the plate surface and the heat removed from the upper surface of the saddle. For the evaluation of the former, the temperature of the outer side of the plate may be approximated as $\sim T_{src}$, in which case:

$$\dot{Q}_{cp} = k_o \cdot S_{cp} \cdot \left[\left(C_{la} \cdot |T_{src} - T_{amb}|^{\frac{1}{4}} + C_{tu} \cdot |T_{src} - T_{amb}|^{\frac{1}{3}}\right) \cdot (T_{src} - T_{amb}) + \varepsilon \cdot \sigma \cdot (T_{src}^4 - T_{amb}^4)\right] \tag{3.24.}$$

The coefficients $C_i$ are evaluated in the same manner as in (3.17), with the only difference that, as the characteristic dimension in Table 3-1, the plate width $W_{cp}$ is used instead of $D_{out}$. The factor $k_o$ depends on the plate orientation and assumes values according to Table 3-2

Table 3-2

Values of the orientation factor $k_o$

| Value | Orientation |
|---|---|
| 1.3 | 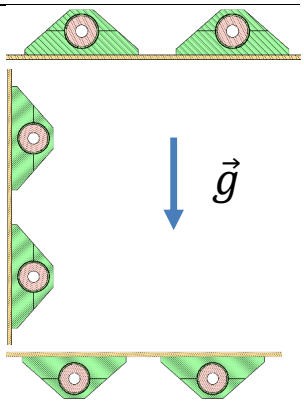 |
| 1 | |
| 0.7 | |



The heat-transfer surface area appearing in (3.24):

$$S_{cp} = L_{cp} \cdot W_{cp} - N_{ev} \cdot w_d \cdot L_w \tag{3.25.}$$

Heat transfer through the "upper" surface of the saddle can be evaluated provided that the saddle surface temperature $T_{sur}$ and the saddle conductance per unit length $g_{sdl,up}$ are known, the method for determining which is described above in Section 3.3. Accordingly:

$$\dot{Q}_{sa} = g_{sdl,up} \cdot L_w \cdot N_{ev} \cdot (T_{src} - T_{sur}) \tag{3.26.}$$

The temperature $T_{sur}$ can be determined by solving an equation analogous to (3.20), with the left-hand side replaced by (3.26) and all quantities expressed per unit length of the evaporator. This yields:

$$g_{sdl,up} \cdot (T_{src} - T_{sur}) = k_o \cdot s_x \cdot \left( C_{la} \cdot |T_{sur} - T_{amb}|^{\frac{1}{4}} + C_{tu} \cdot |T_{sur} - T_{amb}|^{\frac{1}{3}} \right) \cdot \cdot (T_{sur} - T_{amb}) + \varepsilon \cdot \sigma \cdot s_x \cdot (T_{sur}^4 - T_{amb}^4) \quad (3.27.)$$

The parameter $s_x$ represents the area of the external surface of the interface per unit length. It is indicated by the red line in Figure 3-11 and is determined from geometric considerations as follows:

$$s_x = w_{up} + \sqrt{(w_{dn} - w_{up})^2 + 4 \cdot H^2} \quad (3.28.)$$

The heat source temperature $T_{src}$ and the evaporation temperature $T_{ev}$ are related by the following expression:

$$\dot{Q}_{in} + \dot{Q}_{ea}^{con} + \dot{Q}_{ea}^{rad} = g_{sdl,dn} \cdot L_w \cdot N_{ev} \cdot (T_{src} - T_{ev}) \quad (3.29.)$$

Equation (3.29) is used to determine the steady-state temperature $T_{src}$ established at the cooled device. Indeed, the input thermal power from the device $\dot{Q}_{in}$ is known and the heat exchange with the environment has been evaluated. Once the evaporation temperature $T_{ev}$ is determined, (3.29) yields $T_{src}$, which corresponds to the temperature established at the cooled device.

An alternative approach may also be adopted: the temperature $T_{src}$ of the cooled device can be specified a priori—for example, as a requirement defined in the device specification. Equation (3.29) can then be used to calculate the evaporation temperature $T_{ev}$. Subsequently, by analyzing the heat transport toward the condenser, the corresponding condenser parameters can be determined.

**Calculation of Heat Leak and Subcooling**

The heat required for the evaporation of the working fluid at a given mass flow rate $\dot{m}$ is, according to (3.7), equal to

$$\dot{Q}_{ev} = h_{ev}(T_{ev}) \cdot \dot{m} \quad (3.30.)$$

where it is emphasized that the enthalpy of vaporization corresponds to the evaporation temperature $T_{ev}$. Condensation, however, takes place at a lower temperature $T_{cd} < T_{ev}$. Accordingly, the heat released during condensation is given by

$$\dot{Q}_{cd} = h_{ev}(T_{cd}) \cdot \dot{m} \tag{3.31.}$$

Since $h_{ev}(T_{cd}) > h_{ev}(T_{ev})$, the heat released during condensation of the same mass flow rate at a lower temperature exceeds the heat required for evaporation. Therefore, the existence of a steady operating regime of LHP requires the presence of an additional heat-transfer path between the evaporator and the condenser capable of compensating for the difference between $\dot{Q}_{ev}$ and $\dot{Q}_{cd}$. This additional heat-transfer path is provided by the heat leak $\dot{Q}_{hl}$ from the evaporator to the compensation chamber, occurring counter to the direction of the liquid flow returning from the condenser. Moreover, after condensation the working fluid typically undergoes further subcooling while flowing in the liquid state through the condenser channels. As a result, the heat leak must, in practice, exceed the difference between $\dot{Q}_{ev}$ and $\dot{Q}_{cd}$.

Despite its fundamental role in ensuring the steady operation of an LHP, the heat leak is often regarded solely as an undesirable effect, and the physical origin of the heat that must be compensated is not analysed in detail. Instead, this entire amount of heat is commonly referred to as the subcooling heat $\dot{Q}_{sc}$. This quantity can be evaluated by noting that, in steady operation, the working fluid completes a closed thermodynamic cycle and returns to its initial state characterized by the evaporation temperature $T_{ev}$. Consequently, the liquid entering the compensation chamber from the condenser at temperature $T_{ll,out}$ must be heated back to $T_{ev}$.

Neglecting the temperature dependence of the liquid specific heat capacity $c_{p,l}$, the subcooling heat can be written as

$$\dot{Q}_{sc} = c_{p,l} \cdot \dot{m} \cdot (T_{ev} - T_{ll,out}) \tag{3.32.}$$

The liquid temperature $T_{ll,out}$ appearing in (3.32) can be determined by sequentially considering heat exchange in the vapor line, the condenser, and the liquid line. Equation (3.32) is noteworthy in that it involves temperatures that are readily accessible experimentally. In particular, under steady conditions the vapor temperature at the evaporator outlet can usually be measured with good accuracy and may be taken as $T_{vl,in} \approx T_{ev}$.

Taking into account that, in steady state, the heat flow into the compensation chamber satisfies $\dot{Q}_{cc} = \dot{Q}_{sc}$, Eqs. (3.6) and (3.8) allow the subcooling heat to be expressed in terms of measurable quantities as

$$\dot{Q}_{sc} = \frac{1}{1 + \dfrac{h_{ev}(T_{ev})}{c_{p,l} \cdot (T_{ev} - T_{ll,out})}} \cdot \left(\dot{Q}_{in} + \dot{Q}_{ea} + \dot{Q}_{co} + \dot{Q}_{ca}\right) \tag{3.33.}$$

The evaluation of the heat leak $\dot{Q}_{hl}$ is more challenging, as multiple heat-transfer paths may contribute to it. In theoretical analyses of cylindrical evaporators, it is common to account only

for the radial component of heat transfer, which can be associated with the filtration of the working fluid through the wick from its inner core toward the outer evaporation surface.

In the simplest approximation, the heat leak is obtained as the steady-state solution of the heat-conduction equation for a solid cylindrical body [16]

$$\dot{Q}_{hl} = 2\pi\lambda_w L_w \cdot \frac{(T_{ev} - T_{cc})}{ln\left(\frac{D_{ev,out}}{D_{ev,in}}\right)} \tag{3.34.}$$

where $D_{ev,out}$ and $D_{ev,in}$ are the outer and inner diameters of the wick, respectively, and $L_w$ is the wick length. The presence of the working fluid is taken into account through the use of an effective thermal conductivity $\lambda_w$ of the liquid-saturated wick.

Numerous correlations for evaluating $\lambda_w$have been reported in the literature [17]. For wicks manufactured by sintering metallic powders, the classical Maxwell formulation [5] is commonly employed:

$$\lambda_w = \lambda_m \cdot \frac{2 + \frac{\lambda_l}{\lambda_m} - 2 \cdot \varphi \cdot \left(1 - \frac{\lambda_l}{\lambda_m}\right)}{2 + \frac{\lambda_l}{\lambda_m} + \varphi \cdot \left(1 - \frac{\lambda_l}{\lambda_m}\right)} \tag{3.35.}$$

where $\varphi$ is the wick porosity (approximately 47 % for “Altom” capillary pumps), $\lambda_m$ is the thermal conductivity of the wick material (stainless steel in “Altom” capillary pumps, $\lambda_m \approx 14\ W/(m \cdot K)$ and $\lambda_l$ is the thermal conductivity of the working fluid in the liquid phase.

In reality, the solid-cylinder approximation underlying (3.34) is not fully adequate, since the working fluid flowing through the wick contributes to heat transport not only by conduction but also by advective transport of enthalpy. A more physically consistent refinement of (3.34) can be obtained by assuming local thermodynamic equilibrium between the wick matrix and the working fluid and by applying a steady energy balance to a thin cylindrical control volume of the wick. Under these assumptions, the heat transfer can be described by a single temperature field, and the resulting expression for the heat leak remains compact and analytically tractable.

The resulting refined expression for the heat leak at the evaporation surface is

$$\dot{Q}_{hl} = \dot{m} c_{p,l} \cdot \frac{T_{ev} - T_{cc}}{1 - \left[\frac{D_{ev,in}}{D_{ev,out}}\right]^{\frac{c_{p,l}\dot{m}}{2\pi\lambda_w L_w}}} \tag{3.36.}$$

Equation (3.36) represents the heat leak evaluated at the outer surface of the wick, i.e., in the evaporation zone. This choice is consistent with the definition adopted for the subcooling heat,

since the evaporation zone is taken as both the starting and ending point of the working-fluid cycle. It can be readily shown that, in the limiting case $\dot{m} \to 0$, Eq. (3.36) reduces to the purely conductive expression given by (3.34).

The same result can also be obtained from the steady-state energy equation for a moving medium with a convective term

$$u\frac{\partial T}{\partial r} = \frac{\lambda_w}{c_{p,l} \cdot \rho_l}\,\frac{1}{r}\frac{\partial}{\partial r}\left(r \cdot \frac{\partial T}{\partial r}\right) \tag{3.37.}$$

where $u$ is the radial velocity of the working fluid and $\lambda_w$ is the effective thermal conductivity of the liquid-saturated wick defined by (3.35). Solving this equation jointly with the continuity condition

$$\frac{\partial (u \cdot r)}{\partial r} = 0 \tag{3.38.}$$

yields (3.36) when evaluated at $r = D_{ev,out}/2$. In this formulation, the temperature at the center of the wick is assumed to be equal to the compensation chamber temperature $T_{cc}$. This approximation is acceptable for compact evaporators but may not hold for large evaporators such as MECOP-type designs.

In practice, the heat leak from the evaporator to the compensation chamber is not limited to heat transfer through the wick alone. Additional heat-transfer paths may exist, such as conduction through the evaporator casing or direct heat transfer from the heat source when the compensation chamber is located in close proximity due to design constraints. An increase in the heat leak leads, according to (3.9), to an increase in the subcooling heat and, consequently, to a lower required sink temperature. The resulting increase in the temperature difference between the heat source and the heat sink reduces the overall thermal conductance of the loop, thereby degrading its heat-transfer performance.

For this reason, the design of LHP systems typically aims to thermally isolate the compensation chamber from heat sources in order to reduce the heat leak to the minimum level required for stable operation.

From a modelling standpoint, (3.36) may therefore be supplemented by additional terms whose structure depends on the specific evaporator design. For instance, the evaporator may be represented as a network of parallel and series thermal resistances, whose values can be evaluated using numerical heat-transfer simulations (e.g., CAE ANSYS), in a manner analogous to the interface-conductance calculations presented in Section 3.3. In the simplest approximation, sufficient accuracy can often be achieved by adding to (3.36) a term linear in the temperature difference between the compensation chamber and either the heat source or the evaporation zone:

$$\dot{Q}_{hl} = \dot{m}c_{p,l} \cdot \frac{T_{ev} - T_{cc}}{1 - \left[\frac{D_{ev,in}}{D_{ev,out}}\right]^{\frac{c_{p,l}\dot{m}}{2\pi\lambda_w L_w}}} + \frac{T_* - T_{cc}}{R_{HL}} \tag{3.39.}$$

Here, $T_*$ denotes either the source temperature $T_{src}$ or the evaporation temperature $T_{ev}$, depending on the evaporator configuration. For example, in a flat evaporator composed of two "Altom" capillary pumps used in an in-wheel motor cooling loop, $T_* = T_{src}$ should be employed, whereas for an LHP used in an LED luminaire, $T_* = T_{ev}$ is more appropriate. This distinction reflects the presence or absence of a direct thermal path from the heat source to the compensation chamber.

The thermal resistance $R_{HL}$ may be determined either by numerical heat-transfer simulations or empirically through calibration tests, by separating the fraction of the heat flow that is transmitted through the wick from other parasitic heat-transfer paths.

In summary, the problem of evaluating the heat leak and the subcooling heat reduces to determining the temperature distribution along the LHP loop, specifically the evaporation temperature $T_{ev}$, the steady-state temperature in the compensation chamber $T_{cc}$, and the liquid temperature at the outlet of the liquid line $T_{ll,out}$.

**Calculation of the Compensation Chamber Temperature**

The calculation of the temperature $T_{cc}$ in the compensation chamber is based on the assumption that, under steady-state conditions, the working fluid in the compensation chamber is in a saturated state. The steady saturated vapor pressure in the compensation chamber $P_{cc}$ can be determined from the saturation pressure in the evaporator $P_{ev}(T_{ev})$ by evaluating the pressure losses across the individual components of the LHP

$$P_{cc} = P_{ev} - \Delta P_{ev} - \Delta P_{vl} - \Delta P_{cd} - \Delta P_{ll} - \Delta P_b - \Delta P_g \tag{3.40.}$$

Here, $\Delta P_{ev}$, $\Delta P_{vl}$, $\Delta P_{cd}$, $\Delta P_{ll}$, and $\Delta P_b$ denote the hydrodynamic pressure drops in the evaporator, vapor line, condenser, liquid line, and bayonet, respectively, while $\Delta P_g$ represents the gravitational pressure head.

The calculation of hydrodynamic pressure losses in the various sections of the loop is based on the assumption that the local motion of the working fluid obeys the Navier–Stokes equations. These equations can be significantly simplified by adopting a one-dimensional description, since the flow in LHPs typically occurs in channels whose transverse dimensions are much smaller than their lengths. In this case, the Navier–Stokes equations may be averaged over the cross-section, leading to a one-dimensional formulation. Under steady-state conditions, the pressure gradient in a channel oriented along the $z$-axis can then be written as [18]

$$\frac{dP}{dz} = -\varrho \cdot v\frac{dv}{dz} - \frac{\Pi}{S} \cdot \tau_w - \rho \cdot g \cdot \sin\,\vartheta \tag{3.41.}$$

Here, $S$ is the cross-sectional area of the channel and $\Pi$ is its perimeter. All quantities in (3.41), except for the wall shear stress $\tau_w$, are averaged over the channel cross-section, while $\tau_w$ is averaged over the channel perimeter.

The first term on the right-hand side of (3.41) is associated with acceleration and deceleration of the working fluid. If the transport lines of the loop do not contain significant contractions or expansions, this term differs appreciably from zero only in the evaporation and condensation zones. Since the working fluid circulates in a closed loop and returns to its initial state under steady-state conditions, the pressure decrease due to acceleration is compensated by the pressure increase during deceleration, and the net contribution of this term to the overall pressure balance in (3.40) is zero.

The third term in (3.41) accounts for the effect of gravity. When integrated over the entire loop, it yields the gravitational pressure contribution

$$\Delta P_g = (\rho_l - \rho_v) \cdot g \cdot L_g \cdot \sin\,\vartheta \tag{3.42.}$$

where $\vartheta$ is the inclination angle of the LHP with respect to the horizontal. For $0 < \vartheta \leq \pi/2$, the evaporator is located above the condenser and gravity opposes the circulation of the working fluid. For $-\pi/2 \leq \vartheta < 0$, the evaporator is located below the condenser and gravity assists the LHP operation. Here, $L_g$ is the distance between the evaporator and the condenser, and $\rho_l$ and $\rho_v$ are the densities of the liquid and vapor phases, respectively.

Consequently, in practical calculations of hydraulic resistance, only the second term in (3.41), associated with viscous friction, is usually retained. Integrating (3.41) along the channel length yields the pressure drop in the form commonly written as

$$\Delta P = \xi \cdot \frac{\rho \cdot v^2}{2} \cdot \frac{L}{d} \tag{3.43.}$$

where $L$ is the channel length and $d$ is the hydraulic diameter, defined as

$$d = \frac{4S}{\Pi} \tag{3.44.}$$

For a round channel, the hydraulic diameter coincides with the internal channel diameter. The friction factor $\xi$ is expressed in the Darcy form: $\xi = 64/Re$ for laminar flow (Hagen–Poiseuille) and $\xi = 0.316/Re^{0.25}$ for turbulent flow (Blasius). The Reynolds number $Re_k = 2300$ is commonly adopted as the nominal transition point between laminar and turbulent flow regimes.

In reality, the transition between laminar and turbulent flow is not abrupt, and an intermediate transitional regime exists. To achieve a more accurate description of the friction factor over a wide range of Reynolds numbers, various semi-empirical correlations have been proposed in the literature. Among them, the Churchill [19] correlation is particularly convenient, as it provides a continuous representation of laminar, transitional, and turbulent regimes and allows the effect of wall roughness to be taken into account:

$$\begin{cases} \xi = 8 \cdot [(\frac{8}{Re})^{12} + \frac{1}{(A+B)^{\frac{3}{2}}}]^{\frac{1}{12}} \\ A = [2.457 \cdot ln\frac{1}{(\frac{7}{Re})^{0.9} + 0.27 \cdot \frac{\epsilon}{D}}]^{16} \\ B = [\frac{37530}{Re}]^{16} \end{cases} \quad (3.45.)$$

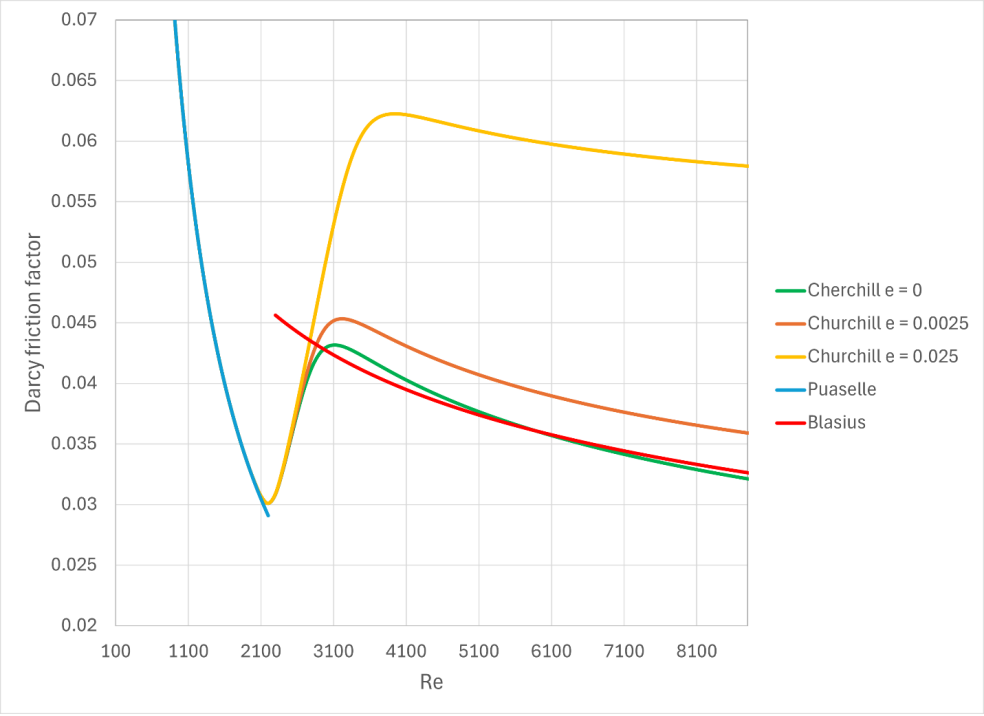


Figure 3-12. Dependence of the Darcy friction factor on the Reynolds number in the Churchill form compared with the Poiseuille and Blasius correlations

Equation (3.45) is used to calculate the pressure drops in the vapor line $\Delta P_{vl}$, liquid line $\Delta P_{ll}$, and bayonet $\Delta P_b$, as well as for single-phase flow regions in the condenser (zones 3–4 and 4–5 in Figure 3-1).

The Churchill correlation provides an accurate match with the Poiseuille solution in the laminar regime and a good agreement with the Blasius correlation in the turbulent regime, while also accounting for wall roughness through the parameter $\varepsilon$. Typical roughness values for various materials are available in the literature. For seamless metallic tubes commonly used in vapor lines, liquid lines, and condenser channels, a roughness value of $\varepsilon = 0.0025$ was adopted. For vapor channels in the primary wick manufactured by sintering metallic powder, a roughness value an order of magnitude higher, $\varepsilon = 0.025$, was assumed. This choice reflects the characteristic surface texture of porous metallic structures. Figure 3-12 compares the Poiseuille and Blasius friction-factor correlations with the Churchill correlation for different roughness values ($\varepsilon = 0$, $0.0025$, and $0.025$). The results demonstrate that the Churchill formulation ensures an excellent agreement with the Poiseuille regime and a good agreement with the Blasius regime.

The pressure drop $\Delta P_{ev}$ accounts for the losses in the vapor-collecting grooves of the capillary pump. In Altom evaporators, transverse grooves are formed by threading the inner surface of the capillary pump, while longitudinal grooves are machined on the surface of the wick (Figure 3-13).

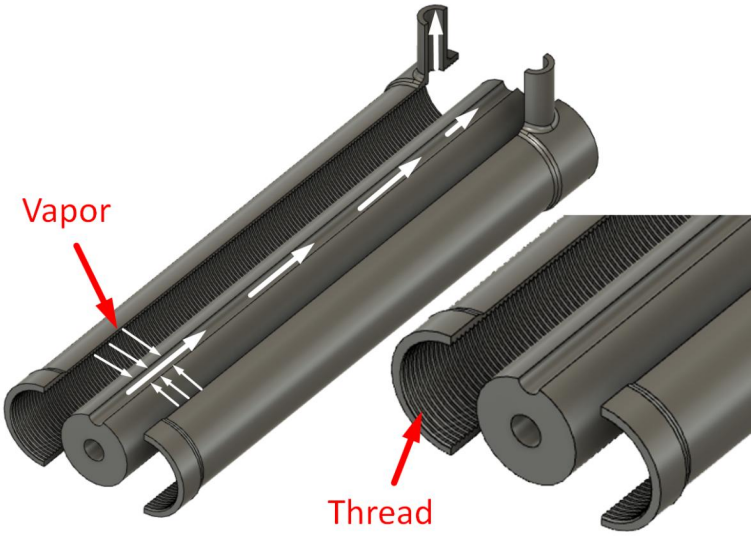


Figure 3-13. Vapor-collecting grooves in the Altom capillary pump

When calculating the hydraulic resistance of the vapor grooves, it is necessary to account for the gradual increase in vapor flow rate toward the vapor outlet of the capillary pump. Assuming that evaporation in the grooves occurs with uniform intensity, the local vapor mass flow rate as a function of the axial coordinate $z$, measured from the groove inlet, may be expressed as:

$$\dot{m}_z = \dot{m} \cdot \frac{z}{L} \tag{3.46.}$$

The local flow velocity $v$ and friction factor $\xi$ in (3.43) can be expressed in terms of $\dot{m}_z$ and therefore become functions of $z$. The total pressure drop in a groove is then obtained by integrating along its length:

$$\Delta P = \frac{\rho}{2 \cdot d} \cdot \int_0^L \xi(z) \cdot v^2(z) dz \tag{3.47.}$$

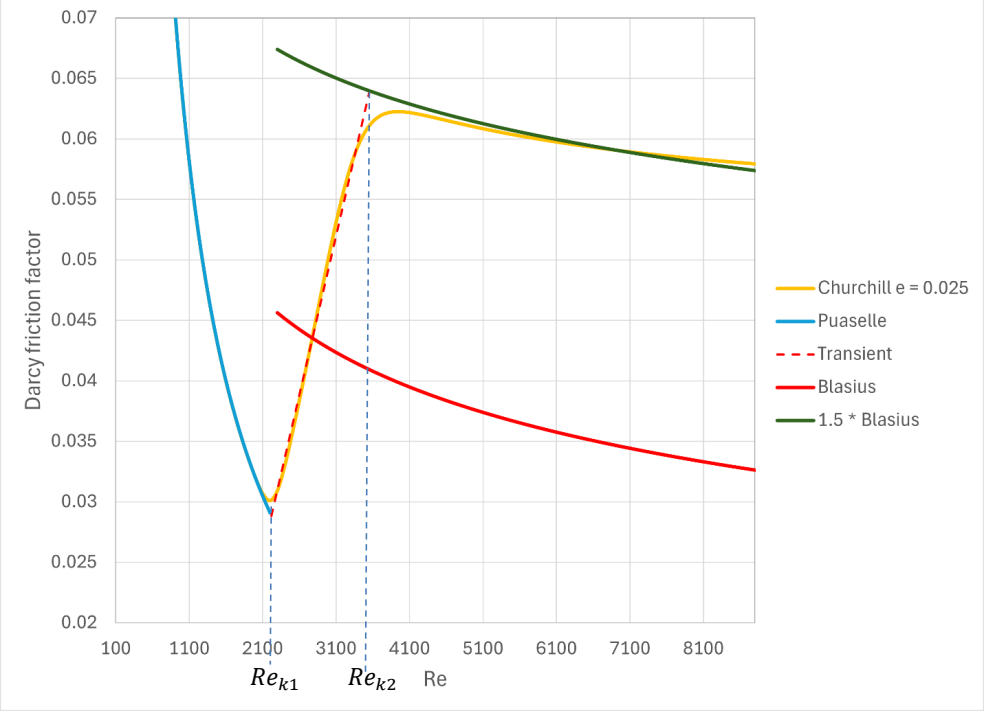


Figure 3-14. Approximation of the Churchill correlation.

This integral can be evaluated numerically using the Churchill correlation given by (3.45). If the Poiseuille and Blasius forms are employed instead, the integral in (3.47) can be evaluated analytically. To account for the transitional regime, it may be noted that the dependence $\xi(Re)$ in this region is close to linear. This approach is illustrated in Figure 3-14.

The limiting Reynolds numbers defining the transition regions are taken as $Re_{k1} = 2220$ for the laminar-to-transitional transition and $Re_{k2} = 3550$ for the transitional-to-turbulent transition. The resulting piecewise representation of the friction factor is then given by

$$\begin{cases} \xi = \dfrac{64}{Re}, & Re \leq 2220 \\ \xi = 2.63 \cdot 10^{-5} \cdot Re - 0.02957, & 2220 < Re < 3550 \\ \xi = 1.5 \cdot \dfrac{0.316}{Re^{0.25}}, & Re \geq 3550 \end{cases} \tag{3.48.}$$

As can be seen, wall roughness is accounted for by the multiplicative factor applied to the Blasius correlation. Substituting (3.48) into (3.47) allows analytical expressions for the pressure drop in the evaporator grooves to be obtained after integration.

The temperature in the compensation chamber $T_{cc}$ is related to the pressure $P_{cc}$ through the saturation pressure–temperature relation $P(T)$ of the selected working fluid. The same relation applies to the evaporation and condensation zones: $P_{cc} = P(T_{cc})$, $P_{ev} = P(T_{ev})$, and $P_{cd} = P(T_{cd})$. The saturation pressure dependence $P(T)$was obtained by interpolation of tabulated data from the NIST (National Institute of Standards and Technology, USA [20]) database with a sufficiently fine temperature resolution (0.1 °C). Once $P_{cc}$ has been determined from (3.40), the compensation chamber temperature is obtained as

$$T_{cc} = P^{-1}(P_{cc}) \tag{3.49.}$$

which is required for the subsequent calculation of the heat leak through the wick $\dot{Q}_{hl}$.

**Calculation of the Subcooled Liquid Temperature**

To determine the temperature of the subcooled liquid at the inlet of the compensation chamber, $T_{ll,out}$, the heat transfer along the working-fluid path must be evaluated by following the fluid motion along the loop and calculating the heat flows in the vapor line $\dot{Q}_{vl}$, in the condenser $\dot{Q}_{cd}$, and in the liquid line $\dot{Q}_{ll}$.

Heat transfer in the transport lines is generally associated with natural heat exchange with the ambient environment. The condenser is specifically designed to remove heat from the loop and may transfer heat either to the surrounding environment or to another heat-transfer circuit. The condenser design, as well as the design of the thermal interface, depends on the particular

application. Nevertheless, a number of general principles governing their design and calculation can be identified.

Transport lines typically consist of elongated cylindrical tubes; therefore, their heat exchange with the environment is conveniently described in terms of thermal conductance per unit length, $g$. If no forced convection is applied to the transport lines, heat exchange with the environment must be evaluated according to the rules of natural convection. In this case, the temperature of the outer tube surface $T_{sur}$ must be known. This temperature may vary along the length of the transport line following the temperature variation of the working fluid.

An analytical expression for the outlet temperature of a transport line can be obtained if the wall temperature is assumed to be constant. Under this assumption, the temperature variation along the transport line is governed by the one-dimensional differential equation

$$c_{p,l} \cdot \dot{m} \cdot \frac{dT}{dz} = -g_{eff} \cdot (T - T_{sur}) \tag{3.50.}$$

where $g_{eff}$ is the effective thermal conductance per unit length accounting for heat transfer from the liquid to the inner wall, $g_{in}$, and heat conduction through the tube wall, $g_m$:

$$g_{eff} = \frac{g_{in} \cdot g_m}{g_{in} + g_m} \tag{3.51.}$$

The conductance $g_{in}$ is calculated using (3.12) and (3.13), while $g_m$ is evaluated using (3.19). The solution of (3.50) establishes the relationship between the inlet and outlet temperatures of the transport line:

$$T_{out} = T_{sur} + (T_{in} - T_{sur}) \cdot e^{-\frac{g_{eff}}{c_{p,l} \cdot \dot{m}} \cdot L} \tag{3.52.}$$

In practical calculations, transport lines are subdivided into a number of short segments of length $\Delta L$, within which variations of the surface temperature can be neglected. The surface temperature $T_{sur,i}$ of the $i$-th segment is determined by solving an equation analogous to (3.20):

$$\begin{aligned} g_{eff} \cdot (T - T_{sur,i}) \\ = \pi D_{out} \cdot [\left( C_{la} \cdot |T_{i,sur} - T_{amb}|^{\frac{1}{4}} + C_{tu} \cdot |T_{sur,i} - T_{amb}|^{\frac{1}{3}} \right) \\ \cdot (T_{sur,i} - T_{amb}) + \varepsilon \cdot \sigma \cdot (T_{sur,i}^4 - T_{amb}^4)] \end{aligned} \tag{3.53.}$$

The outlet temperature of the working fluid from the $i$-th segment serves as the inlet temperature for the $(i+1)$-th segment. The inlet and outlet temperatures of each segment are related by

$$T_{out,i} = T_{sur,i} + \left(T_{in,i} - T_{sur,i}\right) \cdot e^{-\frac{g_{eff}}{c_{p,l} \cdot \dot{m}} \Delta L} \tag{3.54.}$$

The required number of segments cannot be determined a priori. Therefore, trial calculations must be performed using different discretizations, and the results compared. Once further refinement of the segmentation leads to changes smaller than the required accuracy of the problem, the corresponding number of segments may be considered sufficient.

The methodology described above is applicable to single-phase flow conditions. In practice, however, under strong interaction with the environment, low heat loads, or very long transport lines, condensation may occur in the vapor line or evaporation in the liquid line. In such cases, transport lines must be analysed in the same manner as the condenser.

Accordingly, transport lines may be treated as one-dimensional tubular condensers, and the same computational modules used for condenser analysis are applied to them. This approach has been implemented in the software tool developed by the author for LHP analysis, which is described in more detail in Section 3.7.

**Modelling of Condenser Operation**

In the general case, a condenser represents a channel or a system of channels intended for the transport of the working fluid and a heat exchanger interacting with an external thermal circuit or the ambient environment. The calculation of the heat exchanger corresponds to the third task listed at the beginning of this chapter, and its solution depends on the specific condenser design.

However, to a certain extent, the calculation of an LHP can be unified by introducing an intermediate heat-sink temperature $T_{sink}$. In this formulation, the transport of the working fluid and heat transfer within the condenser channels can be described in the same manner as for the transport lines. In this context, the temperature $T_{sink}$ plays a role analogous to the surface temperature $T_{sur}$ used in the analysis of transport lines.

The calculation of heat transfer from $T_{sink}$ to the ambient temperature $T_{amb}$ or to another external thermal circuit cannot be unified in the same way and varies from one application to another.

Figure 3-15 illustrates a fragment of a fin of a flat condenser with an embedded fluid channel and the corresponding equivalent thermal resistance network. The figure reflects the typical assumptions employed for flat condensers. Since the plate thickness is usually much smaller than its characteristic in-plane dimensions (for space radiators, for example, it can be reduced to as little as 1.2 mm), the temperature distribution across the plate thickness is assumed to be uniform. Under this assumption, the problem of heat transfer within the plate becomes two-dimensional.

Heat transfer from the plate to the environment depends on the external heat-exchange mechanism (natural or forced convection, radiation, or prescribed plate temperature), as well as on the presence of fins and the direction of external flow in the case of forced convection.

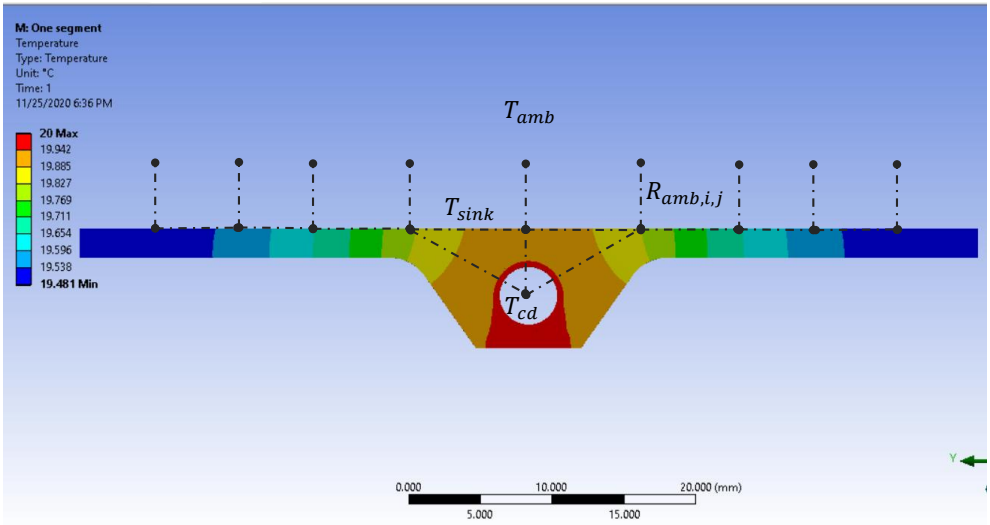


Figure 3-15. Fragment of a flat condenser fin with an embedded fluid channel.

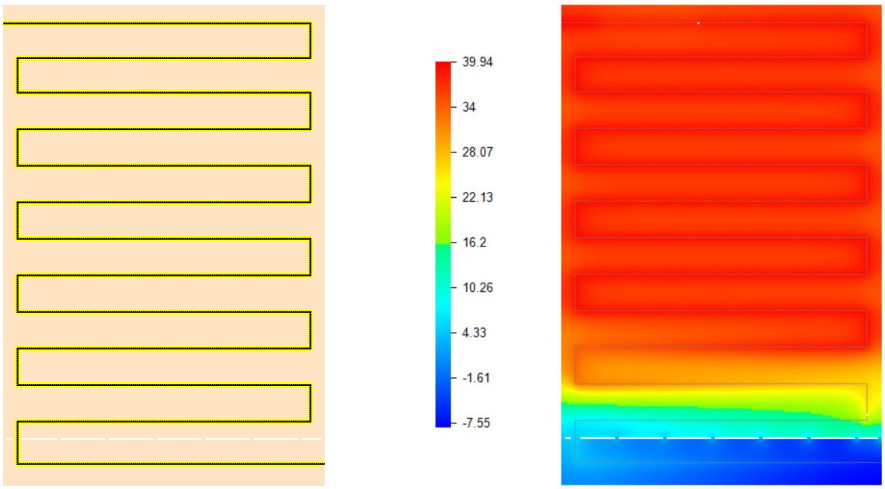


Figure 3-16. Calculated temperature field on the surface of a flat condenser.

The simplest condenser designs allow the analysis to remain within a one-dimensional mathematical framework. For example, condensers in the form of finned tubes or plates with parallel, identical channels can be treated using the same formalism as that applied to transport lines. In practice, however, condenser geometries are often more complex and require models that account for lateral heat transfer between different channel segments.

In practice, most of the considered condensers are high-thermal-conductivity plates with S-shaped embedded channels. For this reason, a two-dimensional numerical model has been developed and implemented. Figure 3-16 shows an example of a flat condenser and the calculated temperature distribution over its surface obtained using the "Altom-LHP" software.

The calculation is performed using an iterative Gauss–Seidel numerical algorithm with Picard linearization. The condenser is represented as two interacting subsystems: the fluid channel, through which the working fluid flows, and the solid plate. The plate is discretized into elementary square cells of size $\Delta s \times \Delta s$, where $\Delta s$ is chosen to be on the order of the external diameter of channel.

In steady state, the thermal balance for each cell $(i, j)$ can be written in the general form:

$$\begin{aligned}\lambda \cdot \left(T_{i,j} - T_{i,j-1}\right) \cdot \frac{2 \cdot \tau_{i,j} \cdot \tau_{i,j-1}}{\tau_{i,j} + \tau_{i,j-1}} + \lambda \cdot \left(T_{i,j} - T_{i,j+1}\right) \cdot \frac{2 \cdot \tau_{i,j} \cdot \tau_{i,j+1}}{\tau_{i,j} + \tau_{i,j+1}} + \lambda \\ \cdot \left(T_{i,j} - T_{i-1,j}\right) \cdot \frac{2 \cdot \tau_{i,j} \cdot \tau_{i-1,j}}{\tau_{i,j} + \tau_{i-1,j}} + \lambda \cdot \left(T_{i,j} - T_{i+1,j}\right) \cdot \frac{2 \cdot \tau_{i,j} \cdot \tau_{i+1,j}}{\tau_{i,j} + \tau_{i+1,j}} \\ + \dot{Q}_{i,j,ext}(T_{i,j}, T_{amb}) + \dot{Q}_{i,j,int}(T_{i,j}, T_f) = 0\end{aligned} \tag{3.55.}$$

Here, $\lambda$ is the thermal conductivity of the plate material, and $\tau_{i,j}$ is the thickness of the $(i, j)$ -th cell, which may vary across the plate. The first four terms describe heat conduction between neighbouring cells, while $\dot{Q}_{i,j,\text{ext}}$ represents heat exchange with the ambient environment.

In general, the external heat exchange term is expressed as the sum of radiative and convective contributions:

$$\dot{Q}_{i,j,ext} = \Delta s^2 \cdot [\varepsilon \cdot \sigma \cdot \left(T_{i,j}^4 - T_{amb}^4\right) + \alpha \cdot \left(T_{i,j} - T_{amb}\right)] \tag{3.56.}$$

The last term in (3.55) accounts for the thermal interaction between the condenser plate and the fluid channel and therefore depends on both the local plate temperature $T_{i,j}$ and the fluid temperature $T_f$. This term is nonzero only for cells adjacent to the channel.

From the standpoint of fluid flow, the condenser can be divided into three functional regions. The first region corresponds to cooling of superheated vapor down to the saturation temperature (segment 3–4 on the ($P$–$T$) diagram in Figure 3-1). The second region is the condensation zone (point 4), and the third region corresponds to subcooling of the liquid (segment 4–5). In the first

and third regions, the flow is single-phase, and the formalism described in the previous section applies.

In the central region, condensation of the working fluid takes place. Unfortunately, no unified and rigorous theory describing two-phase flows with condensation exists. Instead, a variety of semi-empirical correlations are available for calculating heat-transfer coefficients during condensation in channels, depending on the flow regime, channel geometry, and orientation with respect to gravity [21].

In the present work, the method proposed by M. Shah [22] is employed, which provides an average accuracy of approximately 18 % based on validation against data for 51 working fluids. Due to the high heat-transfer coefficients characteristic of two-phase condensation in channels, the thermal resistance associated with condensation is typically small compared to other resistances in the heat-transfer path. Therefore, in LHP calculations it is considered acceptable to neglect the thermal resistance of condensation, except in cases of extremely low heat loads where vapor flow stagnation may occur and other modelling limitations become dominant.

The difficulties inherent in modelling two-phase condensation also extend to the prediction of hydraulic resistance [23]. For channels with diameters larger than approximately 3 mm, acceptable results can be obtained using the separated-flow theory developed by Lockhart and Martinelli and later modified by Chisholm [24].

Within the Lockhart–Martinelli framework, the two-phase pressure drop is estimated by introducing hypothetical single-phase flows in which the vapor and liquid phases are assumed to flow independently with mass flow rates $\chi \cdot \dot{m}$ and $(1-\chi) \cdot \dot{m}$, respectively. The corresponding single-phase pressure gradients are then corrected using empirical two-phase multipliers.

Expressing the two-phase pressure gradient in terms of the liquid-phase multiplier $\phi_l^2$, one obtains

$$(\frac{dP}{dz})_{2p} = \phi_l^2 \cdot (\frac{dP}{dz})_l \tag{3.57.}$$

The two-phase multiplier is related to the Martinelli parameter $X$ through the empirical Chisholm parameter $C$:

$$\phi_l^2 = 1 + \frac{C}{X} + \frac{1}{X^2} \tag{3.58.}$$

The Martinelli parameter is defined locally as the ratio of the pressure gradients of the two hypothetical single-phase flows:

$$X^2 = \frac{(\frac{dP}{dz})_l}{(\frac{dP}{dz})_v} \tag{3.59.}$$

The value of the Chisholm parameter $C$ is selected according to Table 3-3, depending on the flow regimes of the liquid and vapor phases.

Table 3-3.

Chisholm parameter for the two-phase flow

| Liquid | Vapor | Chisholm parameter C |
|---|---|---|
| Laminar | Laminar | 5 |
| Turbulent | Laminar | 10 |
| Laminar | Turbulent | 12 |
| Turbulent | Turbulent | 20 |

The single-phase pressure gradients are calculated using Darcy friction factors and, when expressed in terms of mass flow rate, take the form

$$(\frac{dP}{dz})_l = -\xi_l \cdot \frac{\dot{m}^2 \cdot (1-\chi)^2}{2 \cdot \rho_l \cdot S^2 \cdot d} \tag{3.60.}$$

$$(\frac{dP}{dz})_v = -\xi_v \cdot \frac{\dot{m}^2 \cdot \chi^2}{2 \cdot \rho_v \cdot S^2 \cdot d} \tag{3.61.}$$

Here, $d$ is the hydraulic diameter of the channel and $S$ is its cross-sectional area. Flow regimes for determining the Chisholm parameter and the friction factors $\xi_i$ are identified using the Reynolds numbers for liquid and vapor:

$$Re_l = \frac{(1-\chi) \cdot \dot{m} \cdot d}{\eta_l \cdot S} \tag{3.62.}$$

$$Re_v = \frac{\chi \cdot \dot{m} \cdot d}{\eta_v \cdot S} \tag{3.63.}$$

The Darcy friction factor is expressed as $\xi = 64/Re$ for laminar flow (Hagen–Poiseuille) and $\xi = 0.316/Re^{0.25}$ for turbulent flow (Blasius). Substituting (3.60) and (3.61) into (3.59) yields the Martinelli parameter in the form

$$X^2 = \frac{\xi_l}{\xi_v} \cdot \frac{\rho_v}{\rho_l} \cdot \frac{(1-\chi)^2}{\chi^2} \tag{3.64.}$$

Finally, the pressure drop in the condensation region is obtained by integrating (3.57) with respect to vapor quality from 1 to 0, which leads to

$$\Delta P_{2p} = \frac{\dot{m}^2}{2 \cdot \rho_l \cdot S^2 \cdot d} \int_0^1 \phi_l^2 \cdot \xi_l \cdot (1-\chi)^2 \cdot (\frac{dz}{d\chi}) \cdot d\chi \tag{3.65.}$$

This integral is evaluated numerically. The derivative $dz/d\chi$ appearing in the integrand establishes the relationship between the condensation rate and the pressure drop along the channel. In the case of uniform condensation, this factor is constant and can be taken outside the integral.

It should be noted that, in engineering practice, there exists an approach in which the two-phase pressure drop in a condenser with uniform condensation is approximated as one half of the pressure drop calculated for vapor flow over the same length [25].

**Calculation of the Maximum Transferable Power**

The maximum heat-transfer capacity of a two-phase device depends on the evaporator design, the configuration of the loop itself, and the selected working fluid. Various mechanisms can limit the operating envelope of an LHP; however, the maximum transferable power is primarily governed by two factors: the capillary limit and the sonic limit.

The capillary limit is reached when the total pressure drop along the loop becomes equal to the capillary pressure generated by the wick:

$$\frac{2\sigma}{r_p} = \sum \Delta P \tag{3.66.}$$

The sum on the right-hand side is composed of the hydraulic pressure losses in the loop and therefore increases with increasing working-fluid flow rate. In turn, the mass flow rate increases with increasing applied thermal power. It should be noted that, in addition to the pressure drops listed in (3.40), the right-hand side of (3.66) must also include the pressure loss associated with liquid filtration through the wick from its core toward the evaporation zone. For a cylindrical wick, this pressure drop can be expressed as:

$$\Delta P_w = \frac{\eta_l}{K} \cdot \frac{\dot{m}}{2 \cdot \pi \cdot \rho_l \cdot L_w} \cdot ln(\frac{D_{out}}{D_{in}}) \tag{3.67.}$$

By solving (3.66), the maximum allowable mass flow rate $\dot{m}$ can be determined and, consequently, the maximum transferable thermal power of the LHP can be evaluated.

The sonic limit is reached when the vapor velocity in a channel attains the local speed of sound. Under these conditions, flow choking occurs, preventing any further increase in mass flow rate. Since an LHP typically contains several vapor passages with different cross-sectional areas—such as vapor-removal grooves in the wick, the vapor line, and the vapor manifold—the thermal power corresponding to the sonic limit must be evaluated separately for each vapor channel. The minimum of these values then defines the overall sonic limit of the device:

$$\dot{Q}_{s,lim} = h_{ev} \cdot \rho_v \cdot v_s \cdot S_c \tag{3.68.}$$

Here, $v_s$ is the speed of sound of the working fluid vapor, and $S_c$ is the cross-sectional area of the considered vapor channel.

## 3.5 Transient LHP Model Based on the Thermal Dynamics of Compensation Chambers

Evaporators developed using the “Altom” technology and comprising on the order of ten capillary pumps and multiple compensation chambers are characterized by substantial mass and overall dimensions and, consequently, by high thermal inertia. For example, the multi-evaporator cold plate MECOP presented in Section 2.4 has a mass of approximately 4.5 kg and overall dimensions of 330 mm× 300 mm. This evaporator is intended for operation in a loop designed to transport heat over distances exceeding 10 m and coupled to a large radiator.

The radiators shown in Figure 2-10 have an area of approximately 2.5 m² and a total channel length of about 9 m. Such LHP is charged with nearly 1000 ml of working fluid and is intended for heat removal from electronic equipment with time-varying dissipation. The above considerations indicate that, under realistic operating conditions, the loop will operate predominantly in a transient regime, which motivated the development of a transient LHP model.

Variations in external inputs—such as the thermal load or the sink temperature—initiate several transient processes within the loop, characterized by different time scales. The key aspect of model formulation is a correct assessment of these time scales and identification of the most inertial processes. The slowest processes ultimately govern the overall evolution of the system toward a new equilibrium state.

An analysis of MECOP operation indicates that the most inertial process is the establishment of thermal equilibrium in the compensation chambers. On the thermodynamic cycle of an LHP, this process corresponds to segment 6–7, highlighted by red hatching in Figure 3-17.

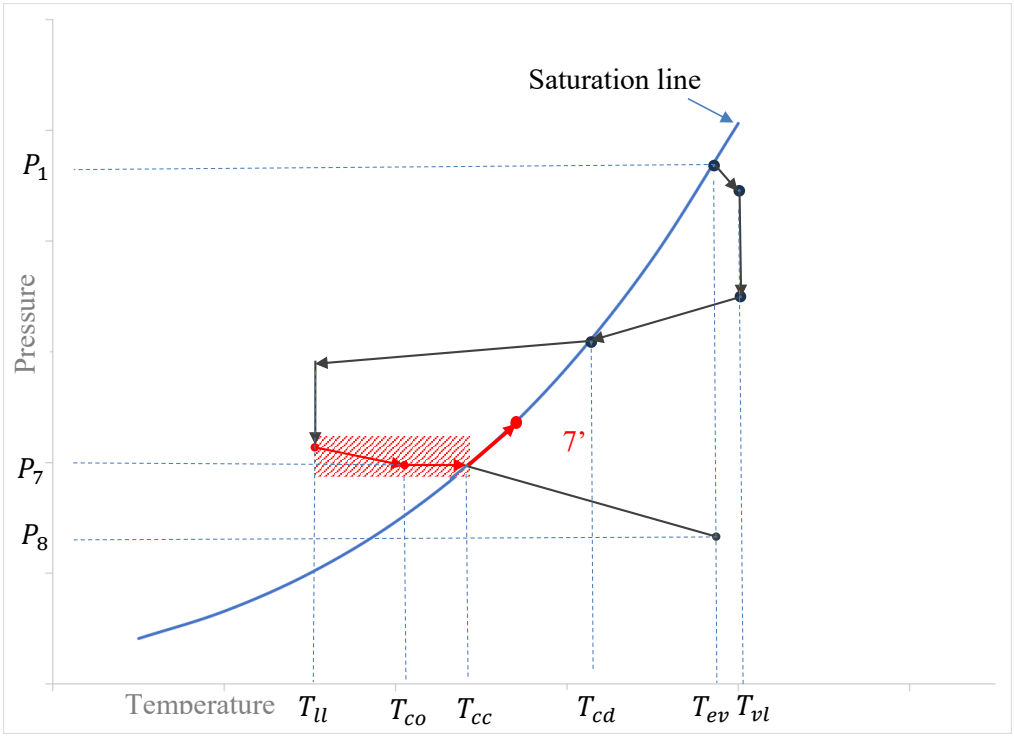


Figure 3-17. Thermodynamic Cycle of an LHP Illustrating a Transient Operating Model

Accordingly, the compensation-chamber temperature $T_{cc}$ may be regarded as a reference (or "support") temperature whose evolution largely determines the behavior of the entire loop. This is schematically illustrated on the thermodynamic cycle by the displacement of point 7 to position 7′. A change in the compensation-chamber temperature results in a global reconfiguration of the LHP operating state.

It is assumed that the characteristic time associated with the adjustment of the remaining loop elements is significantly smaller than the characteristic time of thermal processes in the compensation chambers. Within the model, this reconfiguration is therefore treated as quasi-instantaneous relative to the dynamics of $T_{cc}$. This key assumption implies that:

- variations in the thermal load are directly reflected in the working-fluid mass flow rate;
- pressure equalization throughout the loop occurs on time scales negligible compared to the thermal inertia of the compensation chambers;
- the evaporation and condensation temperatures rapidly adjust to the current load;

- phase equilibrium at the characteristic points of the cycle (1, 4, and 7) is established without noticeable delay;
- redistribution of the working fluid within the loop, including condenser reconfiguration, occurs much faster than the temperature evolution of the compensation chambers.

LHP evaporators are designed so that the subcooled liquid arriving from the condenser is delivered as close as possible to the evaporation zone. This is achieved by incorporating a so-called bayonet tube within the evaporator. The bayonet is a small capillary (or a set of capillaries in large evaporators such as MECOP) connected on one end to the liquid line outlet and terminating within the wick core. The bayonet is routed such that, on its path toward the wick, it passes through all compensation chambers and cools them. This feature is essential for ensuring LHP operability under transient conditions. In MECOP-type evaporators, the length of a single bayonet may reach 0.5 m with an outer diameter of 2.5 mm. The heat exchange between the compensation chambers and the bayonet constitutes the basis of the present model. The working fluid exits the bayonet at temperature $T_{co}$, which in general differs from the compensation-chamber temperature, as indicated in Figure 3-17.

To simplify the description without loss of generality, the LHP is assumed to be thermally insulated from the environment. Consequently, the heat flows $\dot{Q}_{ea}$ and $\dot{Q}_{ca}$ describing heat exchange between the evaporator and the environment, and between the compensation chamber and the environment (as introduced in (3.6) and (3.8)), are set to zero. In addition, no control heat is supplied to the chambers, i.e., $\dot{Q}_{co} = 0$. Under these assumptions, the equilibrium condition (3.9) reduces to

$$\dot{Q}_{hl} = \dot{Q}_{sc} \tag{3.69.}$$

When external conditions change, this balance is disturbed and drifts toward a new equilibrium state following the evolution of the compensation-chamber temperature $T_{cc}$.

Assume that the initial state of the LHP is known, i.e., the temperature distribution of the working fluid along the loop is known, and hence $T_{co}$ and $T_{cc}$ are known. During start-up it is often assumed that all temperatures are initially equal.

Based on the assumptions regarding rapid pressure equalization and rapid attainment of phase equilibrium, points 1, 4, and 7 are assumed to remain on the saturation curve, and their pressures and temperatures are related via the saturation relation $P = P(T)$ and its inverse $T = T(P)$. Hence, the pressure in the compensation chamber is determined from the known initial temperature $T_{cc}$ as

$$P_{cc} = P(T_{cc}) \tag{3.70.}$$

The evaporation-zone temperature is then given by

$$T_{ev} = T(P_{cc} + \Delta P) \tag{3.71.}$$

where $\Delta P$ is the hydraulic pressure drop from the evaporation zone to the compensation chamber in accordance with (3.40):

$$\Delta P = \Delta P_{ev} + \Delta P_{vl} + \Delta P_{cd} + \Delta P_{ll} + \Delta P_b \tag{3.72.}$$

A change in heat load causes a change in the mass flow rate $\dot{m}$, which leads to a change in hydraulic resistance and thus a change in $T_{ev}$ via (3.71).

The evaporation temperature $T_{ev}$ is related to the mass flow rate $\dot{m}$ through a relation following from (3.6), (3.7), and (3.36):

$$\dot{Q}_{in} = \dot{m} \cdot h_{ev} + \dot{m} \cdot c_{p,l} \cdot \frac{T_{ev} - T_{co}}{1 - \left[\frac{D_{ev,in}}{D_{ev,out}}\right]^{\frac{c_{p,l} \cdot \dot{m}}{2\pi\lambda_w L_w}}} \tag{3.73.}$$

This nonlinear equation must have a solution within the interval $\left[0, \dot{Q}_{in}/h_{ev}\right]$, provided that the applied heat load exceeds a minimum value defined by the limiting case

$$\dot{Q}_{min} = \lim_{\dot{m}\to 0} \dot{Q} = 2\pi\lambda_w L_w \cdot \frac{(T_{ev} - T_{co})}{ln\left(\frac{D_{ev,out}}{D_{ev,in}}\right)} \tag{3.74.}$$

This limit corresponds to the case where the entire applied heat input leaks into the wick core rather than being used for evaporation. Therefore,

$$\dot{Q}_{in} > \dot{Q}_{min} \tag{3.75.}$$

This condition can also be expressed as a constraint on the evaporation temperature:

$$T_{ev} < T_{co} + \frac{\dot{Q}_{in}}{2\pi\lambda_w L_w} \cdot ln\left(\frac{D_{ev,out}}{D_{ev,in}}\right) \tag{3.76.}$$

As a result, determination of $T_{ev}$ and $\dot{m}$ requires solving the nonlinear system subject to constraint (3.76):

$$\begin{cases} T_{ev} = T(P_{cc} + \Delta P(\dot{m})) \\ \dot{Q}_{in} = \dot{m} \cdot h_{ev} + \dot{m} \cdot c_{p,l} \cdot \dfrac{T_{ev} - T_{co}}{1 - \left[\dfrac{D_{ev,in}}{D_{ev,out}}\right]^{\frac{c_{p,l}\dot{m}}{2\pi\lambda_w L_w}}} \end{cases} \tag{3.77.}$$

The system is solved using an iterative procedure. First, a zero-order estimate for $\dot{m}$ is constructed based on an a priori estimate of the heat leak (for example, in MECOP the average heat leak is on the order of 10 % of the applied power). The first equation in (3.77) then yields $T_{ev}$, and constraint (3.76) is checked. If the constraint is violated, the initial estimate of $\dot{m}$ is too large; it is then reduced iteratively (e.g., halved at each step) until (3.76) is satisfied. In practice, the a priori estimate is typically sufficient to provide an initial pair $(\dot{m}_0, T_{ev,0})$ for solving the second equation.

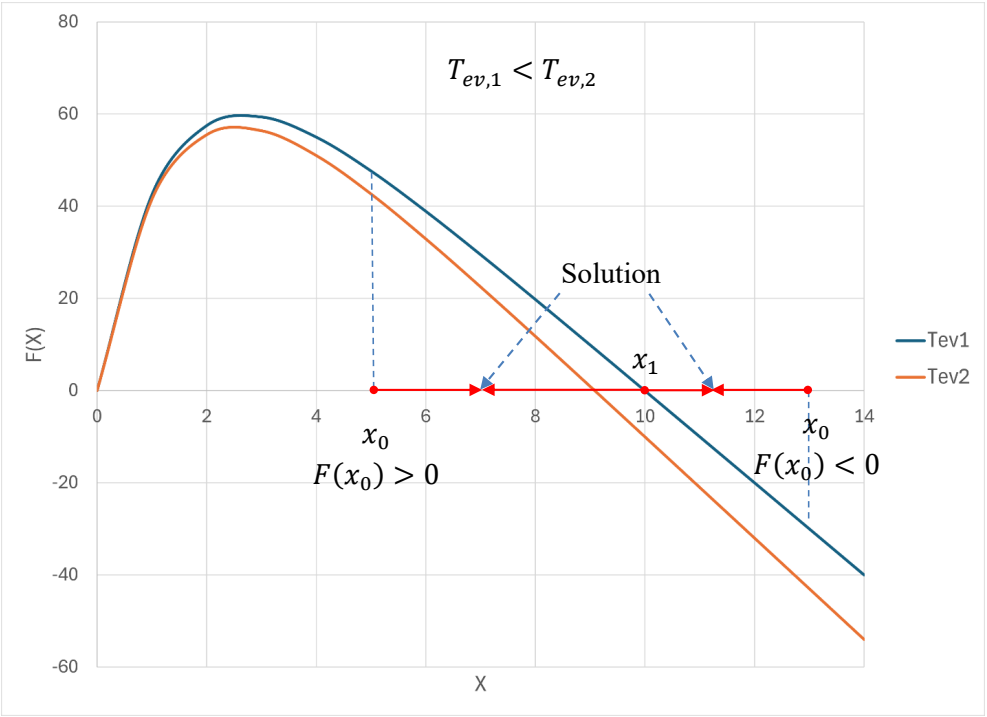


Figure 3-18. Illustration of the solution of system (3.77)

Let the second equation in (3.77) be rewritten by denoting the unknown mass flow rate as $x$:

$$F(x) = \left(\dot{Q}_{in} - h_{ev} \cdot x\right)\left(1 - \left[\frac{D_{ev,in}}{D_{ev,out}}\right]^{\frac{c_{p,l}}{2\pi\lambda_w L_w}\cdot x}\right) - c_{p,l} \cdot (T_{ev} - T_{co}) \cdot x = 0 \tag{3.78.}$$

The function $F(x)$ has two roots: the trivial root $F(0) = 0$, and a non-trivial root $x_1$. The latter can be found numerically, for example using Newton's method, since $dF/dx$ can be obtained analytically.

In general, the obtained root $x_1$ is either larger or smaller than the initial estimate $x_0$ depending on the sign of $F(x_0)$, as illustrated in Figure 3-18. Furthermore, as $T_{ev}$ increases, the root $x_1$ decreases. This is shown by two curves $F(x)$ corresponding to two evaporation temperatures $T_{ev,1}$ and $T_{ev,2}$, with $T_{ev,1} < T_{ev,2}$. For the present algorithm this implies that, regardless of the relative positions of $x_0$ and $x_1$, the solution of the coupled system lies between them. Therefore, a bisection procedure can be applied safely by using the midpoint $x_2 = (x_0 + x_1)/2$ as the next estimate. Convergence is controlled by the criterion $| F(x_2) | \leq \varepsilon$, where $\varepsilon$ defines the required numerical accuracy, while the bracketing interval is updated according to the sign change condition $F(x_0)F(x_2) < 0$.

Once $T_{ev}$ and $\dot{m}$ are determined, the temperature field along the loop can be computed in the same way as in the steady-state model, yielding in particular the liquid temperature entering the bayonet from the liquid line, $T_{ll,out}$.

A change in load results in redistribution of the working fluid within the loop. When the load increases, the condensation zone expands and a portion of liquid is displaced from the condenser into the compensation chambers. This effect is modelled as an instantaneous injection of a liquid mass $\Delta M_{cc}$ at temperature $T_{co}$ into the chambers. After mixing with the existing working fluid, a new equilibrium chamber temperature $T'_{cc}$ is obtained from the chamber energy balance

$$\begin{aligned} c_{v,l} \cdot \Delta M_{cc} \cdot (T'_{cc} - T_{cc}) + \left(c_{v,l} \cdot (1 - \chi_0) + c_{vv} \cdot \chi_0\right) \cdot M_{cc} \cdot (T'_{cc} - T_{cc}) + C_s \cdot M_s \\ \cdot (T'_{cc} - T_{cc}) + h_{ev} \cdot [\chi \cdot (M_{cc} + \Delta M_{cc}) - \chi_0 \cdot M_{cc}] = 0 \end{aligned} \tag{3.79.}$$

The injected mass $\Delta M_{cc}$ is known because the condenser calculation at the previous step provides the change in the working-fluid inventory in the condenser $\Delta M_{cd}$, which is related to $\Delta M_{cc}$ as

$$\Delta M_{cd} = -\Delta M_{cc} \tag{3.80.}$$

The vapor quality in the chamber for the initial and final states is computed as

$$\begin{aligned} \chi(T'_{cc}) &= \frac{\rho_v \cdot (\rho_l V_{cc} - M_{cc} - \Delta M_{cc})}{(\rho_l - \rho_v) \cdot (M_{cc} + \Delta M_{cc})} \\ \chi_0(T_{cc}) &= \frac{\rho_v \cdot (\rho_l V_{cc} - M_{cc})}{(\rho_l - \rho_v) \cdot M_{cc}} \end{aligned} \tag{3.81.}$$

From (3.81) it follows that

$$\chi(T'_{cc}) \cdot (M_{cc} + \Delta M_{cc}) - \chi_0 \cdot M_{cc} = -\Delta M_{cc} \frac{\rho_v}{\rho_l - \rho_v} \tag{3.82.}$$

The heat capacity of the evaporator structure is represented by the effective term $C_s M_s$. The structure is manufactured from aluminum and stainless steel and is assumed to be in thermal equilibrium with the working fluid in the compensation chambers (an additional model assumption). Solving (3.79) yields the new chamber temperature after redistribution:

$$T'_{cc} \approx \approx \frac{c_{vl} \cdot \Delta M_{cc} \cdot T_{co} + ((c_{vl}(1-\chi_0) + c_{vv}\chi_0) \cdot M_{cc} + C_s M_s) \cdot T_{cc} + h_{ev} \cdot \Delta M_{cc} \frac{\rho_v}{\rho_l - \rho_v}}{c_{vl} \cdot \Delta M_{cc} + (c_{vl}(1-\chi_0) + c_{vv}\chi_0) \cdot M_{cc} + C_s M_s} \tag{3.83.}$$

The updated working-fluid mass in the chambers is

$$M'_{cc} = M_{cc} + \Delta M_{cc} \tag{3.84.}$$

In the opposite case, when the condensation zone contracts, the working-fluid mass in the compensation chambers decreases. For this case, the following relations are used:

$$T'_{cc} = T_{cc},\ M'_{cc} = M_{cc} - \Delta M_{cc},\ \chi = \frac{\rho_v \cdot (\rho_l V_{cc} - M_{cc} + \Delta M_{cc})}{(\rho_l - \rho_v) \cdot (M_{cc} - \Delta M_{cc})} \tag{3.85.}$$

The described redistribution process between the condenser and the compensation chambers is associated with critical transient phenomena referred to in the literature as “cold shock” and “hot shock” [26]. These phenomena may drive the LHP out of its operating state by inducing wick dry-out and circulation stoppage. Their occurrence is mitigated by appropriate evaporator internal design aimed at minimizing the temperature difference between $T_{co}$ and $T_{cc}$.

In the above expressions, thermophysical properties of the working fluid depend on temperature. In calculations, they are evaluated at the local temperature whenever it is known (e.g., at the evaporator temperature or the liquid temperature in the liquid line). If a local temperature is not uniquely defined (e.g., in the chamber balance (3.79), where properties corresponding to different temperatures appear), averaged properties are used, for example evaluated at the mean temperature between $T_{co}$ and $T_{cc}$. It is noted that the present model is differential in time, i.e., a sufficiently small-time increment $\Delta t$ is considered such that parameters do not change significantly within one step.

The temperature $T_{co}$ is obtained from the bayonet–chamber heat-exchange calculation. For a bayonet control volume of length $\Delta z$, the energy balance yields

$$\frac{dT}{dz} = -\frac{2\pi r_b \cdot g_b}{c_{p,l} \cdot \dot{m}} \cdot (T - T_{cc}) \tag{3.86.}$$

whose solution gives the updated outlet temperature from the bayonet:

$$T'_{co} = T_{cc} + (T_{ll,out} - T_{cc}) \cdot e^{-\frac{2\pi r_b \cdot g_b}{c_{p,l} \cdot \dot{m}} L_b} \tag{3.87.}$$

The heat flow transferred from the bayonet to the chambers is

$$\dot{Q}_{b,cc} = c_{p,l} \cdot \dot{m} \cdot (T_{ll,out} - T'_{co}) \tag{3.88.}$$

Hence, if $\dot{Q}_{b,cc} < 0$, the chambers release heat and $T_{cc}$ decreases, and vice versa.

The heat flow entering the wick core through the wick body, evaluated at the inner wick surface, is

$$\dot{Q}_{hl,int} = c_{p,l}\dot{m} \frac{T_{ev} - T_{co}}{1 - \left[\frac{D_{ev,in}}{D_{ev,out}}\right]^{\frac{c_{p,l}\dot{m}}{2\pi\lambda_w L_w}}} \left[\frac{D_{ev,in}}{D_{ev,out}}\right]^{\frac{c_{p,l}\dot{m}}{2\pi\lambda_w L_w}} \tag{3.89.}$$

This heat warms the liquid entering the core, and $T'_{co} \to T_{co}$. If $T_{co} > T_{cc}$, boiling may start inside the core and vapor bubbles may enter the chambers, thereby transferring heat from the core to the chambers. A well-designed LHP aims to satisfy $\max(T_{co}) = T_{cc}$. If $T_{co} < T_{cc}$, convective or conductive heat transfer from the chambers to the core is expected, raising the core temperature to an intermediate value $T''_{co}$ such that $T_{co} < T''_{co} < T_{cc}$. Taking these effects into account, the chamber heat balance can be written as

$$\dot{Q}_{cc} = c_{p,l} \cdot \dot{m} \cdot (T_{ll,out} - T'_{co}) + c_{p,l} \cdot \dot{m} \cdot (T_{co} - T''_{co}) \tag{3.90.}$$

Determination of the intermediate temperature $T''_{co}$ requires modeling of heat transfer between the chambers and the wick core and depends on the specific evaporator design. In the present description, an idealized case is adopted in which the liquid in the core is heated up to $T_{cc}$ by heat exchange with the chambers. Then the resulting net heat flow into the chamber can be written as

$$\dot{Q}_{cc} = c_{p,l} \cdot \dot{m} \cdot \left(T_{ll,out} - T'_{co}\right) + c_{p,l} \cdot \dot{m} \frac{T_{ev} - T_{co}}{1 - \left[\frac{D_{ev,in}}{D_{ev,out}}\right]^{\frac{c_{p,l}\dot{m}}{2\pi\lambda_w L_w}}} \left[\frac{D_{ev,in}}{D_{ev,out}}\right]^{\frac{c_{p,l}\dot{m}}{2\pi\lambda_w L_w}} - c_{pl} \cdot \dot{m} \cdot (T_{cc} - T'_{co}) + \frac{T_* - T_{cc}}{R_{HL}} \tag{3.91.}$$

The first term represents bayonet heat exchange, the second term represents heat input through the evaporator body (via the wick), the third term describes temperature equalization between the core and the chamber, and the fourth term accounts for additional heat-leak paths from the heat source discussed in Section 3.4 (see the justification of (3.39)). Rearranging the terms in (3.91) and expressing the heat leak at the outer wick surface yields

$$\dot{Q}_{cc} = c_{p,l} \cdot \dot{m} \cdot \left[ \frac{T_{ev} - T_{cc}}{1 - \left[\frac{D_{ev,in}}{D_{ev,out}}\right]^{\frac{c_{p,l}\dot{m}}{2\pi\lambda_w L_w}}} + T_{ll,out} - T_{ev} \right] + \frac{T_* - T_{cc}}{R_{HL}} \tag{3.92.}$$

At equilibrium, $\dot{Q}_{cc} = 0$ is recovered.

The transient evolution is described using a time step $\Delta t$, assumed sufficiently small so that finite increments can be treated in differential form. The energy input $\Delta E$ to the chamber over the interval $\Delta t$ is

$$\Delta E = \dot{Q}_{cc} \cdot \Delta t \tag{3.93.}$$

This results in changes in the internal energy of the working fluid and the evaporator structure, which can be written (in differentials) as

$$\Delta E = \left( \left( \frac{de_v}{dT} - \frac{de_l}{dT} \right) \chi + (e_v - e_l) \frac{d\chi}{dT} + \frac{de_l}{dT} \right) \cdot M_{CC} \cdot \Delta T_{cc} + C_s \cdot M_s \cdot \Delta T_{cc} \tag{3.94.}$$

The derivative $d\chi/dT$ is obtained by differentiating (3.81)

$$\frac{d\chi}{dT} = \chi \left[ \left( \frac{1}{\rho_v} + \frac{1}{\rho_l - \rho_v} \right) \frac{d\rho_v}{dT} + \left( \frac{V_{CC}}{\rho_l V_{CC} - M_{CC}} - \frac{1}{\rho_l - \rho_v} \right) \frac{d\rho_l}{dT} \right] \tag{3.95.}$$

Assuming that thermophysical properties and their temperature derivatives are known, substitution of (3.95) into (3.94), and then (3.94) and (3.92) into (3.93), yields an equation for the chamber temperature change $\Delta T_{cc}$ over one iteration step. The chamber temperature for the next time step is then updated as

$$T_{cc} \rightarrow T_{cc} + \Delta T_{cc} \tag{3.96.}$$

The model contains three tuning parameters: the bayonet conductance per unit length $g_b$, the parameter $R_{HL}$ defined in the steady-state model, and an effective evaporator heat capacity $C_s M_s$, which must be estimated from the evaporator structure and the heat capacities of the constituent materials. In addition, computation of the working-fluid inventory distribution requires the initial charge $M_{ch}$. The remaining parameters, such as the compensation-chamber volume $V_{cc}$ and the bayonet geometry ($L_b$ and $r_b$), are structural and are assumed known.

## 3.6 Working Fluid Selection. Figures of Merit

The selection of a suitable working fluid is one of the key stages in the design of a thermal management system. Therefore, the study of thermophysical properties of working fluids in the context of two-phase systems is of independent interest . Particular attention is paid to the compatibility between the working fluid and the materials of the LHP. The working fluid must retain its properties and remain chemically stable with respect to the LHP materials throughout the entire planned service life. This requirement is essential to prevent the formation of non-condensable gases, which can block working-fluid circulation.

Compatibility is assessed based on the known chemical properties of the materials involved and is additionally verified experimentally. In the author's practice, experimental compatibility verification is based on the fact that chemical reaction rates increase exponentially with temperature. For this purpose, simple heat-transfer devices—thermosyphons—are fabricated from the same materials used in the LHP and in contact with the working fluid. These thermosyphons are charged with the working fluid and subjected to long-term life tests.

Figure 3-19 shows a test setup used for simultaneous life testing of twelve thermosyphons. During the test, the evaporators of the thermosyphons are maintained at the highest practically achievable elevated temperature. The temperature difference between the evaporator and the condenser is continuously monitored. An increase in this temperature difference indicates the formation of non-condensable gases, which accumulate at the upper part of the thermosyphon and block heat transfer in the condenser.

Another factor affecting device lifetime is the purity of the working fluid and the quality of cleaning of the heat-transfer loop components during manufacturing. Contamination can also promote the formation of non-condensable gases. Therefore, the described life test serves not

only as a compatibility assessment but also as a criterion for evaluating the quality of component cleaning during LHP fabrication.

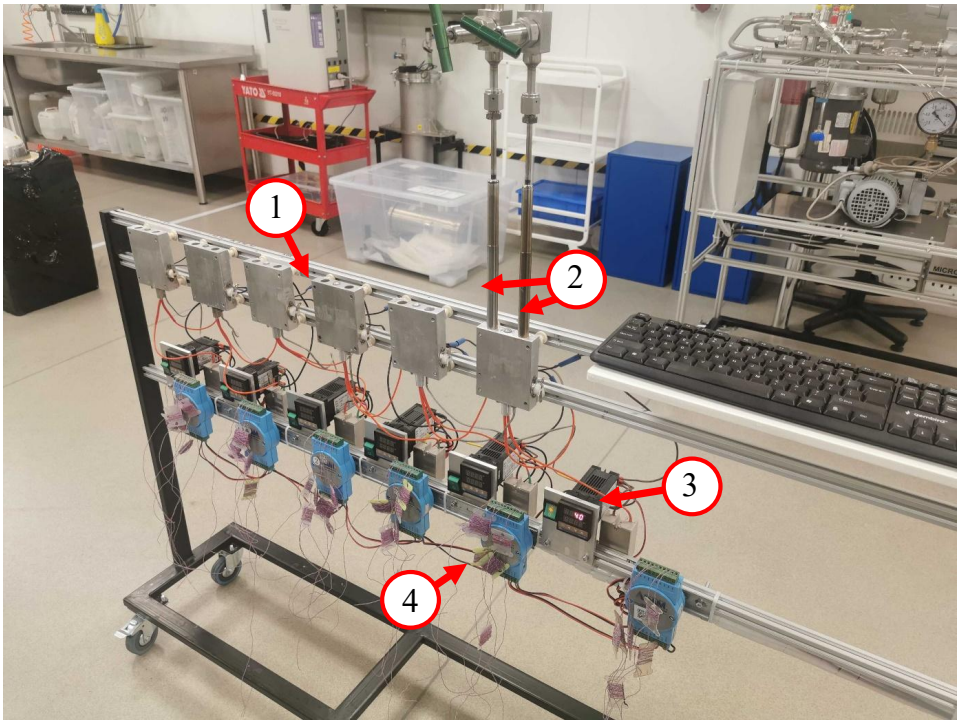


Figure 3-19. Thermal fluids Life-time test setup. 1 – test block for one fluid with electric heaters and cylindrical holes for thermosyphons; 2 – pair of thermosyphons located in the test block; 3 – temperature PID controller; 4 – data acquisition system with thermocouples.

To rank working fluids according to their heat-transfer performance, a system of figures of merit (FOMs) specific to LHPs has been developed [28]. Of primary interest are criteria allowing comparison of working fluids in terms of maximum transferable power and thermal conductance.

The criteria related to maximum transferable power follow directly from (3.66). Retaining only the hydraulic resistances of the vapor and liquid lines and assuming turbulent vapor flow and laminar liquid flow, the governing equation can be reduced to the following form:

$$F(\dot{Q}) = \frac{K_v}{F_{m,v}}\dot{Q}^{1.75} + \frac{K_l}{F_{m,l}}\dot{Q} - 1 = 0 \qquad (3.97.)$$

The positive root of this equation corresponds to the maximum transferable power. Here, the parameters $K_v$ and $K_l$ contain the structural characteristics of the loop, while $F_{m,v}$ and $F_{m,l}$ depend solely on the thermophysical properties of the working fluid.

It is straightforward to show that $F(\dot{Q})$ is a monotonically increasing function for $\dot{Q} > 0$ and has a single positive root. This root increases as the derivative $F'(\dot{Q})$ decreases:

$$F'(\dot{Q}) = 1.75 \frac{K_v}{F_{m,v}} \dot{Q}^{0.75} + \frac{K_l}{F_{m,l}} \tag{3.98.}$$

Since $F'(\dot{Q})$ decreases with increasing values of $F_{m,v}$ and $F_{m,l}$, these parameters are naturally chosen as figures of merit for ranking working fluids according to maximum transferable power:

$$(F_{m,l})_{LHP} = \frac{\rho_l \cdot h_{ev} \cdot \sigma}{\eta_l} \tag{3.99.}$$

$$(F_{m,v})_{LHP} = \frac{\rho_v \cdot h_{ev}^{1.75} \cdot \sigma}{\eta_v^{0.25}} \tag{3.100.}$$

The thermal conductance of an LHP is defined as

$$G_{LHP} = \frac{\dot{Q}}{\Delta T} \rightarrow max \tag{3.101.}$$

Conductance increases as the temperature drop $\Delta T$ across the loop decreases. The latter can be related to the hydraulic pressure drop as

$$\Delta T \approx \frac{dT}{dP} \Delta P \tag{3.102.}$$

Using the same considerations for $\Delta P$ as in the derivation of the maximum power criteria, one obtains

$$\Delta P \propto (\frac{K_v}{F_{m,v}} \dot{Q}^{1.75} + \frac{K_l}{F_{m,l}} \dot{Q}) \sigma \tag{3.103.}$$

At the maximum transferable power, the expression in parentheses equals unity, yielding

$$G(\dot{Q}_{max}) \approx \frac{dP}{dT} \frac{\dot{Q}_{max}}{\sigma} \tag{3.104.}$$

Thus, the conductance increases with increasing slope of the saturation curve. This leads to the following figure of merit for conductance

$$F_{m,G} \propto \frac{\frac{dP}{dT}}{\sigma} \tag{3.105.}$$

Using the Clausius–Clapeyron equation, the following estimate can be obtained:

$$\frac{dP}{dT} = \frac{h_{ev}}{T(\frac{1}{\rho_v} - \frac{1}{\rho_l})} \approx \frac{h_{ev} \cdot \rho_v}{T} \tag{3.106.}$$

Substitution into (3.105) yields the third figure of merit:

$$(F_{m,G})_{LHP} = \frac{h_{ev} \cdot \rho_v}{\sigma} \tag{3.107.}$$

If conductance is considered independently of the maximum transferable power, the relevant quantity to be maximized is

$$\frac{F_{m,G}}{\frac{K_v}{F_{m,v}}\dot{Q}^{0.75} + \frac{K_l}{F_{m,l}}} \tag{3.108.}$$

Maximum conductance is achieved when all figures of merit attain large values. It should be noted that surface tension cancels out in some of the expressions, while the conductance generally decreases with increasing temperature.

The developed approach can be extended to loop thermosyphons. For LTSs, gravity replaces capillary forces as the primary driving mechanism. While capillary pressure scales with surface tension, the gravitational head in an LTS is proportional to the density difference between liquid and vapor ($\rho_l - \rho_v \approx \rho_l$, since $\rho_v \ll \rho_l$). Accordingly, the LTS figures of merit can be obtained by replacing surface tension with liquid density in the LHP criteria. The vapor-side criterion becomes

$$(F_{m,v})_{LTS} = \frac{\rho_v \cdot h_{ev}^{1.75} \cdot \varrho_l}{\eta_v^{0.25}} \tag{3.109.}$$

The liquid-side criterion may be relevant when a wick is used in the LTS:

$$(F_{m,l})_{LTS} = \frac{\rho_l^2 \cdot h_{ev}}{\eta_l} \tag{3.110.}$$

Surface tension affects only the criterion associated with maximum conductance at maximum transferable power. Within the present framework for LTSs, this criterion takes the form:

$$(F_{m,G})_{LTS} = \frac{h_{ev} \cdot \rho_v}{\rho_l} \tag{3.111.}$$

## 3.7 The Altom-LHP Software for LHP Design and Analysis

The models described above were implemented by the author in the form of a computational tool written in C#, featuring a user-friendly graphical interface. Figure 3-20 shows the main screen of the program.

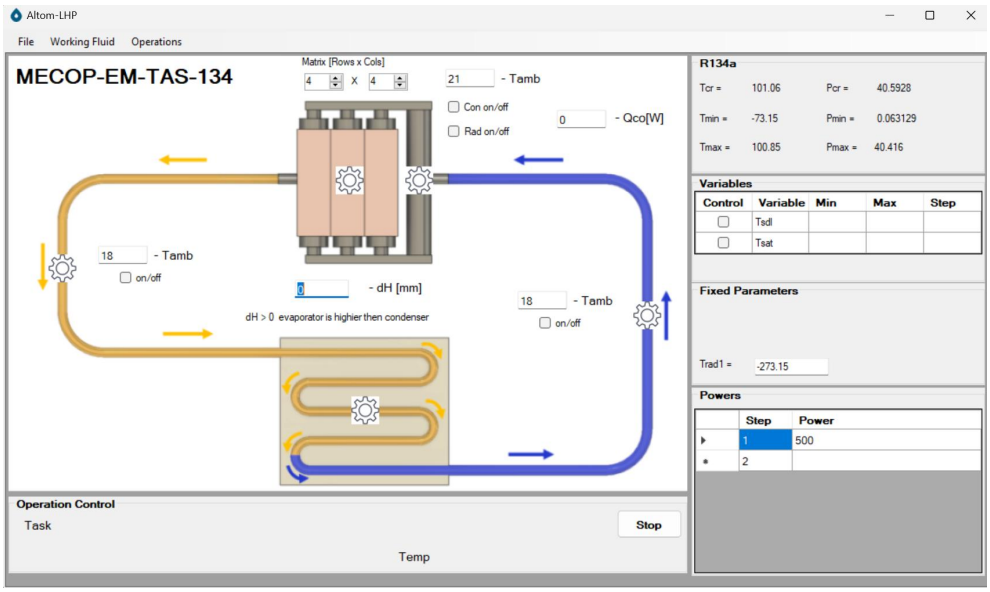


Figure 3-20. Main screen of the Altom-LHP software.

The main screen allows the user to specify problem parameters such as the ambient temperature for the evaporator, vapor line, and liquid line. These temperatures can be assigned individually for each element. Interaction with the environment can be enabled or disabled

separately for each component. For the evaporator, the type of heat exchange with the environment can be selected, including convection and/or radiation. In addition, a controlled heat input to the compensation chamber can be specified.

The upper horizontal menu provides access to the working-fluid database. New working fluids can be easily added by copying a text file of a predefined structure, containing tabulated thermophysical properties, into the corresponding working directory.

On the right-hand side of the main screen, an interface is provided for entering calculation parameters depending on the task, such as power and temperature values. Each LHP element is associated with a “gear” icon; clicking on it opens the configuration window for the corresponding component. Figure 3-21 illustrates the configuration window for a liquid transport line.

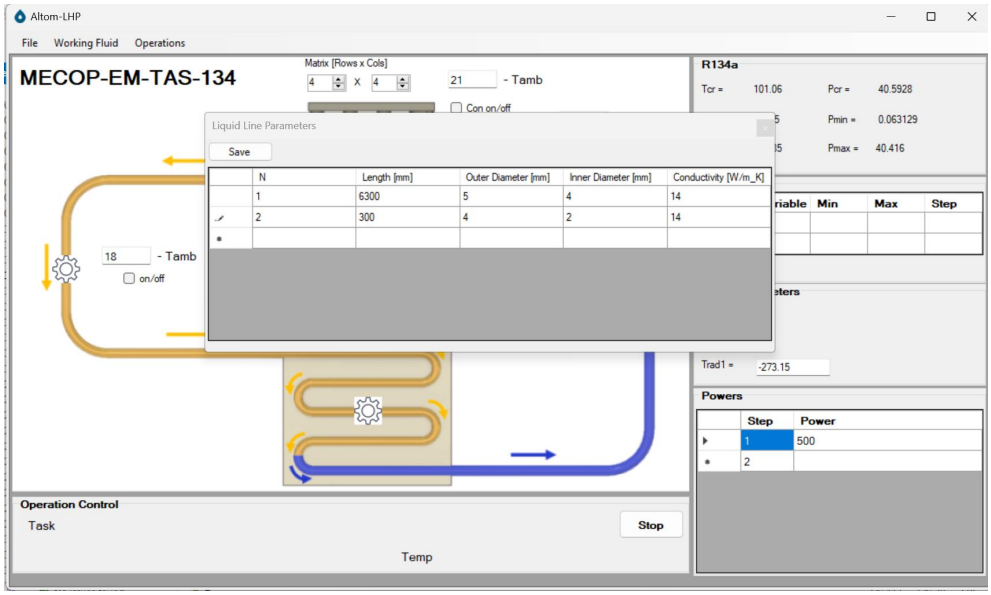


Figure 3-21 Configuration window for a transport line.

For each transport line, parameters such as length, inner and outer diameters, and the thermal conductivity of the material can be specified. This option also allows the introduction of thermal insulation. Transport lines may consist of multiple segments, which is common in practical systems and enables modelling of fittings or shut-off valves if present.

Figure 3-22 shows the configuration window for a modular evaporator composed of several capillary pumps.

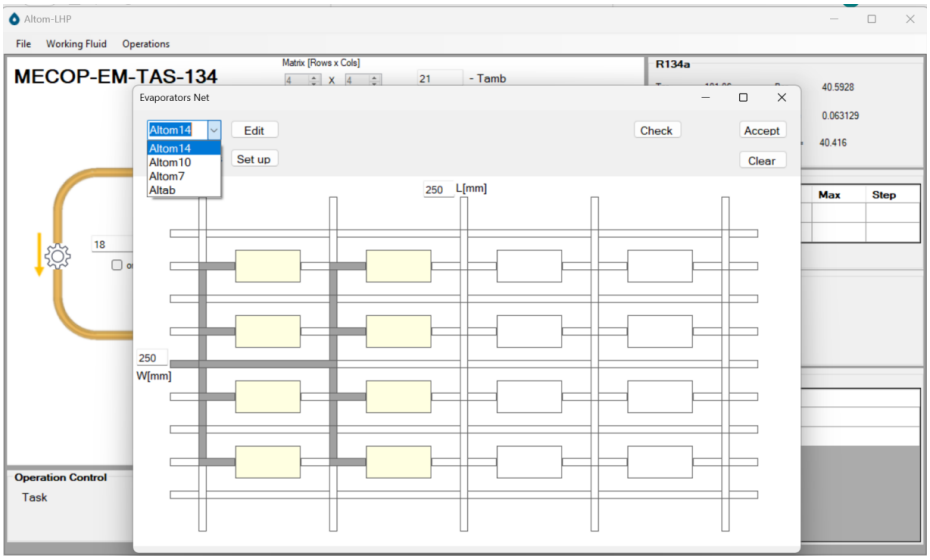


Figure 3-22. Configuration of a capillary pump array.

The array is used to configure the vapor collector. Each connection has its own configuration window, allowing specification of tube length and inner and outer diameters.

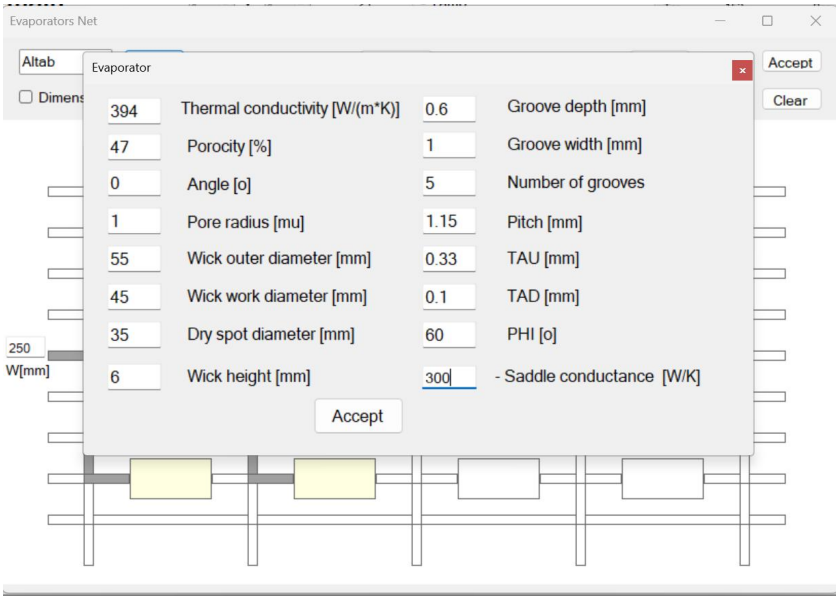


Figure 3-23. Capillary pump configuration window.

In the upper left corner of Figure 3-22, the type of capillary pump can be selected from a drop-down list. Pressing the Edit button opens a detailed configuration window for the capillary pump parameters (Figure 3-23). Both internal structure parameters (wick properties) and external structure parameters (thermal interface characteristics) can be specified.

Condenser modelling is implemented as a separate module. Figure 3-24 shows the condenser modelling window. The program supports six different condenser types and three heat-transfer modes: convection, radiation, and constant surface temperature (cold-plate mode).

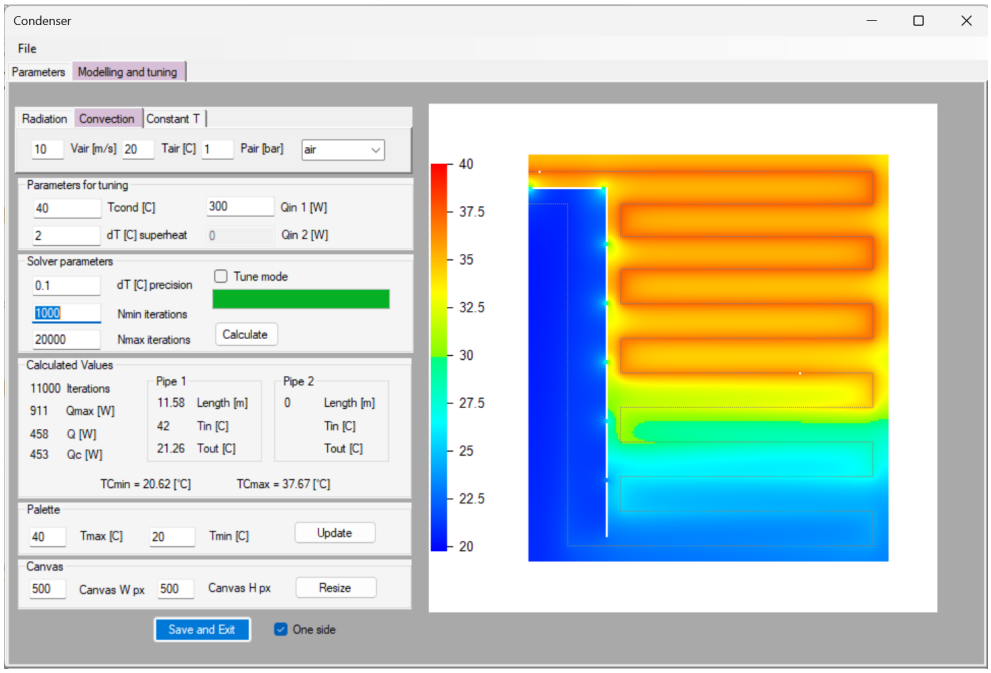


Figure 3-24. Condenser modelling window.

According to the model described above, steady-state operating points are determined using an iterative procedure by enforcing the equilibrium condition given (3.9), which is rewritten as

$$\left|\dot{Q}_{CC} - \dot{Q}_{SC}\right| \leq \delta_Q \tag{3.112.}$$

where $\delta_Q$ is the user-defined computational tolerance.

Figure 3-25 illustrates the evolution of $\dot{Q}_{CC}$ and $\dot{Q}_{SC}$ as functions of the evaporator temperature $T_{ev}$ during the iterative procedure. The intersection of the curves $\dot{Q}_{CC}(T)$ and $\dot{Q}_{SC}(T)$ corresponds to the sought steady-state operating point.

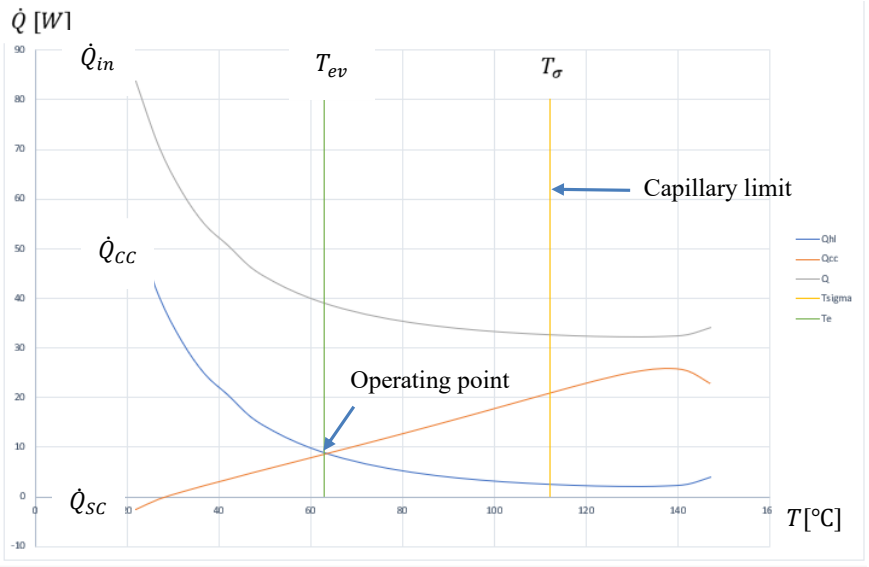


Figure 3-25. Convergence of the algorithm in computing the steady-state operating point of the LHP.

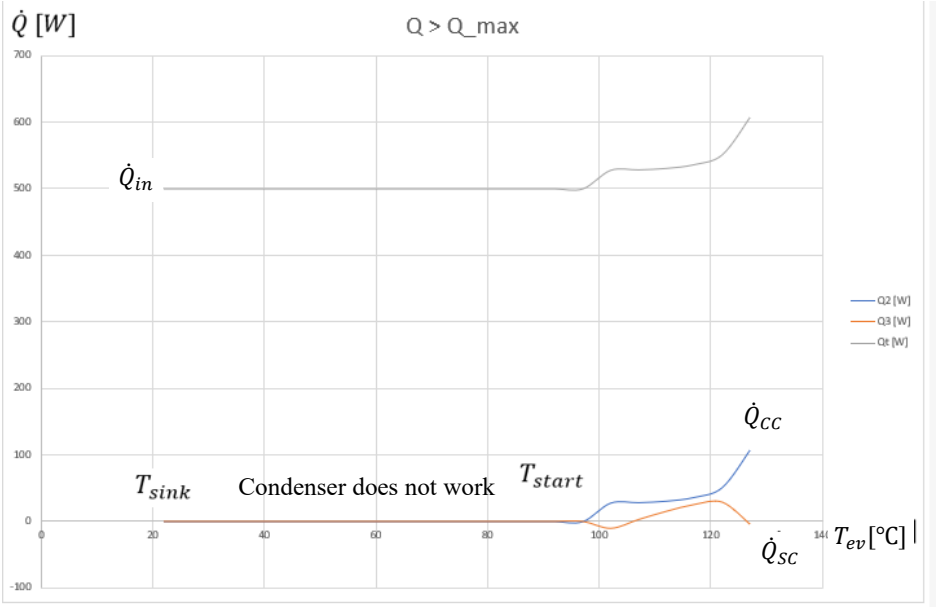


Figure 3-26. Illustration of algorithm divergence due to insufficient condenser dimensions.

The temperature $T_\sigma$ corresponds to the capillary limit with respect to the transferable power. In other words, if the intersection point of $\dot{Q}_{CC}$ and $\dot{Q}_{SC}$ lies to the right of $T_\sigma$, or if the curves do not intersect, the applied thermal load exceeds the heat-transfer capability of the LHP.

The software allows determination of the maximum transferable heat load $\dot{Q}_{max}$, the temperature distribution along the loop, the effective thermal conductance of the LHP, and the limiting heat load $\dot{Q}_{lim}$ associated with the evaporator itself. The latter depends solely on the evaporator characteristics and the working fluid and corresponds to the idealized case of negligible external loop resistance, where the condenser is capable of removing the entire heat load $\dot{Q}_{lim}$.

Figure 3-26 illustrates a case where the heat-transfer performance of the LHP is limited by the condenser capacity.

Up to a certain working-fluid temperature, the heat dissipated by the condenser is insufficient to ensure vapor condensation, which is reflected by the horizontal line. At higher temperatures, the working fluid begins to exit the condenser in the liquid phase; however, this is still insufficient to stabilize LHP operation. As a result, the curves $\dot{Q}_{CC}$ and $\dot{Q}_{SC}$ diverge, since the condenser does not provide sufficient subcooling of the liquid.

# 4 THERMAL MANAGEMENT OF AN IN-WHEEL ELECTRIC MOTOR

## 4.1 Problem Relevance

The reduction of fossil fuel consumption is one of the key strategic objectives of the European Union in achieving a climate-neutral economy [29]. The trend toward improved energy efficiency is accompanied by growing demand for personal mobility [30], including the widespread use of electric scooters [31],[32], electric bicycles [33], and other small electric vehicles, which has recently accelerated and is expected to further stimulate the development of electric vehicles (EVs) in the near future [34].

Electric vehicles can generally be divided into two major categories: pure electric vehicles (PEVs) and various configurations of hybrid electric vehicles (HEVs). While PEVs consist exclusively of electric propulsion systems with their associated characteristics and losses, HEVs are primarily internal combustion engine vehicles optimized for specific operating points. Therefore, PEVs are more closely aligned with the concept of a climate-neutral economy.

The primary consumer of electrical energy in a PEV is its electric propulsion system (EPS), which provides vehicle traction. The EPS consists of four main subsystems: the electric motor (EM), which converts electrical energy into mechanical energy; the power electronic converter (motor driver), which conditions and supplies electrical energy; the mechanical transmission (gearbox, shafts, wheels, etc.), which transfers mechanical power; and the energy source, typically a battery or fuel cell. Energy conversion and transmission in each of these subsystems are inevitably associated with thermal losses and therefore require appropriate thermal management.

Compared to losses in the power electronics, transmission, and battery, the losses in the electric motor are typically dominant. These thermal losses increase the temperature of motor components, thereby reducing their reliability and service life. The losses in rotating electric machines can be categorized as follows: copper (winding) losses account for up to 60 % of load-dependent losses, iron (core) losses are on the order of 10 %, and internal mechanical losses—primarily due to bearings and friction elements—are approximately 30 %. Copper losses originate from the electrical resistance of the windings and increase with temperature. Iron losses occur in regions where the magnetic field is present.

Regardless of vehicle type, most electric motors used in PEVs are permanent magnet synchronous motors (PMSMs) [35]. In PMSMs, the majority of losses are concentrated in the stator windings. A significant portion of these losses is associated with direct current resistance of copper, which increases with temperature. Additional alternating-current losses arise due to the

skin effect and proximity effect, induced by the high-frequency switching pulses generated by the power electronic motor driver [36].

Cooling of electric motors in PEVs is a challenging task due to the spatial separation between the main heat sources and locations suitable for effective heat rejection. Furthermore, electric motors in PEVs are typically installed and operated within confined enclosures, which further complicates thermal management. These challenges highlight the importance of efficient heat transport from the heat source to the heat sink. Such heat transport can be most effectively realized using two-phase LHP systems.

In thermal analyses of in-wheel motors, maximum winding temperatures have been observed in excess of 110 °C under steady-state operating conditions, and even higher under peak loads, approaching 130 °C, which approaches insulation and magnetic material limits [37]. These levels can significantly accelerate degradation of motor components and reduce service life.

Detailed studies show that approximately two-thirds (≈68 %) of the heat generated within an in-wheel motor is dissipated by convection, with only the remainder conducted through structural parts, indicating the limitations of passive air cooling for high-power applications.

In this chapter, the advantages of a two-phase LHP-based cooling architecture are demonstrated using an in-wheel electric motor as a case study. For this purpose, a modular LHP was designed and manufactured, and its evaporator was integrated into the motor stator using a dedicated thermal interface. The modified cooling system was experimentally tested, and the results were compared with the performance of a standard air-cooled motor of similar configuration.

## 4.2 State-of-the-Art Electric Motor Cooling Methods

In the context of electric motor cooling, traditional thermal management solutions are primarily based on single-phase technologies, including passive and forced air convection, as well as active liquid cooling systems.

Another cooling technique is spray cooling, in which oil droplets are directly sprayed onto the heated components of the electric machine. A comprehensive review of spray cooling applications in various electric machine configurations is presented in [38]. This method enhances heat transfer by increasing the effective contact between the coolant and the heated surfaces; however, it requires additional pumping and control systems.

More efficient thermal management solutions can be achieved using passive two-phase heat-transfer devices, such as HPs and LHPs. An example of a two-phase cooling approach applied to electric machines is described in [39], where the authors experimentally compared water cooling and refrigerant-based cooling (HFC-134a) for a PMSM intended for EV applications. The refrigerant-based solution demonstrated several advantages over conventional water cooling in terms of heat removal capability.

In terrestrial applications, hybrid cooling systems combining single-phase and two-phase loops are also employed. For instance, [40] presents a HEV motor cooling system integrating heat pipes with a liquid cooling circuit. Moreover, a recent review [41] on the use of heat pipes in electric machines concludes that, despite their technical attractiveness, widespread implementation is currently limited by cost considerations.

In many cases, designers attempt to enhance the thermal performance of existing electric machine designs by retrofitting them with two-phase heat-transfer devices. However, a more rational approach would be to incorporate such technologies at the early stages of machine design, allowing structural optimization for two-phase integration. The authors of [41] express optimism that advances in manufacturing technologies and materials will gradually remove the current barriers to broader adoption of two-phase cooling systems in electric motor applications.

The use of LHPs for electric motor cooling is particularly justified when heat must be transported over relatively long distances from the motor, when gravitational and inertial forces must be counteracted, or when a flexible and compact thermal solution is required. Typical scenarios include operation under severe thermal conditions where local heat rejection is impractical, or cases where the available surface area within the motor compartment is insufficient for effective heat dissipation. Additionally, loop heat pipes are advantageous when the cooling system must ensure protection of the motor from dust and moisture, maintaining environmental sealing while providing efficient heat removal.

## 4.3 Specific Features of In-Wheel Motor Cooling

Most PEVs are based on a propulsion architecture employing a single electric motor combined with a conventional transmission system. An alternative approach is the use of in-wheel motors (also referred to as hub motors), which provide a direct mechanical connection between the wheel and the electric drive [42]. In such configurations, each wheel of the vehicle is equipped with its own electric motor.

In-wheel motor architectures offer several advantages, including improved energy efficiency, reduced overall vehicle mass, and significant simplification of the drivetrain, as heavy components such as gearboxes, drive shafts, and differentials can be eliminated. In addition, direct-drive configurations enable improved dynamic performance of electric vehicles.

However, the cooling of in-wheel motors presents specific challenges. First, since the motor is integrated within the wheel assembly, implementing an efficient cooling solution is inherently difficult. Second, due to the compact geometry of in-wheel motors, it is challenging to introduce multiple dedicated cooling circuits for different components. In particular, the central part of the wheel (the rim or hub structure) provides only limited surface area available for air cooling. As a result, either a single common cooling solution must be employed, or cooling is focused only on the primary heat sources and the components most sensitive to overheating.

Third, in in-wheel configurations, environmental conditions such as mud, dust, or clay can significantly impair air-based heat exchange. Such conditions frequently occur precisely when the electric motor is required to operate at high power, for example during off-road driving. Finally, the upper temperature limit in in-wheel motors is particularly critical due to the close proximity of the motor to the inflated rubber tire, whose thermal limits impose additional safety constraints.

In practice, three primary approaches are widely used for in-wheel motor cooling: air cooling, oil cooling, and water cooling [43]. Forced-air cooling and thermal analysis of in-wheel motors for EV applications are described in [44], where the authors present a finite-element-based thermal model of the motor. An air-cooled YASA-type motor (axial-flux, yokeless, and segmented armature design) is discussed in [45]. A water-cooled PMSM is described in [46], where the authors propose the design and optimization of water jackets. Oil cooling of electric machines is examined in [38], and oil cooling via internal housing channels is reported in [47].

In-wheel motors are particularly widespread in personal mobility vehicles (PMVs). In such systems, heat generated within the electric motor is typically conducted to the aluminium housing (which is structurally integrated with the wheel hub) and then dissipated to the ambient environment primarily through natural convection. More specialized PMV configurations may encounter even more severe cooling challenges due to partial or complete thermal enclosure of the motor [2]. Furthermore, electric motors in PMVs often operate under highly dynamic conditions characterized by irregular duty cycles and frequent acceleration–deceleration sequences, which contribute to thermal accumulation and overheating.

The implementation of a LHP system for transporting heat from the motor to a compact and more efficient external heat exchanger enables a reduction in motor operating temperature. This, in turn, allows for increased permissible current density in the windings, improved reliability, higher achievable power, and extended service life of the electric motor.

## 4.4 Investigated In-Wheel Electric Motor and Its Cooling System

As a test object, an in-wheel electric motor equipped with a three-phase induction machine integrated into the wheel hub was selected. The motor has a rated power of 500 W and operates at a nominal voltage of 36 V (Figure 4-1).

The primary source of heat within the motor is the stator winding, shown in Figure 4-2 This is confirmed by the infrared image of the temperature distribution in the motor stator under steady-state operating conditions, presented in Figure 4-3.

The electric current flowing through the stator windings generates resistive (Joule) losses, resulting in heat generation within the winding region. This heat raises the temperature of the stator core and is subsequently transferred across the air gap to the motor end cover. From there, it is dissipated to the ambient environment primarily through natural convection.

Figure 4-1. Wheel with an integrated three-phase induction motor.

Figure 4-2. Electric motor stator.

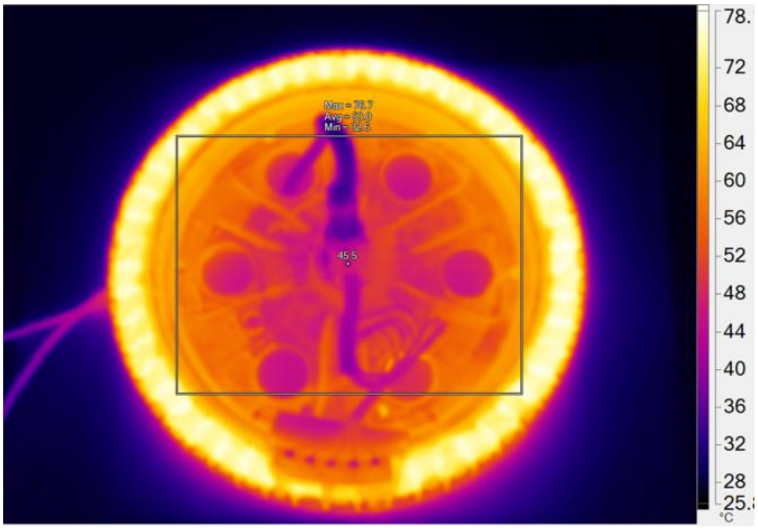

Figure 4-3. Temperature distribution in the motor under steady-state operation measured using an infrared camera.

While this solution is cost-effective and structurally simple, it is far from thermally optimal. First, a relatively high thermal resistance exists between the stator windings and the motor housing. Second, the effective heat-transfer surface area between the motor housing and the surrounding air is limited. These constraints significantly restrict the permissible operating temperature and, consequently, the allowable current density in the windings.

The aforementioned limitations can be mitigated by implementing a cooling system based on a LHP, enabling efficient heat extraction directly from the primary heat source and its transport to a more effective external heat sink.

## 4.5 Cooling System Design

The implementation of a loop heat pipe (LHP) enables heat to be transported away from the motor to a location where it can be effectively dissipated, thereby overcoming the limitation of the restricted heat-exchange surface available within the wheel assembly.

A key design question concerns the optimal placement of the LHP evaporator. Since the primary heat generation occurs in the stator windings, it is logical to position the evaporator as close as possible to this heat source. This is achieved by introducing a dedicated thermal interface between the stator windings and the evaporator. The interface must exhibit low thermal resistance

while ensuring efficient heat transfer from the windings to the evaporator. The design of this interface is shown in Figure 4-4.

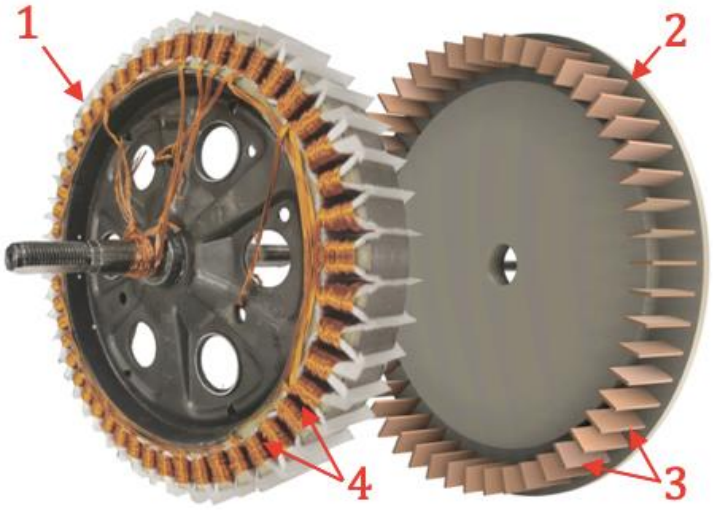


Figure 4-4. LHP – stator interface. 1- stator; 2 - interface; 3 - copper fins; 4 - gaps in winding.

The thermal interface consists of an aluminium plate with a diameter equal to that of the stator (200 mm), into which rectangular copper inserts (fins) are soldered. The drawings of the plate and fins are presented in Figure 4-5 and Figure 4-6. The fins are tightly inserted into the gaps between the stator winding turns, providing good thermal contact.

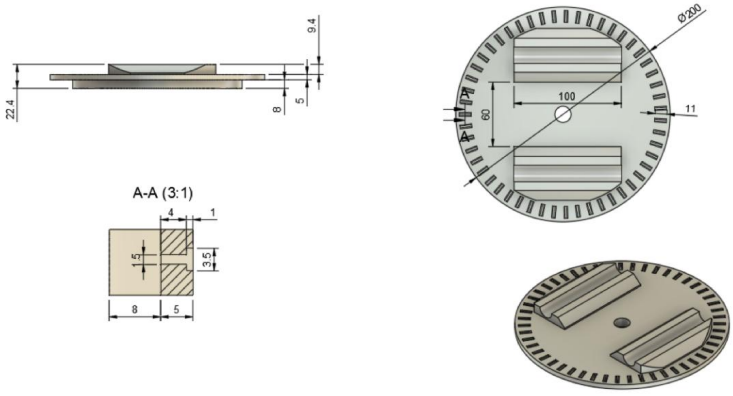

Figure 4-5. Dimensions of stator-LHP interface.

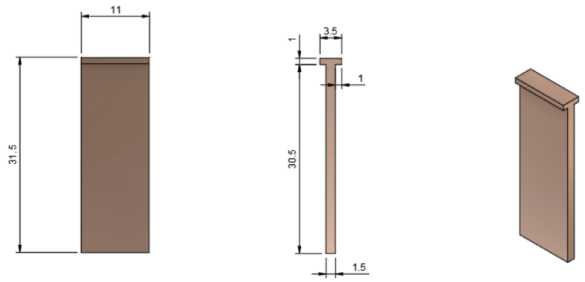


Figure 4-6. Dimensions of interface fin.

Since the original motor design did not include gaps within the stator winding, the motor was modified under laboratory conditions. The stator winding was replaced, resulting in a reduction of the stator winding wire cross-sectional area by approximately one third.

The heat generated in the winding is conducted through the copper fins to the aluminium plate, which simultaneously serves as the lower part of the evaporator saddle (Figure 4-7)

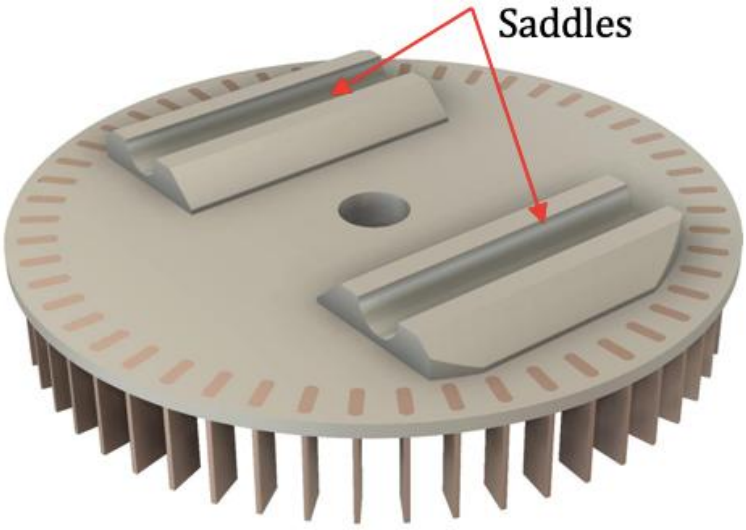


Figure 4-7. LHP–stator interface with integrated saddles of capillary pump units.

When designing the evaporator, it was taken into account that heat must be collected from a relatively large surface area (200 mm diameter). For such dimensions, a classical single capillary

pump configuration would not provide the desired performance due to increased thermal resistance of the interface and elevated local heat fluxes in the evaporation zone.

The application of a “Altom” modular design comprising two capillary pumps allows heat to be distributed between the pumps and reduces the effective thermal path from the stator winding to the evaporation region.

The final LHP configuration, including an evaporator composed of two parallel capillary pumps (1) and two compensation chambers (2), is shown Figure 4-8.

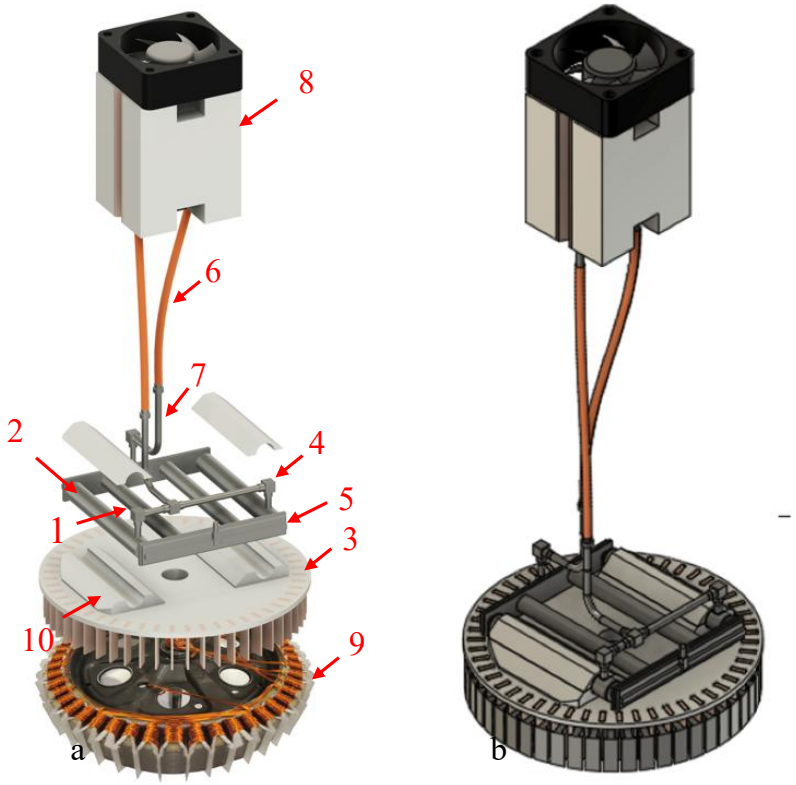


Figure 4-8. a) Stator and LHP composition: 1 - Two parallel capillary pumps. 2 - Two compensation chambers. 3 - Evaporator-stator thermal interface. 4 - Vapor manifold. 5 - Liquid manifold. 6 - Plastic transport lines. 7- Stainless-steel transport lines. 8 - Condenser with electric fan. 9 - Stator. 10 - Two saddles of evaporator. b) Stator and LHP assembly.

Composite transport lines were used for both liquid and vapor transport, consisting of rigid stainless-steel tubes (7) and flexible plastic tubes (6). The flexible plastic sections (225 mm in length) provide freedom in positioning the heat-rejection element — the condenser with a fan (8) — which is essential for practical applications.

The flexible lines may be extended to several meters, provided that the hydraulic resistance remains within the capillary limit of the system. This allows the condenser to be placed in a location offering a larger heat-exchange surface suitable for natural convection. An increase in transport line length requires a corresponding increase in the compensation chamber volume; however, as shown in Figure 4-7, this can be implemented by modifying the geometry of the liquid manifold (5).

The rigid stainless-steel tubes (total length 102 mm) ensure reliable connections between the flexible lines and the vapor (4) and liquid (5) manifolds on one side, and the condenser on the other. The capillary pumps are fixed within the evaporator saddles (10) by soldering.

The working fluid selected for the system is refrigerant R600 (n-butane). The choice was motivated by its widespread availability, environmental compatibility, and extensive practical experience of the author in using this fluid in two-phase heat transfer systems. Compatibility with the materials used in the LHP was experimentally verified in advance.

The condenser consists of two copper plates (105 mm × 65 mm) with fins on one side. The plates are soldered together back-to-back to form a single block. Five parallel grooves are machined into the rear surfaces; after joining, they form five parallel channels for the working fluid with a diameter of 2.5 mm and a length of 50 mm. These channels connect to a vapor manifold on one side and a liquid manifold on the other. Both manifolds are also machined into the copper plates and have a diameter of 5 mm. A fan is mounted at the end of the condenser to provide forced convection over the finned surface. The assembled LHP integrated with the stator is shown in Figure 4-7 (part b). The total mass of the system is 1650 g, of which 950 g corresponds to the thermal interface. The main parameters of the LHP are summarized in Table 4-1. Figure 4-9 shows the fabricated cooling system installed within the motor stator.

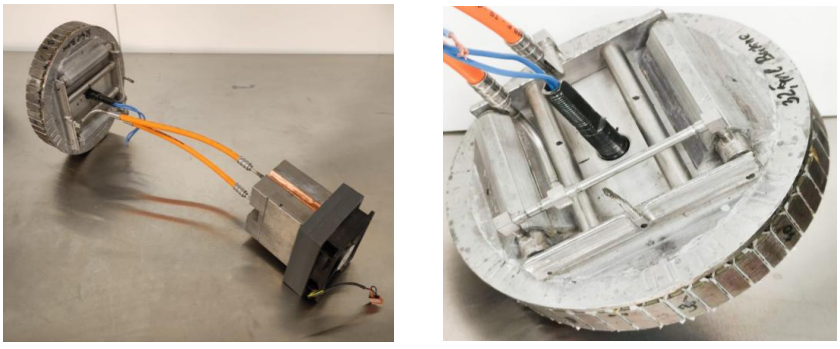

Figure 4-9. Fabricated LHP installed in the motor stator.

Table 4-1

In-wheel motor LHP parameters.

| Element LHP | Parameter | Value | Notes |
|---|---|---|---|
| Transport lines. Rigid part. | Outer diameter | 5 mm | Stainless-steel tube |
| | Inner diameter | 4 mm | |
| | Length | 102 mm | |
| Transport lines. Flexible part. | Outer diameter | 6.1 mm | Plastic hose |
| | Inner diameter | 4 mm | |
| | Length | 225 mm | |
| Condenser | Cu Plate Length x Width | 105 mm × 65 mm | 5 parallel channels between vapor and liquid collectors. |
| | Cu Plate thickness | 8 mm | |
| | Channel: | | |
| | Inner diameter | 2.5 mm | |
| | Length | 50 mm | Air HX fins are located on both sides. |
| | Vapor/liquid collectors: | 5 mm | |
| | Inner diameter | 95 mm | Fan 92 mm × 92 mm flowrate 1.92 m3/min. |
| | Length | | |
| | Cu air HX fins: | 48 × 2 (both sides) | |
| | Number | | |
| | Height: | 28 mm | |
| | thickness | 0.4 mm | |
| Capillary pump | Wick material | Stainless steel | 2 units. |
| | Pore size | ~1μm | |
| | Porosity $\varphi$ | 47% | |
| | Wick length $L_w$ | 100 mm | |
| | Wick Outer diameter $D_{out}$ | 13.6 mm | |
| | Wick Inner diameter $D_{in}$ | 5.6 mm | |
| Compensation chamber | Outer diameter | 12 mm | 2 Stainless-steel tubes |
| | Inner diameter | 11 mm | |
| | Length | 122 mm | |
| Thermal fluid | Butane (R600) | 32.5 ml | |

## 4.6 In-Wheel Electric Motor and LHP Thermal Analysis

The investigated motor is powered by alternating current. However, experimental evaluation of thermal losses is more conveniently performed when all windings are connected to a direct current source. Under DC excitation, the motor produces no mechanical output, and the entire electrical power supplied is converted into heat. It is therefore appropriate to assess the applicability of the results obtained to the case of AC operation. The AC loss resistance $R_{AC}$ exceeds the DC resistance $R_{DC}$ due to skin and proximity effects. This relationship may be expressed as

$$R_{AC} = K_{AC}(\eta) \cdot R_{DC} \tag{4.1.}$$

where the dimensionless coefficient $K_{AC}(\eta)$ depends on the dimensionless parameter $\eta$, defined for a single conductor strand as

$$\eta = D/\delta \tag{4.2.}$$

Here, $D$ is the conductor height and $\delta$ is the skin-effect depth, calculated as:

$$\delta = \sqrt{\frac{\rho}{\pi \cdot f \cdot \mu_0}} \tag{4.3.}$$

where $\rho$ is the resistivity of copper, $f$ is the AC frequency, and $\mu_0$ is the permeability of free space. For multilayer, multistranded conductors such as stator windings, the proximity effect must also be considered. The arrangement of wires in the slot of the investigated motor is shown in Figure 4-10.

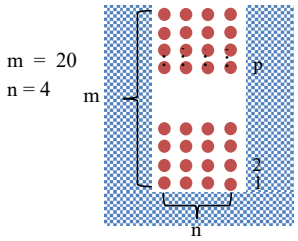


Figure 4-10. The arrangement of wires in the slot. $m = 20$ – the number of layers, $n = 4$ – the number of wires in one layer.

For multilayer conductors, the coefficient $K_{AC}(\eta)$ depends on the layer position $p$ (counted from the slot bottom) and can be expressed as

$$K_{AC}(\eta) = \varphi(\eta) + p \cdot (p-1) \cdot \psi(\eta) \tag{4.4.}$$

The first term corresponds to the skin effect, and the second to the proximity effect, where

$$\varphi(\eta) = \eta \frac{\sinh 2\eta + \sin 2\eta}{\cosh 2\eta - \cos 2\eta} \tag{4.5.}$$

$$\psi(\eta) = 2\eta \frac{\sinh \eta - \sin \eta}{\cosh \eta + \cos \eta} \tag{4.6.}$$

The equations (4.4 – 4.6) are derived for the strands of rectangular shape and the parameter $\eta$ should be calculated as

$$\eta = \sqrt{\frac{n \cdot b}{w_s}} \cdot \frac{h}{\delta} \tag{4.7.}$$

where $w$ is the strand width, $h$ is the strand height, and $w_s$ is the slot width. This theory may be applied approximately to round wires by assuming

$$w = h = d \tag{4.8.}$$

where $d$ is the wire diameter.

Averaging expression (4.4) over all layers $p = 1 \ldots m$ yields

$$\overline{K_{AC}(\eta)} = \varphi(\eta) + \frac{m^2 - 1}{3} \psi(\eta) \tag{4.9.}$$

Using the parameters corresponding to the investigated motor:

$m = 20,\ n = 10,\ d = 0.56$ mm
$w = 6.2$ mm, $f = 400$ Hz,
$\rho = 1.724 \cdot 10^{-8}\ \Omega \cdot$ m ($t = 20$°C)
$\mu_0 = 4\pi \cdot 10^{-7}$ N/A$^2$

the averaged coefficient is found to be $\overline{K_{AC}(\eta)} \approx 1$. Thus, for the investigated motor, copper losses under AC excitation may be considered approximately equal to DC losses.

The thermal resistance of the stator–LHP interface was evaluated using a steady-state thermal solver in the ANSYS software package. Figure 4-11 presents the calculated steady-state temperature distribution over the interface surface.

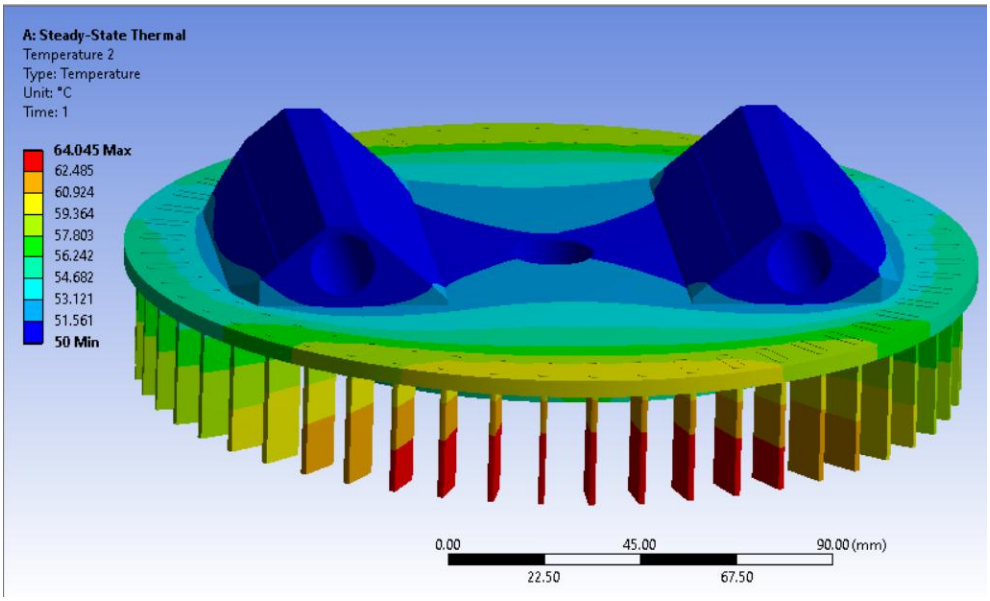


Figure 4-11. Temperature distribution over stator --LHP interface. Q ̇=100 W

The calculations were performed assuming uniform heat generation along the stator winding. The total heat flow was set to $\dot{Q} = 100$ W, and the temperature at the contact region between the evaporator housing and the saddle was fixed at 50 °C. The resulting thermal resistance of the interface was $R_i \approx 0.08\, K/W$. To more accurately represent real operating conditions, the thermal contact resistances between the interface and the winding $R_{i,w}$ and between the interface and the evaporator housing $R_{i,e}$ must be included. The total thermal resistance between the winding and the evaporator is therefore

$$R_{w,e} = R_{i,w} + R_i + R_{i,e} \tag{4.10.}$$

Since analytical evaluation of the contact resistances is difficult, empirical values were used. The value of $R_{i,e}$ was estimated based on accumulated experience in manufacturing evaporators

of different configurations and comparing their thermal characteristics. For the proposed LHP–stator interface, the total resistance was estimated as $R_{w,e} \approx 0.3\ K/W$.

The heat transfer characteristics of the LHP were calculated using the model described in Chapter 3. The evaporator consisted of two parallel capillary pumps, each 100 mm in length. The composite structure of the transport lines was also taken into account.

According to the manufacturer's specifications, the motor efficiency ranges from 80% to 88% at an input power of 500 W. This implies that thermal losses may reach approximately 100 W. At such relatively low power levels, heat exchange between the LHP components and the ambient environment must be considered; otherwise, significant discrepancies with experimental results may arise. This applies to the evaporator, transport lines, and compensation chambers.

Heat exchange between the transport lines, evaporator, and ambient air occurs via natural convection. The formalism described in Section 3.4 was applied. The ambient air temperature was taken as $T_{amb} = 15\ °C$. For tubes with an external diameter $D_{out} = 5$–$6$ mm, the Rayleigh number lies in the range $Ra \sim 1$–$2 \times 10^3$. Thus, the external Nusselt number according to (4.14) was calculated as

$$Nu_{out} = 0.75 \cdot Ra^{1/4} \tag{4.11.}$$

The equation (3.53) for determining the external surface temperature $T_{sur}$ of the transport lines becomes

$$g_{eff} \cdot (T - T_{sur}) = A \cdot (T_{sur} - T_{amb})^{5/4} \tag{4.12.}$$

where $T$ is the fluid temperature and the coefficient $A$ is

$$A = 0.75 \cdot \pi \cdot \lambda_a \cdot [K_{nc} \cdot D_{out}^3]^{1/4} \tag{4.13.}$$

Here, $g_{eff}$ is the effective conductance from the fluid to the external tube surface per unit length. For thin-walled metallic tubes, wall resistance may be neglected, so $g_s \approx g_{in}$. For plastic sections, the thermal resistance of the tube wall must be taken into account, and the effective conductance $g_{eff}$ is calculated in accordance with (3.51). The thermal conductivity of the plastic material was taken as $\lambda_m \approx 0.3\ W/(K \cdot m)$.

The compensation chambers are manufactured from two metallic tubes with an outer diameter of 12 mm and a length of 122 mm. Heat exchange with the ambient air occurs by natural convection; therefore, the same reasoning as that applied above to the transport lines can be used for the compensation chambers. The Rayleigh number is of the same order of magnitude ($Ra \approx 2 \cdot 10^4$).

For the calculation of heat rejection from the condenser to the ambient air, the theory of forced convective heat transfer in narrow flat channels was applied. In the considered condenser, the flat channels are formed by the fins of the heat exchanger arranged with a pitch of 1 mm on both sides of the condenser plate. The Nusselt number for flow in flat channels can be calculated using the following correlations:

$$Nu_a = \begin{cases} 1.24 \cdot \left(\frac{Re_a \cdot d_{eff}}{L_f}\right)^{0.4}, & Re \leq 3000 \\ 0.018 \cdot Re^{0.8}, & Re > 3000 \end{cases} \tag{4.14.}$$

where $L_f$ is the fin length, and the $d_{eff}$ is determined in accordance with (3.44) $d_{eff} = 4S/\Pi$. with $S$ being the cross-sectional area of the channel and $\Pi$ its wetted perimeter. The heat transfer coefficient at the fin surface is then given by

$$h_{eff} = \eta_f \cdot Nu_a \cdot \frac{\lambda_a}{d_{eff}} \tag{4.15.}$$

Here, the parameter $\eta_f$, referred to as the fin efficiency, accounts for the non-uniform temperature distribution along the fins. For flat rectangular fins, it can be calculated as

$$\eta_f = \frac{\tanh(\beta \cdot H_f)}{\beta \cdot H_f} \tag{4.16.}$$

where $H_f$ is the fin height, and for a thin fin the parameter $\beta$ is defined for thin fin as:

$$\beta = \sqrt{\frac{2 \cdot h_f}{\lambda_a \cdot \tau_f}} \tag{4.17.}$$

with $\tau_f$ being the fin thickness.

Substituting the numerical values into (4.16) and (4.17) yields $\eta_f \approx 0.84$.

For the Reynolds number $Re_a$, it was assumed that the employed fan provides an air velocity in the channels of approximately 9 m/s.

When analysing the flow of the working fluid in the condenser channels, it is convenient to use quantities referred to unit channel length. Since the channels are uniformly distributed, the fin conductance per unit channel length can be expressed as

$$g_a = h_{eff} \cdot S_x \tag{4.18.}$$

where $S_x$ is the fin surface area per unit channel length.

The thermal resistance of the copper plate can be neglected; therefore, the overall effective conductance of the condenser $g_{c,eff}$ yields:

$$g_{c,eff} = \frac{g_{in} \cdot g_a}{g_{in} + g_a} \tag{4.19.}$$

$g_{in}$ has the same meaning as in (3.51). The calculated parameters are summarized in Table 4-2.

Table 4-2.

The calculated parameters of in-Wheel motor LHP

| Parameter | Units | Meaning | Value |
|---|---|---|---|
| $R_i$ | $\frac{K}{W}$ | Thermal resistance of the EM–LHP interface | 0.08 |
| $R_{w,e}$ | $\frac{K}{W}$ | Thermal resistance between the winding and the evaporator | 0.3 |
| $g_w$ | $\frac{W}{m \cdot K}$ | Thermal conductance of the plastic tube wall per unit length | 1.69 |
| $g_a$ | $\frac{W}{m \cdot K}$ | Thermal conductance of the condenser fins per unit channel length | 90 |
| $d_{eff}$ | $mm$ | Effective hydraulic diameter of the air channel | 1.93 |
| $\eta_f$ | | Fin efficiency of the air heat exchanger | 0.84 |

## 4.7 Experimental Investigation of Motor Cooling

The experimental campaign was carried out in two stages. During the first stage, the thermal performance of the motor without the two-phase heat-transfer system was investigated. The three stator windings were connected in series and supplied with direct current. Under this configuration, the entire supplied electrical power is converted into heat. The stator was installed in its original position inside the motor housing so that cooling occurred under natural convection conditions, closely resembling real operating conditions. Five thermocouples were installed at

different locations within the stator winding, and one additional thermocouple was used to measure the ambient temperature. The data acquisition system recorded the thermocouple readings as well as the voltage and current values in the windings at 5-second intervals. The data were transmitted to a computer and processed using a dedicated program developed in the LabVIEW environment. The electrical power consumed by the motor was calculated as the product of current and voltage. The objective of the experiment was to determine the input power at which the winding temperature reached the upper allowable limit of 110 °C. To this end, the current supplied to the windings was gradually increased so that the input power rose in increments of approximately 20 W, starting from an initial value of 20 W. For each power level, sufficient time was allowed for the temperatures to reach steady-state conditions. The experimental results are presented in Figure 4-12.

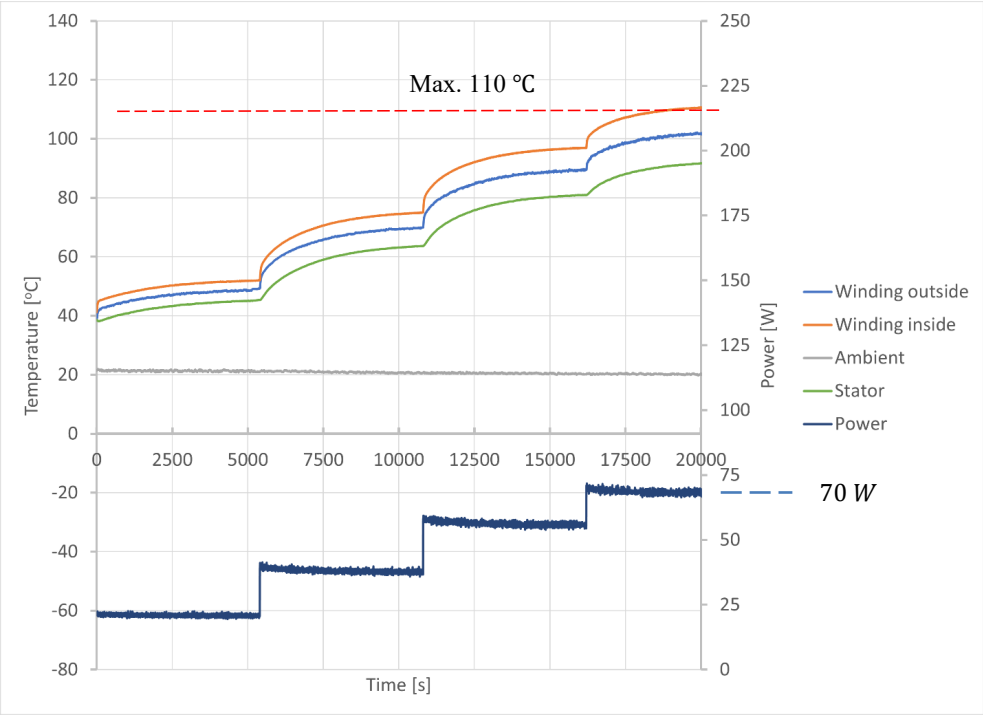


Figure 4-12. EM test without LHP. Dependence of stator temperatures on time for different powers.

As shown in the graph, the maximum input power was 70 W, which approximately corresponds to the upper efficiency limit of the motor. The ambient temperature during the experiment was 20 °C.

The next series of tests was conducted with the stator equipped with the LHP. Butane (R600) was used as the working fluid. Two operating configurations were investigated. In the first configuration, the stator with the LHP was not installed inside the wheel housing; instead, it was thermally insulated. Under these conditions, heat dissipation through the motor housing was eliminated, and the entire thermal load was removed by the LHP. The experimental results for this configuration are presented in Figure 4-13.

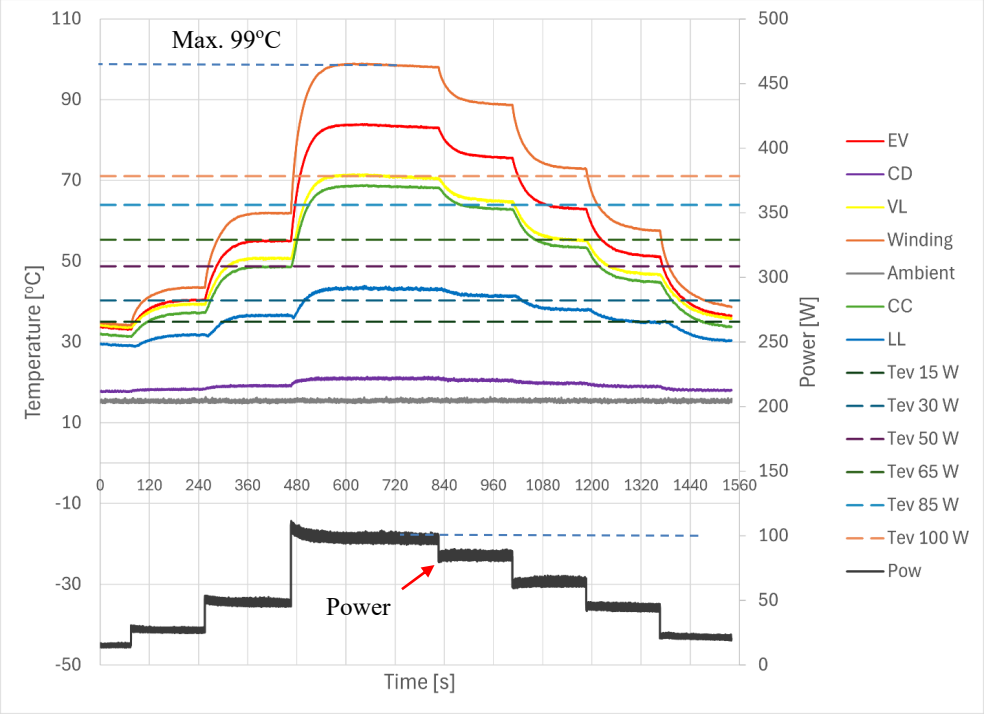


Figure 4-13. Temperature distribution over LHP for different powers. The stator is thermally isolated. EV – evaporator and saddle; VL – vapor line; LL – liquid line; CC – compensation chambers; CO – condenser's fins. The dashed lines correspond to the vapor temperatures calculated based on the model.

The orange line corresponds to the average winding temperature. As observed in the experiment, at an input power of 100 W the maximum stator temperature did not exceed 99 °C. It should be noted that the ambient temperature in this experiment was 15 °C, i.e., 5 °C lower than in the reference test (20 °C). Therefore, under identical ambient conditions, the winding temperature can be expected to reach approximately 104 °C. The red line represents the temperature measured on the outer surface of the evaporator saddle. The yellow line corresponds

to the vapor temperature at the evaporator outlet. Assuming that this temperature is close to the evaporation temperature $T_{ev}$, the difference between the red and yellow curves characterizes the thermal resistance of the saddle, including the contact resistance between the capillary pump and the thermal interface. The liquid temperature (LL) is measured at the outlet of the liquid line, i.e., at the inlet to the evaporator liquid manifold ($T_{ll,out}$). The green curve (CC) indicates the temperature measured on the outer surface of the compensation chamber and corresponds to the compensation chamber temperature $T_{cc}$. The curve denoted as CO represents the temperature measured on the outer surface of the condenser fins.

The second operating configuration was intended to represent a realistic scenario in which the LHP would be installed in an actual wheel. In this case, both cooling mechanisms — heat removal by the LHP and natural convection from the motor housing — operated simultaneously. The thermal insulation was removed, and the motor was reinstalled in its original housing. The results of these tests are presented in Figure 4-14.

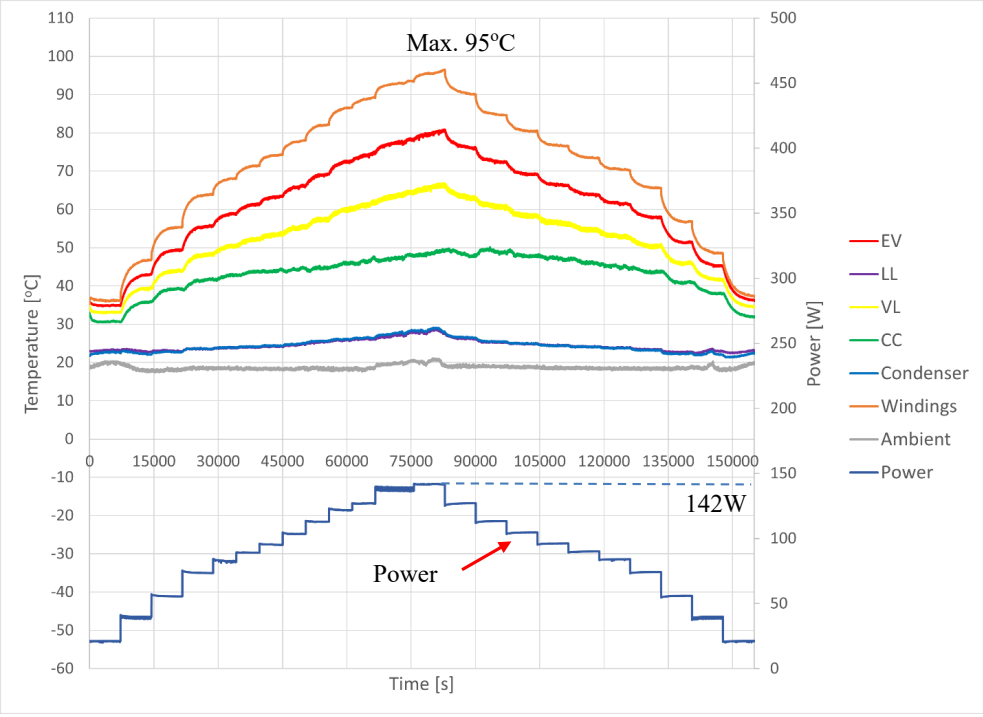


Figure 4-14. Temperature distribution over LHP for different powers with the stator installed inside the hub and covered with a metal plate.

As seen from the figure, at an input power of 142 W the average stator temperature did not exceed 95 °C. The ambient temperature during this experiment was 20 °C.

## 4.8 Results and Discussion

The experimental configuration with the thermally insulated motor is particularly convenient for comparison with the model predictions. Since the motor housing was insulated, all heat-transfer paths other than the LHP were effectively eliminated.

If only the radial heat leakage through the evaporator body, described by expression (3.36), is taken into account, the calculated temperature distribution along the LHP for the experimentally realized power levels is shown in Figure 4-15.

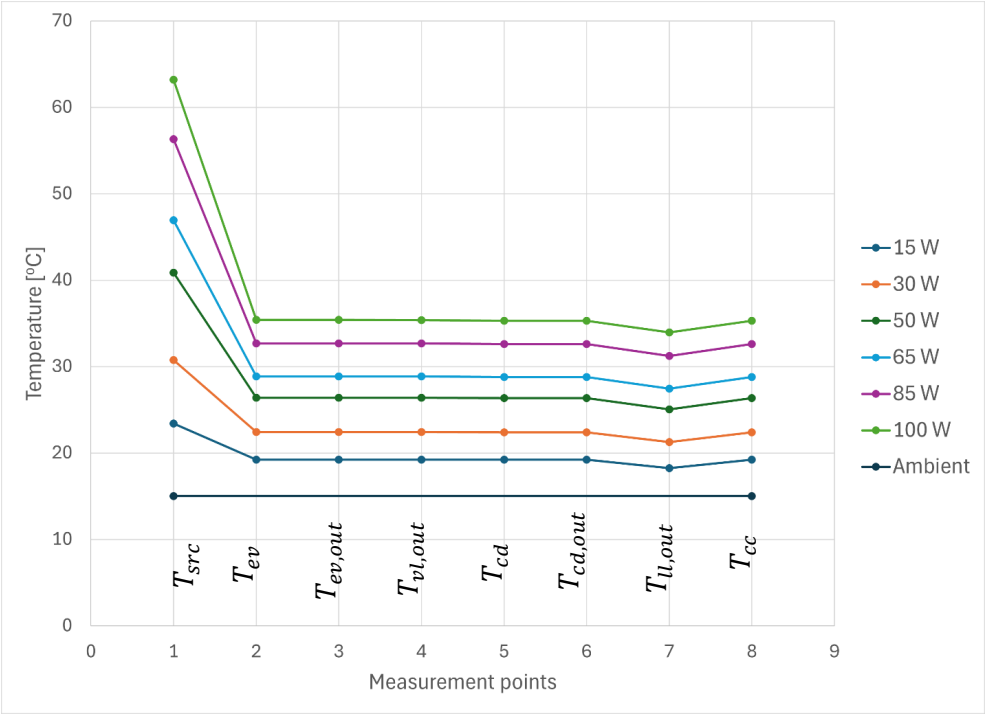


Figure 4-15. Temperature distribution over LHP for different powers. Calculated based on steady model with radial heat leak only.

The points shown in the figure correspond to the following temperatures: $T_{src}$ – winding temperature; $T_{ev}$ –evaporation temperature; $T_{ev,out}$ – vapor temperature at the exit of the evaporator; $T_{vl,out}$ – vapor temperature at the exit of the vapor line (entrance to condenser); $T_{cd}$ –

condensation temperature; $T_{cd,out}$ – temperature of subcooled liquid at the exit of the condenser; $T_{ll,out}$ – temperature of liquid at the exit of the liquid line; $T_{cc}$ – temperature at the compensation chamber

As can be seen from Figure 4-15, for a thermal load of 100 W the calculated winding temperature does not exceed 65 °C, while all other temperatures remain in the range of 20 °C –35 °C. Thus, calculations that consider only the radial heat leakage through the wick provide overly optimistic results. This conclusion is also supported by the experimentally observed temperature distribution. The temperature difference between the vapor and the compensation chamber (yellow and green curves in Figure 4-13) is small. These two temperatures determine the heat leak through the wick, as reflected in expression (3.36). At the same time, the experiment shows a significant temperature difference between the vapor and the liquid entering the compensation chambers. According to expression (3.32), this difference determines the subcooling heat $\dot{Q}_{sc}$.

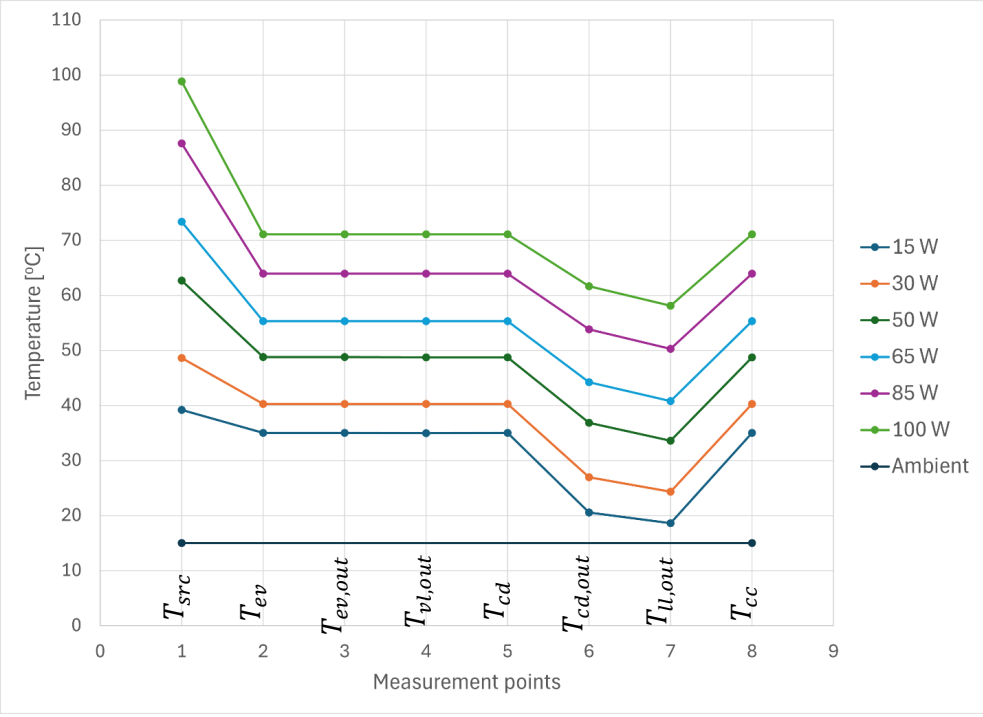


Figure 4-16. Temperature distribution over LHP for different heat loads. Conditions correspond to the test presented in Figure 4-14.

This indicates the presence of an additional heat-leak path to the compensation chamber, such as through the evaporator shell or via the liquid manifold. This heat leak cannot be neglected in

the calculation. According to the theory presented in Section 3.4, as a first approximation this additional heat leak may be assumed proportional to the temperature difference between the heat source and the compensation chamber, i.e., proportional to $T_{src} - T_{cc}$. In this case, the total heat leak should be calculated using expression (3.39), with an appropriately selected thermal resistance $R_{HL}$.

For the considered loop, selecting $R_{HL} = 2.4$ K/W yields a calculation that adequately reproduces the observed LHP behaviour. Figure 4-16 presents the calculated temperature distributions for the heat loads applied during the experiment.

As can be seen from Figure 4-16, for this LHP configuration and range of thermal loads, the working fluid moves from the evaporator to the condenser in an almost isothermal manner ($T_{ev} \approx T_{vl} \approx T_{cd}$). This is not the case for the liquid line, where heat exchange with the environment plays a significant role. For clarity, the theoretically calculated values of $T_{ev}$ are plotted in Figure 4-13 as dashed lines and should be compared with the measured vapor-line temperature (VL), shown in yellow.

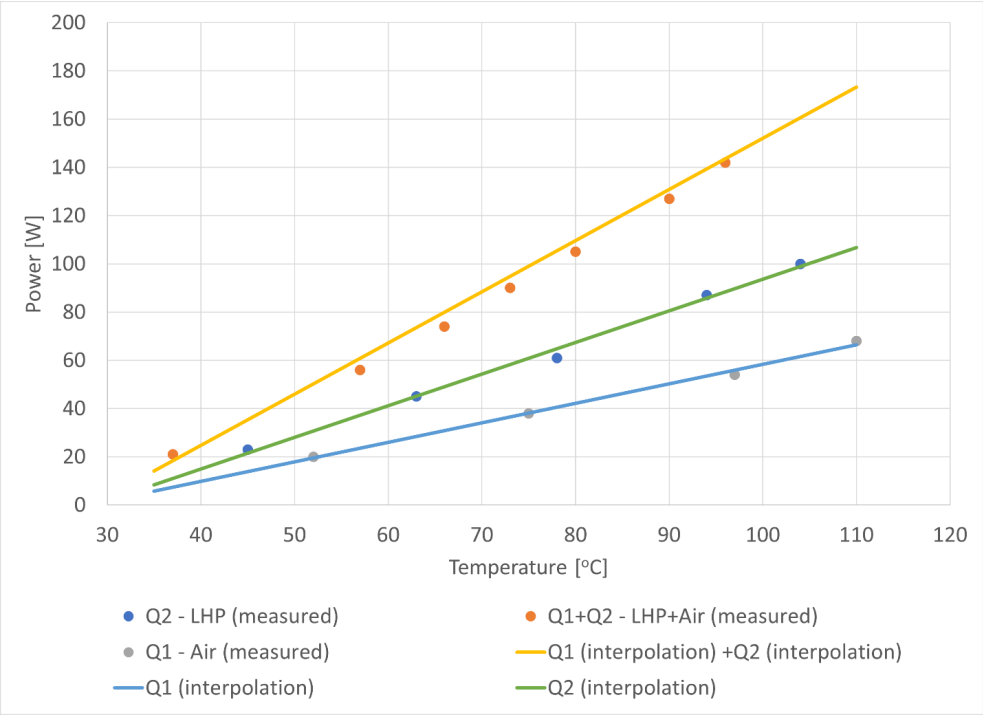


Figure 4-17. Dependence of dissipated heat flow on the maximum winding temperature for the three studied configurations. The blue and green lines represent linear interpolations of the measured data. The yellow line corresponds to their sum.

The agreement between theory and experiment is very good for all investigated power levels. This agreement primarily validates the adopted model of heat leakage to the compensation chamber.

It is instructive to analyse the dependence of the dissipated power on the maximum winding temperature, $\dot{Q}(T_{max})$, for all three investigated configurations. The measured data are well approximated by linear functions, as shown in Figure 4-17.

For natural air cooling (natural convection), the dependence can be expressed as:

$$\dot{Q}_1 = 0.81 \cdot T_{max} - 21.75 \tag{4.20.}$$

For the configuration with the LHP only:

$$\dot{Q}_2 = 1.31 \cdot T_{max} - 37.56 \tag{4.21.}$$

Summing (4.20) and (4.21) gives:

$$\dot{Q}_3 = \dot{Q}_1 + \dot{Q}_2 = 2.12 \cdot T_{max} - 60.16 \tag{4.22.}$$

The yellow line in Figure 4-17 corresponds to (4.22). It can be seen that the experimentally measured values for the configuration in which heat is removed simultaneously by the LHP and natural convection lie very close to this line.

This observation indicates that the two heat-dissipation mechanisms operate essentially independently. Their thermal contributions to the cooling of the electric motor are additive.

From (4.22), a maximum allowable winding temperature of 110 °C corresponds to a dissipated heat flow of approximately 173 W. This value is about 2.5 times higher than the heat flow achievable by natural air cooling alone at the same temperature.

If the fraction of heat losses relative to the total motor power remains approximately constant, this result suggests that the motor could potentially operate at a power level about 2.5 times higher when cooled using the LHP-based system.

The result may also be interpreted from another perspective. If the required motor power remains unchanged, the application of the two-phase cooling system enables a significant reduction of the winding operating temperature. For the same dissipated power, the maximum winding temperature is reduced by approximately a factor of 1.8 compared to air cooling alone.

## 4.9 Conclusions for Chapter 4

Analysing the obtained results, it should be emphasized that the original motor design did not account for the integration of an LHP-based thermal interface. The motor was modified under laboratory conditions to accommodate the evaporator assembly, which required reducing the

cross-sectional area of the stator winding by approximately one third. This modification increased the electrical resistance and, consequently, the heat generation by a factor of approximately 1.5.

Therefore, the experimentally observed 2.5-fold increase in heat removal capability compared to natural convection does not fully reflect the intrinsic potential of the LHP-based cooling approach. When corrected for the artificially increased heat generation caused by the reduced winding cross-section, the effective performance gain is approximately 1.7.

However, this limitation is methodological rather than fundamental. If the use of an LHP cooling system is considered at the early stage of electric motor design and supported by predictive thermal modelling, the full potential of two-phase heat transport can be realized without compromising the electromagnetic structure of the motor.

A promising design solution for in-wheel motors is the integration of evaporators directly into the stator body, as illustrated in Figure 4-18.

.

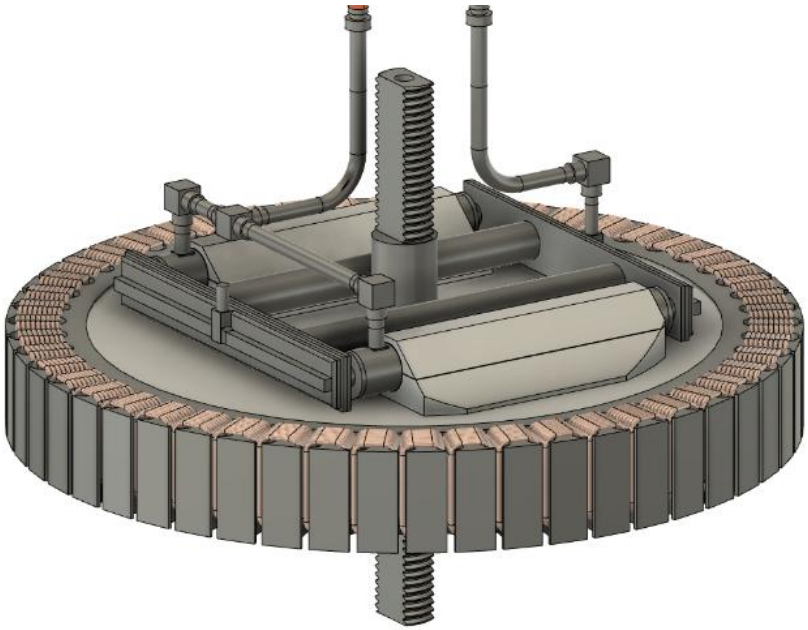

Figure 4-18. Stator body design with built-in evaporators.

In this concept, the intermediate thermal interface with copper inserts placed between winding gaps is eliminated. Heat is conducted directly from the stator teeth—on which the windings are placed—to the embedded evaporators. This architectural simplification:

- preserves the original winding cross-section,

- reduces structural complexity,
- lowers motor mass,
- and decreases the winding-to-evaporator thermal resistance by approximately 30 %.

Figure 4-19 shows the calculated temperature distribution for the stator body serving directly as the winding–LHP interface under identical boundary conditions.

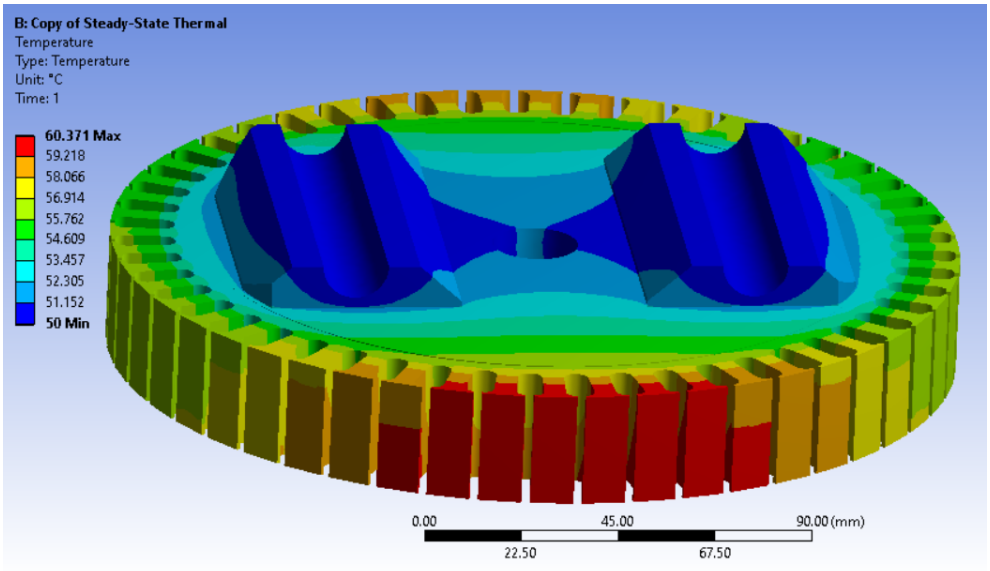


Figure 4-19. Temperature distribution over the stator body acting as a winding–LHP interface ($\dot{Q} = 100$ W).

Comparison of the temperature fields demonstrates a reduction of the temperature non-uniformity by approximately 4 °C, consistent with the estimated 30 % decrease in interface thermal resistance.

It should be noted that such an integrated motor–LHP architecture is feasible only in a factory-level design where thermal management is incorporated as a primary constraint rather than an auxiliary subsystem.

Thus, the presented results indicate that the introduction of two-phase heat loops into electric motor design does not merely represent an incremental improvement in cooling performance. Rather, it enables a transition toward a new design paradigm for high power-density in-wheel drives, in which thermal transport is treated as an active structural element of the motor rather than an external add-on.

When implemented at the conceptual design stage, this approach allows simultaneous optimization of electromagnetic, mechanical, and thermal subsystems, thereby unlocking higher allowable current densities, improved reliability margins, and increased compactness without sacrificing efficiency.

# 5 THERMAL MANAGEMENT OF LED LUMINAIRE

## 5.1 Problem Relevance

Thermal management of modern electronic systems faces increasing challenges, as chip-level power dissipation has grown by approximately a factor of 3.5 over the past two decades [1], resulting in a proportional increase in required heat removal capacity. An illustrative example of high-power electronics is provided by LED-based lighting systems. High-power LED luminaires constitute thermally intensive devices in which a substantial fraction of the supplied electrical power is converted into heat. Despite continuous improvements in luminous efficacy, modern high-intensity LEDs still dissipate a significant portion of the input power as thermal energy. For individual high-power LED units, the local heat flux density, calculated over the recommended solder pad area, may reach $150\,W/cm^2 - 180\,W/cm^2$ [4]. This places LED devices in the category of high heat flux electronics, comparable to IGBT modules or laser diodes.

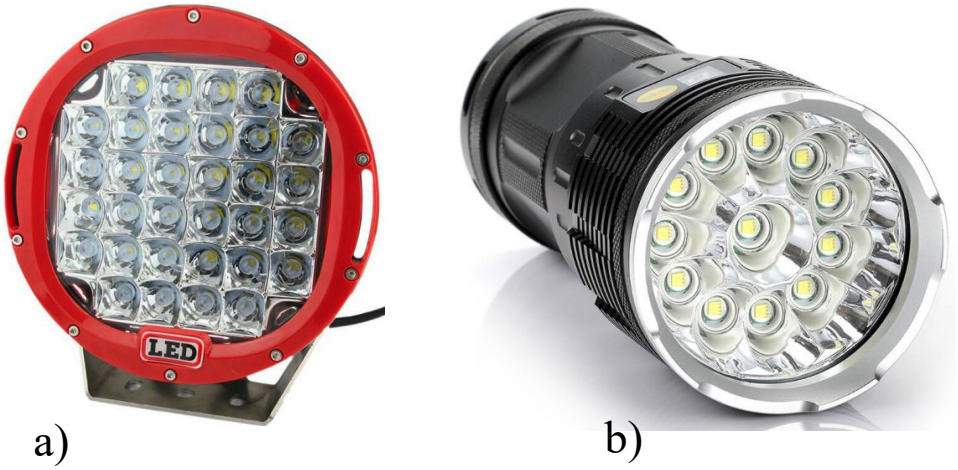


Figure 5-1. Example of modern powerful LED-based spotlight (a) and flashlight (b).

Consequently, integration of several LED units within a compact area or volume becomes severely constrained by thermal limitations. Junction temperature must remain below the critical limit: $T_j \leq T_{crit}$ to prevent luminous flux degradation, color shift, accelerated material aging and reduced lifetime (Arrhenius-type dependence). Current engineering practice often addresses the thermal constraint by distributing LEDs over extended surfaces and employing multi-lens or

reflector assemblies to recombine individual beams into a unified illumination field (Figure 5-1). While this approach mitigates local overheating, it introduces additional optical losses, reduces overall energy efficiency, and compromises beam uniformity. Thus, the thermal management problem directly influences not only the reliability and lifetime of LED devices but also the achievable optical architecture of the luminaire.

A representative and technologically demanding example of LED luminaires is surgical lighting systems. (Figure 5-2).

Figure 5-2. Example of typical modern LED-based lights for operating rooms.

In such applications, the lighting device must simultaneously satisfy stringent photometric and ergonomic requirements. It must provide high illuminance at the operating field to ensure precise visual discrimination of fine anatomical structures. The system must also allow adjustment of the correlated colour temperature in order to tailor the spectral characteristics of illumination to different medical procedures and clinical preferences. Accurate reproduction of tissue colours requires a high colour rendering index, while minimal shadow formation in the surgical zone demands careful spatial coordination of multiple light sources. The simultaneous fulfilment of these optical requirements typically necessitates the use of numerous LEDs operating at different spectral ranges and controlled independently. Although such configurations provide excellent photometric performance, they substantially increase the structural complexity and overall dimensions of the luminaire. In practice, modern surgical lighting systems are often bulky and mechanically elaborate, occupying considerable volume in operating rooms and presenting challenges in manoeuvrability and positioning [4]. A fundamental reason for this

design outcome lies in the thermal limitation that prevents optimal spatial clustering of high-power emitters within a compact focal region.

Two-phase heat transfer devices, such as heat pipes and loop heat pipes, are attractive candidates for addressing the high heat flux associated with LED applications due to their ability to utilize latent heat transport. However, classical heat pipes are typically constrained by geometric configuration and gravitational orientation, and their performance may deteriorate when the heat source is positioned above the condenser. Loop heat pipes enable greater flexibility in routing vapor and liquid transport lines, yet their integration into compact optical systems introduces mechanical and structural complexities, particularly with respect to evaporator positioning and condenser support.

Therefore, in the field of LED luminaire design, a technological gap remains for thermal management solutions that combine the heat transfer efficiency of two-phase heat loops with the structural simplicity and integration capability characteristic of conventional heat pipes. The development of such solutions is essential for enabling compact, high-intensity LED lighting systems with improved optical quality and reduced structural dimensions.

## 5.2 State-of-the-Art LED luminaire Two-Phase Cooling Methods

A wide range of thermal management technologies have been investigated for high-power LED applications. Among them, two-phase cooling solutions attract particular attention due to their capability to sustain high heat flux densities while operating in a fully passive mode. In contrast to active techniques such as spray cooling [49], two-phase devices rely on capillary and gravitational forces to drive the working fluid, thereby eliminating the need for pumps and external power consumption.

Extensive research has been conducted on the implementation of various two-phase technologies for LED cooling, including conventional heat pipes [50], [51], mini heat pipe arrays [52], thermosiphons [53], [54], vapor chambers [55], and loop heat pipes [56], [57], [58]. These devices exploit latent heat transport and therefore offer substantially higher effective thermal conductivity compared to purely conductive heat sinks.

Conventional heat pipes are widely adopted due to their structural simplicity, cylindrical geometry, and relative ease of integration. In many LED applications, especially where emitters are distributed over moderate areas, thin heat pipes can be directly embedded into the supporting structure or positioned beneath LED modules with minimal design modification. However, their performance is strongly dependent on the distance between evaporator and condenser and may degrade under adverse gravitational orientation.

Mini heat pipe arrays and vapor chambers extend this concept by providing quasi-two-dimensional heat spreading, which is advantageous when heat must be redistributed over larger surfaces before being rejected to ambient air. Thermosiphons, relying primarily on gravity-driven return flow, can achieve high heat transport capability but are inherently orientation-sensitive.

Loop heat pipes represent a more advanced class of capillary-driven two-phase systems. Due to the separation of vapor and liquid transport lines and the presence of a dedicated capillary evaporator, LHPs can sustain higher heat loads over longer distances and are less sensitive to gravitational effects compared to conventional HPs. For this reason, LHPs may significantly outperform heat pipes and thermosiphons in unfavourable configurations, such as when the heat source is located above the heat sink.

Nevertheless, the application of LHPs in LED luminaires reveals certain practical limitations. In scenarios where high-power LEDs must be densely packed to function as a quasi-point light source within a compact optical assembly [59], integration of a loop system becomes mechanically and geometrically challenging. While insertion of a cylindrical heat pipe beneath LED modules can often be achieved with minimal redesign, an LHP requires careful routing of vapor and liquid lines, secure positioning of the evaporator at the focal region, and appropriate support of the condenser structure. As a result, the integration complexity may offset some of the thermodynamic advantages of the loop architecture.

Similar trade-offs between integration simplicity and thermal performance are observed in other engineering fields. For instance, cylindrical heat pipes are favoured in solar thermal collectors [60] due to their geometry, yet their operation distance remains limited. In electric vehicle battery thermal management systems, both HPs and LHPs are actively investigated [61]. While heat pipes can meet industrial performance requirements, challenges related to size optimization, mass reduction, safety, and environmental compatibility of working fluids still constrain their widespread adoption.

It should also be noted that the majority of reported studies on LHP-based LED cooling are conducted under static conditions with fixed orientation of the heat source relative to the heat sink, particularly with respect to the gravitational field. This applies to laboratory-scale experiments on 40 mm × 50 mm LED modules [57], as well as to street lighting systems with power levels of 100 W–110 W [56], [57], [58]. However, real-world luminaires, especially surgical and mobile lighting systems, may operate under variable spatial orientations, where gravitational sensitivity becomes a critical factor.

Therefore, despite the demonstrated high thermal performance of existing two-phase solutions, a fundamental trade-off persists between thermal transport capability, geometric flexibility, integration simplicity, and orientation independence. This trade-off defines the current state of the art and highlights the need for thermal management concepts that combine the compact integration advantages of conventional heat pipes with the long-distance and high-load capability of loop-based systems

## 5.3 Development of an LED Luminaire with a Cooling Loop Based on the HLP Architecture

The HLP architecture described in Section 2.2 was successfully implemented for thermal management of a high-intensity LED luminaire. The combination of geometric configuration and enhanced heat transport capability of the HLP enabled the development of a compact lighting device with a localized high-power light source.

The general arrangement of the HLP-based luminaire is presented in Figure 5-3. Owing to its cylindrical geometry, the HLP performs not only heat transport functions but also serves as a structural backbone of the luminaire. This dual functionality simplifies mechanical integration and reduces overall system mass.

A concentrated light source was achieved by mounting eighteen high-power LEDs directly onto the evaporator housing (3). The corresponding assembly is shown in Figure 5-4. The LED cluster is positioned at the focal point of a parabolic reflector (2), ensuring the formation of a quasi-parallel luminous flux. The cylindrical HLP arrangement does not obstruct or distort the optical path and provides improved spatial control of the emitted beam.

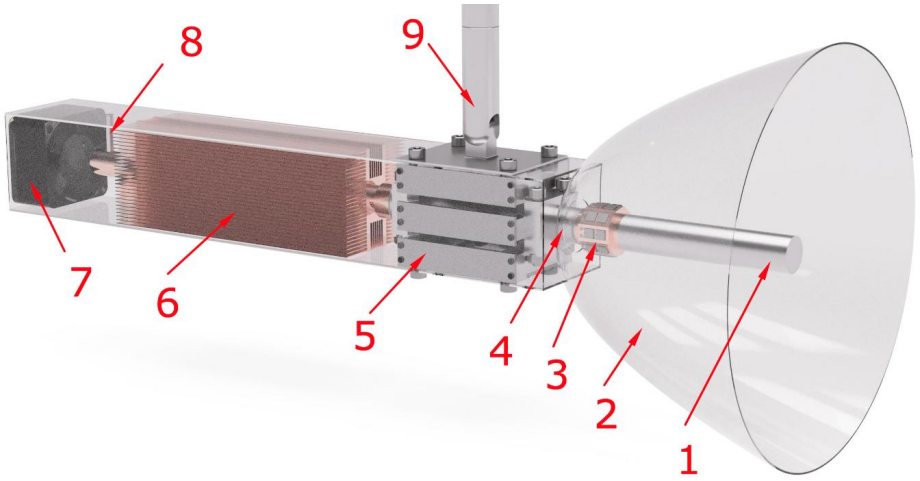


Figure 5-3. LED luminaire with HLP-based cooling system. 1 – compensation chamber; 2 – parabolic reflector; 3 – evaporator with mounted LEDs; 4 – transport (adiabatic) zone; 5 – control electronics; 6 – condenser; 7 – fan; 8 – charging port.

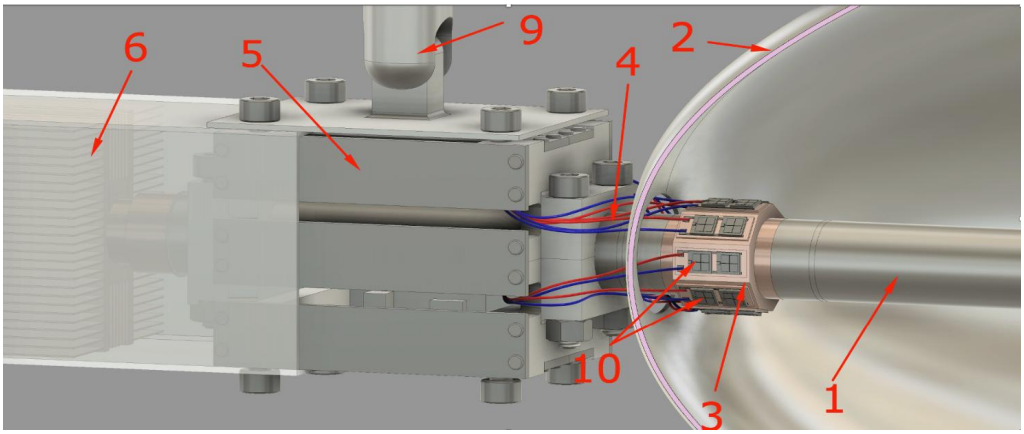


Figure 5-4. Light source composed of 18 LEDs (10) mounted on the evaporator housing (3) and positioned at the focal point of the parabolic reflector (2).

The compensation chamber (1) is located along the reflector axis. Experimental observations confirmed that its presence does not introduce noticeable disturbance to the light flux distribution.

The LED driver electronics (5) can be integrated along the adiabatic section (4) of the HLP, where vapor and liquid transport channels are concentrically arranged. In the present prototype, however, the driver was placed in a separate high-level control unit.

Heat dissipation to the ambient environment is accomplished via forced convection provided by a fan (7) with a maximum volumetric flow rate of 0.268 $m^3$/min. The fins of the air heat exchanger (6) are soldered to the condenser housing, ensuring low thermal resistance between the condenser wall and the external airflow. The overall length of the HLP is 350 mm, with a housing tube diameter of 15 mm. The shortest evaporator-to-condenser distance exceeds 100 mm. The luminaire prototype, including LEDs and reflector but excluding the driver electronics, has a total mass slightly below 1.2 kg. The HLP was charged with 20 g of n-butane as the working fluid.

A 40 $\mu m$ copper mesh was employed as the secondary wick and as the liquid retention structure within the condenser. In the evaporator, the secondary wick was wound around the bayonet and hydraulically connected the core of the primary wick to the compensation chamber. In the condenser section, the mesh was wound around the liquid return line, forming a capillary structure designed to collect condensate near the inlet of the liquid channel. This arrangement promotes stable liquid supply to the evaporator under varying operating conditions. The internal components of the HLP are presented in Figure 5-5.

The upper part of the figure shows the luminaire elements prior to assembly, including the HLP with LEDs (1 – compensation chamber; 3 – evaporator; 4 – transport/adiabatic zone with concentric vapor and liquid channels; 6 – air heat exchanger; 8 – charging port), the condenser envelope and air duct (11), and the fan (7).

The middle section illustrates the primary and secondary wicks together with the evaporator assembly. The lower section presents the internal structure of the condenser, including the rolled copper mesh acting as a capillary liquid collector.

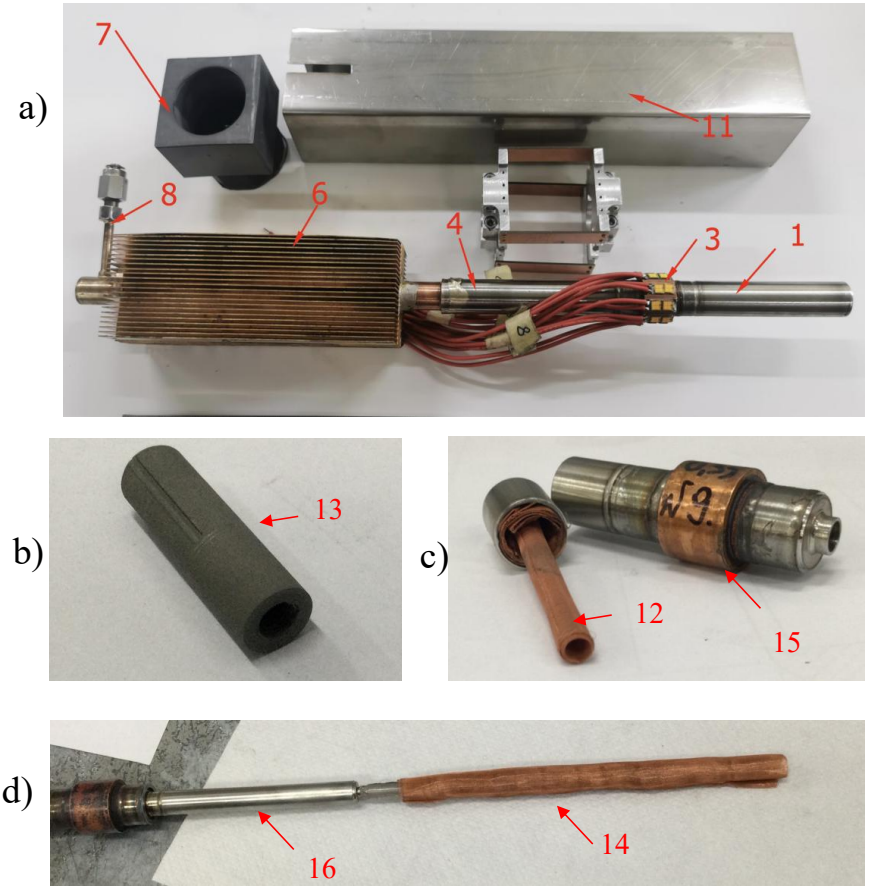


Figure 5-5. (a) Structural elements of the luminaire prior to assembly. (b–d) Structural components of the HLP prior to assembly. 13 – primary evaporator wick; 12 – secondary evaporator wick; 15 – assembled evaporator; 14 – condenser capillary structure;16 – liquid return line within the vacuum envelope.

A ceiling lighting system composed of three independently positionable HLP-based luminaires is shown in Figure 5-6. Autonomous orientation of each module allows flexible

formation of a luminous spot with predefined geometry, demonstrating scalability of the proposed architecture.

The implemented configuration demonstrates that the cylindrical HLP architecture enables simultaneous realization of several typically conflicting requirements: high heat transport capability, compact focal light source formation, and mechanical integration within an optically symmetric system.

In conventional loop heat pipe systems, separation of vapor and liquid lines ensures high capillary performance and operational stability but complicates mechanical integration in axisymmetric optical assemblies. In contrast, classical cylindrical heat pipes are structurally convenient for placement along the optical axis, yet their heat transport distance and capillary performance are inherently limited.

Figure 5-6. Ceiling lighting system composed of three HLP-based LED luminaires with independent positioning.

Table 5-1

HLP specification

| HLP element | Parameter | Value |
|---|---|---|
| Tubular Housing | Length | 350 mm |
| | Inner Diameter | 14 mm |
| | Outer Diameter | 15 mm |
| Primary wick made of 316l SS powder by sintering in vacuum | Porosity, $\varphi$ | 0.47 |
| | Permeability, $K$ | $1.5 \cdot 10^{-13}$ m$^2$ |
| | Thermal conductivity, $k_w$ | 6 $\frac{\mathrm{W}}{\mathrm{m \cdot K}}$ |
| | Effective pore size | ~1 µm |
| | Length, $L_w$ | 30 mm |
| | Inner Diameter, $D_{in}$ | 5.5 mm |
| | Outer Diameter, $D_{out}$ | 14 mm |
| Condenser | Length | 160 mm |
| | Fins [Thickness × Height × Number] | 0.5 mm×12.5mm×40 |
| | Fan type | AFB0412HB-8C1R |
| | Fan dimensions | 40×40 mm |
| | Fan max. air flow | 0.268 m$^3$/min |
| Transport Zone | Length | 90 mm |
| | Liquid Line Inner Diameter | 2.5 mm |
| | Liquid Line Outer Diameter | 6 mm |
| | Vacuum gap | 1.5 mm |
| | Vapor Line Inner Diameter | 9 mm |
| | Vapor Line Outer Diameter | 14 mm |
| Compensation Chamber | Length | 70 mm |
| | Inner Diameter | 14 mm |
| | Outer Diameter | 15 mm |

The adopted HLP configuration combines concentric vapor–liquid transport channels within a single cylindrical envelope. Such geometry preserves the axial symmetry required for reflector-based optical systems while maintaining capillary-driven operation characteristic of loop architectures. As a result, the thermal management system becomes an integral structural element of the luminaire rather than an externally attached subsystem. This integration eliminates the need for additional routing of transport lines or dedicated support structures and enables high-

power LED clustering at the reflector focus without compromising optical alignment or gravitational robustness.

## 5.4 Experimental Investigation of LED Luminaire Cooling

The luminaire was experimentally tested under various orientations with respect to the gravitational field and at different input power levels. Electrical power was supplied to the LED module in stepwise increments from 10 W up to 80 W. The location of thermocouples is shown in Figure 5-7. The colour coding of the thermocouples corresponds to the colour of the respective temperature curves presented in the measurement graphs.

To minimize the influence of ambient conditions, the compensation chamber and the transport (adiabatic) zone were covered with a layer of thermal insulation.

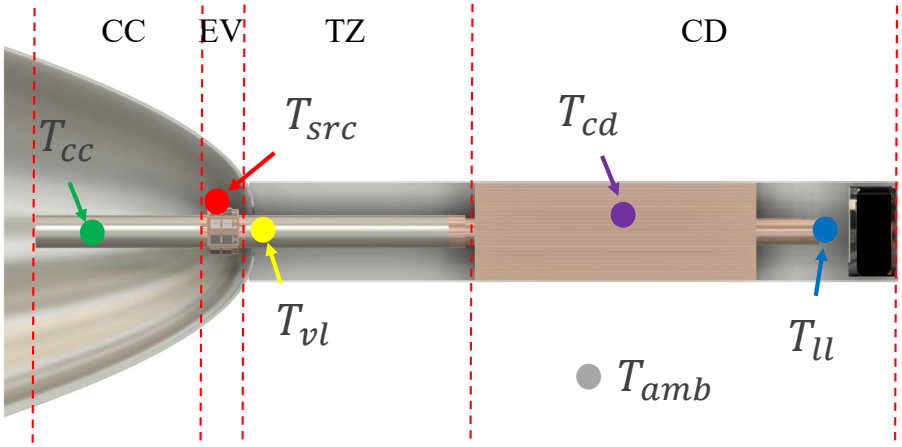


Figure 5-7. Location of thermocouples on the HLP-based luminaire: $T_{src}$ – LED ($T_{LED}$), $T_{vl}$ – vapor line, $T_{cd}$– condenser, $T_{amb}$– ambient, $T_{ll}$ – liquid line, $T_{cc}$ – compensation chamber.

The thermocouple signals were acquired using an ADAM-4018 data acquisition module and recorded via a LabVIEW-based program. The same software controlled the power supply unit, ensuring precise adjustment of the applied LED power. The luminaire was mounted on a tripod allowing rotation about the horizontal axis over a range of 180°. Photographs of the luminaire oriented at different angles relative to the vertical axis during the experimental campaign are presented in Figure 5-8.

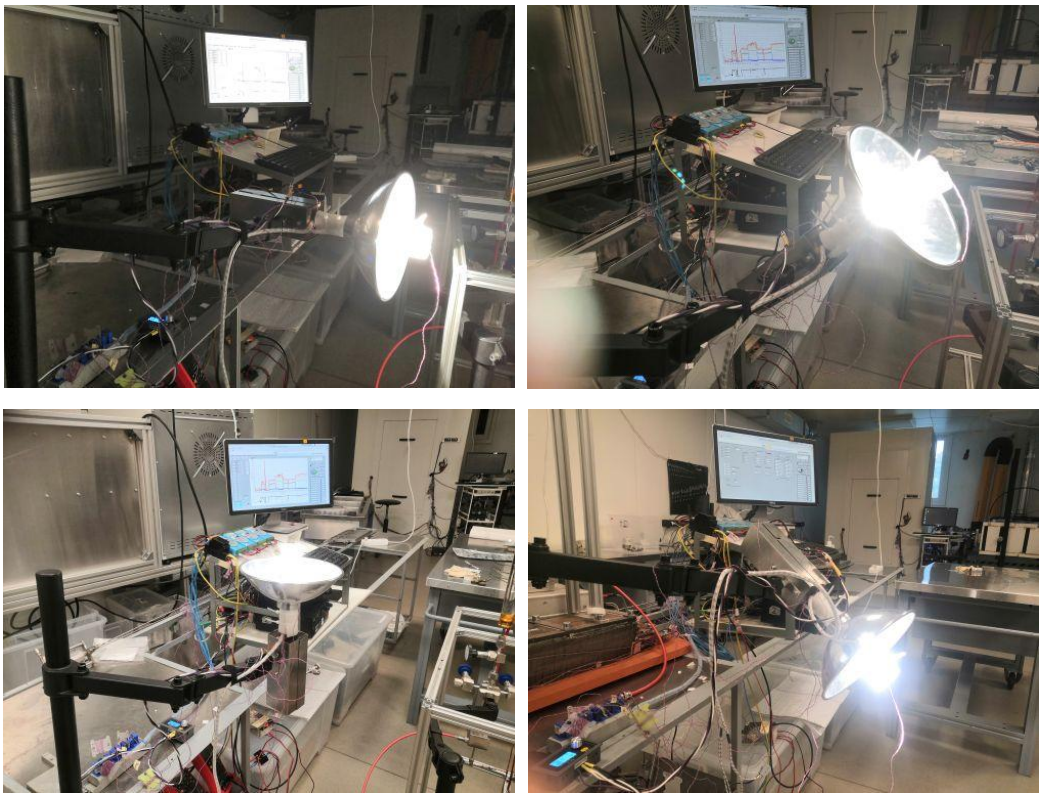

Figure 5-8. Experimental setup for LED luminaire testing under different gravitational orientations.

The measured transient temperature profiles for the HLP operating in vertical orientation with the evaporator located above the condenser (gravity-unfavourable configuration) during power ramping tests are presented in Figure 5-9.

Orientation sensitivity was investigated by varying the HLP inclination angle in 45° increments from −90° (evaporator below condenser, gravity-favourable) to +90° (evaporator above condenser, gravity-unfavourable) and back to −90°. The temperature measurement points and representative temperature profiles at 60 W LED power are shown in Figure 5-10.

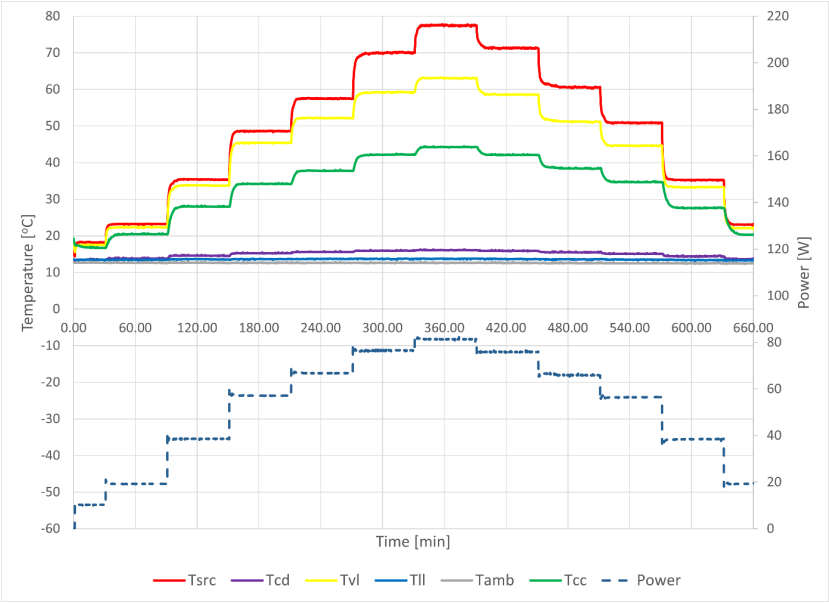


Figure 5-9. Temperature evolution of HLP components during stepwise increase and decrease of LED power. Vertical orientation (+90°, evaporator above condenser).

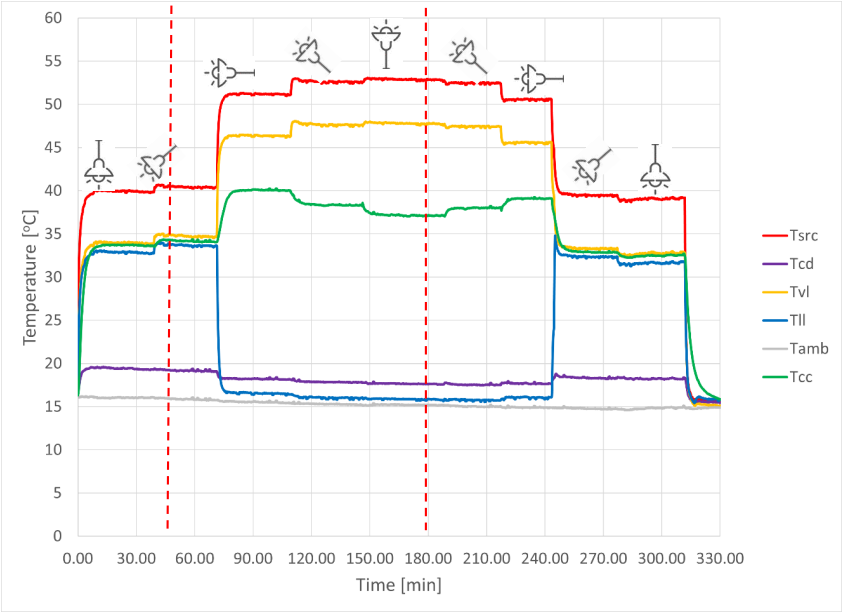


Figure 5-10. Temperature measurement locations and temperature profiles at various HLP orientations (LED power 60 W).

## 5.5 Results and Discussion

For a consistent interpretation of the experimental results, it is first necessary to establish how the measured temperatures correspond to the characteristic temperatures used in the LHP model, namely: the vapor temperature in the evaporation zone, the liquid temperature at the evaporator inlet, and the compensation chamber temperature. This mapping is particularly important in the orientation tests, as the HLP demonstrates substantially different temperature distributions depending on its spatial position (see Figure 5-10).

Since the HLP was tested as a cooling system integrated into a specific application — an LED luminaire — the maximum transferable power was limited not by intrinsic HLP constraints (e.g., the capillary limit), but by the maximum allowable LED temperature (80 °C). The experimentally observed overall thermal resistance can therefore be represented as the sum of three contributions:

$$R = R_{LED} + R_{HLP} + R_{sink} \tag{5.1.}$$

where $R_{LED}$ is the LED–evaporator contact resistance, $R_{HLP}$ is the effective thermal resistance of the HLP between evaporation and liquid return, and $R_{sink}$ is determined by the air heat exchanger geometry and fan performance. The vapor temperature measured at the evaporator outlet (yellow thermocouple) is taken as representative of the evaporation zone temperature. The heat source temperature is measured at the LED module, $T_{src} \equiv T_{LED}$. The interface resistance is then:

$$R_{LED} = \frac{T_{src} - T_{vl}}{\dot{Q}} \tag{5.2.}$$

The liquid return line is located inside the vapor channel and cannot be measured directly. However, in several orientations, the liquid temperature can be inferred from the blue thermocouple positioned at the condenser end near the liquid return entrance. When the condenser is below or at the same level as the evaporator (positions 3–7 in Figure 5-10), subcooled liquid accumulates at the condenser outlet. In these configurations, the blue thermocouple measures the subcooled liquid temperature $T_{ll}$ In gravity-unfavourable configurations (positions 1–2 and 8–9), the phase state at the condenser end is not obvious. Therefore, the interpretation of the blue thermocouple as $T_{ll}$ requires theoretical justification. Case 5 is selected as a reference case with unambiguous liquid accumulation, while Case 2 represents an orientation where interpretation is uncertain. The measured data are summarized in Table 5-2.

Table 5-2

TC readings are used for estimating the temperature of subcooled liquid

| Case | Time[min] | $\boldsymbol{T_{vl}}$[°C] | $\boldsymbol{T_{cc}}$[°C] | $\boldsymbol{T_{ll}}$[°C] |
|---|---|---|---|---|
| 5 | 180 | 47.75 | 37.16 | 15.90 |
| 2 | 60 | 34.68 | 34.11 | ? (33.62) |

Under steady-state conditions, assuming negligible ambient heat exchange of the compensation chamber and evaporator, the energy balance reduces to

$$\dot{Q}_{hl} = \dot{Q}_{sc} \tag{5.3.}$$

$$\dot{Q}_{in} = h_{ev} \cdot \dot{m} + \dot{Q}_{hl} \tag{5.4.}$$

Expressing the mass flow rate $\dot{m}$ from (5.4) and substituting it into (3.32), taking (5.3) into account, the liquid return temperature $T_{ll}$ can be written as:

$$T_{ll} = T_{ev} - \frac{h_{ev}}{c_{pl} \cdot (\frac{\dot{Q}_{in}}{\dot{Q}_{hl}} - 1)} \tag{5.5.}$$

To estimate the heat leak $\dot{Q}_{hl}$, the effective thermal conductivity of the wetted wick must be evaluated. Taking the thermal conductivity of liquid butane as $\lambda_l \approx 0.1$ W/(m·K) and that of stainless steel as $\lambda_m \approx 14$ W/(m·K), and considering the wick porosity $\varphi = 0.47$, it follows from (3.35) that the effective thermal conductivity of the wet wick, $\lambda_w$, depends only weakly on $\lambda_l$ and can be approximated as $6\ \mathrm{W/(m \cdot K)}$. Thus, $\lambda_w$ may be treated as a constant for the present estimate. Knowing $\lambda_w$, the heat leak $\dot{Q}_{hl}$ can be evaluated using (3.34). Furthermore, the approximation

$$T_{ev} \approx T_{vl} \tag{5.6.}$$

is adopted, since the vapor temperature is measured immediately at the evaporator outlet and superheating is initially neglected in this first-order estimate.

Using the numerical values:

$\dot{Q}_{in} \approx \frac{2}{3} \cdot 60\ \mathrm{W} = 40\ \mathrm{W}$ $\lambda_w = 6\ \frac{\mathrm{W}}{\mathrm{m \cdot K}}$ $L_w = 0.03\ \mathrm{m}$ $D_{out} = 14\ \mathrm{mm}$ $D_{in} = 5.5\ \mathrm{mm}$
$c_{p,l} = 2491\ \mathrm{J/(kg \cdot K)}$ $h_{ev} = 351300\ \mathrm{(J/kg)}$ $T_{vl} = 34.68℃$ $T_{cc} = 34.11\ ℃$

the estimate for Case 2 yields $T_{ll,2} \approx 28.83$ °C. For comparison, the experimentally measured temperature at the blue thermocouple location is 33.62 °C. The discrepancy between the first-order estimate and the measured liquid temperature indicates that the assumptions used in the simplified evaluation of $\dot{Q}_{hl}$ require refinement.

Eq. (3.34) accounts only for radial heat leakage through the wick and does not include other possible heat-leak channels inherent to the HLP architecture and the thermal input power was estimated as $\dot{Q}_{in} \approx \frac{2}{3} P_{LED}$, which is itself an approximation reflecting the conversion efficiency of LEDs.

In Section 3.4, the heat-leak model was progressively generalized: starting from a simplified geometrical conduction model and moving towards a lumped representation in which the total heat leak is expressed through an effective thermal resistance $R_{HL}$ (see (3.39)). In the present configuration, rather than relying on the specific radial conduction form of (3.34), it is more consistent to relax the model and retain only the physically justified proportionality between the heat leak and the temperature difference driving it.

For the HLP geometry considered here, the dominant driving temperature difference is that between the evaporation zone and the compensation chamber. Therefore, the heat leak can be represented in a generalized form as

$$\dot{Q}_{hl} = B \cdot (T_{ev} - T_{cc}) \tag{5.7.}$$

where $B$ is an effective proportionality coefficient.

This representation is fully consistent with the lumped heat-leak approach introduced in Section 3.4, where the heat leak is written through an unknown thermal resistance $R_{HL}$. In the present formulation, this "unknown" is implicitly contained in the parameter $B$. The HLP design suggests that the appropriate reference temperature on the cold side of the leak is the compensation chamber temperature $T_{cc}$. Combining (5.7) with the steady-state condition (5.3) and with (3.32) yields:

$$c_{p,l} \cdot \dot{m} \cdot (T_{vl} - T_{ll}) = B \cdot (T_{vl} - T_{cc}) \tag{5.8.}$$

Writing (5.8) for Case 2 and Case 5 and dividing one by the other eliminates $B$:

$$\frac{c_{p,l,2}\dot{m}_2(T_{vl,2} - T_{ll,2})}{c_{p,l,5}\dot{m}_5(T_{vl,5} - T_{ll,5})} = \frac{T_{vl,2} - T_{cc,2}}{T_{vl,5} - T_{cc,5}} \tag{5.9.}$$

Since the experiment was performed at constant $\dot{Q}_{in}$, (5.4) can be written for both cases and equated:

$$\dot{m}_2 \cdot \left(h_{ev,2} + c_{pl,2}\left(T_{vl,2} - T_{ll,2}\right)\right) = \dot{m}_5 \cdot \left(h_{ev,5} + c_{pl,5}\left(T_{vl,5} - T_{ll,5}\right)\right) \tag{5.10.}$$

which yields

$$\frac{\dot{m}_2}{\dot{m}_5} = \frac{h_{ev,5} + c_{pl,5}\left(T_{vl,5} - T_{ll,5}\right)}{h_{ev,2} + c_{pl,2}\left(T_{vl,2} - T_{ll,2}\right)} \tag{5.11.}$$

Substituting (5.11) into (5.9) produces an algebraically solvable equation for $T_{ll,2}$:

$$T_{ll,2} = T_{vl,2} - \frac{c_{p,l,5}}{c_{p,l,2}} \cdot \frac{F \cdot h_{ev,2}}{1 - F \cdot c_{p,5}} \tag{5.12.}$$

where:

$$F = \frac{T_{vl,2} - T_{cc,2}}{T_{vl,5} - T_{cc,5}} \cdot \frac{T_{vl,5} - T_{ll,5}}{h_{ev,5} + c_{p,l,5}(T_{vl,5} - T_{ll,5})} \tag{5.13.}$$

Substituting thermophysical properties at the corresponding temperatures yields $T_{ll} \approx 33.22℃$

which is consistent with the measured value (33.62 ℃) confirming that the blue thermocouple indeed represents the subcooled liquid temperature for all orientations. Consequently,

$$R_{HLP} = \frac{T_{vl} - T_{ll}}{\dot{Q}} \tag{5.14.}$$

$$R_{sink} = \frac{T_{ll} - T_{amb}}{\dot{Q}} \tag{5.15.}$$

Figure 5-11 shows a pronounced increase in $R_{HLP}$ from approximately 0.03 K/W to approximately 0.8 K/W when the evaporator is positioned above the condenser.

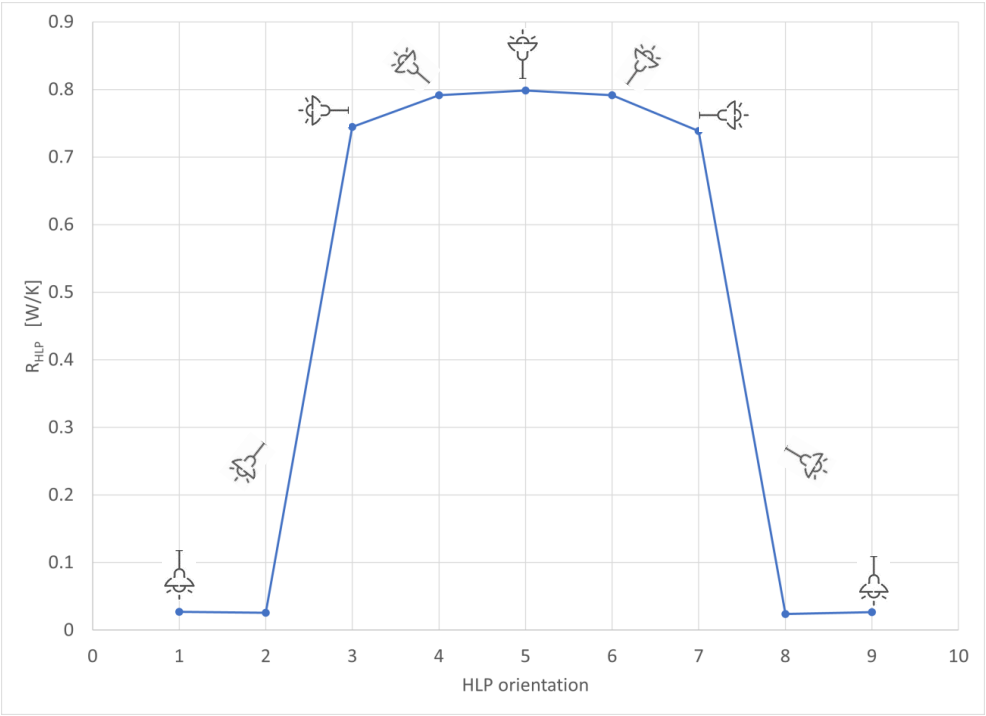


Figure 5-11. HLP thermal resistance on HLP orientation in gravity field

Since the input power was constant, the resistance increase directly reflects an increase in the temperature difference $T_{vl} - T_{ll}$, accompanied by an increase in $T_{vl} - T_{cc}$. This indicates a redistribution of internal heat leak and subcooling balance within the loop.

A (P–T) representation of the HLP cycle (Figure 5-12) allows further interpretation.

The temperature difference between the evaporation zone and the compensation chamber can be estimated from the corresponding pressure drop $\Delta P_{1,7}$ in the (P–T) diagram. Under steady-state conditions limited by the capillary pressure of the wick, the allowable total pressure drop in the loop is bounded by the capillary limit. For the present HLP, the capillary pressure is estimated as $\Delta P_{cap} \approx 200$ mbar. This value represents an upper bound for the total pressure drop across the loop:

$$\Delta P_{1,8} \leq \Delta P_{cap} \tag{5.16.}$$

Accordingly, the pressure drop between the compensation chamber and the evaporation zone is limited by

$$\Delta P_{1,7} \leq \Delta P_{cap} - \Delta P_{7,8} \tag{5.17.}$$

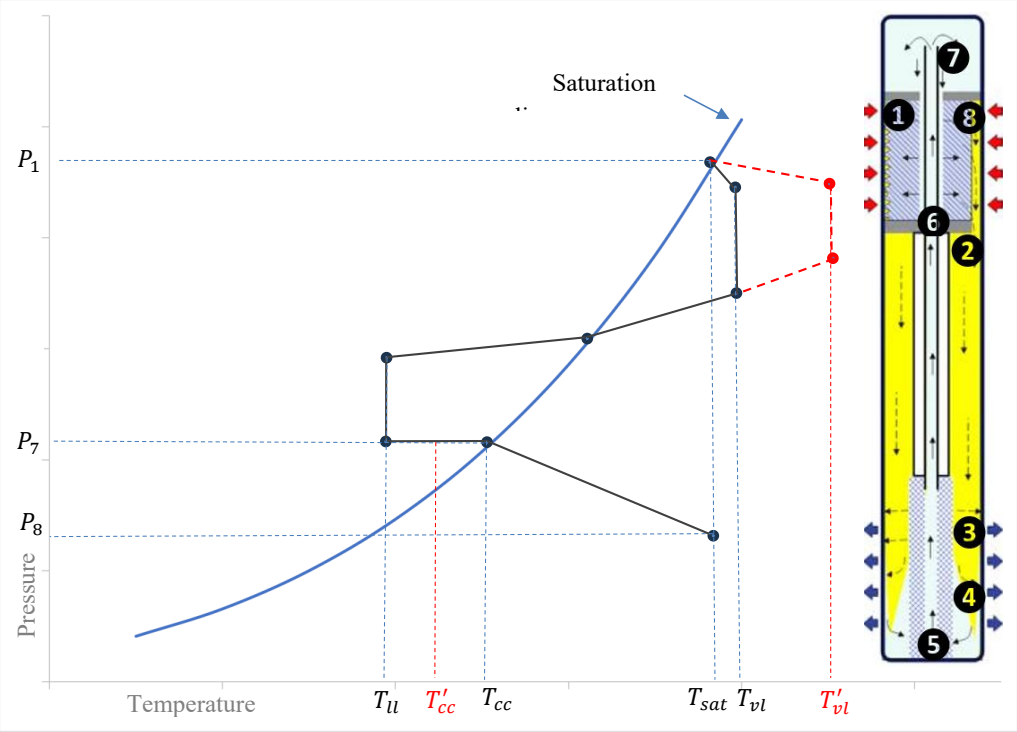


Figure 5-12. P-T diagram of HLP operation cycle

The term $\Delta P_{7,8}$, corresponding to the pressure drop associated with fluid flow through the wick, can be estimated using (3.67). This yields $\Delta P_{7,8} \leq 6$ mbar, which is negligible compared to $\Delta P_{cap}$. Substituting $\Delta P_{1,7} = 200$ mbar into the linearized saturation relation

$$\Delta P_{1,7} \approx \frac{dP}{dT} \Delta T_{1,7} \tag{5.18.}$$

gives the estimate

$$\Delta T_{1,7} \leq 2°\text{C} \tag{5.19.}$$

However, in several orientations, the experimentally observed difference $T_{vl} - T_{cc}$ exceeds this bound by almost a factor of five (e.g., 10.6 °C in Case 5). This inconsistency indicates that the system does not operate under purely saturated conditions.

Two explanations are possible:

- Significant vapor superheating at the evaporator outlet,
- The compensation chamber thermocouple does not represent the bulk saturation temperature.

The second explanation appears unlikely due to the relatively small size of the compensation chamber and the absence of evidence for strong internal temperature stratification. A more physically plausible explanation is vapor superheating associated with displacement of the active evaporation interface deeper into the wick structure under gravity-unfavourable orientation. Vapor superheating as a factor influencing increased thermal resistance of LHP systems has also been reported by other researchers [62].

The observed resistance jump and the simultaneous increase of $T_{vl} - T_{ll}$ are consistent with operation approaching incipient dry-out in the evaporator wick. In this regime, the vaporization zone recedes inside the porous structure, reducing the effective capillary pumping margin and increasing the degree of vapor superheating required for mass transport into the vapor line.

In this case, vapor superheating can no longer be neglected in the evaporator energy balance. Equation (5.4) must therefore be rewritten as:

$$\dot{Q}_{in} = h_{ev} \cdot \dot{m} + c_{p,v} \cdot \dot{m} \cdot (T_{vl} - T_{sat}) + \dot{Q}_{hl} \tag{5.20.}$$

This modification does not invalidate the previous inverse-estimation procedure for determining $T_{ll}$, but it alters the energy balance used to relate Cases 2 and 5. Equation (5.10) then becomes:

$$\begin{aligned} \dot{m}_2 \left(h_{ev,5} + c_{pl,5}\left(T_{vl,5} - T_{ll,5}\right)\right) = \\ = \dot{m}_5 \left(h_{ev,5} + c_{pv,5}\left(T_{vl,5} - T_{sat,5}\right) + c_{pl,5}\left(T_{vl,5} - T_{ll,5}\right)\right) \end{aligned} \tag{5.21.}$$

Accordingly, the parameter $F$ in (5.12) is modified to:

$$F = \frac{T_{vl,2} - T_{cc,2}}{T_{vl,5} - T_{cc,5}} \cdot \frac{T_{vl,5} - T_{ll,5}}{h_{ev,5} + c_{pv,5}\left(T_{vl,5} - T_{sat,5}\right) + c_{pl,5}\left(T_{vl,5} - T_{ll,5}\right)} \tag{5.22.}$$

(5.22)

Assuming $T_{ev,5} \approx T_{cc,5} + 2\,°\text{C} = 39.16\,°\text{C}$, a revised estimate for Case 2 yields $T_{ll,2} \approx 33.33\,°\text{C}$.

This value differs only slightly from the previous estimate (33.22 °C) and remains close to the experimentally measured temperature (33.62°C), confirming consistency of the indirect estimation procedure.

The analysis would be incomplete without evaluating the direct influence of gravity on fluid circulation in the HLP. The gravitational head $\Delta P_g$ contributes to the total loop pressure drop $\Delta P_{1,8}$ with a positive sign when the evaporator is above the condenser and a negative sign in the opposite configuration. According to (3.42), $\Delta P_g$ contains both liquid-line and vapor-line components, corresponding to segments 5–6 and 2–3 in the (P–T) diagram, respectively.

For the considered temperature range, working fluid (butane), and characteristic loop length $L \sim 0.2$ m, the maximum gravity-induced pressure deviation is on the order of 20–30 mbar, corresponding to a temperature difference of approximately 0.3 °C. Therefore, the direct effect of gravity on circulation can be considered negligible compared to the observed temperature deviations.

In complex systems such as the HLP, abnormal behaviour rarely arises from a single mechanism but rather from a combination of interacting effects. Possible contributing phenomena include local boiling within the wick structure and formation of transient vapor blockages [63]. Nevertheless, power ramping tests demonstrated stable operation without significant hysteresis. The HLP started reliably in all orientations at 10 W input power and was capable of transferring and dissipating more than 80 W while maintaining LED temperature below the specified limit of 80°C, even in the gravity-unfavourable orientation where partial wick dry-out was likely present.

## 5.6 Conclusions for Chapter 5

The present work confirmed the viability of the new loop heat pipe architecture, referred to as the Heat Loop Pipe, and demonstrated its applicability as a cooling system for a high-power LED luminaire. The cylindrical geometry of the HLP enables placement of a concentrated light source at the focal point of a parabolic reflector without significantly disturbing the spatial distribution of the luminous flux. In this configuration, the thermal management system becomes structurally integrated into the optical axis of the luminaire.

The coaxial arrangement of vapor and liquid transport lines provides mechanical robustness and compactness comparable to a conventional heat pipe, while simultaneously incorporating essential elements of a loop heat pipe — separated transport paths and a localized capillary pumping structure. Vacuum insulation enables stable operation of this coaxial configuration by minimizing parasitic heat exchange between the transport lines.

The HLP demonstrated stable operation in various orientations relative to the gravitational field, transferring up to 60 W of thermal power (corresponding to approximately 90 W of LED electrical input power) while maintaining LED temperature within specified limits.

A drawback of the current HLP configuration is the significant increase in thermal resistance under gravity-unfavourable operation (evaporator above condenser). The performed analysis indicates that this behaviour is most likely associated with vapor superheating within the vapor channels of the primary wick. Such superheating can arise from redistribution of the working fluid inside the HLP, leading to displacement of the boiling front deeper into the porous structure. This mechanism does not represent a fundamental limitation of the concept but rather a design-sensitive regime that may be mitigated through further geometric and hydraulic optimization of the wick and transport channels.

The study also highlights that heat and mass transfer processes in loop heat pipe systems can be more complex than the simplified classical representation of purely phase-change-driven heat transport. Conventionally, it is assumed that heat transfer in LHPs is governed exclusively by the liquid–vapor–liquid phase transition cycle. However, an additional heat-transfer mechanism may become significant — namely, sensible heat transport associated with vapor superheating.

In optimal operating regimes, the vapor generated at the evaporation interface remains close to saturation conditions, and superheating in the vapor channels is negligible. In such cases, the vapor temperature at the evaporator outlet is commonly assumed to coincide with the saturation temperature. However, under certain conditions — such as reduced heat load or displacement of the evaporation interface into the depth of the wick — the vapor may experience substantial superheating while flowing through the porous channels. This sensible heat contribution can meaningfully influence the thermal resistance and overall performance of the heat transfer device and should therefore be considered in advanced modelling and design of HLP/LHP systems.

# 6 FUEL CELL STACK THERMAL MANAGEMENT

## 6.1 Problem Relevance

Fuel cells (FCs) are electrochemical energy conversion devices that directly transform the chemical energy of a fuel into electrical energy and heat, bypassing conventional combustion processes. Owing to this direct conversion mechanism, FCs offer high conversion efficiency, low pollutant emissions, and broad applicability ranging from transportation systems to stationary and distributed power generation [64].

Several fuel cell technologies exist, differing in operating temperature, electrolyte type, and fuel compatibility. Among them, proton exchange membrane fuel cells (PEMFCs) have achieved the widest industrial adoption due to their relatively low operating temperature, rapid start-up capability, high power density, and overall system versatility. In PEMFCs, hydrogen is used as fuel and oxygen (typically from ambient air) as oxidant, while water is the primary reaction product. At the cell level, no $CO_2$ is emitted, which makes PEMFCs particularly attractive for hydrogen-based energy storage and conversion systems in transportation, industry, and distributed energy supply, where decarbonization requirements are increasingly stringent.

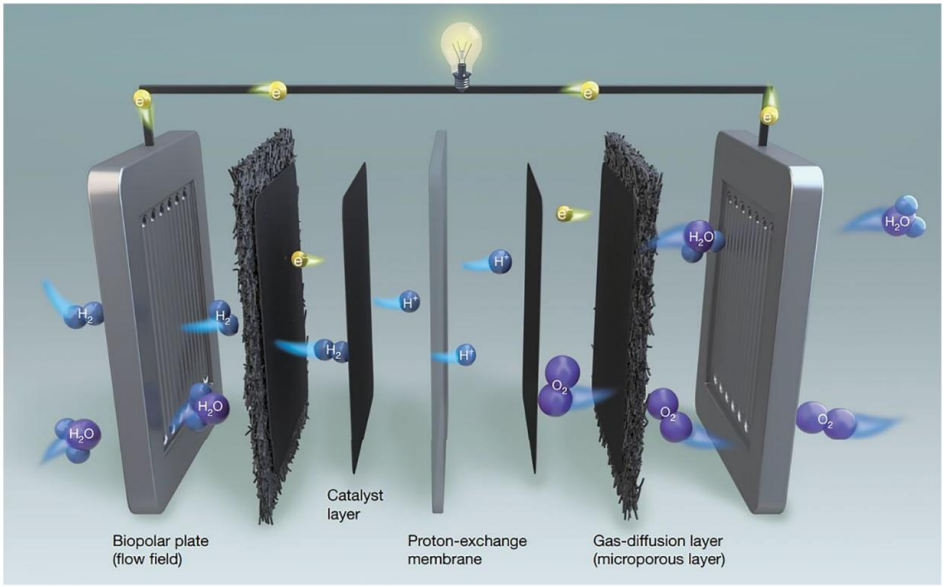


Figure 6-1. PEMFC conceptual design. Figure is taken from [66]

Figure 6-1 illustrates the typical structure and operating principle of a PEMFC. A conventional cell consists of multiple functional layers assembled into a compact multilayer architecture. Bipolar plates (BPs), located at the outer sides of the cell, perform several simultaneous functions: distribution of hydrogen and oxidant gases, current collection, mechanical support, and partial heat removal.

The electrochemically active region comprises the anode and cathode catalyst layers (CL), typically based on platinum-group catalysts. In the anode catalyst layer, hydrogen molecules dissociate into protons and electrons. The protons migrate through the proton exchange membrane, while electrons are forced to pass through the external circuit, generating electrical power. At the cathode, oxygen is reduced and reacts with protons to form water. Gas diffusion layers (GDLs), usually composed of porous carbon-based materials, ensure uniform reactant distribution and facilitate water management.

The proton exchange membrane acts as a selective ionic conductor, transporting protons while preventing gas crossover and electron conduction. Since the voltage of a single cell under load is typically in the range of 0.6–0.7 V, practical systems consist of multiple cells electrically connected in series to form a stack. Consequently, stack-level integration imposes strict requirements on layer thickness, mechanical tolerances, electrical isolation, and thermal uniformity.

Despite their high electrochemical efficiency, fuel cells convert a substantial fraction of the input chemical energy into heat. For PEMFCs operating under practical load conditions, approximately 50 % of the fuel's lower heating value is released as thermal energy [3]. This heat must be continuously removed to maintain the cell temperature within the permissible operating window.

PEMFC performance and durability are strongly temperature-dependent. For low-temperature PEMFCs (LT-PEMFCs), the recommended operating range is typically 60–80 °C, whereas high-temperature PEMFCs (HT-PEMFCs) operate in the range of approximately 120–200 °C. Deviation from the prescribed temperature interval leads to reduced membrane conductivity, increased ohmic losses, accelerated catalyst degradation, membrane dehydration or flooding, and ultimately reduced lifetime.

Thermal management in PEMFC systems is therefore not merely an auxiliary subsystem but a critical enabling function that directly affects efficiency, electrochemical stability, and long-term durability. The problem is fundamentally non-trivial for several fuel-cell-specific reasons:

- heat generation is volumetric and arises from multiple coupled mechanisms, including reaction enthalpy release, activation overpotentials, ohmic losses in the membrane and electrodes, and mass-transport limitations,
- the active layers are highly compact and mechanically integrated, which limits geometric freedom for heat exchanger integration,
- the thermal management system must remain electrically benign, avoiding leakage currents, parasitic resistances, or electrochemical interference,

- solutions developed at the single-cell level must remain scalable and compatible with stack-level integration, where cumulative thermal gradients can become critical.

At the same time, the substantial heat release of PEMFCs may be regarded as a beneficial feature in combined heat and power (CHP) applications. In such systems, both electrical and thermal outputs can be utilized, potentially increasing overall system efficiency. In this context, the central question is not the presence of heat, but rather the effectiveness of its collection, transport, and controlled utilization without compromising electrochemical performance.

## 6.2 State-of-the-Art Fuel Cell Cooling Methods

A notable characteristic of the PEMFC thermal-management literature is the absence of a unified and universally accepted classification of cooling technologies. Different review papers adopt different taxonomies, reflecting both the diversity of technical approaches and the hybrid nature of practical implementations. For example, 2021 review [65] grouped solutions into air cooling, heat spreaders, liquid cooling, and phase-change cooling. A 2022 review [66] proposed a different partition—air cooling, liquid cooling, passive cooling, and phase-change cooling—while emphasizing evaporative and spray-based approaches for automotive stacks, where attention shifts from cell-level heat extraction toward enhanced radiator-side heat rejection. In a 2026 review [3], evaporative and boiling cooling were placed on the same hierarchical level as air and liquid cooling, whereas the term “phase-change cooling” was reserved for systems employing phase-change materials with high latent heat of melting. In the same work, passive evaporation–condensation systems implementing a closed cycle were consolidated under the broader category of heat pipes.

Taken together, these differences indicate that PEMFC cooling remains a multi-criteria engineering problem rather than a field converged toward a single dominant concept. The variety of classifications reflects not confusion, but rather the coexistence of several physically distinct heat-transfer mechanisms and architectural constraints.

An important constraint arises from the fuel-cell structure itself. The highly integrated layered design of PEMFCs leaves limited geometric freedom for placing heat-removal elements. In practice, most cooling concepts rely on modifications of the bipolar plates (BPs) or on heat-extraction elements located in their immediate vicinity. Consequently, BP becomes not only an electrical and mechanical component but also the primary interface between the electrochemical core and the thermal management system.

Air cooling represents the simplest implementation and is primarily suitable for low-power systems, typically below 5–10 kW. It relies on single-phase convective heat transfer. In open-cathode configurations, air simultaneously acts as oxidant and coolant. This approach minimizes hardware complexity but suffers from limited heat removal capability due to the low heat capacity of air and introduces the risk of membrane dehydration under high flow rates. Alternatively, forced air cooling through dedicated channels integrated into the BPs provides

better control of the cooling flow, since air is used exclusively as a coolant. However, achieving sufficient temperature uniformity requires a large number of channels and high volumetric flow rates, which lead to increased pressure losses. Fundamentally, the low specific heat capacity of air restricts scalability to higher power densities.

Liquid cooling, typically employing deionized water, constitutes the baseline solution for medium- and high-power PEMFC systems in the range of 5–100 kW. Although still based on single-phase convective heat transfer, liquid cooling benefits from approximately fourfold higher heat capacity of water compared to air, enabling more effective heat removal at moderate flow rates. Nevertheless, the improvement in thermal performance is accompanied by increased system complexity. Pumps, piping, filters, radiators, expansion tanks, and control systems are required, leading to higher parasitic power consumption and stricter electrical insulation requirements. Technological advancements within this class are largely confined to channel optimization and to modifications of coolant properties. The use of nanofluids has been reported to enhance effective thermal conductivity and heat-transfer coefficients, while also potentially reducing ionic contamination. However, the fundamental mechanism remains sensible heat transport, which scales with mass flow rate and allowable temperature rise.

Phase-change cooling technologies exploit the latent heat of vaporization to enhance heat removal. This class typically includes evaporative cooling and boiling-based cooling. In evaporative cooling, subcooled water is injected into the cathode region, where it evaporates and is removed together with product water before being reconditioned for reinjection. In boiling-based cooling, the coolant undergoes phase transition within a dedicated evaporator integrated into the BP. While these approaches increase local heat-transfer coefficients due to latent heat utilization, their implementation remains mechanically active and often shifts optimization efforts toward the external heat-rejection stage. In automotive systems in particular, evaporative and spray-based concepts increasingly focus on improving radiator performance, since geometric constraints severely limit modifications at the cell level. Spray cooling enhances heat rejection by impinging fine droplets onto cooled surfaces, thereby intensifying evaporation and convection.

Passive cooling technologies constitute a distinct category characterized by the absence of external mechanical circulation devices such as pumps or fans. Within this group, two fundamentally different mechanisms can be distinguished. The first includes solid heat spreaders made of high-conductivity materials such as copper, aluminium, expanded graphite, or advanced carbon-based structures. These devices redistribute heat from the active volume toward the periphery, improving temperature uniformity. However, they do not, by themselves, provide long-distance heat transport and therefore must be integrated into a broader cooling architecture.

The second mechanism involves closed two-phase systems capable of transporting heat via evaporation and condensation without mechanical pumping. These devices correspond to the class of two-phase heat loops introduced earlier in this work as smart thermal management devices. From a functional standpoint, they combine efficient heat collection at the evaporator with long-distance heat transport toward a remote condenser.

A meaningful comparison of cooling technologies requires decomposition of the PEMFC thermal-management task into distinct physical subproblems. At the single-cell level, the essential requirements include heat collection from distributed volumetric sources, maintenance of temperature within the prescribed operating window, and temperature uniformity across functional layers. At the stack level, an additional requirement arises: transport of heat over significant distances to an external heat sink. Among passive technologies, only loop-type systems with separated vapor and liquid transport lines inherently address this latter requirement.

In the context of PEMFC cooling, however, the practical implementation of heat loops is in most cases narrowed to loop heat pipes (LHPs). Despite their high effective heat-transfer performance [67], relatively few studies have investigated LHP integration in PEMFC systems [3]. In most reported cases, LHPs operate at the stack level, removing heat from the stack as a whole, while cell-level heat extraction is accomplished by conventional means. Only a single reported study proposes direct integration of a flat LHP evaporator into a fuel cell [75], achieving a copper evaporator with dimensions of 76 × 54 mm and a thickness of 6 mm. Considering that compactness is critical for stack assembly and that heat spreaders already achieve thicknesses on the order of 2 mm, competitive implementation of LHP technology requires substantial reduction of evaporator thickness.

Even if such geometrical constraints are overcome, integration challenges remain. Each evaporator requires both liquid and vapor transport lines, potentially leading to a densely populated stack-level cooling system. Multi-evaporator configurations with shared transport lines provide a technically feasible solution and have been studied in related contexts [68]-[70].

LTSs represent a simplified variant of HLs in which circulation is driven by gravity rather than capillary forces. Their structural simplicity and reduced manufacturing complexity make them attractive for terrestrial applications. However, gravity dependence limits their applicability in transportation and mobile systems, which has often led to their exclusion without detailed evaluation. At the same time, many PEMFC applications, including stationary power systems, backup units, and infrastructure installations—operate under stable orientation conditions where gravitational constraints are not prohibitive. As will be demonstrated in subsequent sections, appropriate design modifications can further enhance operational stability and expand the practical applicability of loop thermosyphon-based solutions.

From a thermodynamic perspective, the most compact and energetically efficient cooling strategies are those that exploit latent heat transfer while minimizing parasitic power consumption and maintaining the capability for long-distance heat transport. Passive two-phase heat loops uniquely combine these attributes. Nevertheless, their broader adoption in PEMFC systems remains constrained by integration complexity and fabrication challenges, leaving significant space for further research and technological development.

## 6.3 Concept of a Heat-Loop-Based Cooling System for PEMFC Stacks

Despite the recognized advantages of passive two-phase devices, no heat-loop architecture has yet demonstrated reliable integration at the PEMFC cell level while simultaneously satisfying geometric compactness, electrical compatibility, and stable phase-change operation. In particular, the evaporator remains the key unresolved element limiting the practical use of heat loops in fuel-cell thermal management. This section introduces the conceptual heat-loop configuration considered in this work and outlines the design constraints governing the transition from stack-level heat transport to cell-level heat extraction.

Excluding evaporative and open-cathode air cooling, most PEMFC cooling approaches utilize either the BPs themselves or the immediate vicinity of the BPs as the primary interface for heat extraction. The same boundary condition applies to heat-loop evaporators intended to act as cell-level heat extractors. In the ideal case, the BP would simultaneously perform the function of an evaporator, analogous to liquid cooling where the BP also serves as a heat exchanger. At the current stage, however, this represents a cell-design-level challenge. A more realistic intermediate solution is the integration of a thin evaporator into the BP without disturbing its primary electrochemical function. A similar strategy has been demonstrated in combined cooling systems based on micro heat pipe arrays embedded into BPs and followed by air cooling at the stack level [71]-[74], where individual heat pipes with thicknesses on the order of 2 mm were accommodated in dedicated slots machined into the BPs.

The layered architecture of a fuel cell further restricts evaporator geometry, effectively limiting it to a flat configuration. In addition, the fuel-cell stack constitutes an electrical system in which individual cells are connected in series through BPs. Consequently, evaporators forming a common heat loop must satisfy two conflicting requirements: they should be manufactured from electrically conductive materials to maintain compatibility with the BP environment, while remaining electrically isolated from each other to prevent unintended current paths. Considering these constraints, a conceptual heat-loop configuration is proposed (Figure 6-2) in the form of a multi-evaporator LTS.

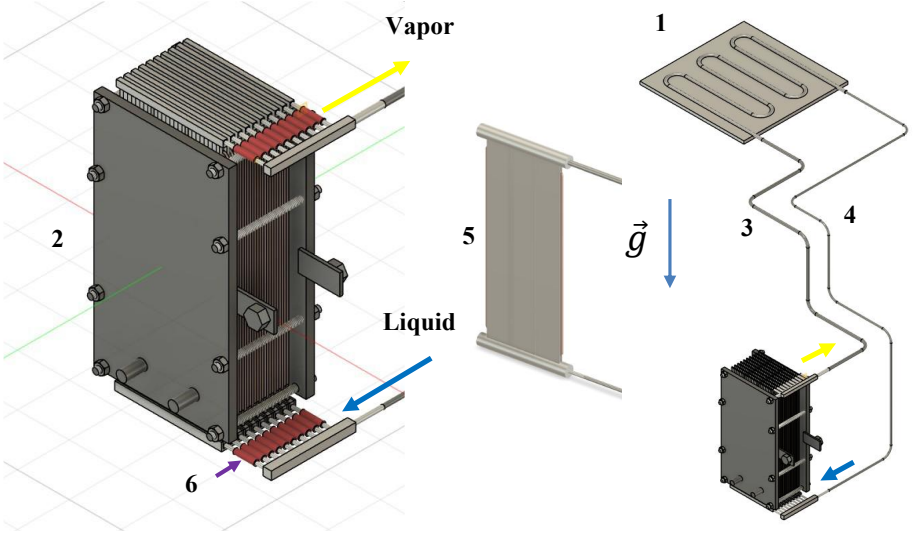


Figure 6-2. PEMFC two-phase heat loop layout

The condenser (1) is positioned above the PEMFC stack (2), with the vapor line (3) located above the liquid line (4) in accordance with gravitational circulation. Individual flat evaporators (5) are connected in parallel to the transport lines through dielectric inserts (6), providing electrical isolation between evaporators while maintaining hydraulic continuity. The inserts may be fabricated from electrically insulating materials compatible with the working fluid. Since the evaporators are hydraulically interconnected, the working fluid must also exhibit dielectric properties.

Such a configuration is naturally suited for terrestrial applications and for planetary surface systems (e.g., lunar or Martian rovers). For microgravity operation, the same architectural logic would require implementation as a multi-evaporator loop heat pipe (LHP), where orientation relative to gravity is no longer critical. LHPs, however, impose significantly stricter requirements on evaporator design due to the need for internal phase separation and the incorporation of a compensation chamber at the liquid inlet side (for instance, the compensation chamber was implemented as a flat cavity in [75]).

The development of the proposed system can be factorized into several sub-tasks: 1) selection of materials and working fluid; 2) design and experimental evaluation of the evaporator, including single-evaporator thermosyphon testing; and 3) assembly and testing of a multi-evaporator configuration with dielectric inserts. The present work focuses on the first two aspects.

## 6.4 Selection of Structural Materials and Working Fluid

Considering that the system mass must be minimized and that evaporators integrated into the bipolar plates must not introduce significant electrical resistance, aluminium was selected as the primary structural material of the system. A known challenge associated with aluminium is the formation of surface oxide layers, which may increase electrical contact resistance. However, this issue can be mitigated by appropriate surface treatment and is therefore not considered a prohibitive limitation for the present application.

The working fluid was selected based on the following criteria: it must be electrically insulating, compatible with aluminium, operate within the temperature ranges of both LT-PEMFC (60–80 °C) and HT-PEMFC (120–200 °C), exhibit moderate vapor pressures in these ranges, and provide favourable heat-transfer characteristics. Toluene was selected as the working fluid. Toluene is a good dielectric, has a low freezing point (−95.0 °C), a critical temperature of 320 °C—well above the operating range and sufficiently far from the critical region, which is advantageous for two-phase systems—and a normal boiling point of 110.6 °C. Consequently, LT-PEMFC operation occurs at sub-atmospheric pressure, whereas HT-PEMFC operation corresponds to pressures of several atmospheres (e.g., approximately 1.3 bar at 120 °C).

In Section 3.6, merit numbers for working fluids intended for loop thermosyphons were introduced, namely $(F_{m,v})_{LTS}$, $(F_{m,l})_{LTS}$, $(F_{m,G})_{LTS}$, which characterize the ability of a fluid to transport thermal power and to provide maximum effective thermal conductance.,

While thermal systems are often designed to maximize conductance, in PEMFC applications excessively high conductance may under certain conditions become undesirable. If heat is rejected to a cold environment while the cell temperature must be maintained within the 60–80 °C range, high conductance can lead to overcooling.

The above merit numbers account only for hydrodynamic contributions. For thermosyphons, another characteristic parameter derived from Nusselt's theory for film condensation on vertical surfaces [76] is commonly used. The parameter group governing the temperature difference between the thermosyphon wall and the condensation temperature can be expressed as:

$$(F_{m,Nu})_{LTS} = \left[\frac{h_{ev} \cdot \rho_l^2 \cdot \lambda_l^3}{\eta_l}\right]^{\frac{1}{4}} \tag{7.1.}$$

Figure 6-3 present comparative plots of the merit numbers for toluene and other candidate fluids, including water and ammonia, which are often regarded as optimal fluids for two-phase systems. Acetone was also included, as it is frequently used in aluminium heat-transfer systems. The temperature ranges corresponding to LT-PEMFC and HT-PEMFC operation are highlighted.

Although acetone exhibits slightly higher merit numbers than toluene, its electrical conductivity is 5–8 orders of magnitude higher [77], [78] and increases dramatically in the presence of trace amounts of water, whereas toluene does not dissolve water. In addition, acetone

has lower thermal stability at elevated temperatures and significantly higher vapor pressures (e.g., ~4.8 bar at 120 °C).

Taking into account dielectric properties, chemical compatibility, vapor-pressure levels, thermal stability, and merit-number analysis, toluene is considered the more suitable aluminum-compatible working fluid for PEMFC heat-loop cooling systems, particularly for high-temperature applications.

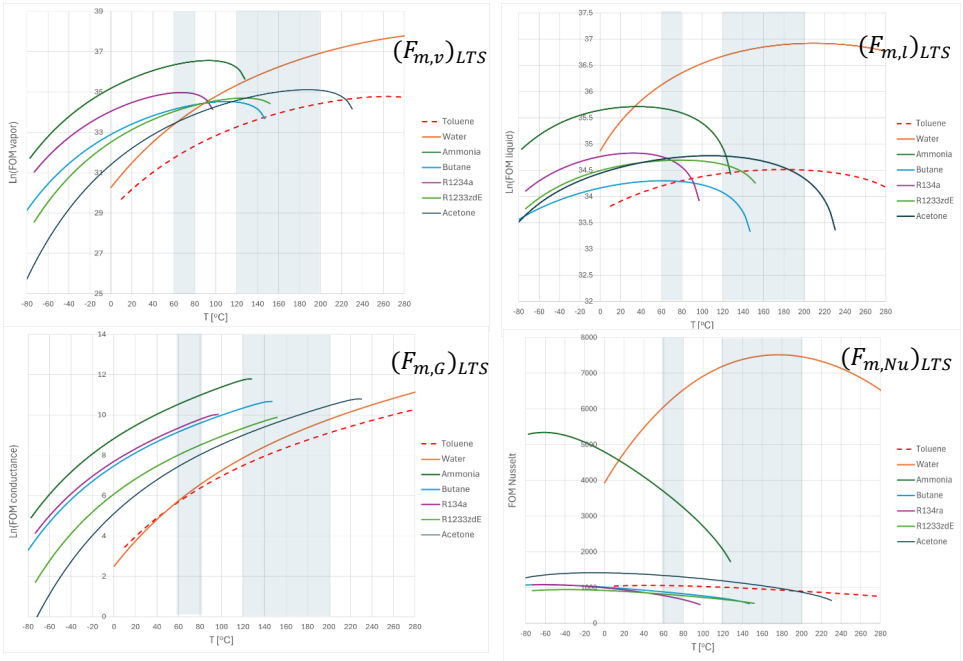


Figure 6-3. Comparison of working fluids using merit numbers. The numbers in the figure correspond to the criterion indices. For criteria $(F_{m,v})_{LTS}$, $(F_{m,l})_{LTS}$, $(F_{m,G})_{LTS}$, the values are plotted on a logarithmic scale

## 6.5 Evaporator Design and Thermosyphon Assembly

Microchannel aluminium flat tubes (MAFTs) with thicknesses of 2.15 mm (1) and 3.72 mm (2) were selected for evaporator fabrication (Figure 6-4).

Similar MAFTs are widely used in multi-channel flat heat pipes. For example, in [79], a 3 mm thick MAFT was employed to manufacture a micro heat pipe array for a photovoltaic–thermal system. In another study [80], an LTS with an evaporator made from a 6 mm thick aluminum multi-channel profile and using R134a as the working fluid was experimentally

investigated under low heat flux. In PEMFC cooling systems based on micro heat pipe arrays [72], MAFTs of approximately 2 mm thickness have also been used (with acetone as the working fluid).

Therefore, to develop a competitive cooling solution for fuel cells, the target LTS evaporator thickness should be on the order of 2 mm. However, because aluminium is challenging for assembling thin-walled structures, thicker profiles were initially used to establish and refine the joining methodology. Two joining techniques were considered: vacuum brazing and TIG welding. Although brazing is regarded as more promising for future mass production, welding provided the most reliable results at the present development stage. Figure 6-4 shows the main evaporator components: the evaporator body (3,4) and the side manifolds (5).

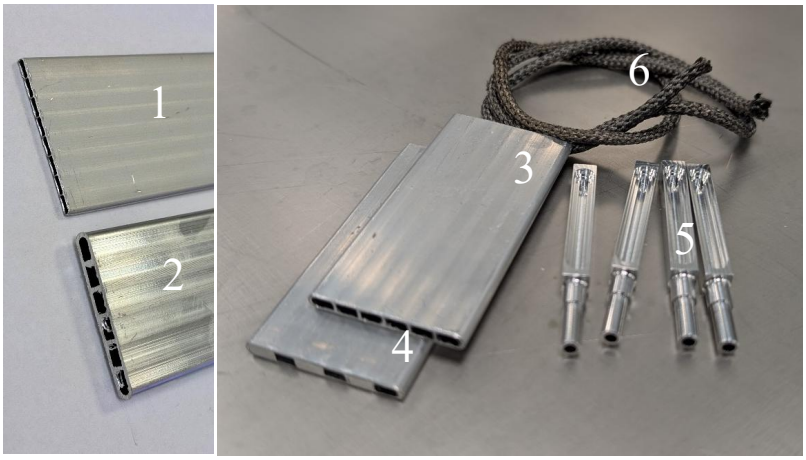


Figure 6-4. Raw materials and evaporator components.

A conventional LTS evaporator does not require a wick, since fluid circulation is gravity-driven rather than capillary-driven. However, a wick can perform additional functions that may significantly improve LTS performance. Therefore, in addition to reference wickless evaporators, wick-assisted designs were also fabricated. The wick material consisted of braided stainless-steel metallic fibres (6). In total, five evaporator configurations with different internal structures were investigated: three fabricated from 3.72 mm MAFT (thick MAFT) and two—considered the most promising—from 2.15 mm MAFT (thin MAFT). The wicks were inserted into the evaporator channels and interconnected on the liquid-manifold side. Figure 6-5 presents X-ray images illustrating the internal wick arrangement.

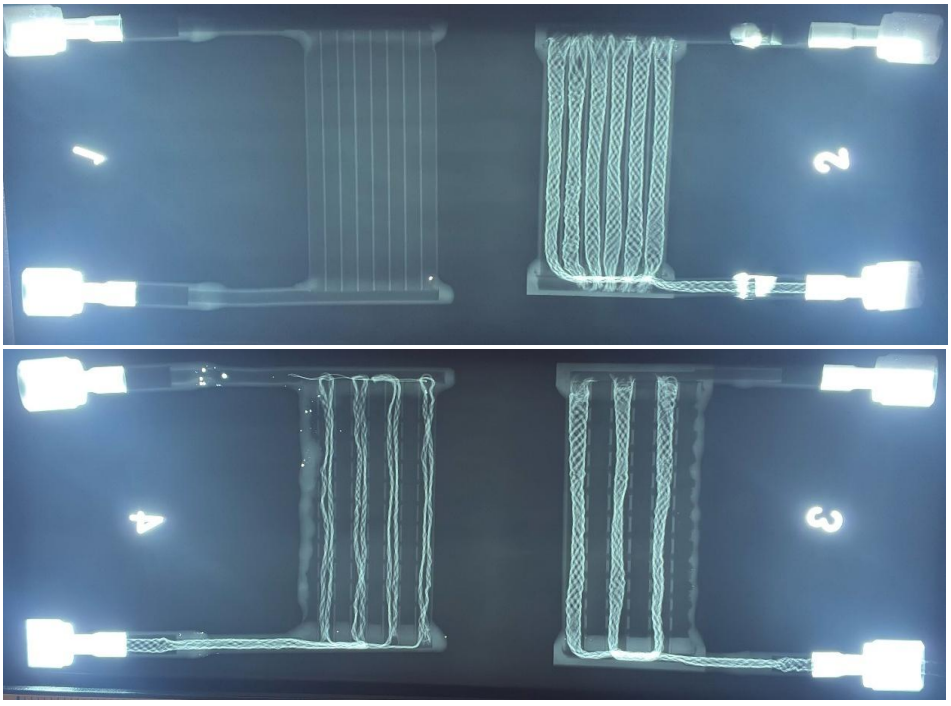


Figure 6-5. X-ray Images of the internal structure of the evaporators

The reference evaporator (1), fabricated from the thin MAFT, contains eight channels (3.5 mm × 0.95 mm). The thick MAFT of the same width contains six channels (4.5 mm × 2.5 mm). Evaporator (2), based on the thick MAFT, incorporates wicks in every channel.

In two additional evaporators (3, 4), part of the channels were intentionally dedicated to vapor evacuation, forming an alternating liquid-channel / vapor-channel structure. The vapor channels were sealed at the liquid-manifold side (Figure 6-4, component 4). Along their length, the vapor channels were connected to adjacent liquid channels through ~1 mm diameter openings spaced at 5 mm intervals. This separation was intended to facilitate vapor removal and reduce the risk of vapor blockage and wick dry-out. Accordingly, wicks were placed only in the liquid channels. Evaporator (3) is fabricated from the thick MAFT, whereas evaporator (4) is based on the thin MAFT.

Because future development targets operation under microgravity conditions, the feasibility of using an LTS with a wick-assisted evaporator in a horizontal, heat-pipe-like mode was also explored. For this purpose, the wick was extended from the evaporator along the liquid line to a condenser located 0.5 m away (Figure 6-6).

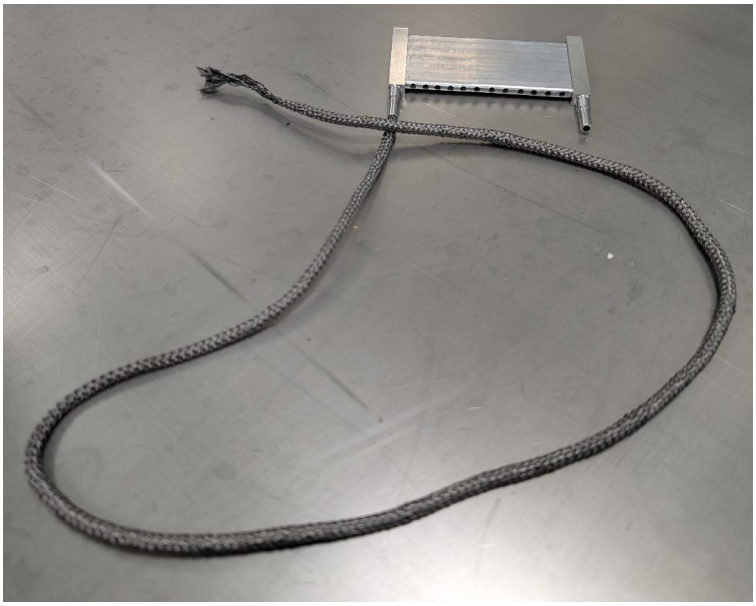

Figure 6-6. Evaporator with an extended wick, prepared for welding.

Two thermosyphon configurations were tested (Figure 6-7):

1. Conventional configuration, with the condenser located in the downcomer. In this case, the vapor line length was 0.5 m and the liquid line was 0.1 m shorter. The inner diameter of the transport lines was 4.57 mm.

2. Symmetric configuration, where both transport lines were identical and 0.5 m long. The inner diameter of the transport lines was 4.00 mm.

Since the flat evaporator section was only 5.5 cm long, it was considered unnecessary to orient the internal channels vertically.

A commercially available S-shaped aluminium condenser (100 × 80 mm) with four parallel flat channels and air cooling served as the heat sink. Heat rejection to ambient air was provided by a fan with a maximum flow rate of 0.83 $m^3$/min.

In the symmetric configuration, the two transport lines are functionally equivalent, and the flow direction is determined by small fabrication asymmetries. Introducing a wick in one line establishes hydraulic asymmetry and stabilizes the functional roles of the vapor and liquid lines, eliminating the need to position the condenser specifically in the downcomer.

The heat source was simulated using flat electric heaters attached to the evaporator surface with thermal paste and secured by a mechanical clamp. The parameters of the LTS are summarized in Table 6-1.

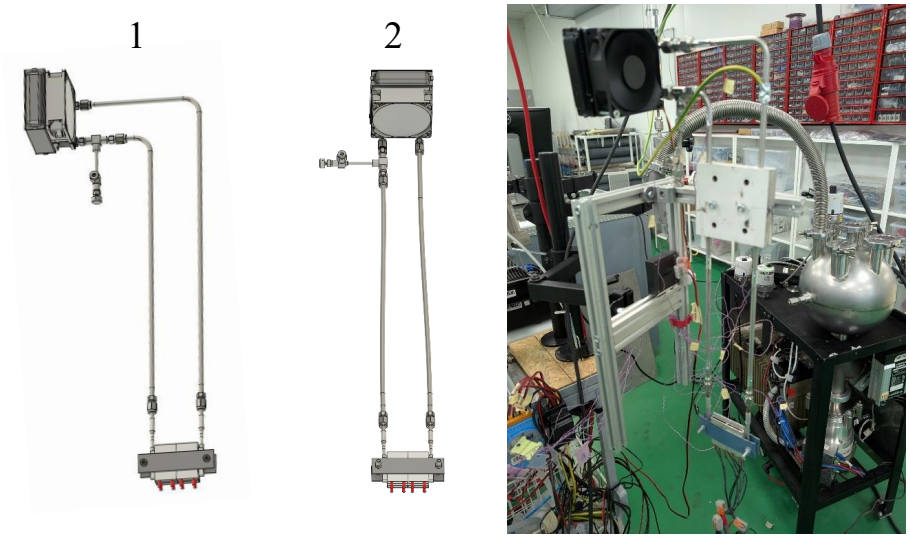


Figure 6-7. Two LTS configurations (1, 2) and the manufactured device during testing (3)

Table 6-1

LTSs specifications.

| LTS component | Parameter | Value (configuration) |
|---|---|---|
| Evaporator | Length | 55 mm |
| | Width | 32 mm |
| | Thickness | 3.72 mm / 2.15 mm |
| | Number of channels | 6 / 8 |
| Transport Lines | Vapor Line Length | 500 mm |
| | Liquid Line Length | 500 mm (2) / 400 mm (1) |
| | Inner Diameters | 4.57 mm (2) / 4 mm (1) |
| Condenser | Length | 100 mm |
| | Width | 80 mm |
| | Thickness | 25 mm |
| | Fan type | JF0825S1ES-R |
| | Fan dimensions | 80×80 mm |
| | Fan max. air flow | 0.83 $m^3$/min |

## 6.6 Experimental Investigation of Loop Thermosyphons with Various Evaporator Designs

Since thin evaporators are of the greatest interest for further application in fuel cells, only the test program and results related to these configurations are presented in this work.

### Study Logic and Configuration Evolution

The experimental study followed a stepwise modification logic. A thermosyphon with the condenser located in the downcomer and a wickless evaporator was selected as the reference configuration. The test series performed with this device provided a baseline for evaluating subsequent design modifications.

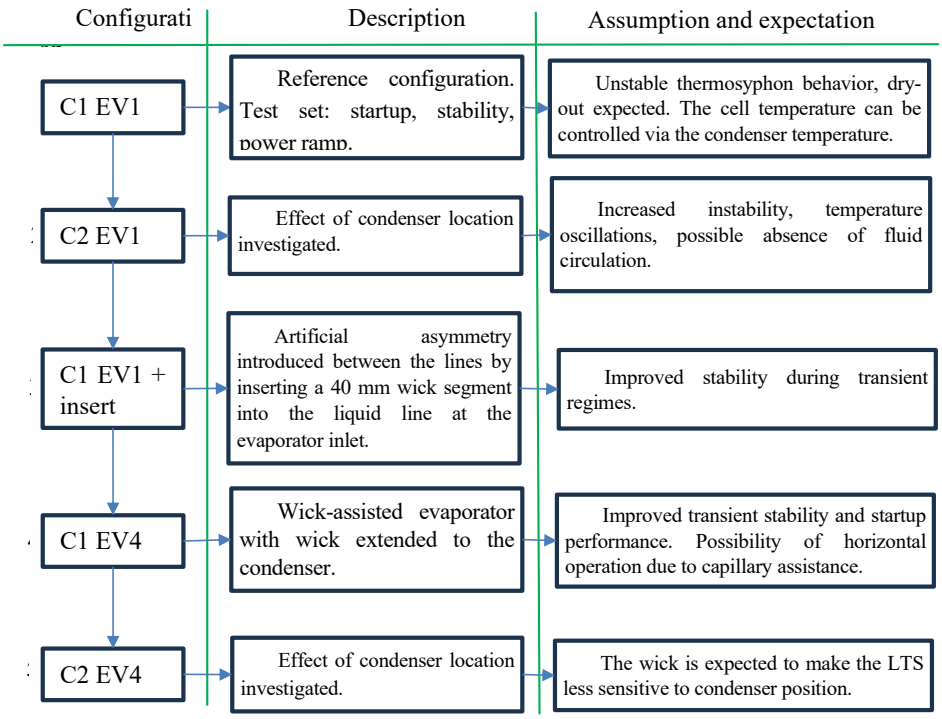


Figure 6-8. Experimental study logic and configuration evolution

The configuration was progressively modified, and for each modification a hypothesis regarding the expected effect on performance or stability was formulated and then verified

experimentally. The sequence of modifications and the corresponding expected effects are summarized in Figure 6-8. The configuration notation C1 EV4 denotes LTS configuration 1 (as defined in Figure 6-7) equipped with evaporator 4 (as defined in Figure 6-5).

### Test Facility and Instrumentation

Figure 6-9shows the schematic diagram of the experimental setup, including the thermocouple locations and designations. Temperature was measured using Amidata Type-T thermocouples.

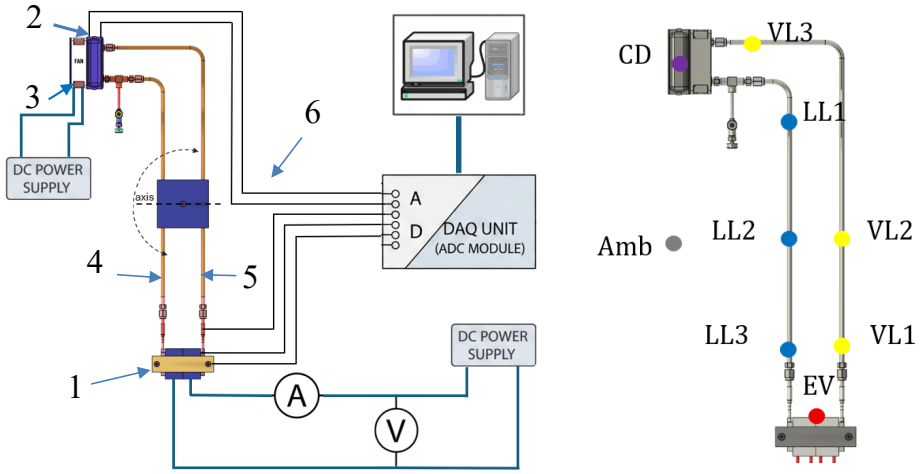


Figure 6-9. Schematic diagram of the experimental setup and position of thermocouples. 1) Evaporator with heaters; 2) Condenser; 3) Fan; 4) Downcomer; 5) Riser; 6) Thermocouples.

The signals were acquired with an Advantech ADAM-4018/4018M analog input module and transmitted to a computer for recording. Data acquisition, processing, and experiment control were implemented in LabVIEW. The electrical power supplied to the heaters was calculated as the product of the measured current and voltage.

The LTS was mounted on a laboratory stand via a hinged joint, allowing adjustment of its inclination angle relative to the vertical.

### Heat Loss Calibration

The typical heat flux density in a fuel cell is on the order of 2 W/cm². For the investigated evaporator with a surface area of 17.6 cm², this corresponds to a required heat removal capacity of up to 35 W. At such power levels, heat losses to the ambient become significant; therefore, a “dry” test was performed prior to charging the system. During this test, a prescribed power was

supplied to the heaters, and the steady-state evaporator temperature was recorded. Heat was dissipated to the surroundings by natural convection.

Data processing revealed a linear relationship between the dissipated power and the temperature difference between the evaporator and the ambient air. The dry test showed that, within the evaporator temperature range of 20–100 °C, heat losses to the surroundings can reach up to 20 W. This effect was taken into account in the subsequent experiments.

The obtained relationship made it possible to determine the overall heat loss coefficient of the setup relative to the ambient environment, which was found to be 0.25 W/K.

**Filling Procedure**

The LTS was charged using a calibrated charging device. Prior to filling, the system was evacuated to a vacuum level on the order of $10^{-6}$ mbar. The charging volume was kept constant for all tests at approximately 25 mL of toluene, corresponding to a filling ratio of about 50 %.

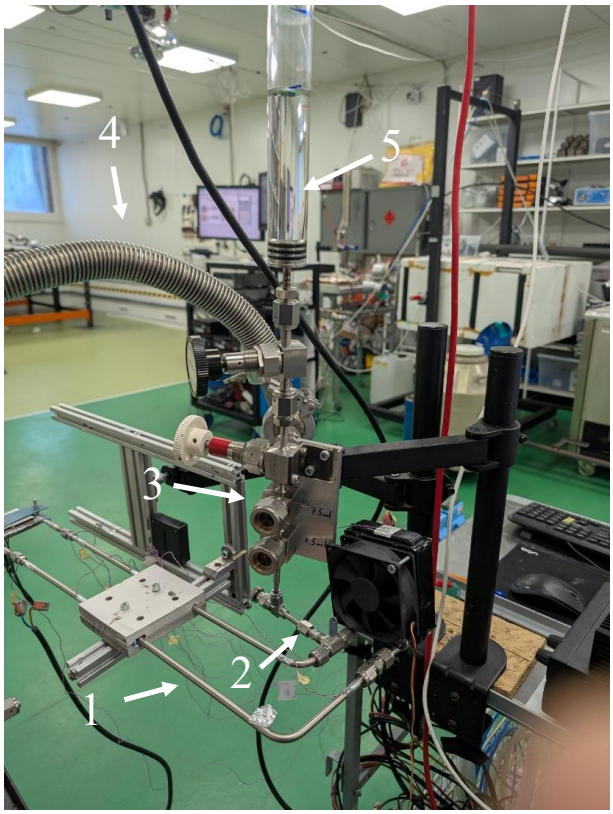


Figure 6-10. Loop Thermosyphon charging setup. 1) LTS; 2) Charging port; 3) Charging station; 4) Hose to vacuum stand; 5) Volume with toluene

## 6.7 Results and Discussion

The experimental program confirmed most of the assumptions formulated in “Section Study Logic and Configuration Evolution”. Figure 6-11 presents a representative test of configuration C1 EV1. This configuration served as the reference case.

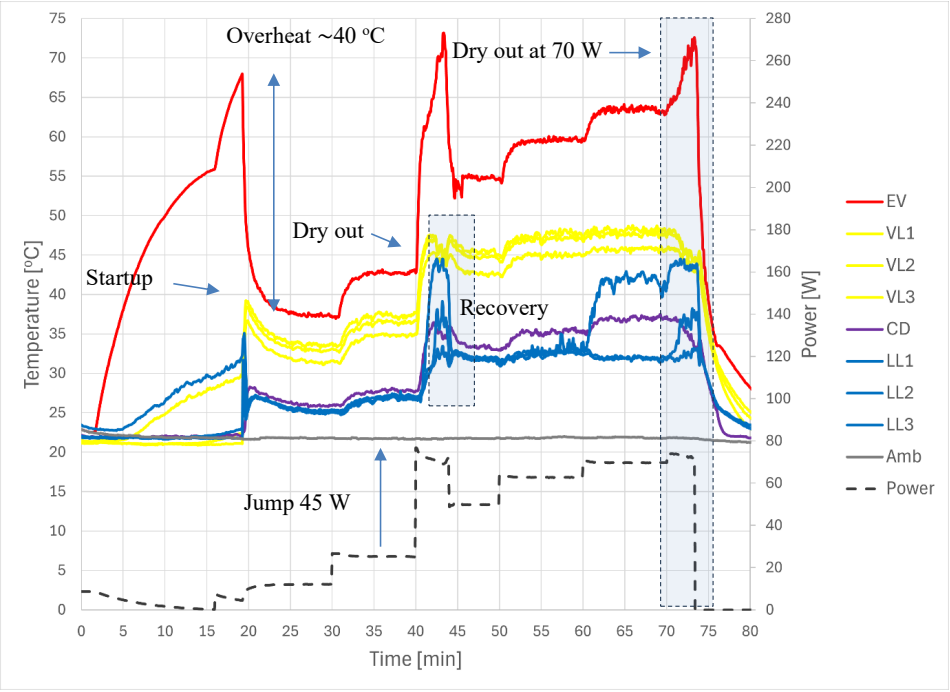


Figure 6-11. LTS testing in configuration C1 EV1

As seen in the figure, the thermosyphon started only after approximately 20 minutes from the moment 9 W of heating power was applied. During the initial stage, the supplied heat was primarily used to warm the evaporator and the working fluid by conduction. A significant temperature difference was observed between the evaporator surface and the liquid. The working fluid temperature could be inferred from the nearly identical readings of thermocouples LL3 and VL1, which increased linearly as the evaporator was heated. After about 15 minutes, it became evident that the evaporator temperature was approaching a steady state, since nearly all the supplied heat was being dissipated to the surroundings. This is illustrated by the dashed power line in the plot, which represents the net power (input power minus heat losses to the

environment). The heater power was therefore increased to 16 W. This led to further superheating of the liquid in the evaporator and ultimately to the onset of boiling.

The response of the temperatures in the vapor and liquid lines indicates that boiling started in an explosive manner, suggesting that the liquid had been in a metastable superheated state. The readings of the liquid- and vapor-line thermocouples diverged, marking the onset of working fluid circulation and, consequently, effective heat transfer from the evaporator to the condenser. As a result, the evaporator temperature dropped by nearly 40 °C. Due to the decrease in evaporator temperature, heat losses to the environment were reduced, and the power transferred by the thermosyphon increased. By the 30-minute mark, thermosyphon operation had largely stabilized, with a transferred power of approximately 12 W and a vapor temperature of about 34 °C.

At the next step, the input power was increased to 26 W, approaching the target operating level. The thermosyphon successfully sustained this step, and the evaporator temperature increased to 43 °C.

The subsequent step demonstrates the response of the thermosyphon to a sharp power increase. The input power peaked at approximately 77 W and then decreased to about 69 W due to environmental heat losses. This led to rapid vapor blockage of the evaporator and cessation of working fluid circulation within about 2 minutes. As shown, by the 42-minute mark the liquid line began to fill with vapor, and the readings of thermocouple LL3 became nearly identical to those of the vapor-line thermocouples. Consequently, the evaporator temperature rose uncontrollably.

Reducing the input power to 50 W restored circulation. The evaporator temperature then stabilized at approximately 55 °C. Subsequent gradual increases in power were tolerated without instability. The evaporator temperature entered the typical operating range (above 60 °C), and overload followed by dry-out occurred at about 70 W. This corresponds to a heat flux density of approximately 4 W/cm², which is about twice the typical value.

The tests show that the baseline configuration is unable to withstand rapid power transients and requires significant superheat for startup. However, under steady conditions it is capable of sustaining heat fluxes approximately twice as high as those typical for PEM fuel cells. The thermal conductance of the thermosyphon in this configuration is relatively high with respect to the chosen heat-sink temperature (ambient air), which results in cell temperatures below the desired operating range.

This behaviour is directly linked to the boundary conditions imposed by the condenser. In the experimental setup considered, an air-cooled condenser was used to reject heat to the environment at an ambient air temperature of 21 °C. This temperature effectively acts as a reference level that governs the evaporator temperature. When the LTS conductance is high, the cell temperature tends to follow this reference, which may place it below the required operating window.

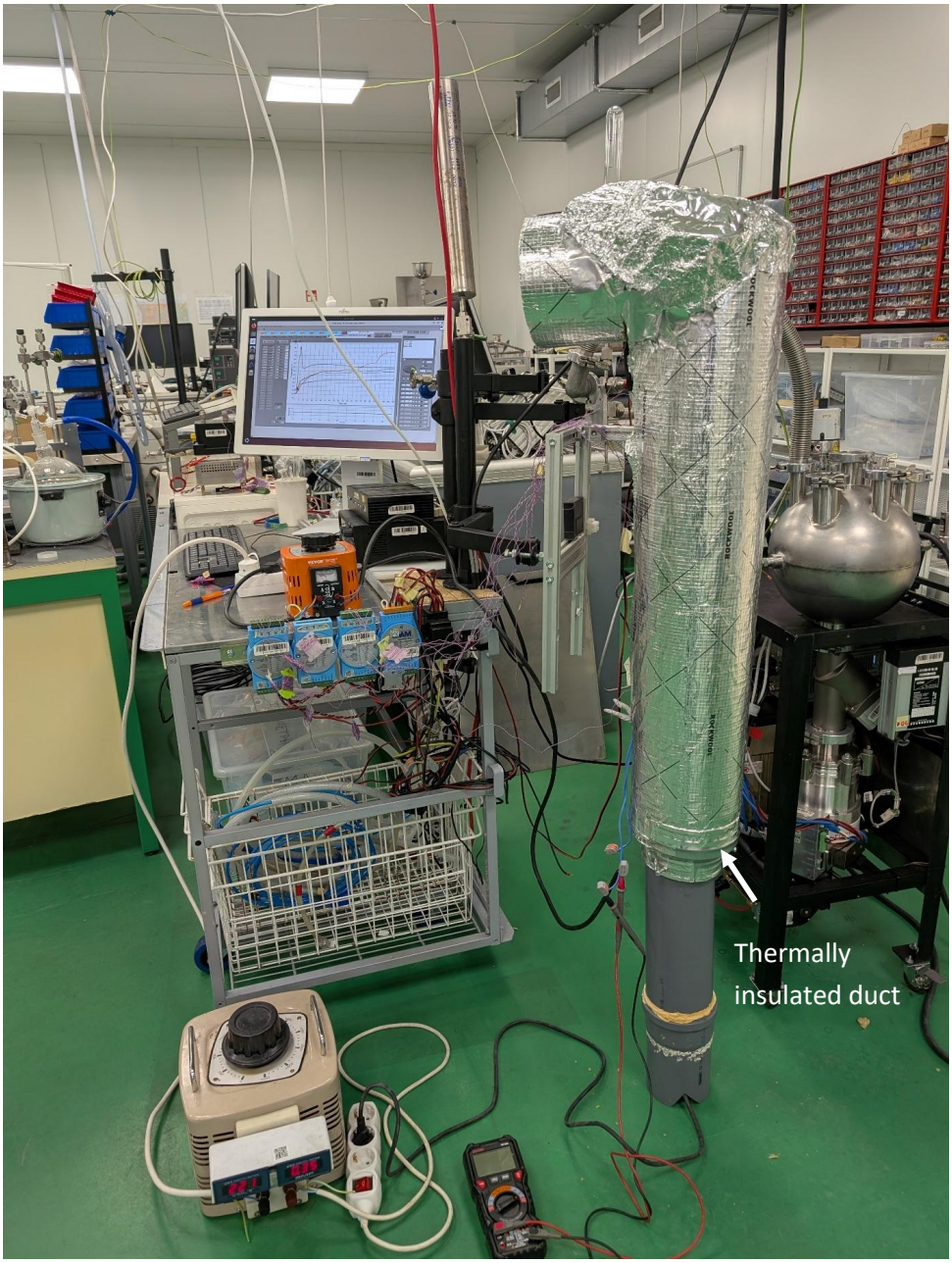


Figure 6-12. Test setup for the elevated environment temperatures.

To increase the operating temperature, either the LTS conductance must be reduced, or the reference temperature must be raised. Reducing conductance requires design modifications of the LTS, whereas increasing the reference temperature provides a more flexible means of regulating the fuel-cell thermal regime. This approach is difficult to implement with a conventional air condenser. However, if the condenser is configured as a cold plate connected to an external heat-transfer loop, the PEMFC temperature can be controlled by adjusting the cold-plate temperature. The feasibility of this concept was demonstrated in the following experiment. Instead of using a cold plate, the same air condenser was retained, but the LTS was placed inside a thermally insulated duct Figure 6-12, where the air temperature was raised to 45 °C.

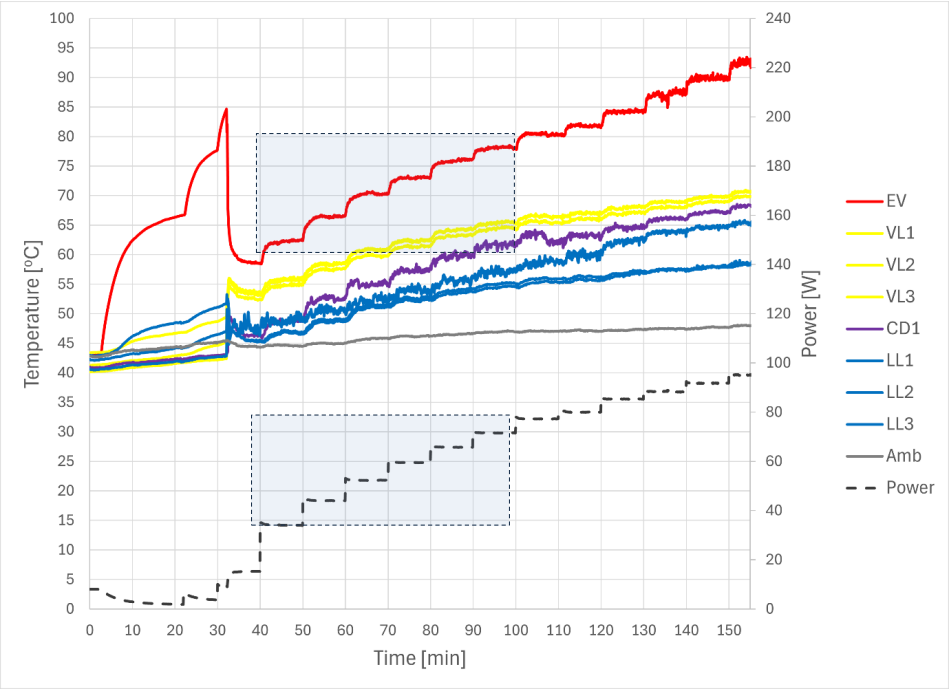


Figure 6-13. LTS startup and power-ramp test at elevated ambient temperature.

As shown in Figure 6-13 the hypothesis was confirmed. Increasing the reference temperature shifted the cell temperature into the desired operating range starting from an input power of approximately 40 W. It is also noteworthy that thermosyphon dry-out was not observed even at powers up to 97 W. This suggests that the dry-out observed in the previous experiment was not solely caused by insufficient hydrostatic head but may be associated with more complex critical phenomena related to phase distribution and flow stability in the evaporator.

In configuration C2 EV1, the two transport lines differ only in that one of them (the liquid line) contains the charging port; thus, the design is nearly symmetric. shows a portion of the power-ramp test illustrating the unstable behaviour of the thermosyphon.

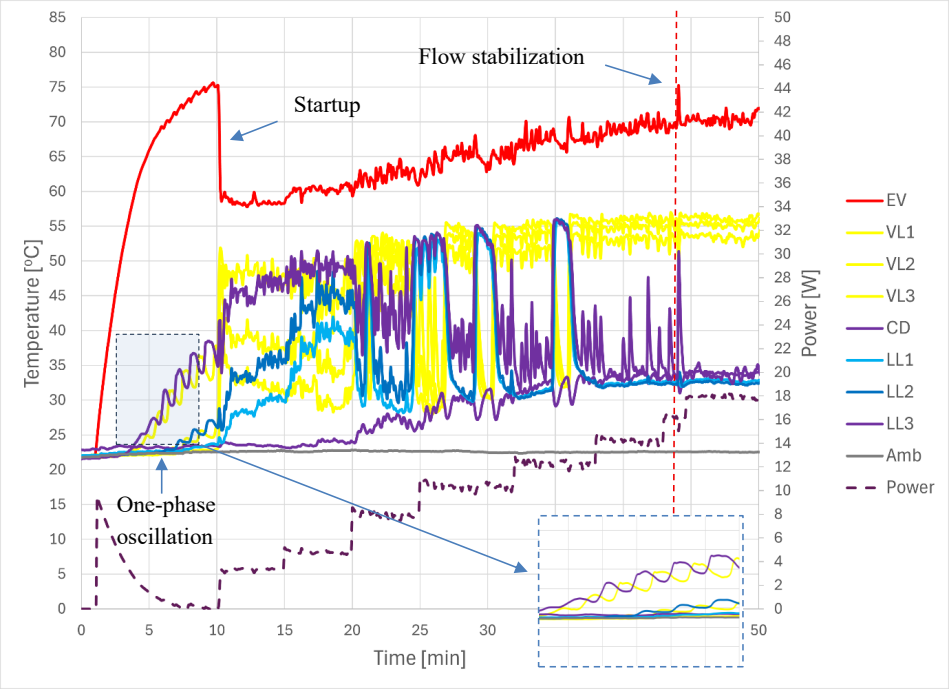


Figure 6-14. LTS testing in configuration C2 EV1 with a symmetrically positioned condenser.

Oscillations began already during the single-phase heating stage. As can be seen in the inset, the liquid temperatures at the evaporator inlet and outlet oscillate in antiphase. After startup, the temperature behaviour becomes highly irregular, indicating unstable two-phase circulation.

It is important to note, however, that the temperature measured at the evaporator surface (red thermocouple) exhibits only small-amplitude fluctuations. This is attributed to the thermal inertia of the evaporator body and represents a favourable feature, since this temperature is directly related to the thermal state of the fuel cell.

As the experiments showed, this configuration exhibits unstable behaviour at low power levels. However, above a certain power threshold (in this case approximately 18 W), the system establishes a preferred direction of working fluid circulation and subsequently operates in a manner similar to a thermosyphon with the condenser located in the downcomer. A slight geometrical or hydraulic asymmetry determines which line has the lower hydraulic resistance,

and the vapor preferentially flows through that line. Further tests with configuration C2 EV4, as well as the introduction of artificial asymmetry by means of a wick insert in the liquid line, demonstrated that such asymmetry suppresses the observed instability. Under these conditions, the thermosyphon behaviour becomes similar to that of a configuration with the condenser located in the downcomer, even at low power levels.

In configuration C1 EV1 + insert, a minor modification was introduced into the LTS design that was expected to reduce its effective thermal conductance and improve its tolerance to power transients. A 4-cm-long insert made of a porous material was placed in the liquid line at the evaporator inlet. The material consisted of a stainless-steel metallic fiber cord, which was additionally compacted to reduce its permeability. The evaporator design itself remained unchanged. A power-ramp test was then conducted using the same power steps as in the reference case. The results are presented in Figure 6-15. The startup phase followed the same scenario as before, which was expected since the evaporator configuration was not modified.

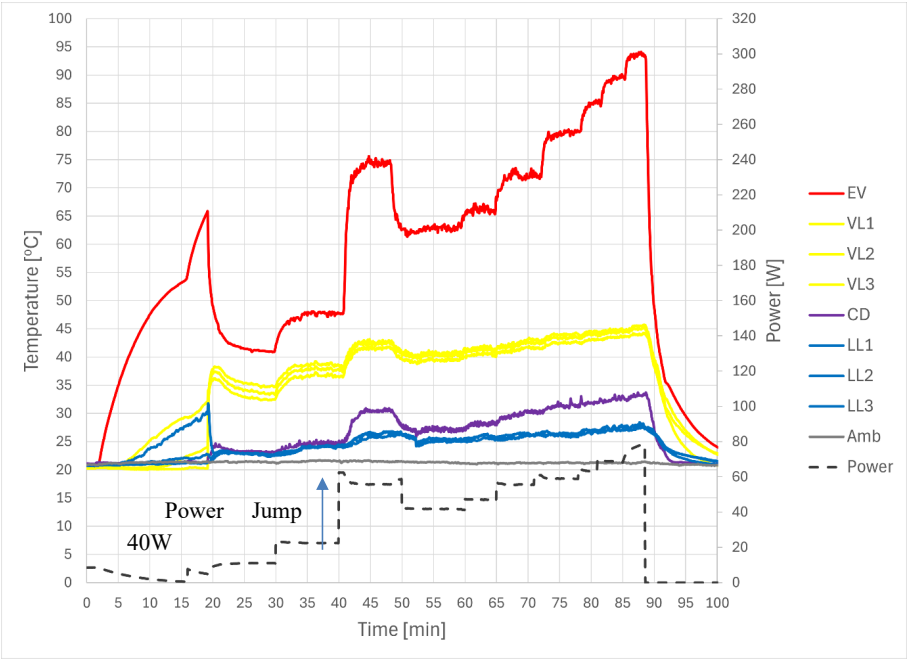


Figure 6-15. LTS testing in configuration C1 EV1 + insert.

However, the porous insert enabled the system to withstand the power jump without instability. This effect is likely associated with suppression of vapor penetration into the liquid line, which otherwise leads to circulation blockage. The insert therefore acts as a hydraulic stabilizing element in transient regimes.

During the experiments, a more pronounced temperature difference between the evaporator wall and the vapor temperature was also observed. This phenomenon requires further investigation.

Tests of configuration C1 EV4, featuring a wick installed in the liquid channels, are of particular interest. In addition to the modified evaporator design, the wick was extended along the entire liquid line up to the condenser. Since the wick length was significantly increased, no additional compaction was applied in order to preserve its permeability at approximately $10^{-8}$ m² (compaction typically reduces permeability by about one order of magnitude). As indicated by the previous experiments, introducing a wick into the liquid line does not degrade performance; on the contrary, the resulting hydraulic asymmetry between the transport lines promotes more stable operation.

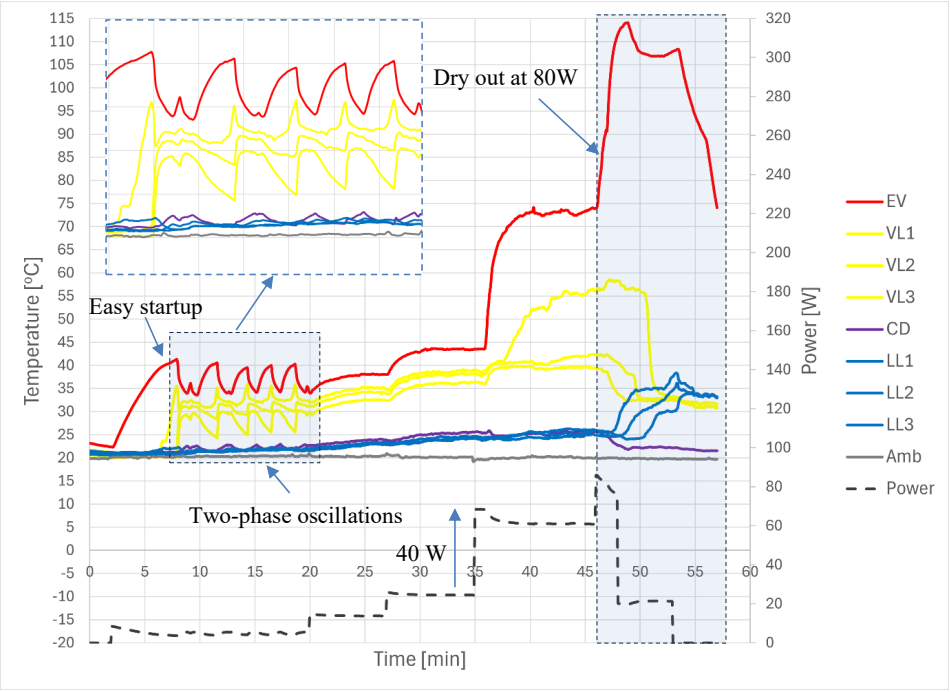


Figure 6-16. LTS testing in configuration C1 EV4 with a wick-assisted evaporator and a wick extended along the liquid line.

Figure 6-16 presents the power-ramp test of the LTS in configuration C1 EV4. A key observation is startup without pronounced superheat. The device also tolerated the power step without instability, while dry-out occurred only at an input power of approximately 80 W. Notably, this dry-out level is comparable to that observed for the reference configuration C1

EV1, suggesting that the ultimate dry-out mechanism may be governed not only by the overall hydraulic resistance of the loop, but also by local critical phenomena in the evaporator, such as phase distribution and vapor removal limitations.

The startup process merits closer examination. The wick reduced the startup superheat to approximately 7 °C. Moreover, the initial power required to initiate operation was only about 8 W (with the net power decreasing to ~5 W after accounting for environmental heat losses).

Another phenomenon observed during the experiment was temperature oscillations at low power (see inset in Figure 6-16). These indicate that continuous circulation had not yet been established and that heat transfer was dominated by intermittent bubble nucleation and release. Increasing the input power stabilized boiling and led to the establishment of a steady flow.

To evaluate whether the long wick in the liquid line could enable heat-pipe-like operation (i.e., reduced dependence on gravity), a series of tests was performed at different inclination angles. The desired horizontal operation was not achieved: the capillary capability of the selected wick was insufficient to sustain heat transport in the horizontal orientation. It should be noted that the distance between the evaporator and condenser was 500 mm, which is relatively large for capillary-driven heat-pipe operation.

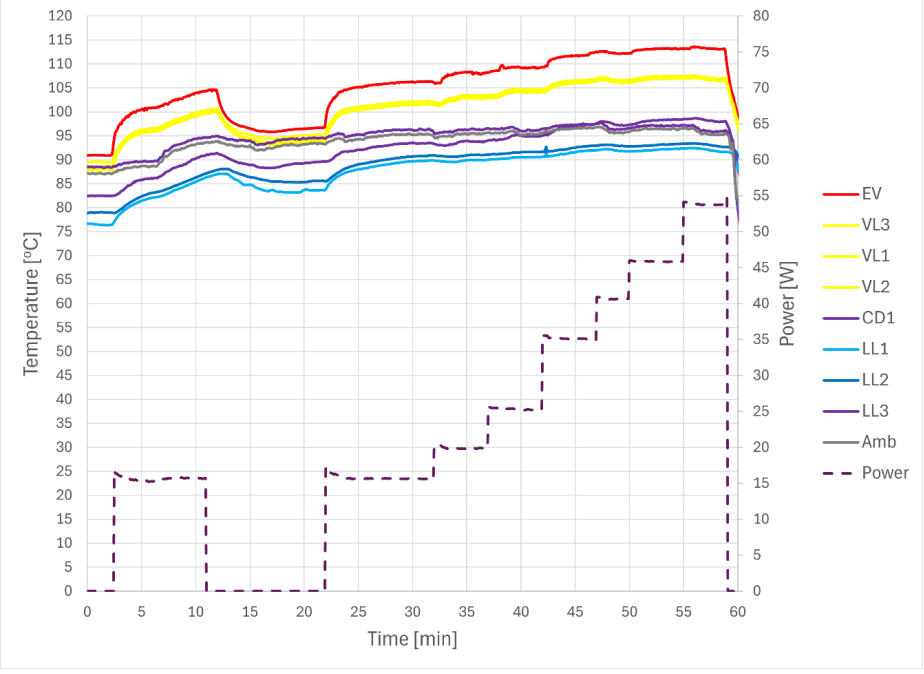


Figure 6-17. LTS testing at elevated temperatures – close to the HT-PEMFC operating range.

Although the primary focus of this work is on thin evaporators intended for integration into fuel cells, one additional test was performed with the thick evaporator No. 3 (Figure 6-5). This experiment is not included in the study logic diagram, as it does not relate to geometric integration aspects, but rather to the high-temperature performance of the working fluid. The test was conducted at temperatures approaching the HT-PEMFC operating range (120–200 °C). The results are presented in Figure 6-17.

The significance of this experiment lies in demonstrating the suitability of toluene as a working fluid for high-temperature applications. At evaporator temperatures above 100 °C, the thermosyphon charged with toluene exhibited noticeably improved heat-transfer performance and stable operation under increasing thermal loads. This behaviour is consistent with the earlier analysis of the figures of merit, which predicted more favourable thermophysical performance of toluene in the temperature range relevant to HT-PEMFC systems.

Thus, while this test does not address evaporator integration directly, it provides experimental confirmation that the selected working fluid remains effective in the upper PEMFC temperature regime, supporting the overall feasibility of the proposed two-phase cooling approach for both LT- and HT-PEMFC applications.

## 6.8 Conclusions for Chapter 6

The present chapter investigated the behaviour of a LTS as a simplified single-evaporator model of a future multi-evaporator passive cooling loop for PEMFC applications. The study focused primarily on evaporator design, startup characteristics, transient stability, and achievable heat-flux limits within geometrical constraints compatible with bipolar-plate integration.

The results demonstrate that evaporator internal structure is the dominant parameter governing system behaviour. Wickless configurations exhibited delayed startup, significant superheat, and sensitivity to rapid power transients, often resulting in vapor penetration into the liquid line and partial circulation breakdown. These instabilities were strongly configuration-dependent and not inherent to the thermosyphon principle itself.

The introduction of hydraulic asymmetry and a porous insert at the evaporator inlet significantly improved transient stability. The most favourable behaviour was observed for wick-assisted evaporators with separated vapor and liquid channels. In this configuration, startup occurred with minimal superheat (≈7 °C), resistance to power steps increased, and dry-out was observed only at heat fluxes of approximately 4 W/cm².

The achieved heat-flux density exceeds typical PEMFC values by approximately a factor of two, indicating a sufficient operational margin for practical fuel-cell applications. Importantly, the tested evaporator thickness remained compatible with bipolar-plate integration constraints.

The experiments further showed that system thermal conductance may exceed the requirements of PEMFC operation under certain boundary conditions. At low condenser temperatures, the evaporator stabilized below the optimal fuel-cell temperature range. However,

modification of the condenser boundary condition shifted the operating point into the desired range, demonstrating that temperature regulation can be achieved through sink-side control.

Hydraulic symmetry was found to induce direction-switching instabilities at low heat loads, whereas small asymmetries stabilized circulation. This observation highlights the importance of controlled internal hydraulic bias in compact loop configurations.

Experimental results at elevated temperatures were consistent with theoretical merit-number analysis and confirmed the suitability of toluene as a working fluid, particularly in the high-temperature regime.

An attempt to achieve orientation-independent operation by extending a wick along the liquid return line was unsuccessful with the wick material used, indicating the need for further investigation of capillary limits and permeability characteristics.

Overall, the chapter establishes the thermal-hydraulic feasibility of thin aluminium LTS evaporators within PEMFC-relevant operating conditions and identifies the key design parameters requiring further optimization.

# CONCLUSIONS

The present Thesis addressed the scientific and technical problem of developing a universal approach to thermal management of electrical equipment based on passive two-phase heat loops. The work was motivated by the growing discrepancy between increasing heat-flux densities in modern electrical systems and the limited scalability, energy efficiency, and autonomy of conventional single-phase cooling solutions.

The working hypothesis stated that replacement of conventional cooling systems by passive two-phase heat loops, designed with consideration of the structural and thermal characteristics of a specific device, leads to a modification of its thermal regime resulting in improved technical characteristics.

The conducted theoretical and experimental investigations confirm this hypothesis.

In the case of the in-wheel electric motor, integration of loop heat pipe–based cooling increased allowable thermal load and decreased operating temperature. The proposed architecture with evaporators structurally integrated into the stator body demonstrated the feasibility of direct heat removal from stator teeth and reduction of internal temperature gradients.

In the case of the LED luminaire, implementation of Heat Loop Pipe architecture enabled efficient redistribution of heat from concentrated heat source while preserving compact geometry.

In the case of the fuel-cell stack, experimental investigation of loop thermosyphons with thin aluminium evaporators demonstrated that passive two-phase loops are capable of operating within PEMFC-relevant heat-flux ranges while providing temperature regulation via boundary-condition control. The feasibility of cell-level integration was established, and the dominant design parameters governing stability and startup behaviour were identified.

Thus, the hypothesis that passive two-phase heat loops represent a scalable and adaptable thermal-management platform for different classes of electrical devices has been experimentally validated.

The first defended statement — that passive two-phase heat loops constitute a universal physical platform for smart thermal management — is supported by comparative analysis of single-phase and two-phase loops, as well as by the demonstrated ability of heat loops to operate autonomously, relying solely on internal physical mechanisms (phase transition, capillary forces, or gravity).

The second statement — concerning the adequacy of the developed mathematical model — is confirmed by the successful prediction of steady-state and transient operating regimes of loop heat pipes and by the agreement between calculated and experimental data across multiple configurations. The model consistently described temperature distributions, effective thermal conductance, maximum transferable power, and heat-leak behaviour.

The third statement — regarding the introduction of working-fluid quality parameters for loop thermosyphons — was substantiated through merit-number analysis and experimental

validation in both low- and high-temperature regimes. The proposed parameters enable justified working-fluid selection and provide predictive capability for operating temperature ranges.

The fourth statement — that modular multi-evaporator architectures enable scaling of two-phase loops toward universal “two-phase cold plate” platforms — was demonstrated through the development of the “Altom” modular technology and the realization of multi-module evaporators capable of transporting kilowatt-level heat loads over meter-scale distances.

The fifth statement that the application of heat loops modifies thermal constraints of electrical devices — was confirmed experimentally in all investigated cases, where reduction of thermal resistance, stabilization of temperature regimes, or extension of allowable heat load were achieved.

The scientific contribution of the Thesis consists in the development of a unified conceptual, theoretical, and experimental framework for the application of passive two-phase heat loops as smart thermal-management systems.

The concept of Smart Thermal Management was introduced as a class of systems based on internal physical feedback mechanisms that enable autonomous heat-flow redistribution without external energy input. Unlike classical active cooling systems, such loops self-adjust their operating state according to boundary conditions.

A thermodynamically consistent interpretation of heat leak and subcooling in loop heat pipes was developed, clarifying their fundamental role in closing the steady-state energy balance of the loop. This interpretation resolves common misconceptions regarding parasitic heat flows in LHP analysis.

A steady-state and transient mathematical model of loop heat pipes was formulated, including environmental heat exchange, gravitational effects, and internal energy redistribution. An algorithm for model tuning based on experimental data was proposed, along with a method for estimating parameters not directly measurable.

Working-fluid quality parameters for loop thermosyphons were introduced, extending the classical figures-of-merit approach to gravity-driven systems.

A new heat-transfer device architecture — the Heat Loop Pipe — was proposed, combining structural features of heat pipes and loop heat pipes to reduce hydraulic resistance while preserving compact cylindrical geometry.

A modular evaporator technology (“Altom”) was developed, enabling scalable construction of multi-evaporator cold plates and facilitating the transition from specialized LHP systems to universal two-phase platforms.

Collectively, these contributions establish a methodological basis for extending the use of passive two-phase heat loops beyond highly specialized applications toward broader classes of electrical equipment.

Further development of passive two-phase heat-loop technology, particularly in the direction of simplified manufacturing, improved serviceability, and enhanced integration with electrical

architectures, may significantly expand its industrial applicability and contribute to the advancement of energy-efficient thermal-management systems.

# REFERENCES


[1] Zhihao Zhang, Xuehui Wang, Yuying Yan “A review of the state-of-the-art in electronic cooling”, e-Prime - Advances in Electrical Engineering, Electronics and Energy 1 (2021) 100009.

[2] Galkin, I.A., Geidarovs, R., Podgornovs, A., Modular segmented motor for power-assist wheelchairs: Proof of concept, (2021) Machines, 9 (10), art. no. 227, DOI: 10.3390/machines9100227.

[3] Xiaomin Shi , Yunhua Gan, “A comprehensive review of heat pipes for the thermal management in proton exchange membrane fuel cells”, International Journal of Thermal Sciences 220 (2026)

[4] XLamp® XHP70.3 LEDsCree- LED Product Family Data Sheet, Web Document (Accessed 14.02.2026) https://cree-led.com/media/documents/XLamp-XHP70.3.pdf

[5] D.A. Reay, P.A. Kew, R. McGlen, “Heat Pipes: Theory, Design and Applications”, Elsevier, 2013

[6] I. Ušakovs, D. Mishkinis, I. A. Galkin, A. Bubovich, and A. Podgornovs, “Experimental thermal characterization of the in-wheel electric motor with loop heat pipe thermal management system,” Case Stud. Therm. Eng., vol. 47, p. 103069, Jul. 2023, https://doi.org/10.1016/j.csite.2023.103069

[7] Igors Ušakovs, Luka Ivanovskis “Advanced Loop Heat Pipe Application for Cooling High Power LED Lights”, Case Studies in Thermal Engineering 57 (2024) 104320 https://doi.org/10.1016/j.csite.2024.104320

[8] I. Ušakovs, D. Mishkinis, I. A. Galkin “Concept and experimental study of two-phase cooling loops for PEM fuel cells with a flat aluminum evaporator”, Case Studies in Thermal Engineering, 2026

[9] Ghahfarokhi, P.S., Rasilo, P., Cardoso, A.J.M., Ušakovs, I., Mishkinis, D., Podgornovs, A., 2025. Proof of Concept of a Two-Phase Thermal Management System for Railway Traction Motors. IEEE Trans. Energy Convers. 1–10. https://doi.org/10.1109/TEC.2025.3583076

[10] Jingyu Cao, Zhanying Zheng, Muhammad Asim, Mingke Hu, Qiliang Wang, Yuehong Su, Gang Pei, Michael K.H. Leung, “A review on independent and integrated/coupled two-phase loop thermosyphons”, Applied Energy 280 (2020) 115885

[11] Mishkinis, D.; Ušakovs, I. SILTUMA CILPAS CAURULE (HEAT LOOP PIPE). LV 15883 A — patent application publication. Application No. LVP2023000021; filing date 2023-03-07; publication date 2024-09-20. Applicant: ALLATHERM, SIA, LV.

[12] Hong, S., Tang, Y., Wang, S., 2018. “An investigation on optimal external cooling condition for an ultra-thin loop thermosyphon-based thermal management system.”,

Energy Conversion and Management 172, 328–342. https://doi.org/10.1016/j.enconman.2018.07.033

[13] Caner, J., Videcoq, E., Benselama, A.M., Girault, M., 2024. Simulation of a two-phase loop thermosyphon using a new interface-resolved phase change model. International Journal of Heat and Mass Transfer 228, 125607. https://doi.org/10.1016/j.ijheatmasstransfer.2024.125607

[14] Sarkar, D., Savory, E., DeGroot, C., 2023. Thermodynamic evaluation of thermosyphons and heat pipes, in: Progress in Canadian Mechanical Engineering. Volume 6. Presented at the Canadian Society for Mechanical Engineering International Congress 2023, Université de Sherbrooke. Faculté de génie, Sherbrooke, Canada. https://doi.org/10.17118/11143/21007

[15] T.Kaya, T.Hoang, Mathematical modeling of loop heat pipes and experimental validation. J. Thermophys. Heat Transfer 13 (1999) 314-320

[16] Siedel, B., Sartre, V., Lefèvre, F., 2015. Literature review: Steady-state modelling of loop heat pipes. Applied Thermal Engineering 75, 709–723. https://doi.org/10.1016/j.applthermaleng.2014.10.030

[17] Collishaw P. G., Evans J. R. G., (1994) An assessment of expressions for the apparent thermal conductivity of cellular materials, Journal of materials science, 29 (1994) 486-498.

[18] Graham B. Wallis, “One-dimensional two-phase flow”, Courier Dover Publications, (2020)

[19] Churchill, S.W. (1977). "Friction factor equation spans all fluid-flow regimes". Chemical Engineering. 84 (24): 91–92.

[20] The National Institute of Standards and Technology (NIST). https://webbook.nist.gov/chemistry/

[21] Başaran, A., Benim, A.C., 2024. Condensation Flow of Refrigerants Inside Mini and Microchannels: A Review. Applied Sciences 14, 2988. https://doi.org/10.3390/app14072988

[22] Shah, M.M., 2022. Improved correlation for heat transfer during condensation in mini and macro channels. International Journal of Heat and Mass Transfer 194, 123069. https://doi.org/10.1016/j.ijheatmasstransfer.2022.123069

[23] Jie, Z., Dang, C., Meng, Q., 2025. A Review of Pressure Drop Characteristics and Optimization Measures of Two-Phase Flow with Low Boiling Point Working Fluids in Microchannels. FHMT 23, 1053–1089. https://doi.org/10.32604/fhmt.2025.066792

[24] Chisholm, D., 1967. A theoretical basis for the Lockhart-Martinelli correlation for two-phase flow. International Journal of Heat and Mass Transfer 10, 1767–1778. https://doi.org/10.1016/0017-9310(67)90047-6

[25] Maydanik, Y., Pastukhov, V., Chernysheva, M., 2018. Development and investigation of a loop heat pipe with a high heat-transfer capacity. Applied Thermal Engineering 130, 1052–1061. https://doi.org/10.1016/j.applthermaleng.2017.11.084

[26] Ivanovskis, L., Mishkinis, D., 2024. Review of “cold shock” cases in operation of loop heat pipes and related thermal instabilities. J. Phys.: Conf. Ser. 2766, 012025. https://doi.org/10.1088/1742-6596/2766/1/012025

[27] P Gakal, D Mishkinis, A Leilands, I Usakovs, R Orlov and Y Rogoviy, Analysis of working fluids applicable for high-temperatureloop heat pipe applications, IOP Conf. Series: Materials Science and Engineering 1226 (2022) 012036 doi:10.1088/1757-899X/1226/1/012036.

[28] Mishkinis, D., Ochterbeck, J.M., n.d. LOOP HEAT PIPES: CRITERIA APPROACH, V Minsk International Seminar “Heat Pipes, Heat Pumps, Refrigerators” Minsk, Belarus , September 8-11, 2003

[29] European Commission. A Clean Planet for all. A European long-term strategic vision for a prosperous, modern, competitive and climate neutral economy. Com 2018, 773, 114.

[30] Springer India-New Delhi. Automotive Revolution & Perspective Towards 2030. Auto Tech Rev 5, 20–25 (2016). https://doi.org/10.1365/s40112-016-1117-8

[31] S. Doyle, "The measure of e-scooters," in Engineering & Technology, vol. 15, no. 6, pp. 92-93, July 2020. doi: 10.1049/et.2020.0635

[32] T. Kim, O. Vodyakho and J. Yang, "Fuel Cell Hybrid Electric Scooter," in IEEE Industry Applications Magazine, vol. 17, no. 2, pp. 25-31, March-April 2011, doi: 10.1109/MIAS.2010.939811

[33] A. Muetze and Y. C. Tan, "Electric bicycles - A performance evaluation," in IEEE Industry Applications Magazine, vol. 13, no. 4, pp. 12-21, July-Aug. 2007, doi: 10.1109/MIA.2007.4283505.

[34] Rastogi, S.K.; Sankar, A.; Manglik, K.; Mishra, S.K.; Mohanty, S.P. Toward the Vision of All-Electric Vehicles in a Decade [Energy and Security]. IEEE Consumer Electronics Magazine 2019, 8, 103–107.

[35] A. M. Bazzi, Y. Liu and D. S. Fay, "Electric Machines and Energy Storage: Over a Century of Technologies in Electric and Hybrid Electric Vehicles," in IEEE Electrification Magazine, vol. 6, no. 3, pp. 49-53, Sept. 2018, doi: 10.1109/MELE.2018.2849900.

[36] R. Wrobel, P. H. Mellor, M. Popescu and D. A. Staton, "Power Loss Analysis in Thermal Design of Permanent-Magnet Machines—A Review," in IEEE Transactions on Industry Applications, vol. 52, no. 2, pp. 1359-1368, March-April 2016, doi: 10.1109/TIA.2015.2489599.

[37] Wang, K., Wang, Y., Zhu, C., Li, S., Tang, J., 2025. Temperature Field Analysis and Heat Dissipation Optimization for In-Wheel Motor Based on Magnetic-Thermal Coupling. Energies 18, 5517. https://doi.org/10.3390/en18205517

[38] P. Shams Ghahfarokhi, A. Podgornovs, A. Kallaste, A. J. Marques Cardoso, A. Belahcen, and T. Vaimann, “The Oil Spray Cooling System of Automotive Traction Motors: The State of the Art,” IEEE Transactions on Transportation Electrification, vol. 9, no. 1, pp. 428–451, Mar. 2023, doi: 10.1109/TTE.2022.3189596.

[39] H. Fujita, A. Itoh, and T. Urano, “Newly Developed Motor Cooling Method Using Refrigerant,” World Electric Vehicle Journal 2019, Vol. 10, Page 38, vol. 10, no. 2, p. 38, Jun. 2019, doi: 10.3390/WEVJ10020038.

[40] J. Huang et al., "A Hybrid Electric Vehicle Motor Cooling System—Design, Model, and Control," in IEEE Transactions on Vehicular Technology, vol. 68, no. 5, pp. 4467-4478, May 2019, doi: 10.1109/TVT.2019.2902135.

[41] Rafal Wrobel, Ryan J. MGlen, “Heat pipes in thermal management of electrical machines – A review”, Thermal Science and Engineering Progress, Volume 26, 2021, 101053, ISSN 2451-9049, doi: 10.1016/j.tsep.2021.101053

[42] S. Cai, J. L. Kirtley and C. H. T. Lee, "Critical Review of Direct-Drive Electrical Machine Systems for Electric and Hybrid Electric Vehicles," in IEEE Transactions on Energy Conversion, 2022, doi: 10.1109/TEC.2022.3197351.

[43] R. -Sanchez et al., “In-Wheel Motor Drive Systems for Electric Vehicles: State of the Art, Challenges, and Future Trends,” Energies 2023, Vol. 16, Page 3121, vol. 16, no. 7, p. 3121, Mar. 2023, doi: 10.3390/EN16073121.

[44] A. Credo, M. Tursini, M. Villani, C. Di Lodovico, M. Orlando, and F. Frattari, “Axial Flux PM In-Wheel Motor for Electric Vehicles: 3D Multiphysics Analysis,” Energies 2021, Vol. 14, Page 2107, vol. 14, no. 8, p. 2107, Apr. 2021, doi: 10.3390/EN14082107.

[45] D. Winterborne, N. Stannard, L. Sjoberg, and G. Atkinson, “An air-cooled yasa motor for in-wheel electric vehicle applications,” 2019 IEEE International Electric Machines and Drives Conference, IEMDC 2019, pp. 976–981, May 2019, doi: 10.1109/IEMDC.2019.8785156.

[46] P. Liang, F. Chai, K. Shen, and W. Liu, “Water Jacket and Slot Optimization of a Water-Cooling Permanent Magnet Synchronous In-Wheel Motor,” IEEE Trans Ind Appl, vol. 57, no. 3, pp. 2431–2439, May 2021, doi: 10.1109/TIA.2021.3064779.

[47] A. Saleem, M. Hyeon Park, T. Ambreen, and S. Chul Kim, “Optimization of oil flow distribution inside the in-wheel motor assembly of electric vehicles for improved thermal performance,” Appl Therm Eng, vol. 201, p. 117753, Jan. 2022, doi: 10.1016/J.APPLTHERMALENG.2021.117753.

[48] Knulst, A.J., Stassen, L.P.S., Grimbergen, C.A., Dankelman, J. Choosing Surgical Lighting in the LED Era. Surgical Innovation. 2009;16(4):317-323. doi:10.1177/1553350609353766

[49] S. Khandekar, G. Sahu, K. Muralidhar, E. Y. Gatapova, O. A. Kabov, R. Hu, X. Luo and L. Zhao. "Cooling of high-power LEDs by liquid sprays: Challenges and prospects." Applied Thermal Engineering 184 (2021): 115640.

[50] K. Delendik, N. Kolyago and O. Voitik. "Design and investigation of cooling system for high-power LED luminaire. “Computers & Mathematics with Applications” 83 (2021): 84-94.

[51] D. V. Pekur, V. M. Sorokin, and Yu E. Nikolaenko. "Thermal characteristics of a compact LED luminaire with a cooling system based on heat pipes." Thermal Science and Engineering Progress 18 (2020): 100549.

[52] J. Yuan, H. Fan and W. Wang. "Investigation of a novel natural convection heat sink for LEDs based on U-shaped mini-heat pipe arrays." Applied Thermal Engineering 204 (2022): 118000.

[53] Z. Xu, “Heat transfer performance of the rectangular heat sinks with non-uniform height thermosyphons for high power LED lamps cooling”, Case Studies in Thermal Engineering 25 (2021)

[54] Z. Xu, “Thermal performance and multi-objective optimization of thermosyphon heat sinks with rectangular radial fins for high power LED lamps cooling”, Case Studies in Thermal Engineering 30 (2022)

[55] C. Ladekar, A. Pise, M. Nukulwar and A. Lingayat. "Comparative analysis of integrated heat sink vapor chamber with conventional heat sink for LED cooling." Materials Today: Proceedings 72 (2023): 1136-1142.

[56] B.-J. Huang, Y.-H. Chuang and P.-E. Yang. "Low-cost manufacturing of loop heat pipe for commercial applications." Applied Thermal Engineering 126 (2017): 1091-1097.

[57] P. Kumar, G. Sahu, D. Chatterjee, S. Khandekar, “Copper wick based loop heat pipe for thermal management of a high-power LED module”, Applied Thermal Engineering 211 (2022)

[58] X. Hu, C. Hu, H. Xu, Y. He, D. Tang, “Polyethersulfone wick and metal wick based loop heat pipe for LED street light thermal management”, Case Studies in Thermal Engineering 49 (2023)

[59] R. Singh, M. Mochizuki, T. Yamada and T. Nguyen. "Cooling of LED headlamp in automotive by heat pipes. “Applied Thermal Engineering” 166 (2020): 114733.

[60] Z. Wang, W. Yang, “A review on loop heat pipe for use in solar water heating”, Energy and Buildings 79 (2014).

[61] M. Bernagozzi, A. Georgoulas, N. Miché, M. Marengo “Heat pipes in battery thermal management systems for electric vehicles: A critical review”, Applied Thermal Engineering 219 (2023)

[62] M.A. Chernysheva, Y.F. Maydanik, “Analysis of the thermal resistance of a loop heat pipe based on the P-T diagram of the working fluid operating cycle”, International Journal of Heat and Mass Transfer 209 (2023) 124157.

[63] A. Takuya, X. Chang, and H. Nagai. "Numerical analysis of loop heat pipe using nucleate boiling model in evaporator core." International Journal of Heat and Mass Transfer 195 (2022): 123207.

[64] Manzo, D., Thai, R., Le, H.T., Venayagamoorthy, G.K., 2025. Fuel cell technology review: Types, economy, applications, and vehicle-to-grid scheme. Sustainable Energy Technologies and Assessments 75, 104229. https://doi.org/10.1016/j.seta.2025.104229

[65] Ahmad Baroutaji, Arun Arjunan, Mohamad Ramadan, John Robinson, Abed Alaswad, Mohammad Ali Abdelkareem, Abdul-Ghani Olabi, “Advancements and prospects of thermal management and waste heat recovery of PEMFC”, International Journal of Thermofluids 9 (2021) 100064

[66] Yicheng Huang, Xuelian Xiao, Huifang Kang, Jianguo Lv, Rui Zeng, Jun Shen. “Thermal management of polymer electrolyte membrane fuel cells: A critical review of heat transfer mechanisms, cooling approaches, and advanced cooling techniques analysis”, Energy Conversion and Management 254 (2022) 115221

[67] Yu.F. Maydanik, “Loop heat pipes”, Applied Thermal Engineering, 25 (2005) https://doi.org/10.1016/j.applthermaleng.2004.07.010.

[68] Fathoni, A.M., Hendrayanto, P.A., Ramadhan, R.S., Putra, N., 2025. Experimental investigation on the startup behavior and visualization of dual-evaporator loop heat pipes. International Journal of Heat and Mass Transfer 246, 127053. https://doi.org/10.1016/j.ijheatmasstransfer.2025.127053

[69] Chang, X., Watanabe, N., Nagai, H., Nagano, H., 2022. Visualization of thermo-fluid behavior of loop heat pipe with two evaporators and one condenser under various orientation with even heat loads. International Journal of Heat and Mass Transfer 198, 123397. https://doi.org/10.1016/j.ijheatmasstransfer.2022.123397

[70] Chang, X., Watanabe, N., Nagai, H., Nagano, H., 2024. Visualization of thermo-fluid behavior of loop heat pipe with two evaporators and one condenser under various orientations with uneven heat loads. International Journal of Heat and Mass Transfer 221, 125054. https://doi.org/10.1016/j.ijheatmasstransfer.2023.125054

[71] Mingguang Yang, Zhenhua Quan, Lincheng Wang, Zichu Liu, Qianwen Zhang, Zejian Chang, Yaohua Zhao, “Characteristics of heat, power generation, and energy efficiency study on a novel air-cooled PEMFC stack based on micro heat pipe arrays”, Applied Thermal Engineering 238 (2024) 122041

[72] Wang, L., Quan, Z., Zhao, Y., Yang, M., Zhang, J., 2022. Experimental investigation on thermal management of proton exchange membrane fuel cell stack using

micro heat pipe array. Applied Thermal Engineering 214, 118831. https://doi.org/10.1016/j.applthermaleng.2022.118831

[73] Wang, L., Quan, Z., Zhao, Y., Yang, M., Jing, H., 2023. Heat transfer process analysis and performance research of micro heat pipe array applied for the thermal management of proton exchange membrane fuel cells. Applied Thermal Engineering 219, 119531. https://doi.org/10.1016/j.applthermaleng.2022.119531

[74] Wang, L., Quan, Z., Zhao, Y., Yang, M., Zhang, J., 2023. Experimental research on the dynamic response characteristics of proton exchange membrane fuel cell thermal management using micro-heat pipe array. J Therm Anal Calorim 148, 4377–4388. https://doi.org/10.1007/s10973-023-11988-7

[75] Joung, W., Yu, T., Lee, J., 2008. Experimental study on the loop heat pipe with a planar bifacial wick structure. International Journal of Heat and Mass Transfer 51, 1573–1581. https://doi.org/10.1016/j.ijheatmasstransfer.2007.07.048

[76] Hussein, H.M.S., Mohamad, M.A., El-Asfouri, A.S., 2001. Theoretical analysis of laminar-film condensation heat transfer inside inclined wickless heat pipes flat-plate solar collector. Renewable Energy 23, 525–535. https://doi.org/10.1016/S0960-1481(00)00149-X

[77] Shell Chemicals. Acetone Product Data Sheet U8903. Shell Global, North America, https://www.shell.com/

[78] Shell Chemicals. Toluene Solvent S — Product Data Sheet. Shell Global, Asia Pacific, 19 Oct 2007, https://www.shell.com/

[79] Deng, Y., Quan, Z., Zhao, Y., Wang, L., Liu, Z., 2015. Experimental research on the performance of household-type photovoltaic–thermal system based on micro-heat-pipe array in Beijing. Energy Conversion and Management 106, 1039–1047. https://doi.org/10.1016/j.enconman.2015.09.067

[80] Wang, L., Zhong, W., Min, W., Yang, T., Yu, N., Cao, X., Yuan, Y., 2024. Experimental investigation on the heat transfer characteristics of loop thermosyphon with a micro-channel evaporator under low heat flux. Applied Thermal Engineering 257, 124498. https://doi.org/10.1016/j.applthermaleng.2024.124498

[81] Fathoni, A.M., Hendrayanto, P.A., Ramadhan, R.S., Putra, N., 2025. Experimental investigation on the startup behavior and visualization of dual-evaporator loop heat pipes. International Journal of Heat and Mass Transfer 246, 127053. https://doi.org/10.1016/j.ijheatmasstransfer.2025.127053

[82] Jingyu Cao, Zhanying Zheng, Muhammad Asim, Mingke Hu, Qiliang Wang, Yuehong Su, Gang Pei, Michael K.H. Leung, “A review on independent and integrated/coupled two-phase loop thermosyphons”, Applied Energy 280 (2020) 11588

**Igors Ušakovs** was born in 1969 in Kachkanar, Russia. He received his Master's degree in Physics and qualification as a theoretical physicist from the University of Latvia in 1993. His Master's Thesis was devoted to the quantum-mechanical description of diatomic molecules and was carried out under the supervision of Prof. Dr. habil. phys. Ruvins Ferbers.

In 2015, he co-founded Allatherm Ltd. together with Dr. Donatas Mishkinis, where he currently works as CEO and lead engineer.

He has been involved in several international projects, including those of the European Space Agency (ESA), focused on the development and experimental validation of two-phase heat-transfer systems. This includes the development of two key technologies for the lunar space station – the xenon refuelling compressor and the multi-evaporator cold plate.

His research interests include two-phase heat transfer, loop heat pipes (LHP), thermosyphons, and smart thermal management of electrical equipment.